Investigation of structural failure mechanisms of LiCoO2 at high voltage and material optimization through aluminum doping

Marie Duffiet

université de BORDEAUX

THÈSE PRÉSENTÉE

POUR OBTENIR LE GRADE DE

DOCTEUR DE

L'UNIVERSITÉ DE BORDEAUX

ÉCOLE DOCTORALE DES SCIENCES CHIMIQUES

SPÉCIALITÉ : PHYSICO-CHIMIE DE LA MATIERE CONDENSEE

Par Marie DUFFIET

Investigation of structural failure mechanisms of $LiCoO_2$ at high voltage and material optimization through aluminum doping

Sous la direction de : Dany CARLIER-LARREGARAY

Soutenue le 12 juin 2019

Membres du jury :

M. DEDRYVERE, Rémi	Professeur, UPPA/IPREM	Président
Mme CASAS-CABANAS, Montserrat	Directeur de recherche, CIC Energigune	Rapporteur
M. BOUCHER, Florent	Directeur de recherche, CNRS/IMN	Rapporteur
M. MAGLIONE, Mario	Directeur de recherche, CNRS/ICMCB	Examinateur
M. CABELGUEN, Pierre-Etienne	Docteur, UMICORE	Examinateur
Mme CARLIER-LARREGARAY, Dany	Professeur, Université de Bordeaux	Directrice de thèse
M. DELMAS, Claude	Directeur de recherche, CNRS/ICMCB	Co-encadrant
Mme MONTESDEOCA SANTANA, Amada	Docteur, UMICORE	Membre Invité

Titre : Compréhension des mécanismes structuraux limitant les performances de $LiCoO_2$ à haut potentiel dans des batteries Li-ion et optimisations des matériaux par dopage Al

Résumé court :

L'oxyde lamellaire $LiCoO_2$ (LCO) est un des matériaux d'électrode positive les plus communément utilisés dans les batteries Li-ion commerciales. Les efforts fournis pour contrôler la morphologie des particules de LCO ont grandement contribué à améliorer la compacité des électrodes, augmentant de fait la densité d'énergie des batteries. Celle-ci pourrait être encore améliorée grâce à l'augmentation du potentiel limite haut atteint lors de la charge de la batterie.

Dans une première partie de ce manuscrit, plusieurs séries de poudres de LCO ont été synthétisées en effectuant un contrôle poussé de la taille des particules et de la stoechiométrie en Li ($1.00 \leq Li/Co \leq 1.04$) dans l'optique de caractériser leurs propriétés électrochimiques. Une étude par diffraction des rayons X (DRX) *in situ* a permis de suivre les changements structuraux observés lors de la désintercalation des ions Li dans deux matériaux LCO chargés à 5.2 V: les transitions de phase observées dans le cas de LCO dit « stoechiométrique » ($Li/Co = 1.00$) s'avèrent être plus nombreuses que précédemment reporté dans la littérature scientifique. La formation des phases H1-3 et O1 est confirmée, avec l'apparition supplémentaire d'une structure hybride entre ces deux phases. L'existence de défauts dans le matériau surlithié n'empêche pas la formation des phases H1-3 et O1, mais retarde leur apparition et modifie leurs paramètres structuraux.

Dans une deuxième partie, le dopage aluminium à $4\%_{at}$ de ces poudres est envisagé. Plusieurs matériaux $LiCo_{0.96}Al_{0.04}O_2$ (LCA) à stoechiométrie Li/(Co+Al) variable ont été synthétisés par voie solide afin d'obtenir un dopage le plus homogène possible. La caractérisation fine de ces matériaux par DRX et spectroscopie RMN du solide des noyaux ^{7}Li, ^{27}Al, ^{59}Co permettent de démontrer qu'une répartition d'aluminium homogène est possible au sein de $LiCo_{0.96}Al_{0.04}O_2$ grâce à une préparation en deux étapes : formation d'un LCA surlithié ($Li/(Co+Al) > 1.00$) suivi d'un réajustement de la stoichiométrie en Li ($Li/(Co+Al) = 1.00$).

Mots clés : Batterie Li-ion, Electrode positive, $LiCoO_2$, Haut potentiel, Transitions de phase, Dopage Al

Title: Investigation of structural failure mechanisms of $LiCoO_2$ at high voltage and material optimization through aluminum doping

Abstract :

Lithium cobalt oxide (LCO) is widely used as positive electrode material for Li-ion batteries. In order to achieve higher energy density, significant improvement of LCO's packing density has been recently done by controlling the particles morphology and electrode processing. However, the upper charge cutoff voltage of LCO has barely changed, and would be a way to further enhance the energy density.

In this PhD, we focus first in a careful preparation of different LCO samples with an accurate control of the Li stoichiometry ($1.00 \leq Li/Co \leq 1.04$) and particles size to characterize their electrochemical properties. For some selected samples, we study the phase transition mechanisms involved at high voltage during Li de-intercalation using in situ synchrotron X-ray diffraction (SXRD): more phase transitions than previously reported have been evidenced for the stoichiometric LCO (Li/Co = 1.00) charged up to 5.2 V. In particular, while the formation of the H1-3 and O1 phases is confirmed, intermediate intergrowth structures are also stabilized. The existence of defects in overlithiated LCO (Li/Co > 1.00) does not hinder, but delay the formation of the high voltage of H1-3 and O1 phases, although structurally modified.

In a second part, we focus on the material optimization though 4% Al-doping using a solid state route. Several compounds were prepared using various Li/(Al+Co) stoichiometries, with different particles sizes. Our efforts were dedicated to accurately characterize the Al doping homogeneity in the samples that affects the electrochemical properties. Using SXRD and ^{7}Li, ^{27}Al and ^{59}Co MAS NMR as complementary tools, we show that homogeneous Al-doping in stoichiometric LCO can be achieved using Li-excess in a first step of the synthesis followed by a stoichiometry readjustment to Li/(Co+Al) = 1.00.

Keywords : Li-ion battery, Positive electrode, $LiCoO_2$, High voltage, Phase transitions, Al doping

Institut de Chimie de la Matière Condensée de Bordeaux

ICMCB/CNRS – UMR 5026

87, Avenue du Dr Schweitzer, 33608 PESSAC

Table of contents.

Résumé étendu en français

L'oxyde lamellaire O3-$LiCoO_2$ (groupe d'espace *R-3m*) est un des matériaux d'électrode positive les plus communément utilisés dans les batteries Li-ion commerciales. Le cyclage de ces batteries se fait généralement entre 3.0 et 4.4 V *vs* graphite (4.3 V vs Li^+/Li), au cours duquel $x(Li^+) = 0.62$ peuvent être désinsérés réversiblement du matériau initial, correspondant à une capacité spécifique de 174 mAh/g.

Un excès en lithium lors de la synthèse a permis de révéler l'existence de composés analogues dits surlithiés[1], notés O3-$Li_{1+t}Co_{1-t}O_{2-t}$, au sein desquels les Li^+ en excès substituent certains Co^{3+} présents dans les feuillets (voir Figure 1). Bien que possédant la même structure de type O3 que $LiCoO_2$, il a été démontré que l'existence de défauts locaux induits par l'excès de Li^+ dans les feuillets de ces composés menait à une signature électrochimique à bas potentiel (< 4.3 V) complètement différente de celle de $LiCoO_2$ (voir Figure 2).

Peu d'articles[2–5] font état du comportement électrochimique de $LiCoO_2$ au-delà de 4.3 V *vs* Li^+/Li, et il n'existe pas à notre connaissance d'étude similaire pour les composés surlithiés. Or, un gain de capacité notable pourrait être envisagé par l'extraction des ions Li^+ restants dans la structure hôte à plus haut potentiel. A l'heure actuelle, les tests menés à de tels potentiels conduisent à une mauvaise cyclabilité globale de la batterie, qui empêche toute application industrielle. Deux phénomènes pourraient être les causes majeures de cette mauvaise performance : la forte dégradation de l'électrolyte, et/ou les transitions de phase (O3 → H1,3 → O1) observées pour $LiCoO_2$, potentiellement incluant des fautes d'empilement. Les structures postulées pour chacune des phases formées à haut potentiel sont schématiquement représentées en Figure 3.

(1) Levasseur, S. *et al. Chem. Mater.* **15,** 348–354 (2003).
(2) Ohzuku, T. & Ueda, A. *J. Electrochem. Soc.* **141,** 2972–2977 (1994).
(3) Amatucci, G. G., Tarascon, J. M. & Klein, L. C. **143,** 1114–1123 (1996).
(4) Chen, Z., Lu, Z. & Dahn, J. R. *J. Electrochem. Soc.* **149,** A1604–A1609 (2002).
(5) Ven, A. V. der, Aydinol, M. K. & Ceder, G. *J. Electrochem. Soc.* **145,** 2149–2155 (1998).

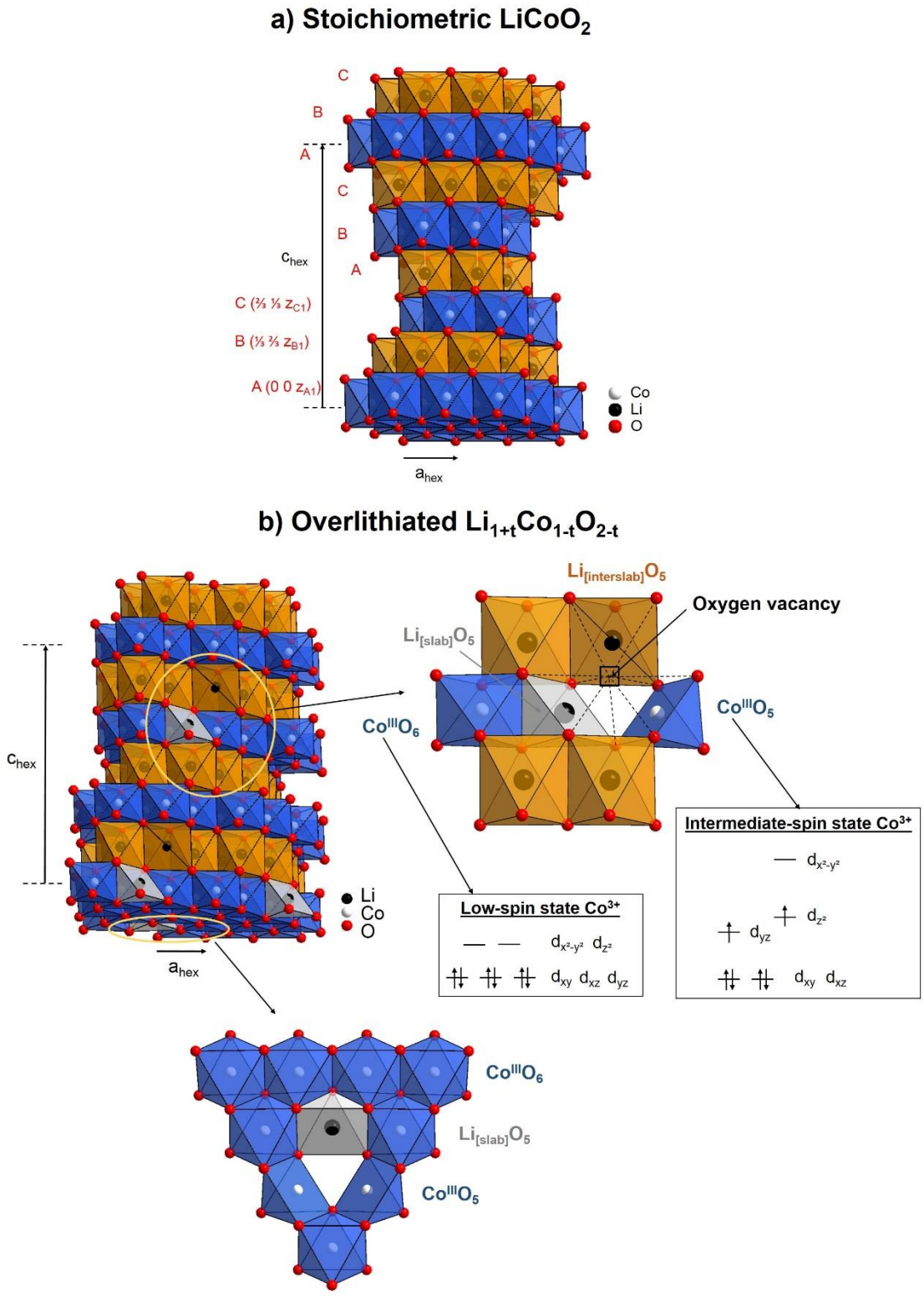

Figure 1. *a) Représentation schématique de la structure de $LiCoO_2$ dit "stoechiométrique" (Li/Co = 1.00) et de son équivalent surlithié (b), de formule « $Li_{1+t}Co_{1-t}O_{2-t}$ » (Li/Co > 1.00).*

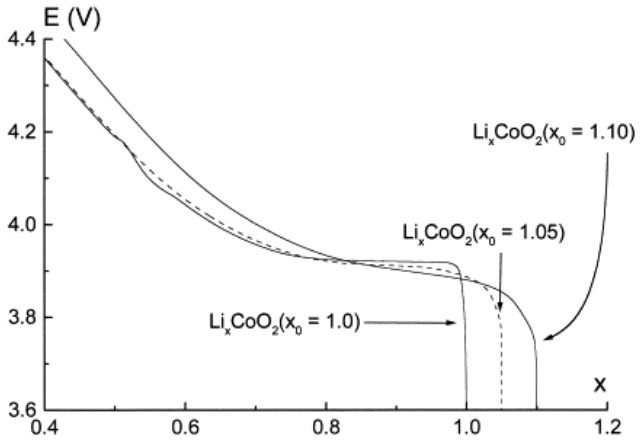

***Figure 2**. Courbe galvanostatique enregistrée lors de la première charge de batteries $LiCoO_2$//Li avec des ratios Li/Co différents (resultat obtenu par Stéphane Levasseur[1]).*

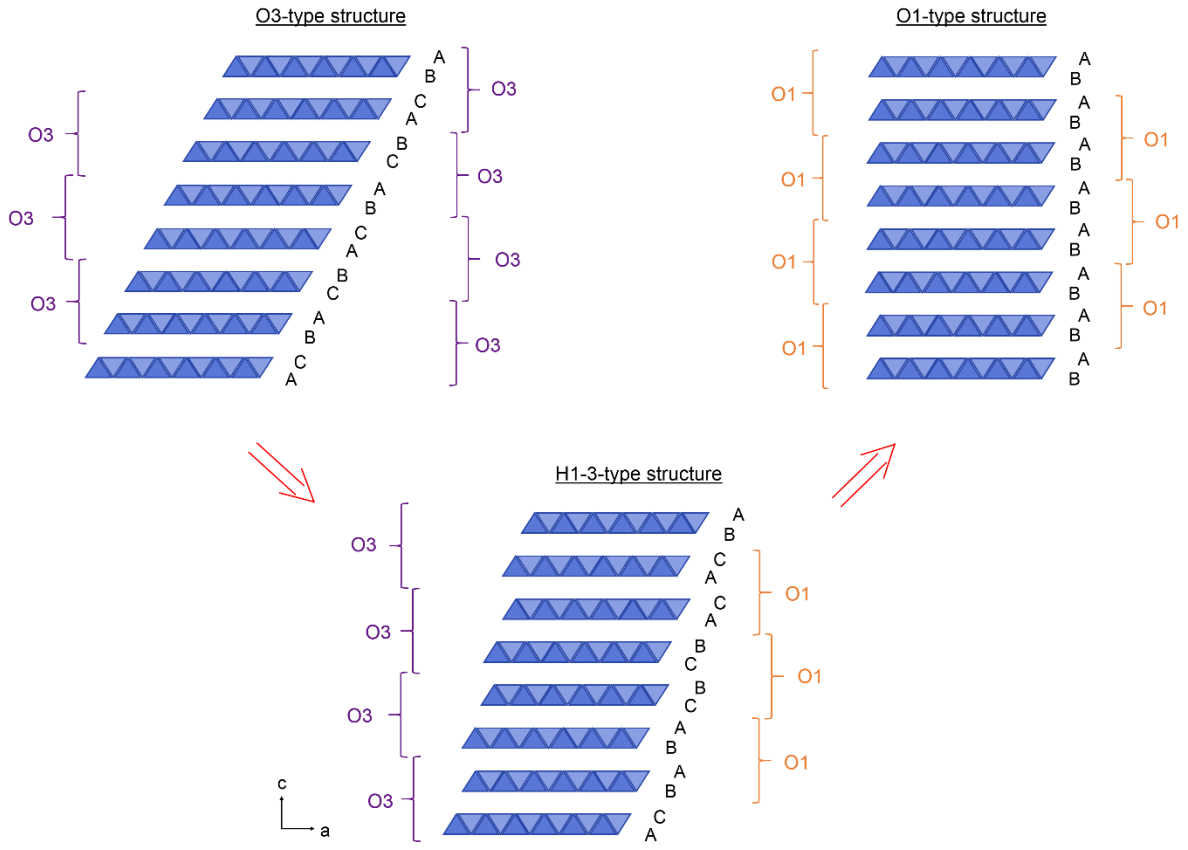

***Figure 3.** Représentation schématique des empilements de feuillets CoO_2 dans des structures de type O3, H1-3 et O1. Les lettres A, B, et C sont associées aux 3 sites possiblement occupés par les atomes d'oxygène, de coordonnées (fixées arbitrairement): (A(0, 0, z_A), B(⅓, ⅔, z_B) and C(⅔, ⅓, z_C).*

Un premier élément de progression est donc la compréhension des mécanismes de formation des phases H1,3 et O1 à haut potentiel selon la stœchiométrie de la phase initiale.

Dans une première partie de ce manuscrit, plusieurs séries de poudres de LCO ont été synthétisées en effectuant un contrôle poussé de la taille des particules et de la stoechiométrie en Li ($1.00 \leq Li/Co \leq 1.04$) dans l'optique de caractériser leurs propriétés électrochimiques. Le contrôle de la stoechiométrie Li/Co des poudres a notamment pu être réalisé grâce à la spectroscopie de résonance nucléaire magnétique (RMN) du ^{7}Li, technique clé pour mettre en évidence la surlithiation des phases $Li_{x0}CoO_2$ (Figure 4). En effet, de nombreux pics supplémentaires sont observables dans les spectres de composés préparés avec $Li/Co > 1.00$, révélant la variété d'environnements chimiques différents du Li trouvés dans ces phases de par la présence de Li en substitution de certains Co dans le feuillet.

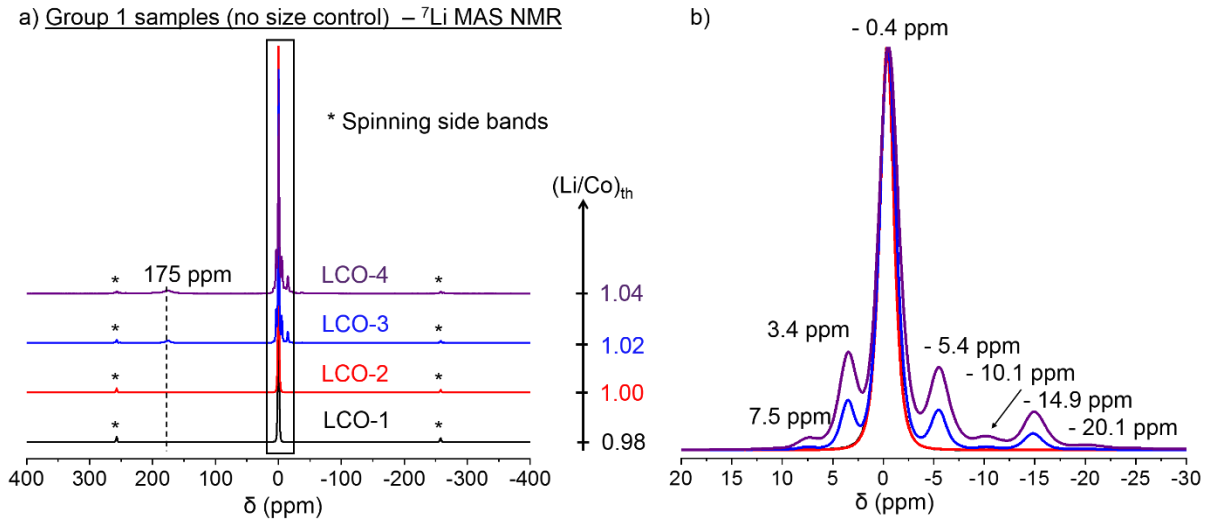

***Figure 4**. Spectres RMN du ^{7}Li des différentes poudres de $LiCoO_2$ synthétisées ($0.98 \leq Li/Co \leq 1.04$) enregistrés à 116.66 MHz pour une fréquence de rotation de 30kHz.*

Une étude par diffraction des rayons X (DRX) *in situ* a permis de suivre les changements structuraux observés lors de la désintercalation des ions Li dans deux matériaux LCO chargés à 5.2 V: les transitions de phase observées dans le cas de LCO dit « stoechiométrique » (Li/Co = 1.00) s'avèrent être plus nombreuses que précédemment reporté dans la littérature scientifique (Figure 5). La formation des phases H1-3 et O1 est confirmée, avec l'apparition

supplémentaire d'une structure hybride entre ces deux phases. L'existence de défauts dans le matériau surlithié n'empêche pas la formation des phases H1-3 et O1, mais retarde leur apparition en termes de potentiel électrochimique et modifie leurs paramètres structuraux. Dans le cas du matériau stoechiométrique, des pics de diffraction suggérant la formation d'une phase (X) intermédiaire avant la phase O1 ont également été observés lors de la charge du matériau. La structure exacte de cette nouvelle phase (X) reste inconnue, le traitement de données étant rendu

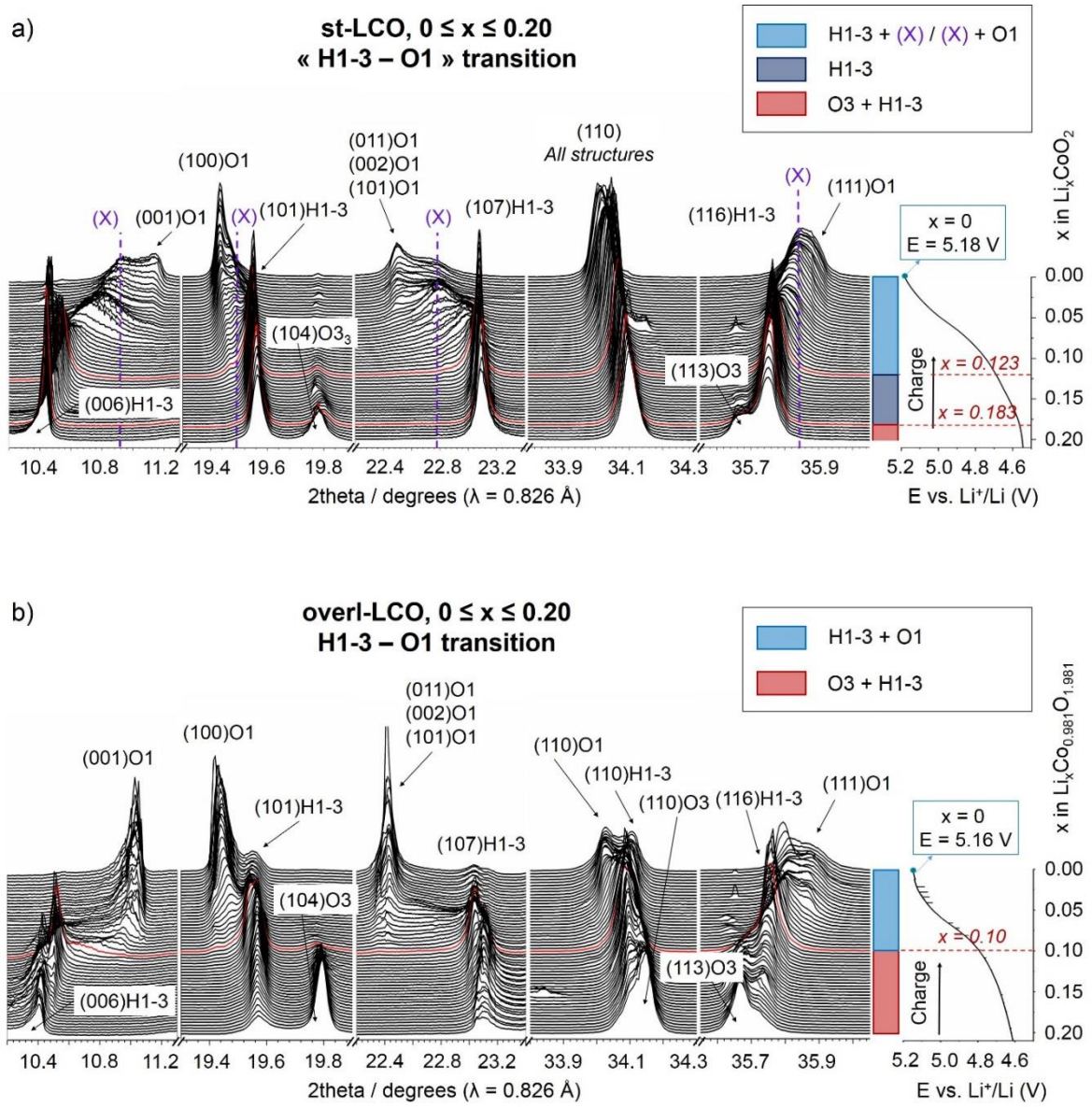

Figure 5*. Diffractogrammes cumulés enregistrés lors de la charge à C/20 de batteries Li_xCoO_2//Li entre 4.30 et 4.55 V (0.40 ≥ x ≥ 0.20) dans le cas d'un matériau initial dit "stoechiométrique" (Li/Co = 1.00) (a) et d'un matériau surlithié (Li/Co = 1.04) (b).*

particulièrement difficile par la présence de fautes d'empilement. Il est néanmoins raisonnable de penser que la phase (X) possède une structure très analogue aux phases H1-3 et O1, alternant entre un empilement AB-AB dit de type « O1 » et la séquence plus complexe de type « H1-3 ».

Une étude DRX *in situ* complémentaire réalisée au synchrotron (SDRX) a permis de confirmer les conclusions tirées lors de l'étude préliminaire réalisée en laboratoire (Figure 5), mais également de plus finement étudier la transition structurale dite « monoclinique » attendue pour x ~ 0.5 Li restants dans le matériau Li_xCoO_2, également plus complexe que précédemment reporté dans la littérature. En effet, la formation de non pas une mais bien deux phases monocliniques distinctes a pu être détectée via l'existence de pics de diffraction distincts (Figure 6). Des travaux complémentaires restent à effectuer.

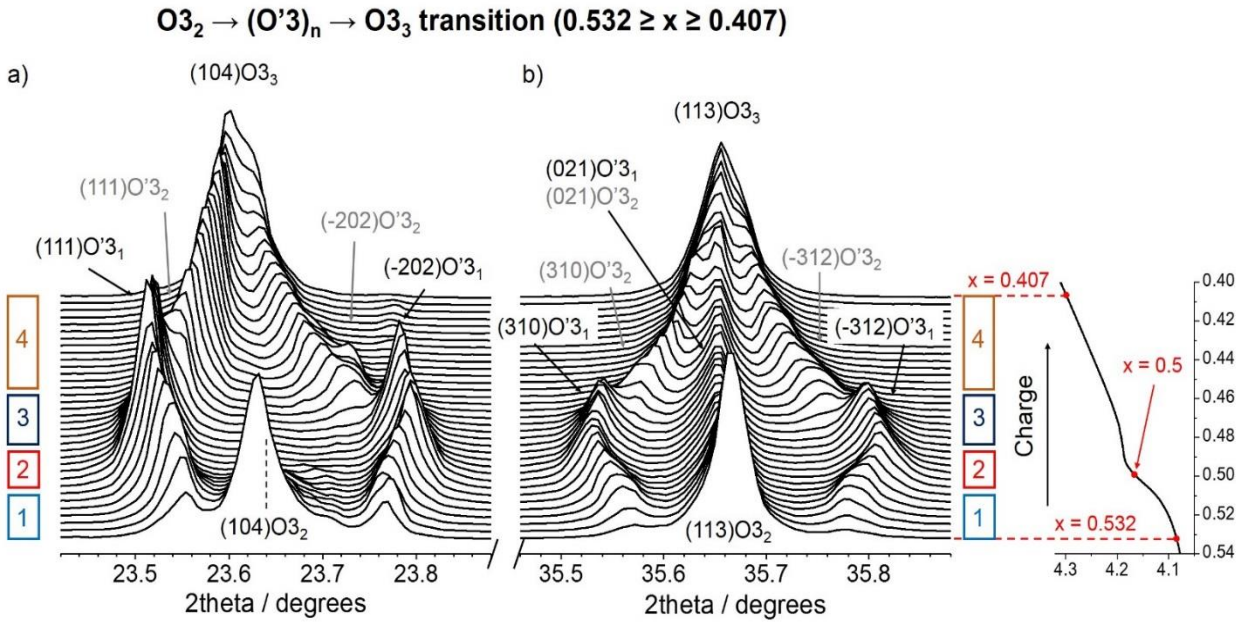

Figure 6*. Changements détectes dans les pics de diffraction* ***a)*** *(104)O3₂ et* ***b)*** *(113)O3₂ pendant la charge d'un matériau Li_xCoO_2 initialement stoechiométrique (Li/Co = 1.00) à C/20 pour 0.532 ≥ x ≥ 0.40, domaine de compositions pour lequel la transition O3 – O'3 est attendue*

Dans une deuxième partie, le dopage aluminium à 4%$_{at}$ de ces poudres a été envisagé. En effet, la majeure partie des articles concernant LCO et publiés ces dernières années est dédiée à l'optimisation de ce matériau via i) la substitution de certains Co^{3+} par de nouveaux dopants[6-8], ii) l'utilisation de « coatings » pour recouvrir les particules de LCO[9] ou iii) les deux approches simultanément, dans le but d'améliorer ses performances à haut potentiel. Bien que le cyclage des phases $LiCo_xAl_{1-x}O_2$ conduisent systématiquement à une perte de capacité en cyclage[10,11], des effets bénéfiques ont été observés sur la structure du matériau, avec notamment des variations de volume fortement réduites[12,13] ainsi que l'absence de phase spinelle $LiCo_2O_4$ en surface des particules[14].

Bien que les premières études des phases $LiCo_xAl_{1-x}O_2$ remontent aux années 1990, peu d'articles se sont concentrés sur des phases avec un taux d'aluminium inférieur à 10 %$_{at}$. Les ions Al^{3+} étant électrochimiquement inactifs, le pourcentage d'Al^{3+} dans le matériau se doit en effet d'être faible pour que les phases $LiCo_xAl_{1-x}O_2$ restent viables industriellement parlant grâce à des capacités théoriques proches de celle du matériau LCO non dopé. Par ailleurs, la stoechiométrie de départ Li/(Co+Al) n'est que très rarement controlée alors même que les études de Levasseur et. al[15] ont démontré la perte de capacité induite par la présence de Li en excès au sein du matériau.

Plusieurs matériaux $LiCo_{0.96}Al_{0.04}O_2$ (LCA) à stoechiométrie Li/(Co+Al) variable ont donc été synthétisés dans le cadre de cette thèse. La préparation de ces matériaux a été exclusivement réalisée via une approche voie solide, déjà largement utilisée pour la production industrielle de LCO (Figure 7), mais jamais considérée dans la littérature scientifique. Cette approche se devait de répondre à plusieurs exigences : i) une stoechiométrie initiale Li/(Co+Al) $\leq$ 1.00 pour toutes les phases $LiCo_{0.96}Al_{0.04}O_2$ préparées – sans pour autant éliminer l'utilisation de Li_2CO_3 en excès à certaines étapes de la synthèse (Figure 7) et ii) une répartition homogène de l'aluminium au sein du matériau.

(6) S. A. Needham, G. X. Wang, H. K. Liu, V. A. Drozd, and R. S. Liu, *J. Power Sources*, **174**, 828–831 (2007).
(7) M. Zou, M. Yoshio, S. Gopukumar, and J. Yamaki, *Chem. Mater.*, **17**, 1284–1286 (2005).
(8) P. Prahasini, M. Sivakumar, R. Subadevi, and F. M. Wang, *Adv. Mater. Res.*, **584**, 345–349 (2012).
(9) Y. J. Kim, J. Cho, T.-J. Kim, and B. Park, *J. Electrochem. Soc.*, **150**, A1723–A1725 (2003).
(10) G. Ceder et al., *Nature*, **392**, 694 (1998).
(11) W.-S. Yoon, K.-K. Lee, and K.-B. Kim, *J. Electrochem. Soc.*, **147**, 2023–2028 (2000).
(12) Y.-I. Jang et al., *J. Electrochem. Soc.*, **146**, 862–868 (1999).
(13) S.-T. Myung, N. Kumagai, S. Komaba, and H.-T. Chung, *Solid State Ion.*, **139**, 47–56 (2001).
(14) H. Wang, Y.-I. Jang, B. Huang, D. R. Sadoway, and Y.-M. Chiang, *J. Electrochem. Soc.*, **146**, 473–480 (1999).
(15) S. Levasseur, M. Menetrier, E. Suard, and C. Delmas, *Solid State Ion.*, **128**, 11–24 (2000).

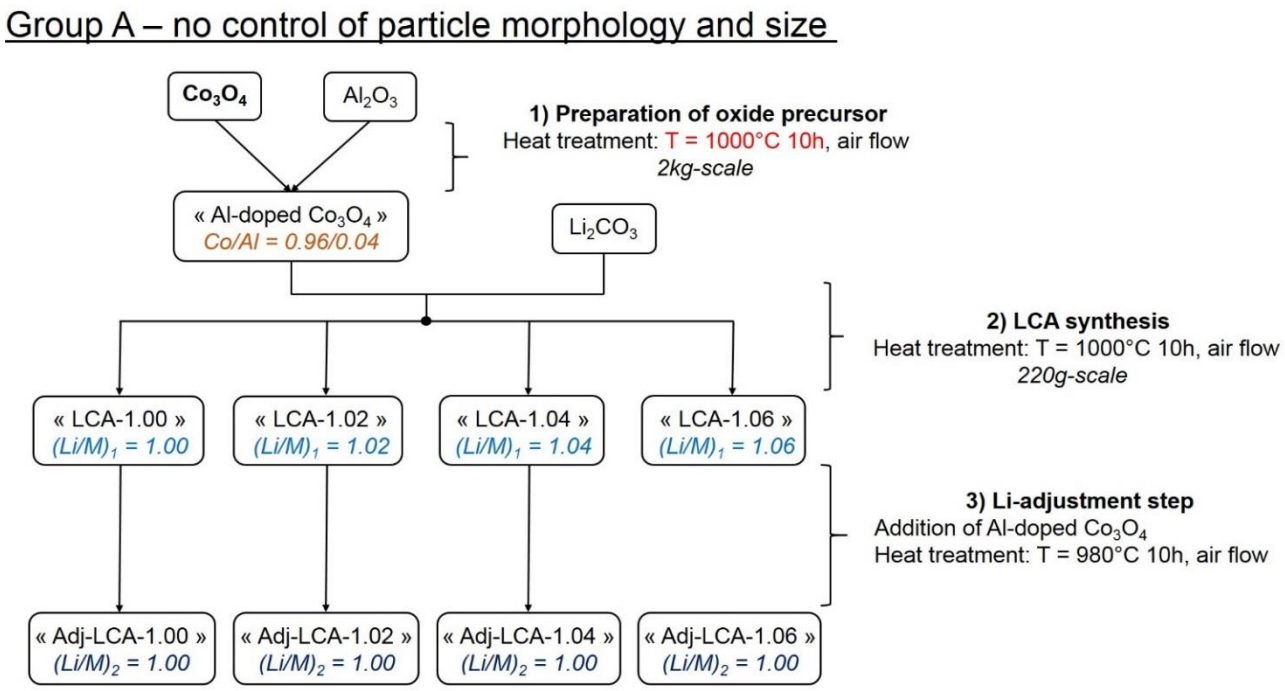

Figure 7. *Schéma des différentes synthèses de $LiCo_{0.96}Al_{0.04}O_2$ (LCA) réalisées dans le cadre du projet de thèse.*

L'utilisation combinée de la SDRX (Figure 8) et de la spectroscopie RMN du solide des noyaux ^{7}Li, ^{27}Al, et ^{59}Co (Figure 9) s'est révélée être la clé dans l'élaboration d'un protocole systématique pour évaluer l'homogénéité du dopage Al dans les phases $LiCo_{0.96}Al_{0.04}O_2$ préparées. En effet, les pics de diffraction de phases $LiCo_{0.96}Al_{0.04}O_2$ au sein desquelles l'aluminium n'est pas réparti de façon statistique présentent de fortes asymétries, de par l'existence d'une distribution de paramètres de maille due à des taux d'Al variant localement (Figure 8). La symétrie des pics de diffraction de certains matériaux $LiCo_{0.96}Al_{0.04}O_2$ constitue donc un premier élément allant dans le sens d'une répartition homogène de l'aluminium.

Dans le cas de la RMN de l'^{27}Al, les pics visibles au sein des spectres sont respectivement caractéristiques des environnements de type Al-(Al_nCo_{6-n}) ($0 \leq n \leq 6$) existant au sein des phases $LiCo_{0.96}Al_{0.04}O_2$ (Figure 9). Les intensités de chaque pic pouvant être estimées via l'utilisation d'une loi binomiale dans l'hypothèse d'une répartition statistique de l'aluminium pour une composition donnée (ici fixée à $4\%_{at}$), les matériaux $LiCo_{0.96}Al_{0.04}O_2$ présentant des pics d'intensité supérieure à celle postulée pour les contributions dites « riches en Al » (telles que Al-(Al_6Co_0), Al-(Al_5Co_1) ou Al-(Al_4Co_2)) présentent donc une distribution d'ions Al^{3+} inhomogène. Des

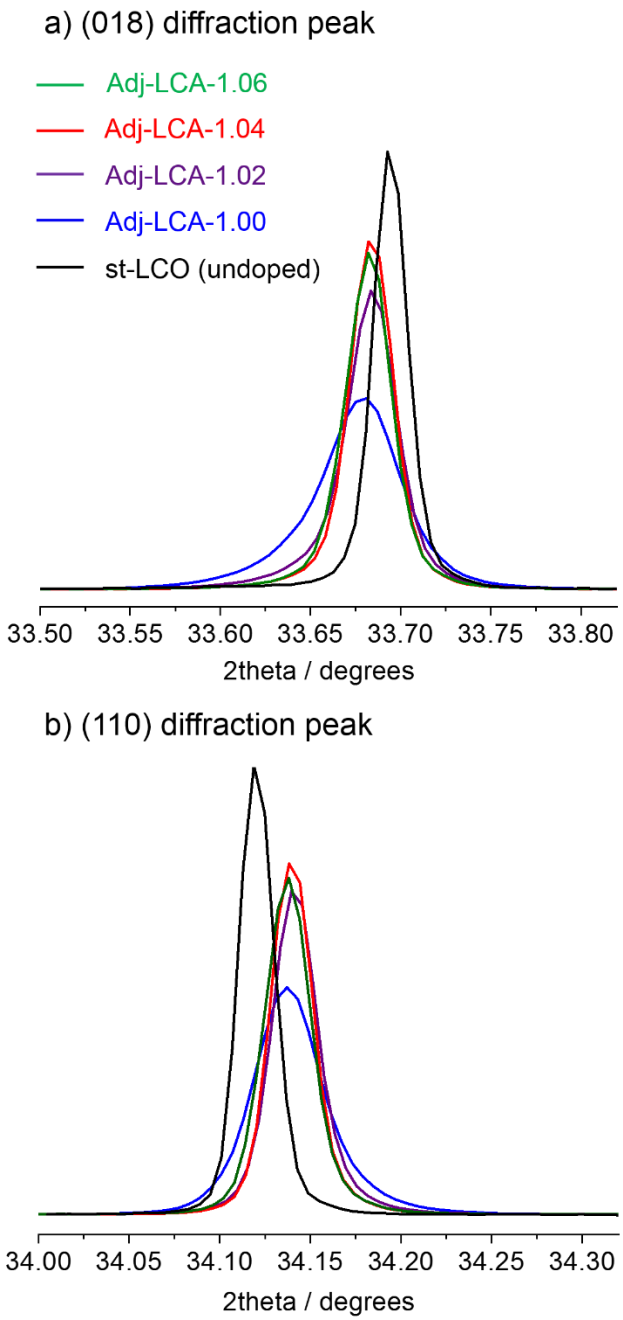

Figure 8. *Zoom sur les pics de diffraction (108) et (110) des diffractogrammes enregistrés pour différents* $LiCo_{0.96}Al_{0.04}O_2$ *(LCA) préparés par voie solide.*

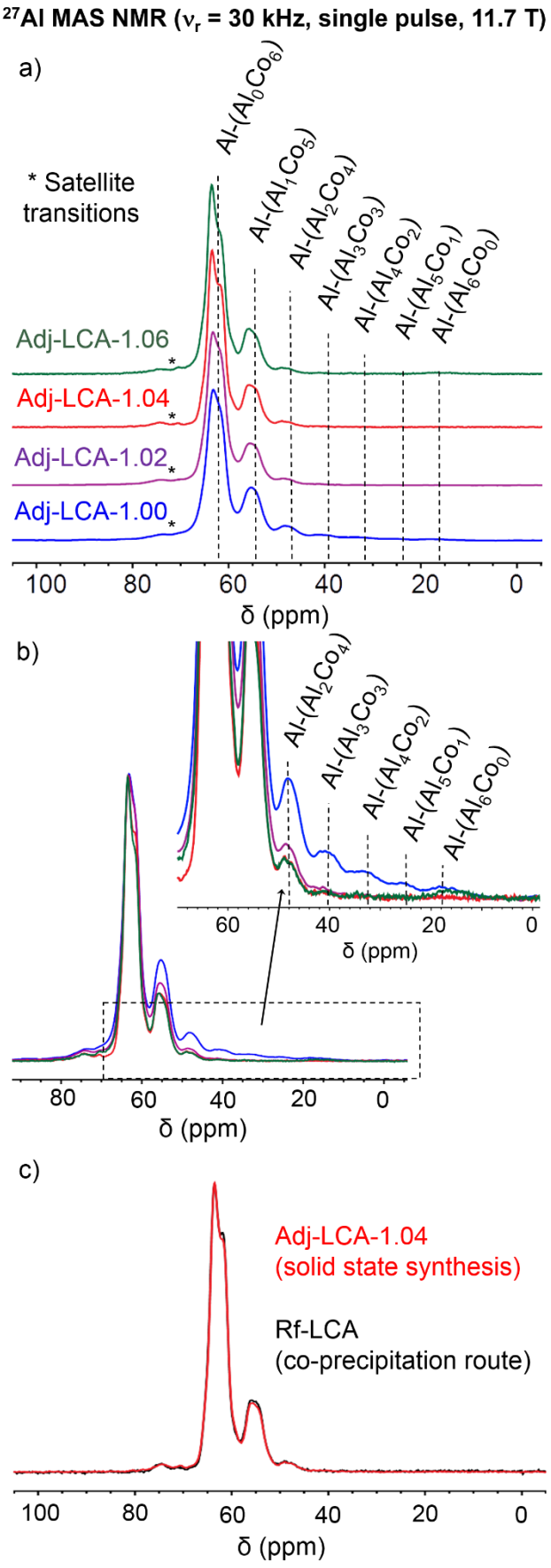

Figure 9. Spectres *^{27}Al MAS NMR spectra enregistés à 130.33 MHz avec une vitesse de rotation de 30 kHz pour les différentes phases $LiCo_{0.96}Al_{0.04}O_2$ (LCA) préparées par voie solide.*

spectres RMN superposables au spectre théorique peuvent donc être considérés caractéristiques de matériaux $LiCo_{0.96}Al_{0.04}O_2$ homogènes.

Le protocole précédent a ainsi permis de mettre en évidence que la synthèse d'un matériau $LiCo_{0.96}Al_{0.04}O_2$ dopé homogènement et de stoechiométrie initiale Li/(Co+Al) = 1.00 est possible par voie solide. Sa préparation a été réalisée en deux étapes : formation d'un LCA surlithié (Li/(Co+Al) > 1.00) suivi d'un réajustement de la stoichiométrie en Li (Li/(Co+Al) = 1.00). Ses performances électrochimiques ainsi que les mécanismes réactionnels impliqués restent néanmoins à évaluer.

General introduction

With a theoretical specific capacity as high as 274 mAh/g, $LiCoO_2$ (LCO) was identified as a promising positive electrode materials for non aqueous secondary batteries by Goodenough[1] in 1980. Its ability to reversibly de-intercalate and re-intercalate lithium with a graphite electrode over hundreds of cycles – coupled with an excellent rate capability and easy synthesis – quickly led to its first commercialization in full Li-ion batteries (LiBs) by Sony[2] in 1991, meant for the portable electronics market. Since then, LCO-based LiBs have been consistently implemented in smartphones (commercialized by Apple, Samsung…) and laptops (Lenovo, Acer, Dell, HP, Toshiba…). LCO has been estimated to represent 33 % of the cathode materials market by Benchmark Minerals Intelligence[3] in 2015. A share as high as 42 % has been put forth by Umicore for the same year (**Figure I1**).

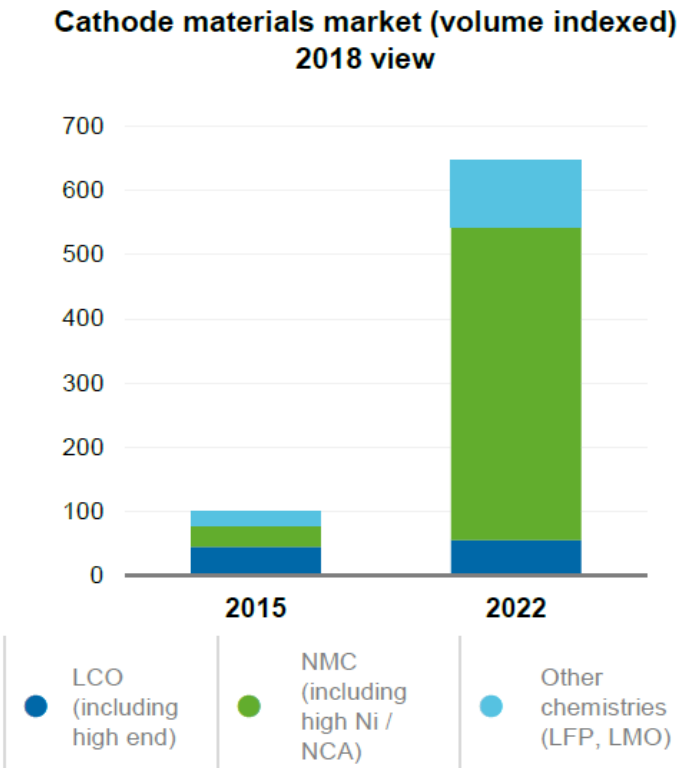

***Figure I1**. Cathode materials market previsions from Umicore for 2015 and 2022.*

In terms of volume, the demand for cathode materials is expected to be multiplied by 6.5 by 2022, with the main part being lithium nickel manganese cobalt oxides (NMC) and lithium nickel cobalt aluminum oxides (NCA) dedicated to electrical vehicles (EV). The high cost of cobalt, coupled with an elevated working voltage, make LCO an unsuitable candidate as positive electrode for such applications. On the other hand, LCO is expected to remain the material of choice for portative applications in the near future thanks to its excellent volumetric energy density, explaining its consistent stable share of the cathode market in 2022 (**Figure I1**).

The significant improvements of LCO's packing density (from 3.3 g/cm^3 in 1991 to 4.1 g/cm^3 nowadays) and the efforts dedicated to electrode processing have largely contributed to make it highly competitive in the energy intensive market. From a chemical point of view, it has consisted to focus on properly control the size and the morphology of LCO particles, which are now commonly found as mixture of large (several 10 micrometers) with smaller ones (a few micrometers) filling the gaps in the LCO-based electrodes. In the meantime, the upper charge cutoff

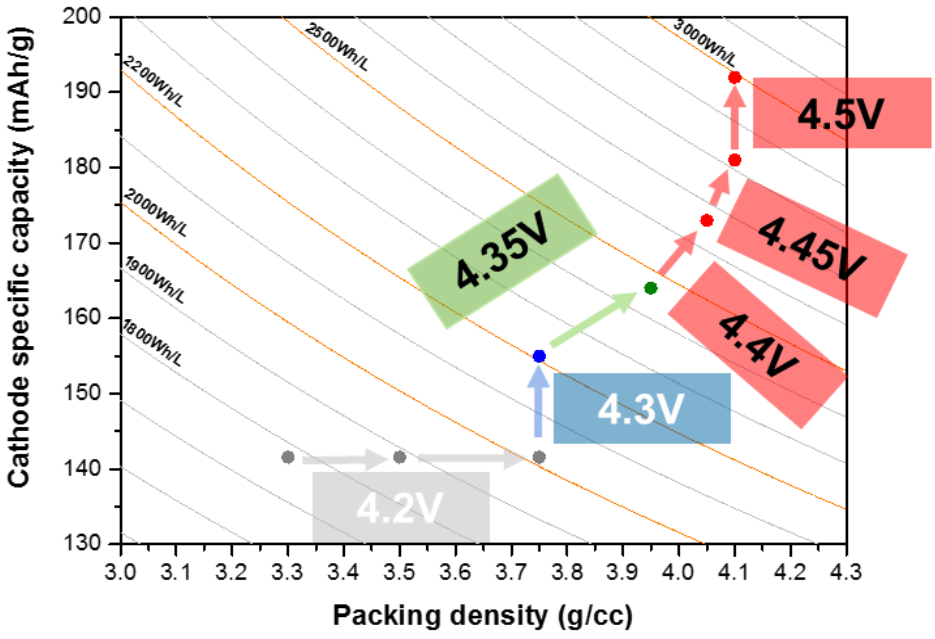

***Figure I2**. Evolution of LCO performance (cathode specific capacity, packing density, charge cutoff voltage) from 1991 (in grey) to nowadays (in red).*

voltage of LCO has barely changed, as depicted in **Figure I2**. Increasing the charge voltage higher than 4.3 V *vs.* Li^+/Li would enable the extraction of more Li^+ ions and reach charge capacities higher than 174 mAh/g, a value still far from the theoretical one. However, poor structural stability and interface issues have prevented any use of LCO at voltage higher than 4.5 V vs. Li^+/Li so far. Since the 2000's, most of the LCO-dedicated research has been directed towards material optimization through the use of coatings and dopings (such as aluminum doping) to overcome these issues, without really trying to gain more fundamental knowledge of these structural instabilities.

This project aims to contribute to the previously discussed aspects, by: i) identifying the formation mechanisms of high voltage Li_xCoO_2 phases during Li removal, ii) gaining more fundamental knowledge of their structures, iii) evaluating the possible influence of the initial Li/Co ratio on their formation and iv) synthesizing industrially-viable optimized Al-doped LCO.

This manuscript is divided into 3 parts in the following.

Part A is meant to lay the foundations for a more systematic investigation of the influence of the initial Li/Co ratio in LCO on the phase transitions occurring at high voltage. This part is dedicated to the careful synthesis and characterization of samples series with well controlled Li/Co ratios, also meeting the industrial expectations regarding the high packing density expected for LCO-based electrodes (therefore with a specific control on the size and morphology of the powders).

Part B is dedicated to the characterization of Li_xCoO_2 phases formed during the high voltage cycling of LCO. In particular, a comparative *in situ* X-ray diffraction (XRD) study of the phase transitions experienced by LCO materials with various initial Li/Co ratios (Li/Co = 1.00 or 1.05) will be provided.

Part C gathers all results regarding the development of a solid state synthesis of homogeneous Al-doped LCO.

Bibliography (general introduction)

(1) Mizushima, K.; Jones, P. C.; Wiseman, P. J.; Goodenough, J. B. Li_xCoO_2 ($0 < x < 1$): A New Cathode Material for Batteries of High Energy Density. *Mater. Res. Bull.* **1980**, *15* (6), 783–789.

(2) Yamahira, T.; Kato, H.; Anzai, M. Nonaqueous Electrolyte Secondary Battery. US5053297A, October 1, 1991.

(3) The Lithum Ion Supply Chain. *Benchmark* **2016**, 44–61. https://www.benchmarkminerals.com.

And more generally based on:

(4) Nitta, N.; Wu, F.; Lee, J. T.; Yushin, G. Li-Ion Battery Materials: Present and Future. *Mater. Today* **2015**, *18* (5), 252–264.

(5) Olivetti, E. A.; Ceder, G.; Gaustad, G. G.; Fu, X. Lithium-Ion Battery Supply Chain Considerations: Analysis of Potential Bottlenecks in Critical Metals. *Joule* **2017**, *1* (2), 229–243.

(6) Wang, L.; Chen, B.; Ma, J.; Cui, G.; Chen, L. Reviving Lithium Cobalt Oxide-Based Lithium Secondary Batteries-toward a Higher Energy Density. *Chem. Soc. Rev.* **2018**, *47* (17), 6505–6602. https://doi.org/10.1039/C8CS00322J.

(7) Fergus, J. W. Recent Developments in Cathode Materials for Lithium Ion Batteries. *J. Power Sources* **2010**, *195* (4), 939–954. https://doi.org/10.1016/j.jpowsour.2009.08.089.

Part A. Evaluation of the influence of initial ratio Li/Co and particle size on the electrochemical performance of $LiCoO_2$. Selection of samples

Part A. Evaluation of the influence of initial ratio Li/Co and particle size on the electrochemical performance of $LiCoO_2$. Selection of samples

A.1 Introduction. Bibliographic context.

A.1.1 Working principle of a Li-ion battery and electrochemical variables

Commercial batteries are made of several packed Li-ion cells, whose schematic representation is given in **Figure A1**. The negative electrode, made of graphite (or mesophase carbon microbeads, MCMB), is classically casted onto a copper current collector. The positive electrode material (here $LiMO_2$ with M = transition metal) is embedded with a conductive carbon additive (carbon black, Super P…) and a polymeric binder (such as polyvinylidene fluoride PVDF) on top of an aluminum current collector. Separators soaked in electrolyte are found between both electrodes. During the charge of the cell, Li ions are de-intercalated from the positive electrode $LiMO_2$ and re-intercalated between the sheets of graphite, as denoted by equations (1) and (3) in **Figure A1,** while the inverse motion is expected during the discharge (equations (2) and (4)). As the electrolyte only allows the motion of Li ions between the electrodes, all generated electrons circulate in the outer circuit.

When M = Co, conventional beliefs are that the charge compensation in $Li_{1-x}CoO_2$ is achieved through the oxidation of Co^{3+} into Co^{4+} during the charge of $LiCoO_2$//C cells (and through the reduction of Co^{4+} into Co^{3+} during the discharge), which has been supported by Co K-edge X-ray absorption[1] (XAS), ^{7}Li magic angle spinning nuclear resonance[2] (^{7}Li MAS NMR) and magnetic susceptibility measurements[3]. However, other processes involving i) partial oxidation[4–6] of both O^{2-} and Co^{3+} or even ii) the sole oxidation[7,8] of O^{2-} have also been experimentally observed. Still today, this matter seems to be debated[9].

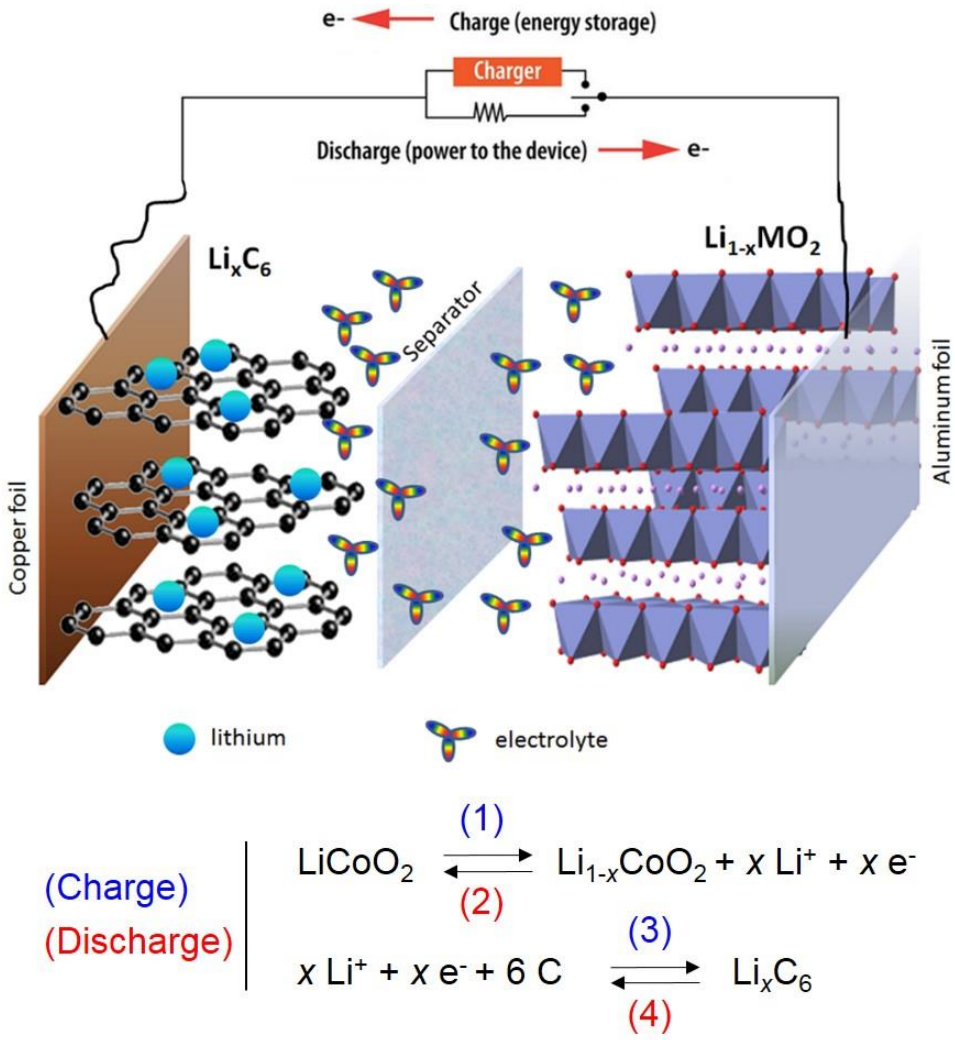

Figure A1. *Schematic working principle of a Li-ion cell (image reproduced from the University of Waterloo website).*

Comparative studies published in the scientific literature, used to assess the suitability of a material as battery component (such as positive or negative electrodes), are usually conducted in so-called "half-cell" setups, as opposed to the full $LiMO_2$//C commercial cells setup presented before. In a half-cell, either one of the electrode is replaced by a pure alkali metal while the second electrode is composed of the tested material usually mixed with a carbon additive and a binder. For instance, the performance of layered $LiMO_2$ phases as positive electrode material for Li-ion batteries has first been established from electrochemical tests using Li as counter electrode. The

comparison of each material's performance may be done through the recording of galvanostatic curves and the use of electrochemical variables, such as the capacity Q or the lithium content x in the active material at a specific time. They may be calculated as follow:

$$Q = I \times t = \frac{F \times \Delta x}{3600 \times M_W} \times m$$

Q: capacity (A.h)

I: current value (A)

t: duration of (dis)charge (h)

F: Faraday's constant (96485 C.mol^{-1})

Δx: number of exchanged charges (e^- or Li^+)

M_W: molecular mass of the active material (g.mol^{-1})

m: mass of the active material (g)

Besides, a maximum theoretical capacity C may also be estimated from the same formula for any electroactive material, considering the highest possible Δx. For $LiMO_2$ phases, this corresponds to Δx = 1. In the hypothesis of no side reactions in the battery, the theoretical capacity is reached after charging the material for a specific time *t* decided by the operator through the cycling rate input C/t. For instance, charging a $LiMO_2$//Li half cell at a C/20 rate means that the theoretical capacity C is reached after 20 hours.

While the estimation of the theoretical capacity has played a major role in further establishing the suitability of candidates as battery materials, the comparison of their galvanostatic curves has proven to be equally important. Indeed, as shown in **Figure A2**, structural changes experienced by these materials are responsible for features such as plateaus or voltage jumps in their associated electrochemical profiles, although their appearance can be impacted by the kinetics. Materials

experiencing many structural changes are usually not favored, as their corresponding change of volume may be detrimental for the battery life time. Abrupt voltage jumps (in red in **Figure A2**) reveals the existence of single phases with a peculiar composition with a well-defined structure. Plateaus are characteristic of biphasic domains, i.e. highlighting the simultaneous existence of two phases with distinct compositions and/or structures. A constant evolution of the voltage vs. x content corresponds to a solid solution behavior where the structure of the material is preserved but the x content varies. Such considerations will be widely applied throughout this manuscript.

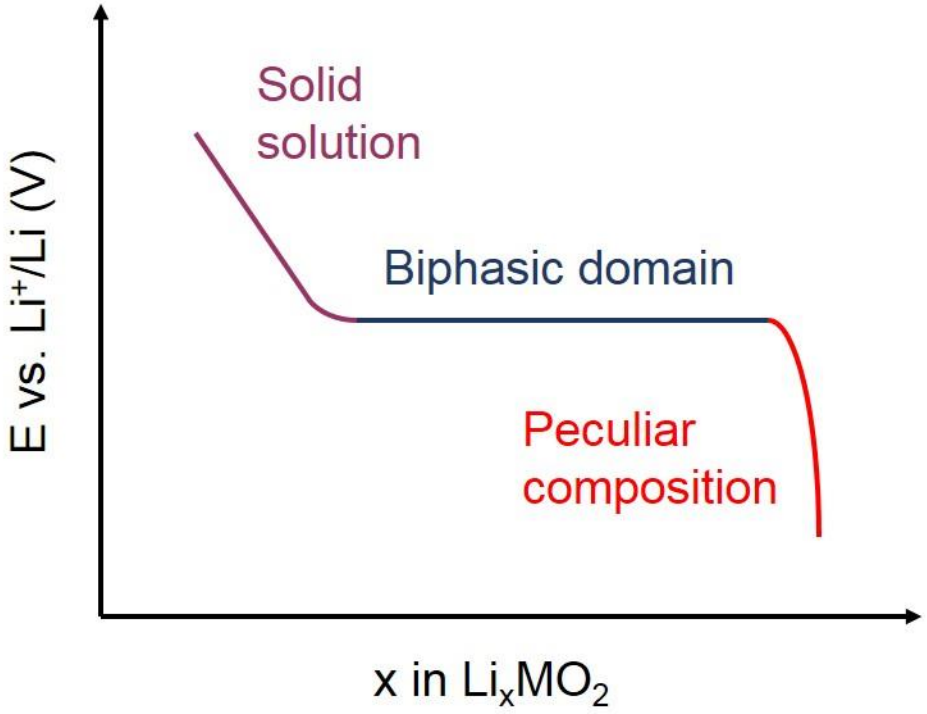

***Figure A2**. Schematic representation of a galvanostatic curve and identification of possible behaviors.*

A.1.2 $LiCoO_2$ as positive electrode for Li-ion batteries: structure, synthesis and electrochemical behavior

A.1.2.1 Structure and synthesis of $LiCoO_2$

LCO-based batteries always feature the so-called O3-$LiCoO_2$ as positive electrode material, also referred to as "HT-$LiCoO_2$". A schematic view of this structure, analogous to α-$NaFeO_2$, is presented in **Figure A3**. Though it is typically indexed in a rhomboedral symmetry (*R-3m* space group), it is more commonly represented in the hexagonal system. In this view, oxygens are found in the 6c (0 0 z_o) Wyckoff positions, and Co^{3+} and Li^+ respectively found in the octahedral 3a (0 0 0) and 3b (0 0 ½) sites. The hexagonal representation helps emphasizing its 2D character, as highlighted by the layers made of either CoO_6 (in blue) or LiO_6 octahedra (in orange) in **Figure A3**.

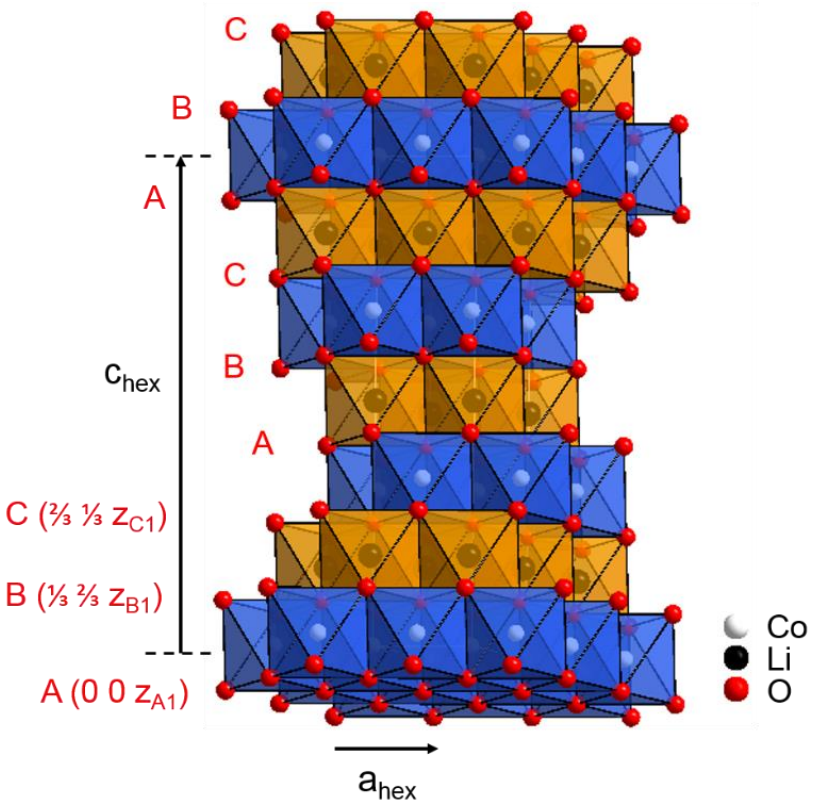

***Figure A3**. Schematic representation of the structure of O3-$LiCoO_2$, also known as HT-$LiCoO_2$. CoO_6 octahedra forming the layers are depicted blue, while LiO_6 octahedra are in orange.*

Note that CoO_2 and LiO_2 layers share edges with each other, and 3 layers of each are found in one unit cell. This crystallographic form is labelled as "O3-$LiCoO_2$" in a nomenclature developed by Delmas et al.[10], as Li is found in **O**ctahedral sites and **3** layers of CoO_2 define the unit cell. This label will be widely used throughout this manuscript. The layers are more commonly described by the oxygen stacking itself, here found as ABCABC type. The existence of such oxygen stacking implies that CoO_6 and LiO_6 units share edges.

Other structures have been reported for $LiCoO_2$ depending on the synthetic route adopted to prepare it, including metastable layered forms, such as the O2- and O4-polytypes[11–13] and a spinel form[14] usually denoted as "LT-$LiCoO_2$". Still, a wide variety of synthetic paths have proven to successfully lead to O3-LCO. Solid state reactions, typically between either Co_3O_4 or $CoCO_3$ and Li_2CO_3 powders, are among the most common methods used in the literature. The "HT" and "LT" notations were adopted following observations of the obtained $LiCoO_2$ phase from this route, as a function of the heat treatment temperature[14,15]: LT-form for $T < 400$ °C and HT structure for $T > 400$ °C. The exact mechanisms involved during the solid state reaction of Co_3O_4 and Li_2CO_3 were surprisingly only recently investigated by Wicker and Walker[16]. Through thermal and diffraction measurements, they evidenced several crucial steps, all taking place in the 700 – 990 K temperature range: i) aggregation of Li_2CO_3 particles (700 – 900 K), ii) melting of Li_2CO_3 (900 – 975 K), iii) liberation of CO_2 and diffusion of Li into Co_3O_4 at the liquid-solid interface, with intermediate formation of Li_2CoO_4 spinel quickly converting into layered $LiCoO_2$. Unlike a previous report from Timoshevskii et al.[17] and Ktalkherman et al.[18], they did not observe any Li_2O formed from the decomposition of Li_2CO_3.

Due to the high temperature (~ 900 – 1000 °C) required for the successful synthesis of O3-LCO from a solid state route[15,19,20], in good agreement with Wicker and Walker's work[16], solution

techniques were rapidly considered in order to prepare it at moderate temperatures. The development of methods in liquid media was also strongly motivated by the necessity to control the particle size and morphology of the LCO powders, which are crucial to their electrochemical performance in LiBs. Various sol-gel-type syntheses starting with Li and Co nitrates[21,22] or acetates[23,24] as reagents followed by a heat treatment at moderate temperature (T = 550 – 600 °C) were reported to form O3-$LiCoO_2$ with submicronic particle size. Attempts to fire the gel at lower temperatures (T ≤ 400 °C) though seems to lead to mixtures[25] of layered and spinel LCO, or pure spinel LCO if short firing times are used[22] (1 hour). Amatucci et al.[26] prepared layered LCO by ionic-exchange reaction between LiOH and CoOOH at T = 100 °C, though remaining organic impurities were detected in the final powder. As a matter of fact, the successful preparation of O3-LCO at such a low temperature is one more reason to discard the "LT" and "HT" notations. Performed at intermediate temperatures compared to sol-gel based- or solid state reactions (T = 650 – 750 °C), molten salt syntheses were also largely reported[27,28]. Micron-sized particles are typically formed from this route (1 to 15 µm).

All of the above-mentioned syntheses are here and there used in the literature. Solid state syntheses are however still favored for the industrial production of LCO, as it is not only easy to implement at a rather low cost. Additionally, large particle size may be achieved if one uses Li_2CO_3 as Li precursor. Indeed, as lithium carbonate melts at T = 723 °C and LCO partially dissolves[29] in melted Li_2CO_3, a beneficial flux role occurs and significantly drives the crystalline growth. Larger particle sizes were systematically reported for final LCO powders prepared in such conditions by Antolini et al.[30], Lundblad et al.[15] and Levasseur et al.[31]. A proportionality between the amount of excess Li_2CO_3 and the average particle size was also demonstrated, as the more excess Li_2CO_3, the larger the particle size. LCO powders prepared in stoichiometric conditions have been showed to

have particles whose average diameter is around 1-2 µm, while those prepared with a 10 % Li excess featured 20 µm sized particles. Even if the use of Li_2CO_3 excess has proven to be very useful to prepare LCO powders with large particle size, it was initially motivated to compensate Li losses during the firing of the precursors. Many groups still report to do so in the experimental sections of their articles. However, they often leave aside the possibility of chemical changes and new stoichiometries $Li_aCo_bO_c$ ($a \neq 1$, $b \neq 1$ and $c \neq 2$) for the resulting LCO phase, known since the late 1990's, as described in the following paragraph.

A.1.2.3 Overstoichiometry in $LiCoO_2$ and consequences on the electrochemical performance of LCO-based Li-ion batteries

The first evidence of lithium overstoichiometry in $LiCoO_2$ is found in an article from 1997 by Carewska et al.[32]. They showed that some Li could enter the structure, changing the Co valence in parallel. Additional data confirming the existence of overlithiated $LiCoO_2$ compounds (Li/Co > 1.00) was later gathered by other groups, and complementary studies were carried out to not only determine which site was occupied by the Li and in which proportions, but also to discuss the charge compensation mechanisms implied by its presence. The presence of paramagnetic cobalt in LCO prepared with an Li_2CO_3 excess was rapidly evidenced by Ganguly et al.[33] and Peeters et al.[34] – the former believing it was Co^{2+} – by the means of nuclear magnetic resonance (NMR) of ^6Li, ^7Li, and ^{59}Co nuclei. Additional peaks were found in the ^7Li NMR spectra of overlithiated LCO, while a single peak is normally expected in the NMR spectrum of stoichiometric LCO, arising from the diamagnetic-only environments of Li (being either low spin LS-Co^{3+} or impurities like Li_2CO_3 or LiOH). Several other groups later agreed on the existence of Co^{2+} in nonstoichiometric LCO, accompanied by oxygen deficiency[35–39]. Levasseur et al.[35] also suggested that the stoichiometry for Co was below 1.00.

Further work from Imanishi et al.[40] and Levasseur et al.[41] eventually reported another charge compensation mechanism, in which the existence of paramagnetic Co^{2+} in nonstoichiometric LCO was no longer considered. Indeed, the former found that all cobalt was in the +III oxidation state[39], and that the electronic neutrality was still maintained thanks to oxygen vacancies. By varying the initial Li/Co ratios used during the preparation of LCO, they also demonstrated that passed Li/Co = 1.15, no more Li could be accepted within the structure – the rest remaining within Li_2CO_3. In the meantime, Levasseur et al.[31,41] also came to the conclusion that all Co remains at the +III

oxidation state in overlithiated LCO. They proposed a potential structure for overlithiated LCO compounds using a set of techniques such as ^{7}Li MAS NMR, electrical conductivity measurements, X-ray and neutron diffraction and electrochemical tests, inspired by previous findings[42] on $Li_{x0}Co_{1-y}Mg_yO_2$ ($x_0 > 1.00$). Its schematic representation may be found in **Figure A4.a**.

In this model system, the excess Li^+ is directly found in the CoO_2 layers of LCO, substituting some of the Co^{3+} ions. The structure itself is analogous to the one of stoichiometric LCO shown in

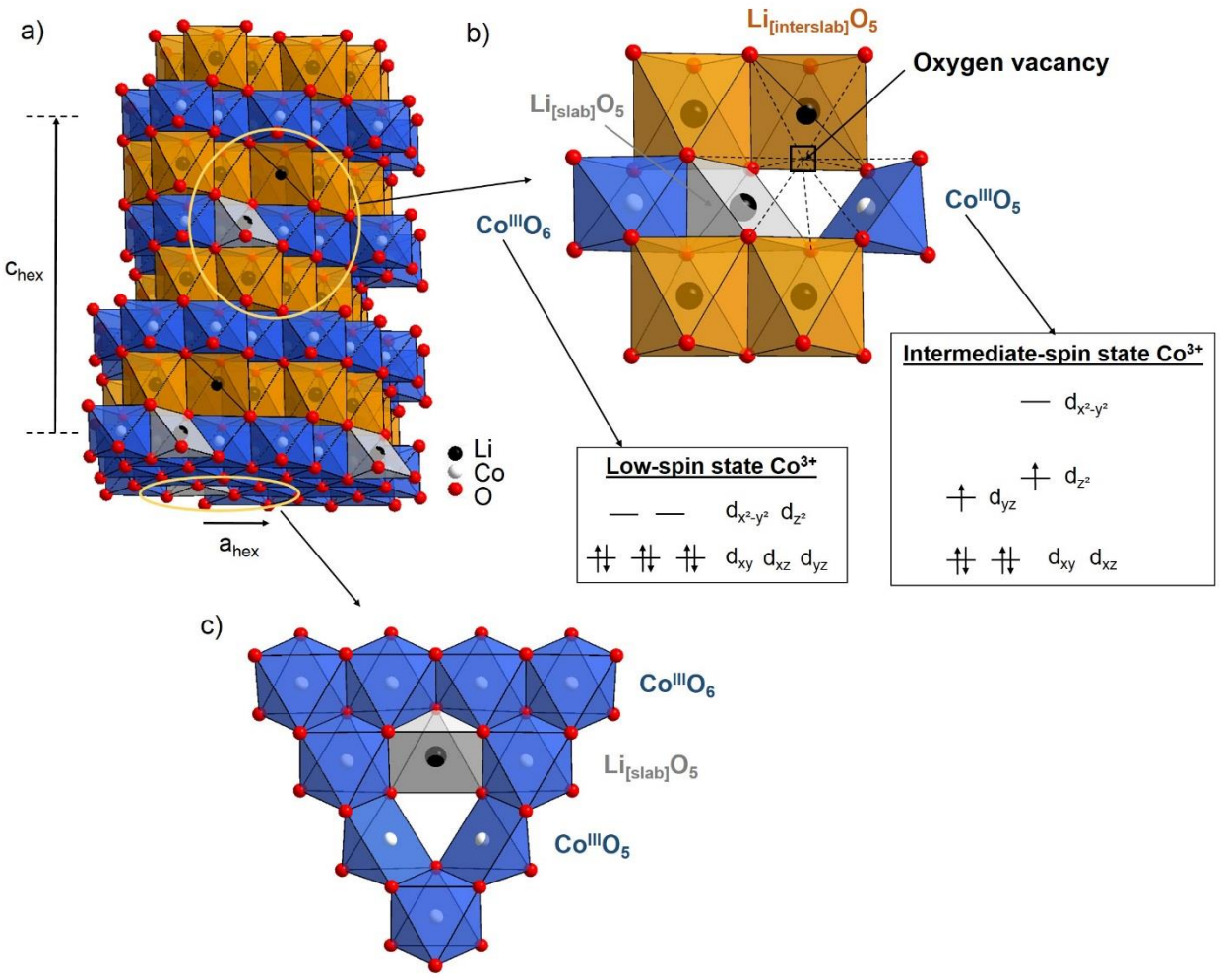

Figure A4: a) *Schematic representation of overlithiated LCO structure. CoO_6 and LiO_6 octahedra are respectively depicted in blue and orange, similarly to Figure A2. Excess Li found in the LiO_5 based-square pyramidal configuration within the layers are in grey. A zoom on the direct surrounding of LiO_5 units is given in* ***b)****, while a view in the (a_{hex}, b_{hex}) plane is provided in* ***c)****.*

Figure A3 (space group *R-3m*), which is why it is also represented in the hexagonal network. No Co^{2+} or Co^{4+} are found within the structure, and no Co has been found migrating in the interlayer space. Following observations from Imanishi[40], the presence of one oxygen vacancy in the proximity of each excess Li is assumed to maintain the electronic neutrality (**Figure A4.b**). Therefore, Li inside the layers is surrounded by only 5 oxygens. As properly shown in **Figure A4.c**, two close-by Co^{3+} are consequently found in square-based pyramidal sites (noted CoO_5), contrasting with the octahedral CoO_6 found within the rest of the layers. These Co^{3+} adopt an intermediate spin (IS) state distribution[41], depicted in **Figure A4.b**. Because of the existence of unpaired electrons in IS-Co^{3+}, their magnetic properties differ from those of LS-Co^{3+}, the former being paramagnetic while the latter are diamagnetic. Further work from Carlier et al.[43] confirmed the existence of IS-Co^{3+} and proposed the electronic configuration shown in **Figure A4.b**. Such assumption therefore corroborates the findings of Ganguly et al.[33] and Peeters et al.[34]. Due to the hyperfine interaction, adjacent Li can thus exhibit the negative or positive shifted additional signals previously reported in the ^{7}Li NMR spectra (out of the narrow chemical shifts range of ^{7}Li), depending on its environment. As a matter of fact, since Rietveld refinements carried out on X-ray and neutron diffraction patterns of overlithiated LCO are of no help to evidence the presence of Li in the Co site, ^{7}Li MAS NMR is considered to be the method of choice to properly establish the real stoichiometry of LCO powders. Assuming the model previously described, chemical formulas can be extrapolated[41] for overlithiated LCO compounds, usually denoted as "$[Li]_{interslab}[Co_{1-t}Li_t]_{slab}O_{2-t}$" or "$Li_{1+t}Co_{1-t}O_{2-t}$".

All the previously mentioned authors concurrently demonstrated that Li overstoichiometry has significant effects on the performance of LCO in LiBs. In particular, Imanishi et al.[40] and Levasseur et al.[35] reported that the discharge capacity of overlithiated LCO cycled up to 4.3 V was lower than those of stoichiometric LCO. Additionally, they showed that stoichiometric and overlithiated LCO did not experience the same phase transitions going along with the Li-removal and re-intercalation from their structure during the charge and the discharge of LCO-based cells cycled up to 4.4 V, as proven by noticeable differences in the associated electrochemical curves. Though structural changes are more rigorously discussed with diffraction data, they induce the presence of voltage jumps or plateaus in their electrochemical curves, which constitutes a good starting point to discuss them. **Figure A5** shows 1st charge curves obtained from the electrochemical testing of LCO powders with various initial Li/Co stoichiometries in Li//LCO cells. These systematic electrochemical studies, associated to other characterization techniques, have helped gaining more knowledge on the nature of the structural changes itself experienced by both stoichiometric and overlithiated LCO.

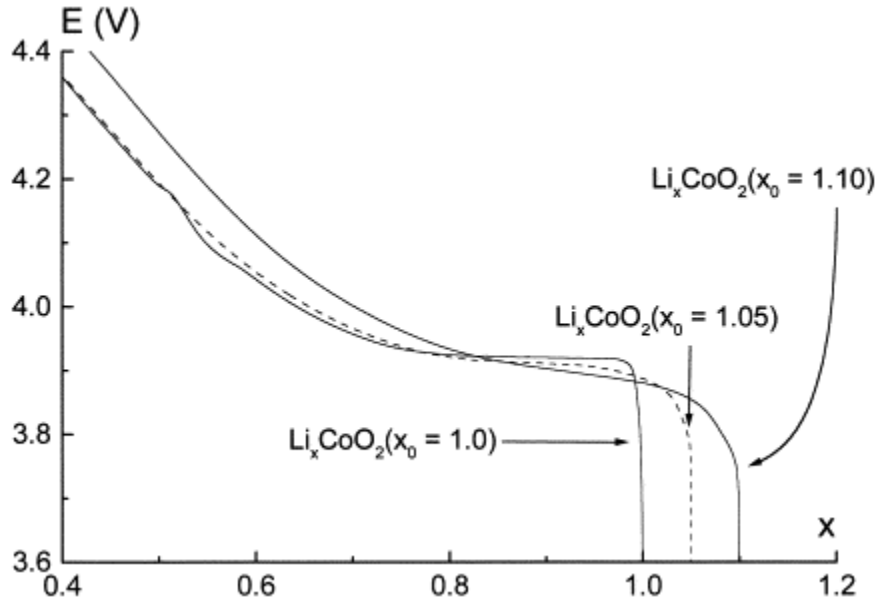

Figure A5. *1st cycle curves of $LiCoO_2$ synthesized with Li/Co = 1.00, 1.05 or 1.10, from Levasseur et al.[35].*

Regarding stoichiometric LCO, the plateau observed at the beginning of the charge of stoichiometric LCO for E = 3.95 V has proven[2,44,45] to be characteristic of the co-existence of two O3 phases with respective Li contents of ~ 0.75 and ~ 1.00. As it induces a change of electronic properties (from insulating to conductive), such change is usually referred to as "insulator-metal transition". The voltage jump at E = 4.12 V was assigned to the ordering of Li in the interlayer space[46–49]. As the monoclinic system is used to describe the unit cell of $Li_{0.5}CoO_2$, it is now commonly denominated as monoclinic transition. Both features are absent of the cycling curves of overlithiated LCO. Diffraction data confirmed that both the insulator-metal and the monoclinic transition are inhibited by the presence of Li inside the CoO_2 layers of overlithiated LCO. Therefore, these changes may be used as a probe for Li stoichiometry in LCO.

In the attempts to de-intercalate more Li from $LiCoO_2$ to access more capacity, additional voltage jumps have more recently been detected[50,51] in the galvanostatic curves of $LiCoO_2$//Li cells charged at higher voltages than 4.4 V. They have been shown to correspond to the O3 – H1-3 and H1-3 – O1 transitions, which will be more deeply explained later in this manuscript. The influence of the initial Li/Co stoichiometry on these transitions has not been established yet, let alone the evolution of charge and discharge capacities at increased cutoff voltages for stoichiometric and overlithiated LCO. In the following, powders of LCO with well controlled initial Li/Co ratios are synthesized and finely characterized to further investigate their electrochemical properties when cycled at high voltage.

A.2 Synthesis and general characterization of $LiCoO_2$ powders.

A.2.1 Description of syntheses

Syntheses described throughout the whole manuscript were carried out at the Umicore R&D center in Cheonan, South Korea.

A first group of $LiCoO_2$ (LCO) powders with various Li/Co (Li/Co = 0.98; 1.00; 1.02 and 1.04, respectively) were synthesized by solid state reaction between Co_3O_4 (Umicore) and Li_2CO_3 (Umicore). After these two precursors were carefully homogenized, the mixtures were heat treated at 980 °C for 10 h. In order to properly control the final Li/Co ratios, rather large amounts of LCO powders were prepared (~ 220 g for each composition). Note that these four samples are referred to as "Group 1 samples" in the following, whose main characteristic is the absence of any control of the size or morphology of the particles. For a better understanding throughout this manuscript, we will also define different Li/Co ratios: $(Li/Co)_{th}$ referring to the theoretical targeted Li/Co for the final LCO powders, as opposed to the measured $(Li/Co)_{exp}$.

A size-controlled series of $LiCoO_2$ powders with equivalent Li/Co ratios was also prepared following a new protocol. In a first step, a $LiCoO_2$ powder with Li/Co = 1.08 was prepared from a 1kg-mixture of Co_3O_4 and Li_2CO_3 heat treated at 980 °C for 10 h. After splitting this lot into four different batches, an appropriate amount of Co_3O_4 – expected to react with the excess Li – was added to each one of them to form the final $LiCoO_2$ powders with Li/Co = 0.98; 1.00; 1.02 and 1.04 at the outcome of a second heat treatment at 980 °C for 10 h. These four samples are now gathered into "Group 2 samples" in the following. Note that the $(Li/Co)_{th}$ and $(Li/Co)_{exp}$ notations still apply, though being linked to the second step of the synthesis. For both Group 1 and Group 2

samples, post-treatment steps such as crushing and sieving were always carried out after the first and second heat treatments. A schematic view of all syntheses may be found in **Figure A6**.

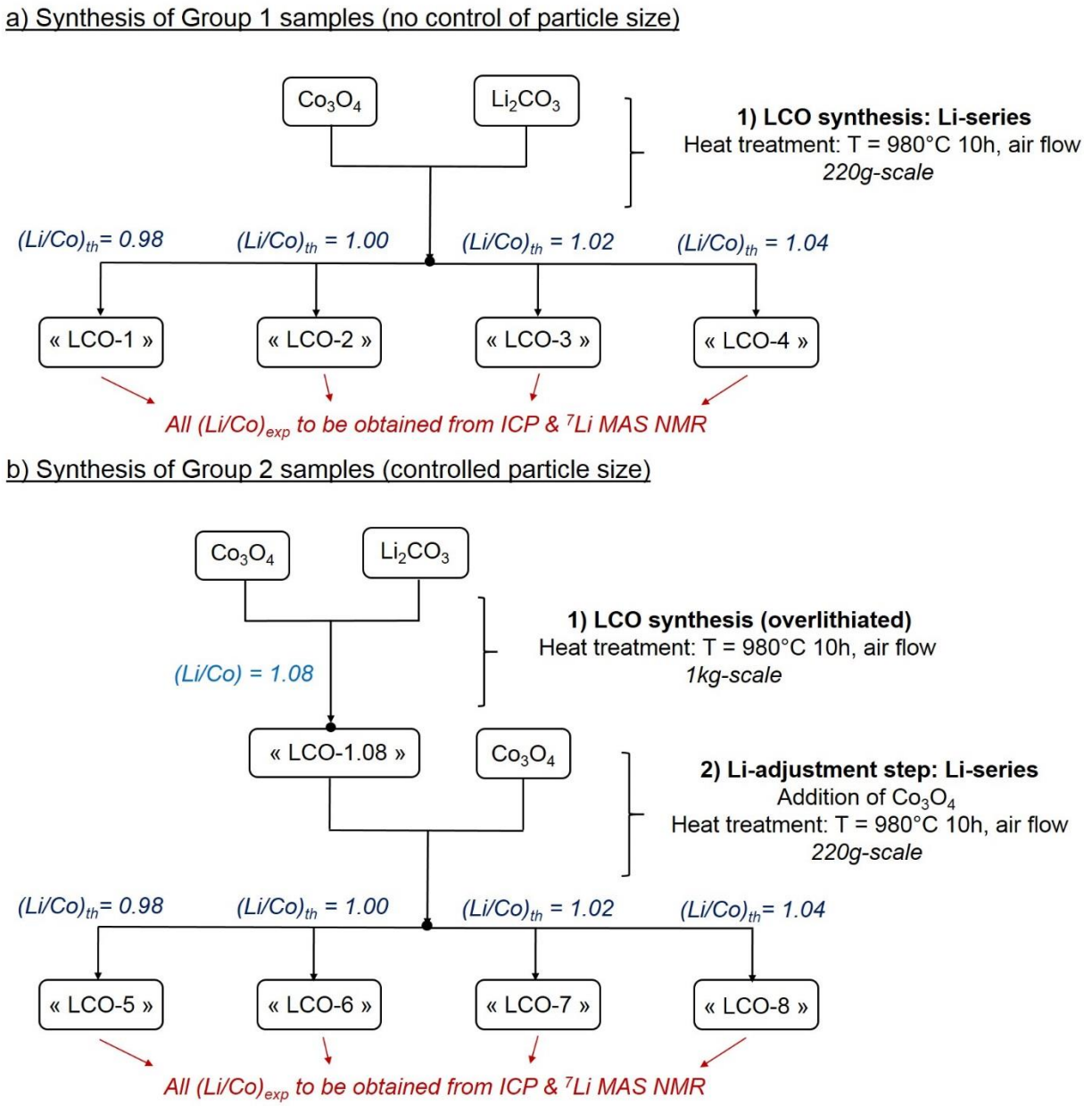

Figure A6*. Schematic representation of the synthetic paths adopted to prepare Li-series of LCO powders.*

A.2.2 Experimental section for general characterization

Scanning electron micrographs (SEM) were taken using a Hitachi Model S-4500 microscope after metallizing the powders with gold.

Inductively coupled plasma (ICP) measurements were carried out on Agilent ICP-720ES equipment after sample digestion using hot plate heating in concentrated HCl solution.

Powder X-ray diffraction (XRD) patterns were collected on a PANalitycal X'pert PRO MPD diffractometer in Bragg-Brentano θ-θ geometry equipped with a Fe filter, a spinner and X'Celerator multi-strip detector. Each measurement was made within an angular range of 2θ = 10 - 120° and lasted for 15 hours with 0.016° intervals. The Co-Kα radiation was generated at 35 kV and 30 mA ($\lambda(K_{\alpha 1})$ = 1.789 Å; $\lambda(K_{\alpha 2})$ = 1.793 Å). Additional high angular resolution synchrotron powder X-ray diffraction (SXRD) was carried out on the BL04-MSPD beamline of the ALBA synchrotron in collaboration with François Fauth (Cerdanyola del Vallès, Spain). All powders were packed in 0.5 mm diameter capillaries. The patterns were recorded in Debye-Scherrer geometry with a wavelength of λ = 0.825 Å. The typical 2Θ angular range was 0 - 70 ° with 0.006° angular step and 3-minute-long accumulation time.

^{7}Li MAS NMR spectra were recorded on a Bruker 300 Advance spectrometer at 116 MHz (7.05 T magnet), with a standard 2.5 mm Bruker MAS probe. A Hahn echo sequence [$t_{\pi/2}$-τ1-t_{π}-τ2] synchronized with one period of rotor rotation was used for a 30 kHz spinning frequency. The 90° pulse duration was equal to $t_{\pi/2}$ = 2.0 μs was determined using a LiCl 1 M solution. A recycle time of D_0 = 40 s was used for stoichiometric LCO, whereas a shorter D_0 = 2s was enough for overlithiated LCO samples, to avoid T_1 saturation effects.

A.2.3 Results and discussion: Chemical and structural properties

A.2.3.1. ICP results

Final $(Li/Co)_{exp}$ ratios obtained by ICP for both Group 1 powders (i.e., without size control) and Group 2 samples (size controlled samples) are gathered in **Table A.T1**. Experimental values are in good agreement with the theoretical ones, though one sample (namely, LCO-4 from Group 1, with $(Li/Co)_{th} = 1.04$) shows a slight deviation to the theoretical value with $(Li/Co)_{exp} \approx 1.05$. Size controlled LCO-6 (prepared with $(Li/Co)_{th} = 1.00$) also shows a slightly higher experimental value with $(Li/Co)_{exp} \approx 1.01$. Additional characterization techniques, such as XRD and ^{7}Li MAS NMR are though required to draw proper conclusions about the exact chemical and structural nature of the phases,whose results will be shown later in this manuscript. Indeed, in the hypothesis of a complete reaction, samples prepared with Li/Co < 1.00 should be obtained as a biphasic mixture of stoichiometric $Li_{1.00}CoO_2$ and Co_3O_4. For Li/Co = 1.00, only stoichiometric $Li_{1.00}CoO_2$ is expected. Powders with Li/Co > 1.00 should lead to overlithiated compounds denoted as "$Li_{1+t}Co_{1-t}O_{2-t}$". For the latter, the chemical formulas given in **Table A.T1** are extrapolated from this general formula, as

$$\frac{Li}{Co} = \frac{1+t}{1-t}.$$

Note that the presence of impurities onto the surface of the particles (like Li_2CO_3) may not be completely dismissed either – which could be another source of deviation for the measured $(Li/Co)_{exp}$. ICP results are still a first step towards evidencing that a proper of $(Li/Co)_{exp}$ was performed for all samples, which was mainly possible thanks to the great quantities of precursors involved in their preparation (~220g mixtures).

Sample reference		$(Li/Co)_{th}$	$(Li/Co)_{exp}$ / ICP	Expected composition
Group 1 No size control	LCO-1	0.98	0.979	$Li_{1.00}CoO_2 + \varepsilon Co_3O_4$
	LCO-2	1.00	1.000	$Li_{1.00}CoO_2$
	LCO-3	1.02	1.015	$\sim Li_{1.008}Co_{0.992}O_{1.992}$
	LCO-4	1.04	1.052	$\sim Li_{1.025}Co_{0.975}O_{1.975}$
Group 2 Size control	LCO-5	0.98	0.986	$Li_{1.00}CoO_2 + \varepsilon Co_3O_4$
	LCO-6	1.00	1.007	$Li_{1.00}CoO_2$ or $Li_{1+\varepsilon}Co_{1-\varepsilon}O_{2-\varepsilon}$
	LCO-7	1.02	1.017	$\sim Li_{1.008}Co_{0.992}O_{1.992}$
	LCO-8	1.04	1.039	$\sim Li_{1.019}Co_{0.981}O_{1.981}$

Table A.T1*. ICP results for the synthesized LCO powders and expected chemical compositions.*

A.2.3.2. Size and morphology of LCO powders

Additional information regarding the average size of the particles and their morphology may be gathered from scanning electron micrographs shown in **Figure A7** for Group 1 samples and **Figure A8** for Group 2 samples.

The micrographs in **Figure A7** reveal that the average primary particle diameter *d* ranges from 1 to 5 µm for LCO-1; 2 to 7 µm for LCO-2; 4 to 10 µm for LCO-3 and 8 to 12 µm for LCO-4. The average particle size thus clearly increases with $(Li/Co)_{th}$, which was expected because of the flux role played by melted Li_2CO_3 during the heat treatment[15,29–31]. Indeed, as discussed in the introduction, the particle growth is promoted with excess Li_2CO_3 during the preparation of LCO.

All four powders show polyhedron-shaped particles, though less pronounced edges are visible for the particles of LCO prepared with the highest $(Li/Co)_{th}$.

Micrographs for Group 2 samples in **Figure A8** show rounder particles than Group 1 samples. All four samples from this series, namely LCO-5 ($(Li/Co)_{th}$ = 0.98), LCO-6 ($(Li/Co)_{th}$ = 1.00), LCO-7 ($(Li/Co)_{th}$ = 1.02) and LCO-8 ($(Li/Co)_{th}$ = 1.04) feature a clearly identified population of particles with similar average diameter around ~ 35 µm. This is the first evidence that a size control of the particles of LCO powders was indeed achieved for Group 2 samples. A second population of small particles (d ~ 1 – 2 µm) is though found in minority for LCO-5, LCO-6 and LCO-7. The relative amount of small particles vs. larger ones is greater with decreasing $(Li/Co)_{th}$, making LCO-5 the sample with the highest number of small particles. Even though the chemical nature of the particles may not be solely discussed from SEM, the preparation method for Group 2 samples

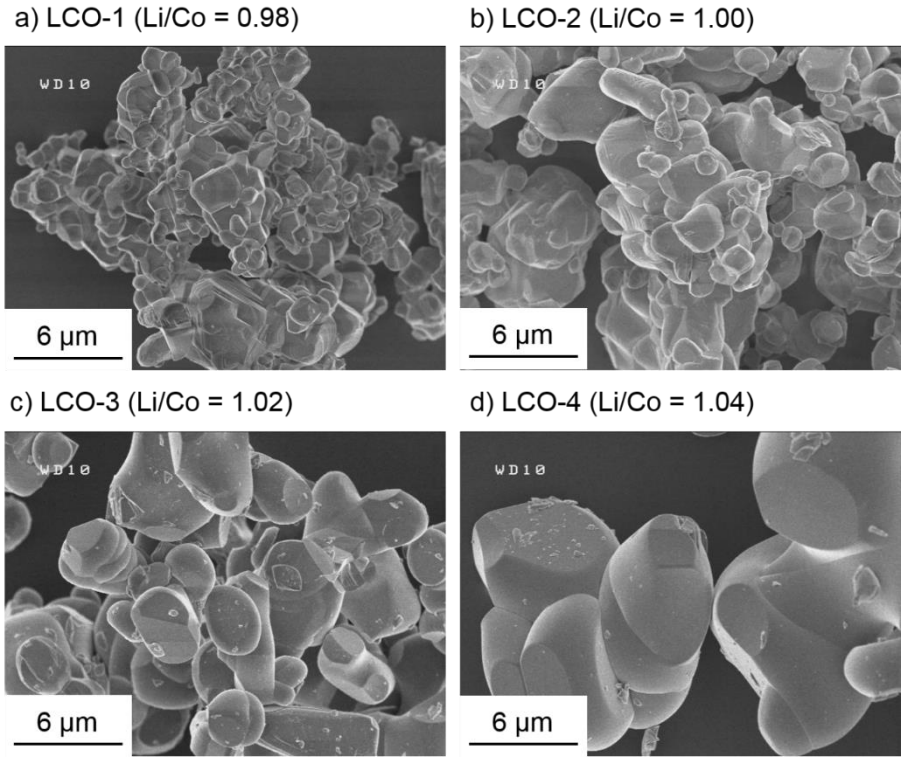

Figure A7*. Scanning electron micrographs for the Group 1 LCO powders: a) LCO-1, b) LCO-2, c) LCO-3 and d) LCO-4.*

already leads to satisfying results regarding the possible packing density of the resulting LCO powders, as the smallest particles may occupy gaps between the largest ones in the electrode.

The overall greater particle diameter of Group 2 samples as compared to Group 1 samples may be simply explained, as well as the presence of the second population of small particles. The first step of Group 2 samples preparation involved the formation of an overlithiated LCO with $(Li/Co)_{th} = 1.08$. At the outcome of this step, significant particle growth occurred, beneficiating from the favorable flux role of melted Li_2CO_3 introduced in larger proportions than any other Group 1 samples. This step played a major role in obtaining the first population of particles with large diameter. The existence of a second population of particles ($d \sim 1 - 2$ µm) is due to the 2nd step of the synthesis, in which Co_3O_4 was added. Whether a lithiation of these particles through a reaction with the overlithiated LCO occurred or not – as SEM is irrelevant to discuss their chemical

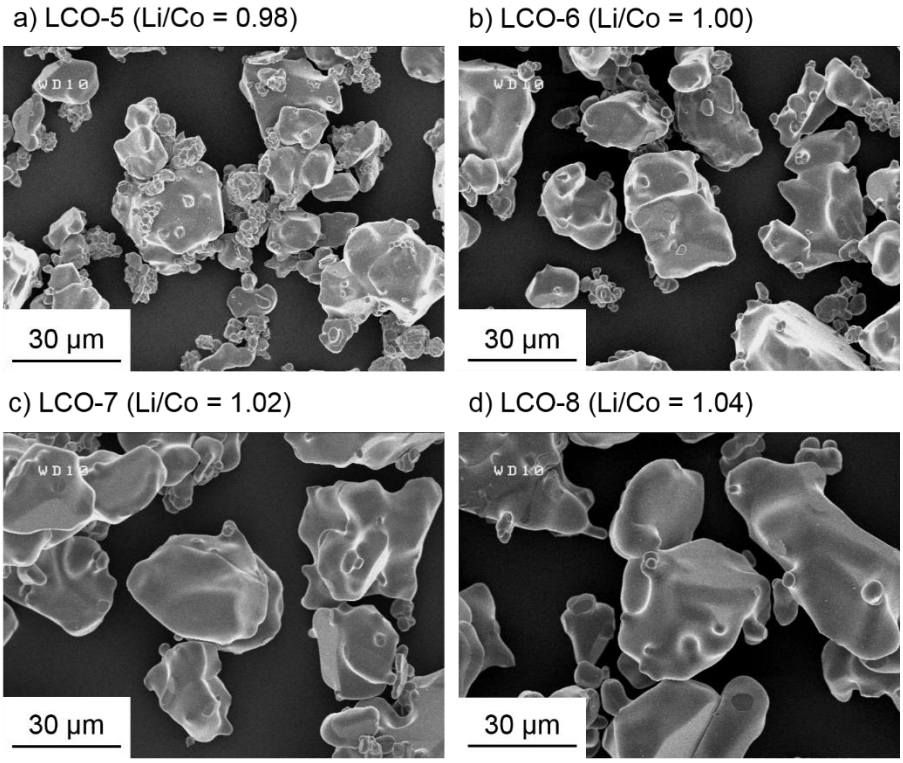

Figure A8*. Scanning electron micrographs for the Group 2 LCO powders: a) LCO-5, b) LCO-6, c) LCO-7 and d) LCO-8.*

nature at this point – they could not beneficiate of the favorable effect of melted Li_2CO_3, already reacted in the 1st step.

A.2.3.3 XRD and SXRD

Figure A9 shows the XRD patterns collected for Group 1 and Group 2 samples, respectively plotted in **a)** and **b)**. An insert for $2\Theta = 42.3 – 46$ ° is given in **c)** and **d)**. All powders show the peaks associated to the layered crystallized (O3) structure of LCO indexed in the *R-3m* space group, confirming the success of the two synthetic routes. Note that an additional diffraction peak is found at $2\Theta = 43.1$ ° in the XRD patterns of LCO-1 and LCO-5, i.e. both samples prepared with $(Li/Co)_{th} = 0.98$. It confirms the presence of Co_3O_4 spinel impurity, as expected for LCO powders prepared with Li/Co < 1.00. It is also a clear evidence that a reaction between Co_3O_4 and the intermediate overlithiated LCO did occur during the second step of Group 2 samples preparation. **Figures A9.c** and **A9.d** arbitrarily shows a magnification of the (101), (006) and (102) diffraction peaks for both groups of samples. Diffraction lines for Group 1 samples are found significantly broader for samples prepared with low $(Li/Co)_{th}$ (such as 0.98 or 1.00, corresponding to LCO-1 and LCO-2). Such effect on peak width may be ascribed to larger coherent domains found in samples prepared with larger amount of Li_2CO_3, ie for higher $(Li/Co)_{th}$. For Group 2 samples, no real difference is observed on the width of the diffraction peaks. Laboratory XRD alone may be inappropriate to conclude that coherent domains in these samples show similar sizes, as the instrumental resolution may be insufficient – though the preparation method used suggest they should be comparable. No clear change of cell parameters or intensity ratios can be observed depending on the (Li/Co) stoichiometries of the eight samples, therefore making laboratory XRD unsuitable to assess the presence of Li in substitution of Co. Similar conclusions were drawn by Stéphane Levasseur during his PhD[31]. All refinements performed on these patterns led to $a_{hex} \approx 2.815$ Å and $c_{hex} \approx 14.052$ Å.

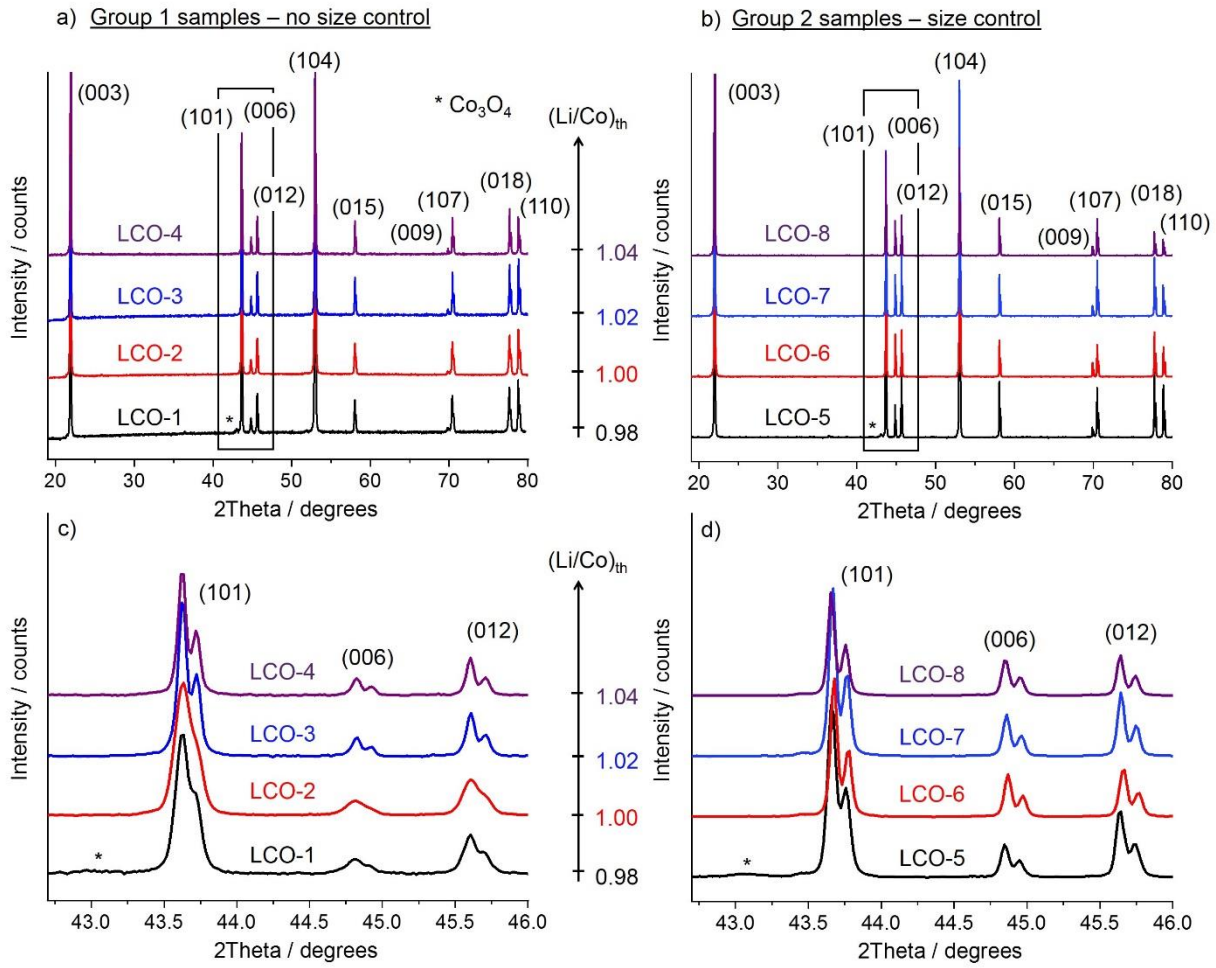

Figure A9. *X-ray diffraction (XRD) data recorded for* ***a)*** *Group 1 and* ***b)*** *Group 2 LCO powders. These patterns were collected using a laboratory diffractometer equipped with a cobalt source (*$\lambda(Co_{K\alpha 1}) = 1.789$ *Å,* $\lambda(Co_{K\alpha 2}) = 1.793$ *Å). Miller indexes are specified for all the peaks visible for* $2\Theta < 80°$*. Zooms on their (101), (006) and (102) diffraction peaks are respectively presented in* ***c)*** *and* ***d)****.*

Note that neutron diffraction was already carried out on overlithiated LCO powders[31]. The presence of Li in the Co site could not be detected either. However, we could not find any patterns of overlithiated LCO (stated as if) recorded with high energy sources in the literature, ie featuring synchrotron radiation, which is known to lead to significant angular resolution increase. We recorded diffraction patterns at ALBA synchrotron for three of these samples, namely LCO-5 ($(Li/Co)_{th} = 0.98$), LCO-7 ($(Li/Co)_{th} = 1.02$) and LCO-8 ($(Li/Co)_{th} = 1.04$). They are plotted in

Figure A10.a. These patterns confirm the high crystallinity obtained for these LCO powders, as thin diffraction lines are clearly visible on the insert provided in **Figure A10.b**. Note that the lines exhibited by our LCO powders were even thinner than the ones of the standards used for calibration due to the technical limitations regarding the MYTHEN detector used – which caused the impossibility to perform Rietveld refinements. No clear difference of peak shape or cell parameters was again observed after Le Bail refinement, though the intensity ratio between the (101), (006) and (102) lines seems to be changed depending on the $(Li/Co)_{th}$ stoichiometry. XRD patterns were simulated for these three stoichiometries in an attempt to link the change of intensity ratio to the presence of Li in the Co site. As no significant difference was observed, the various intensity ratios observed for these peaks most likely arise from preferential orientations in the capillaries.

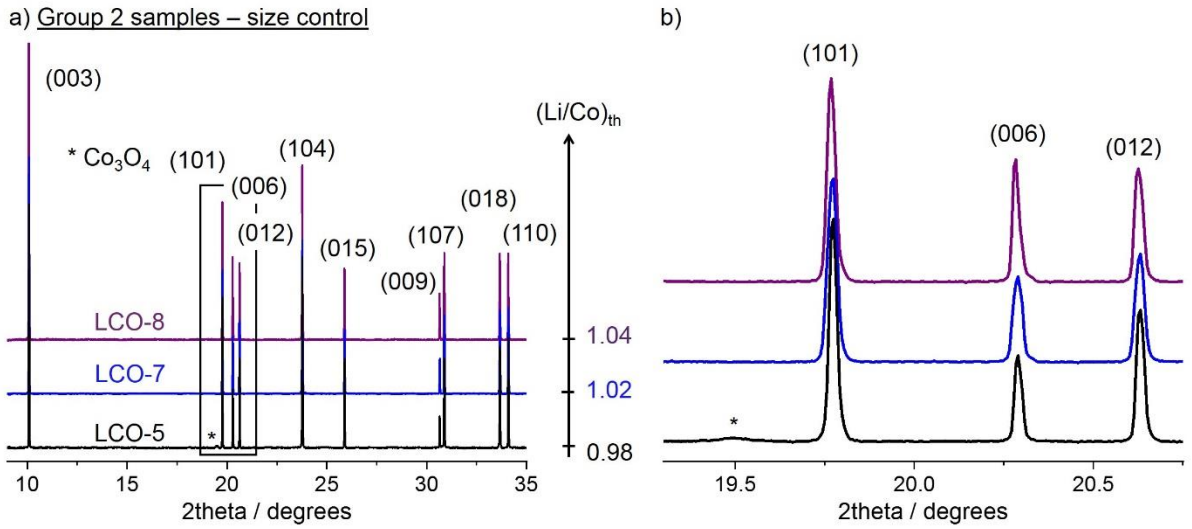

Figure A10. a) *Synchrotron X-ray diffraction (SXRD) patterns recorded for LCO-5, LCO-7 and LCO-8. A zoom on the (101), (006) and (102) diffraction peaks is given in* ***b)****.*

A.2.3.3 ^{7}Li MAS NMR results

Figure A11.a and **Figure A11.b** show a compilation of ^{7}Li MAS NMR global spectra recorded for Group 1 samples. Those of Group 2 samples are provided in **Figure A11.c** and **Figure A11.d**.

Apart from the spinning side bands, a single signal centered at -0.4 ppm is observed in the ^{7}Li NMR spectra of three samples: LCO-1 and LCO-2 (Group 1, **Figure A11.b**) and LCO-5 (Group 2, **Figures A11.c** and **A11.d**). This was already reported[44] as very typical signature for stoichiometric LCO. Indeed, as Li is present in a single diamagnetic environment in stoichiometric LCO since all cobalt ions are in low spin state (LS-Co^{3+}: t_{2g}^{6} eg^{0}), only one contribution around 0 ppm is expected. The chemical composition speculated in **Table A.T1** for LCO-1, LCO-2 and LCO-5 were thus correct. All three samples are indeed $Li_{1.00}CoO_2$, with remaining traces of Co_3O_4 for the two samples prepared with $(Li/Co)_{th} = 0.98$ (LCO-1 and LCO-5). A good agreement between ICP results and ^{7}Li NMR is found.

Six additional signals are observed in the [-30; 20ppm] chemical shift range for the five other samples (respectively found at 7.5; 3.4; -5.4; -10.1, -14.9 and -20.1 ppm) : LCO-3 & LCO-4 for Group 1 samples (Figure 15 b) and LCO-6, LCO-7 & LCO-8 for Group 2 samples (**Figure A11.d**). Additionally, all systematically show a set of signals with weak intensities around 175 ppm. All are characteristic features exhibited by overlithiated LCO. Indeed, intermediate spin state paramagnetic (IS-Co^{3+}, d_{xz}^{2} d_{xy}^{2} d_{yz}^{1} $d_{z^2}^{1}$ $d_{x^2-y^2}^{0}$) cobalt ions are formed due to the presence of Li in the Co site associated with an O vacancy[41]. Due to the hyperfine interaction, adjacent Li can exhibit negative or positive shifted signals (out of the narrow chemical shifts range of ^{7}Li), depending on its environment. The spectrum of every overlithiated LCO does exhibit, therefore, in addition to

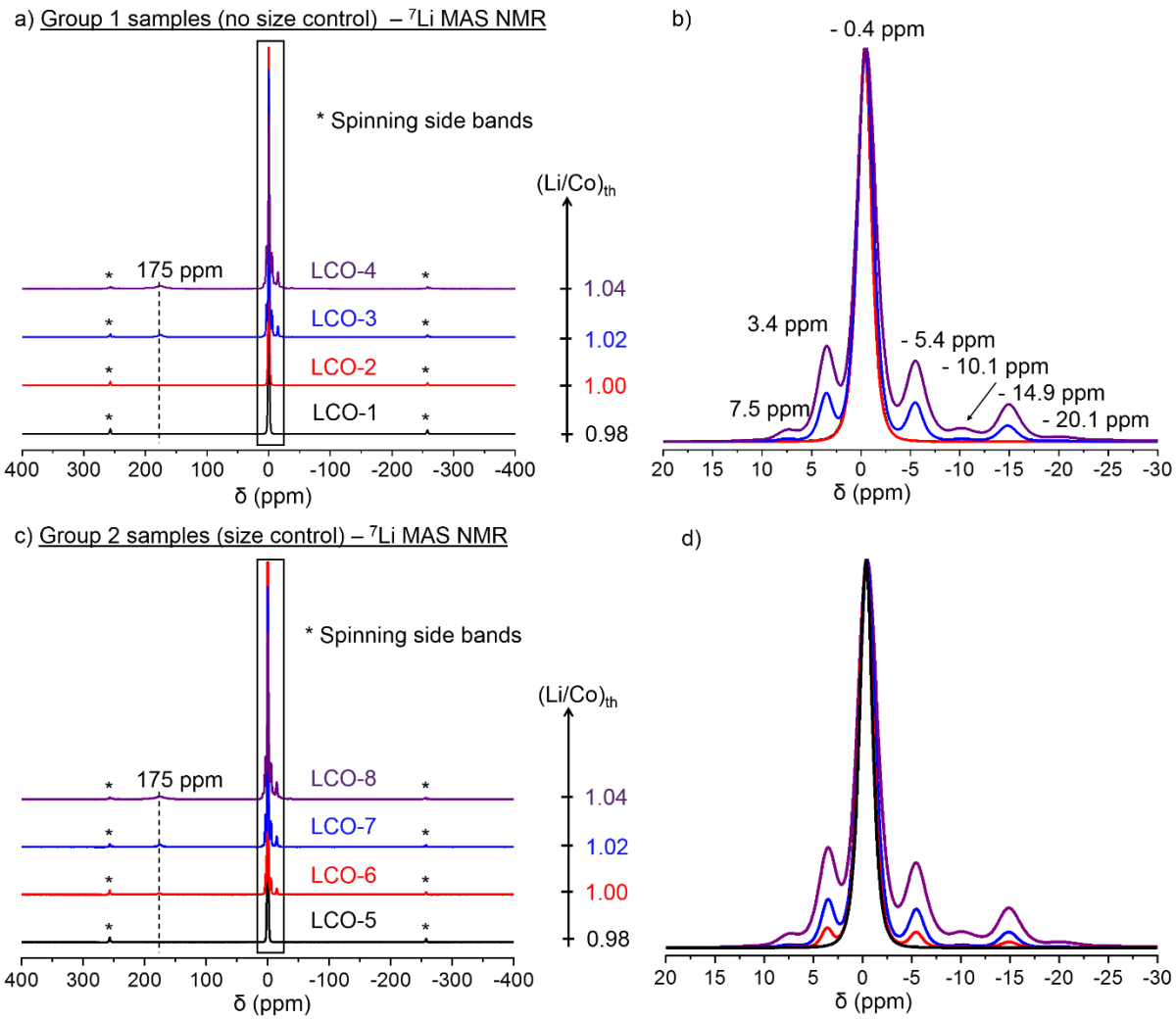

Figure A11. a) *^{7}Li MAS NMR spectra recorded at 116.66 MHz using a 30 kHz spinning frequency of the Group 1 LCO powders, whose zoom on the [-30; 20ppm] region is plotted in* ***b)****. Similar views are given in* ***c)*** *and* ***d)*** *for Group 2 samples.*

the main signal at -0.4 ppm, a large number of Fermi contact shifted signals (not individually assigned yet) observed in **Figure A11.c** and Figure **A11.d**. The set of signals found at ~ 175 ppm can be assigned to ^{7}Li in the CoO_2 layers in close proximity to two IS-Co[3]. Therefore, LCO-3, 4, 6, 7 and 8 are all overlithiated LCO.

Though it was clearly expected for samples prepared with $(Li/Co)_{th}$ = 1.02 or 1.04, this comes as a surprise for LCO-6 $(Li/Co)_{th}$ = 1.00. It reveals the complexity of achieving a fine control of

the Li stoichiometry in LCO – even though the powders were prepared in large quantities to minimize a possible deviation to $(Li/Co)_{th}$ due to mass errors of introduced. As a matter of fact, this result supports the assumptions regarding the chemical composition of LCO-6 stated in **Table A.T1**, arising from the measured $(Li/Co)_{exp}$ ratio (1.007). A good agreement between ICP and ^{7}Li NMR is confirmed again.

Note that the intensity of all additional signals are directly linked to the amount of excess Li found inside the CoO_2 layers of LCO. The more intense the signals are, the higher the overlithiation rate is. Though proper quantitative analysis was not performed as it requires to integrate all signals – including spinning side bands and a proper T_2 relaxation time determination for all signals since a Hahn echo sequence is used here – samples may be ranked according to Li excess content. For Group 1 samples, LCO-4 is more overlithiated than LCO-3, as logically expected from their theoretical $(Li/Co)_{th}$ and measured $(Li/Co)_{exp}$ ratios. Following the same reasoning, LCO-8 shows the highest overlithiation rate among Group 2 samples, while LCO-6 shows the lowest. Few excess Li are most likely found in LCO-6, judging by the very weak intensities of the additional signals.

A.2.3.4 General conclusions on prepared LCO and methods used for characterization

No matter the synthetic path taken, LCO powders with very fine control of Li/Co ratios were successfully obtained. Though the synthesis for Group 1 samples was already widely known and used, the new preparation method developed to get control on the size of the particles of Group 2 samples is thereof validated too. These samples also meet the industrial requirements, as the combination of large and small particles is known to help achieving great packing densities.

Only one sample showed a slight deviation to the expected Li stoichiometry, namely LCO-6 with $(Li/Co)_{th} = 1.00$. Though techniques such as XRD or ICP are mandatory to discuss the layered structure and the chemical nature of the obtained phases, ^{7}Li MAS NMR again proved itself to be the key technique to assess the proper Li stoichiometry of the LCO powders. Indeed, as excess Li in the structure of LCO may not be detected by the means of XRD (even with the use of a highly energetic radiation generated by synchrotron), additional characteristic signature peaks arise in their NMR spectra.

A.3 Influence of Li/Co ratio and particle size on the electrochemical performance of LCO//Li half cells

The following aim to give more insight on the electrochemical behavior of our LCO powders when cycled in LCO//Li half cells.

Although Stéphane Levasseur carried out an equivalent investigation during his PhD[31], the involved amounts of excess Li were significantly greater than ours, with initial Li/Co ratio of either 1.05 or 1.10. He also mainly focused on LCO//Li cells cycled in conventional voltage range, i.e. between 3.0 and 4.3 V, meaning that no information about the electrochemical behavior of LCO powders (including overlithiated ones) was obtained in the high voltage window. Additionally, no size control of the particles was achieved. Powders with higher specific surface areas are expected to suffer substantially more from electrolyte degradation, which can reflect in the electrochemical profiles. Note that the particle size itself also influences the Li intercalation processes, as Li diffusion in larger particles is more challenging. Decomposition products forming the solid electrolyte interphase on LCO (SEI) may also lead to greater polarization in the cycling curves due to a poor resulting electronic conductivity (see Part B). Depending on the chemical nature of the SEI, the Li conductivity may also be impacted. All these parameters are thereof expected to influence the cycling curves obtained for the LCO//Li cells. As a matter of fact, we indeed observed more polarization in the cycling curves of Group 2 samples than those of Group 1 samples. Therefore, the discussion will feature both series of LCO powders depending on the topic in the following. Electrochemical variables such as charge and discharge capacities will be discussed for Group 2 samples – as they show similar specific surface areas and may have similar reactivity towards the electrolyte, making the Li/Co ratio the main changing parameter from one test to another. Note that since the sample prepared with $(Li/Co)_{th}$ = 1.00 (LCO-6) was dismissed for this

study as it is not a real stoichiometric LCO. Sample LCO-5 ($(Li/Co)_{th}$ = 0.98) was used as replacement – since it was proven to be mainly composed of stoichiometric LCO. Group 1 samples will preferentially be used to discuss the lineshape of the cycling curves at high voltage, linked to structural instabilities, as they showed less polarization and more pronounced changes.

A.3.1 Experimental details: electrochemistry

All electrochemical tests for this part were carried out in coin cells. Note that 3 to 4 coin cells were assembled for each test to ensure a good reproducibility. Special efforts on the formulation of the electrodes were also made in order to meet the industrial requirements for the active material loading (10mg/cm²), playing on the viscosity of the prepared slurries and the thickness of the films.

LCO:C:PVDF electrodes (90:5:5 $\%_{wt}$) with the above-mentioned LCO active materials were prepared from a slurry using N-methyl-pyrrolidone (NMP) as solvent casted onto 30µm-thick-aluminum circles. Typical active material loading and diameter for an electrode used for tests was 10mg/cm² and 15mm. The electrodes were dried overnight under vacuum at T = 120 °C and stored in an argon-filled glovebox and the coin cells were assembled using pure lithium as counter-electrode and 1 M $LiPF_6$ in EC:DEC:DMC as electrolyte. All cells were cycled at C/20 between 3.0 V and X (X = 4.5; 4.6; 4.7; 4.8 V).

Note that these conditions are far from ideal to ensure a proper cycle life of the LCO//Li cells, especially with such high cutoff voltages. Additional efforts would be required to optimize it through the use of more stable electrolytes, counter-electrodes and even current collectors – though achieving long cycling life was not the purpose of the study. As all technical requirements were kept equivalent from one material to another, proper conclusions regarding a comparison of the short-term electrochemical performance of each LCO powder (i.e., 1st to 25th cycle) may still be drawn.

A.3.2 Influence of Li/Co ratio on the overall electrochemical performance of LCO//Li cells

A.3.2.1 Reversibily of Li intercalation during the 1st cycle. Charge/discharge capacities and Coulombic efficiency.

Figure A12 shows the 1st cycle curves of the three Group 2 samples selected for electrochemical testing, respectively i) stoichiometric LCO-5, plotted in **Figure A12.a**, ii) 2% overlithiated LCO-7 plotted in **Figure A12.b** and 4% overlithiated LCO-8 plotted in **Figure A12.c**. The four profiles visible on each one of these figures correspond to the 1st cycle curves for various cutting voltages, ranging from 4.5 to 4.8 V. All curves are plotted as a function of both remaining Li in the LCO phase (x in $Li_xCo_{1-t}O_{2-t}$) and the capacity (Q) in mAh/g for easier view. The initial value for x_0 is therefore slightly different depending on the initial $(Li/Co)_{exp}$ of the tested LCO, and so were the molar masses used to calculate Q. At first considerations, some electrochemical features are shared no matter the initial Li stoichiometry of the active LCO material. The higher the cutoff voltage, the higher the charge capacity logically is, as more Li is de-intercalated. This may be more easily seen on **Figure A12.d**, which gives the evolution of charge and discharge capacities (respectively CQ and DQ) as a function of the cutoff voltage. Unlike **Figure A12.a**, **Figure A12.b** and **Figure A12.c**, **Figure A12.d** is based on the results obtained for several coin cells for each test, one experiment being defined by both the active material and the cutoff voltage. Greater polarizations are also observed in the electrochemical window above 4.2 V with an increase of the charge cutoff voltage. This may be due to the presence of insulating SEI at the surface of the particles, whose growth may be driven by greater electrolyte decomposition. Indeed, the electrolyte used for this study is expected to be unstable for E > 4.5 V. In any case, the formation of decomposition products is

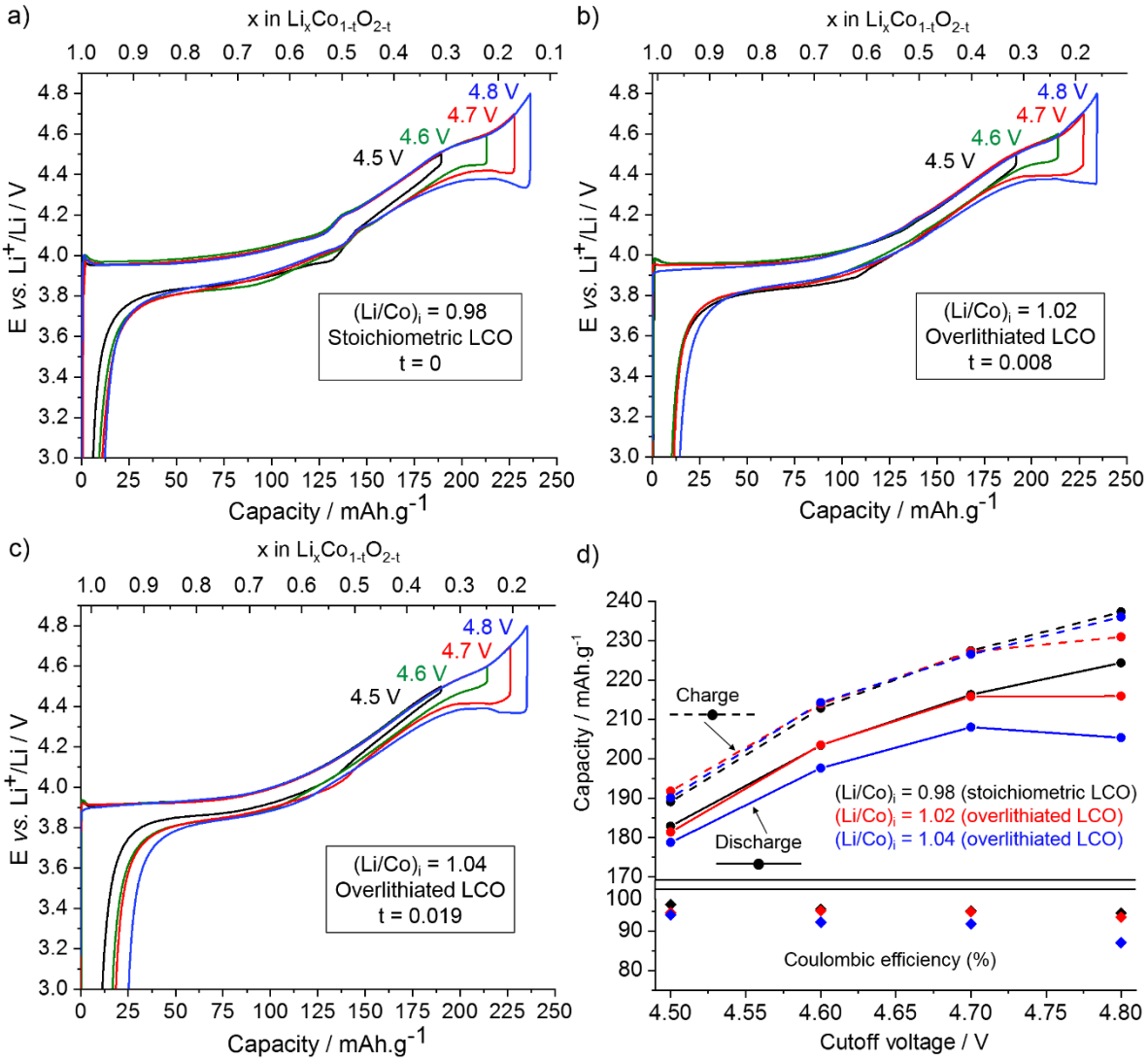

Figure A12. *1st cycle recorded at C/20 and up to various cutoff voltages for LCO-5 (**a**), LCO-7 (**b**) and LCO-8 (**c**) as positive electrode in Li//LCO cells. The initial compositions of the LCO powders are extrapolated from the chemical formulas of overlithiated LCO developed by Levasseur et al.[41]: $Li_{1+t}Co_{1-t}O_{2-t}$. Therefore, the initial Li content x_0 is found equal to 1+t. A summary of the charge and discharge capacity values depending on the initial $(Li/Co)_{exp}$ and the cutoff voltage is given in **d**).*

usually associated to large irreversible capacity losses. One could expect that larger irreversible capacity (noted as Irr) would be achieved with a more pronounced electrolyte decomposition – and thus with a higher charge voltage. Though this trend is clearly followed in the case of

4%-overlithiated LCO-8 (**Figure A12.c)**, as the highest capacity losses are found for E_{cutoff} = 4.8 V and the lowest for E_{cutoff} = 4.5 V, quite similar irreversible capacity is achieved no matter the cutoff voltage for LCO with Li/Co getting closer to 1.00. Note that such information may be more simply discussed in **Figure A12.d** through the calculated Coulombic efficiency (CE), which can be expressed as

$$CE = \frac{DQ}{CQ} \times 100 = \frac{CQ - Irr}{CQ} \times 100 \ .$$

While the coulombic efficiency achieved for the 1st cycle of LCO-8 up to 4.5 V was ~ 94 %, it drops at 84 % with a cutoff voltage of 4.8 V. For stoichiometric LCO-5, it only goes from 96.5 % to 93.5 % with similar voltage range. The cause for the observed polarization at high voltage may thereof linked to other factors, in which the initial $(Li/Co)_{exp}$ may play a role – in addition to the particle size itself. Note that for a same final voltage, the sample with the greater Li excess (LCO-8) always show less discharge capacity – and thus more Irr – than LCO-7 and LCO-5. For instance, the 1st cycle between 3.0 and 4.8 V leads to ~ 84 % Coulombic efficiency for LCO-8, while much better CE of ~ 94 and ~ 95% are respectively obtained for LCO-7 and LCO-5. Therefore, while it is true that the influence of Li excess (in greater amounts) on the electrochemical performances of LCO is not new, it seems that even percentages as small as 4% of Li excess also have a measurable effects on electrochemical variables such as the discharge capacity and the irreversible capacity losses. Differences between LCO-8 and LCO-5 or LCO-7 are though more pronounced as compared to those between LCO-5 and LCO-7, almost undetectable.

A.3.2.2 Cycles 1 to 25: short-term cycleability of LCO

Figure A13 and **Figure A14** show the evolution of the cycling performance between cycle 1 and cycle 25 at different cutoff voltages ($4.5 < E < 4.8$ V) for both stoichiometric LCO-5 ($(Li/Co)_{th} = 0.98$) and 4%-overlithiated LCO-8 ($(Li/Co)_{th} = 1.04$). Note that for the former, no data after cycle 10 up to 4.8 V is shown as cells rapidly die.

A general trend may be observed from both **Figure A13** and **Figure A14**. The higher the number of cycles is, i) smoother profiles are obtained in which voltage jumps are no longer seen, ii) the larger overall polarization is, iii) the lower the charge capacity is – therefore leading to a poor short-term cycling performance.

The final cutoff voltages seem to have a crucial effect on polarization, as it is amplified for higher E_{cutoff} values for both LCO materials. The initial $(Li/Co)_{th}$ also seems to have a conjoint amplifying effect, as the LCO-8-based curves presented in **Figure A14** show larger hysteresis for a same upper charge voltage than those of LCO-5. Cycle 20 or 25 for the LCO-8//Li coin cells cycled up to 4.8 V have square-like shapes. It could suggest that surface reactions most likely occur at the expense of Li-intercalation within the LCO-8 powder. Though no investigation was carried out regarding the possible effect of $(Li/Co)_{th}$ ratio of LCO on the hysteresis evolution of their electrochemical curves with the number of cycles, the effect of cutoff voltage on it was recently studied by Seong et. al[52]. The inverse conclusion was though drawn since they reported that higher cutoff voltage was beneficial in terms of cycle stability of LCO as less overall polarization was achieved for cells cycled up to 4.8 V compared to 4.6 V. No data confirming the reproducibility of their experiment was however provided, as such observations seemed to come from one single coin cell for each upper charge voltage. Although some disagreements may appear between their results

and ours, they demonstrated that the large hysteresis was linked to the presence of a highly resistive spinel phase at the surface of the particles, whose formation may be driven by the structural changes experienced at high voltage by LCO during the cycling. As no further significant electrolyte degradation seems to occur after cycle 1 for any of our coin cells in both **Figure A13** and **Figure A14** – as revealed by the Irr values ~ 0 mAh/g – a link between hysteresis and structural changes may be a reasonable hypothesis here too.

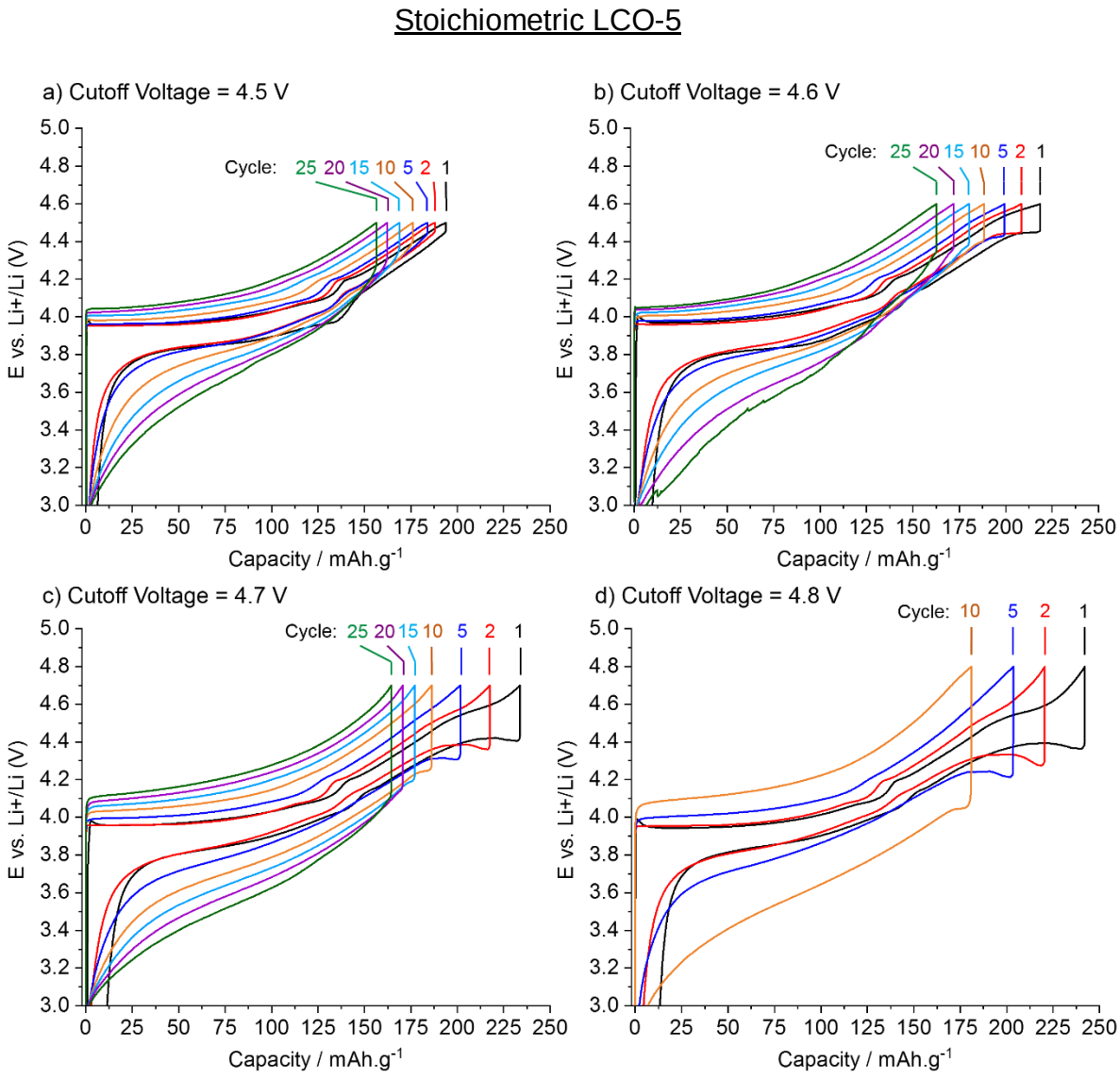

***Figure A13**. Cycle 1-25 recorded for stoichiometric LCO-5 cycled in Li//LCO cells at C/20 up to various cutoff voltages: 4.5 V (**a**), 4.6 V (**b**), 4.7 V (**c**) and 4.8 V (**d**).*

Surprisingly, the change of upper voltage seems to have very little effect on the evolution of charge capacity over cycling – excepted for the two LCO-8//Li cells showing a clear change of electrochemical profiles previously commented (**Figure A14.c** and **A14.d**). For instance, the charge capacity value reported for the 15th cycle of stoichiometric LCO-5//Li cells is always found around ~ 175 mAh/g for any cutoff voltage, while it is around ~ 145 mAh/g in the case of LCO-8//Li cells. At cycle 25, these values remain quite constant again with CQ (LCO-5) ~

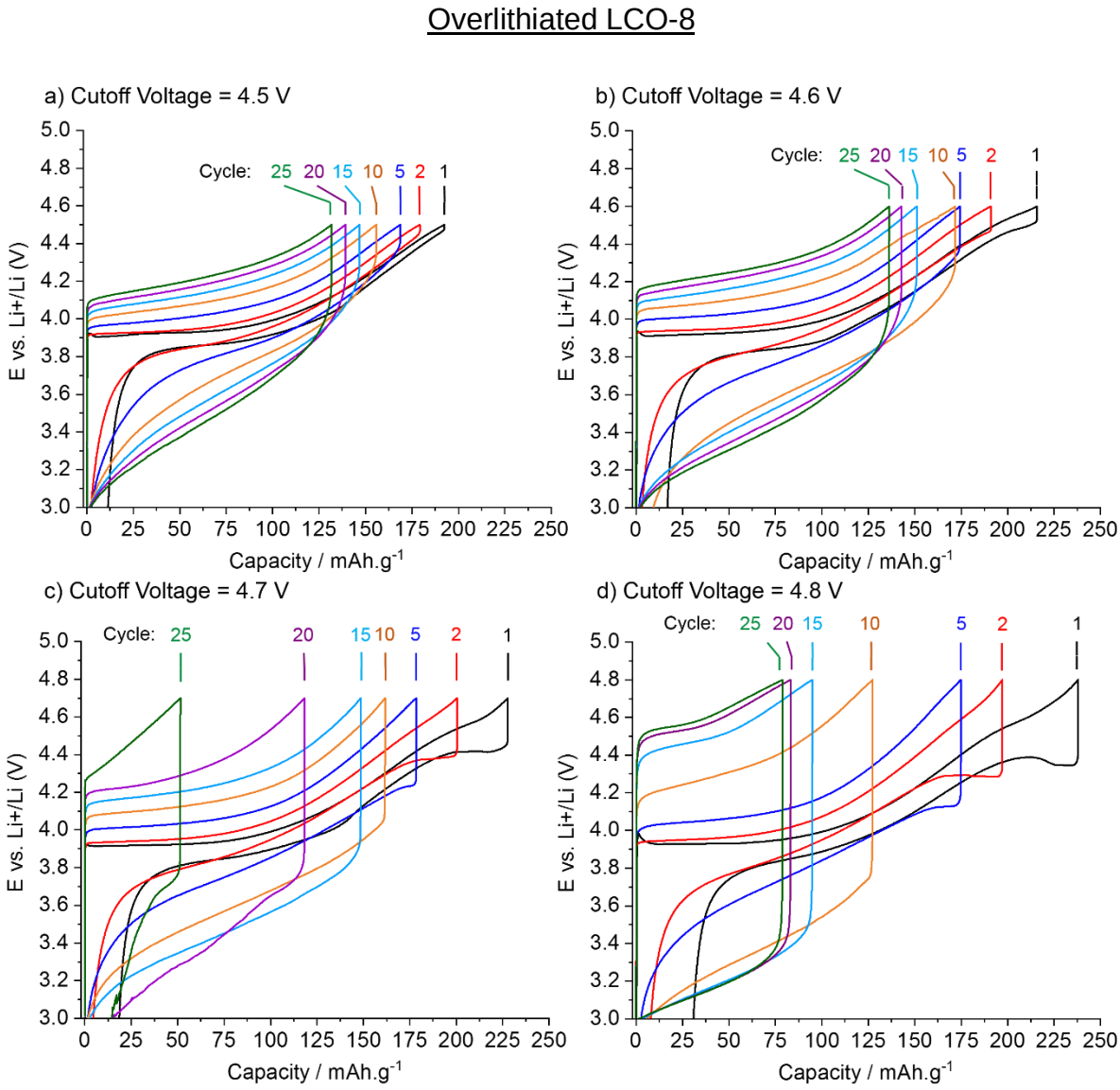

Figure A14*. Cycle 1-25 recorded for overlithiated LCO-8 cycled in Li//LCO cells at C/20 up to various cutoff voltages: 4.5 V (**a**), 4.6 V (**b**), 4.7 V (**c**) and 4.8 V (**d**).*

160 mAh/g and CQ (LCO-8) ~ 130 mAh/g. the difference between the values reported for stoichiometric or overlithiated LCO may still reveal an additional effect of initial Li/Co on the cycle stability of LCO.

A.3.2.3 Evidence of structural changes

Another important consideration to be made regards the overall shape of the profile obtained for LCO-based electrodes with different initial Li/Co. Though **Figure A12.a**, **Figure A12.b** and **Figure A12.c** certainly showed some of the features about to be discussed, the comparison of 1st cycle curves was more thoroughly performed for Group 1 samples, whose polarization at high voltage was significantly decreased. Electrochemical profiles are gathered in **Figure A15.a**, and the associated dQ/dV curves are shown in **Figure A15.b**. Note that a zoom on both the 1st cycle and derivative curves in the high voltage window ($4.35 < E < 4.7$ V) are respectively provided in **Figure A15.c** and **Figure A15.d**.

Both LCO-1 ($(Li/Co)_{th} = 0.98$) and LCO-2 ($(Li/Co)_{th} = 1.00$) samples show very typical features expected for stoichiometric LCO-based cells at low voltage: i) the voltage plateau located at 3.95 V corresponding to the insulator – metal transition occurring as first Li^+ ions are removed[2,44], and ii) the voltage jump corresponding to the O3 $\leftrightarrow$ O'3 monoclinic transition resulting from the formation of a Li-vacancy ordering[44,46,48,49] at $x = 0.5$. The latter may be more explicitly visualized in the dQ/dV curve with the emergence of two well-defined peaks at E ~ 4.06 V and E ~ 4.18 V respectively corresponding to the O3 – O'3 and O'3 – O3 transitions. Overlithiated samples LCO-3 ($(Li/Co)_{th} = 1.02$) and LCO-4 ($(Li/Co)_{th} = 1.04$) do not show any voltage jump for $x = 0.5$ – and thus no associated peak in their derivative profiles, which is again expected as local defects induced

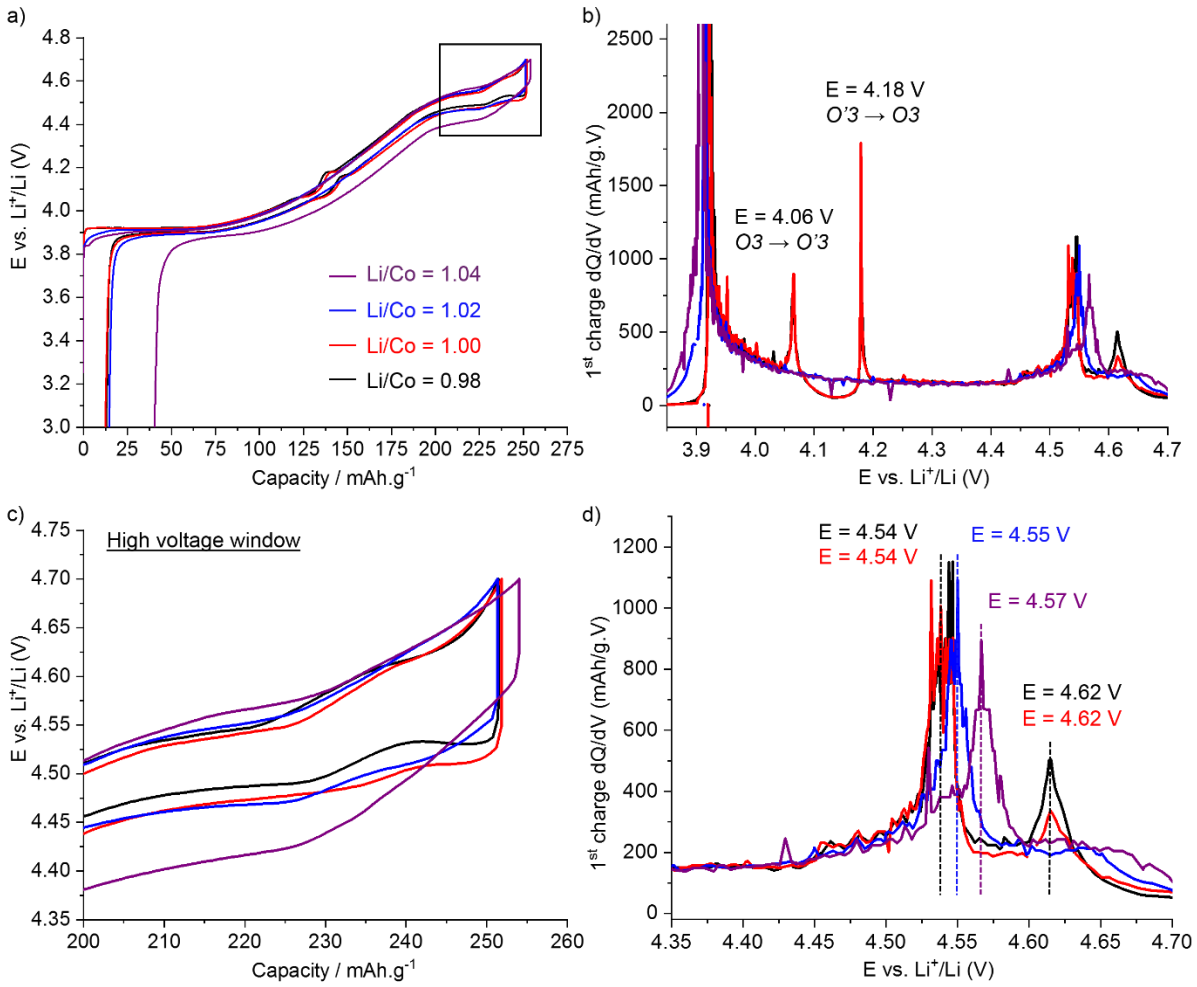

***Figure A15**. (**a**) 1st cycle for Group 1 samples at C/20 in Li//LCO cells up to 4.7 V. (**b**) Corresponding dQ/dV curves (charge only). (**c**) Zoom on the high voltage electrochemical window of the curves plotted in (a), and (**d**) corresponding dQ/dV curves (charge only).*

by the presence of Li in CoO_6 layers perturbate the Li-ordering and lead to the loss of the monoclinic transition at $x \approx 0.5$. The existence of pseudo-plateaus around ~ 3.95 V makes it hard to further discuss the events occurring at the beginning of the charge for LCO-3//Li and LCO-4//Li cells, though evidences[2,41,44] have already pointed at a solid solution O3-Li_xCoO_2 behavior in this domain for overlithiated LCO ($(Li/Co)_{th} = 1.10$). Though all of the above is not new information, it surely can be used as additional probe for the initial Li-stoichiometry in LCO.

On the other hand, the influence of the initial Li/Co on the high voltage electrochemical behavior for LCO has never been discussed so far. Two main phase transitions are expected, namely the O3 – H1-3 and H1-3 – O1 transitions[45,48,47,51]. For stoichiometric LCO-1 and LCO-2, two voltage jumps are evidenced in the [4.35 – 4.7 V] electrochemical window. They seem to occur around E = 4.54 V and E = 4.62 V, as revealed by their associated peaks in the derivative curves. Equivalent voltages have been reported for the high voltage transitions using supposedly stoichiometric LCO as starter in the literature[51]. Note that the nature of the structural changes will be the main focus of Part B, which explains why no further description of the high voltage phase structures are given at this point. Smoother profiles are obtained for overlithiated LCO-3 and LCO-4, though the existence of a peak in the dQ/dV curves at E = 4.55 V for the former and E = 4.57 V for the latter confirms a voltage jump.

These results tend to confirm that the initial Li/Co ratio in LCO does impact the structural changes associated to Li de-intercalation at high voltage. It is suggested that stoichiometric LCO experiences two successive structural changes up to 4.7 V, most likely corresponding to the reported O3 – H1-3 and H1-3 – O1 transitions[45,48,47,51], while overlithiated LCO only seems to experience one, most likely corresponding to the O3 – H1-3 transition. Therefore, there could be a potential delay for the formation of the H1-3 phase depending on the % of excess Li in the initial LCO (2% or 4%).

A.4 Conclusion Part A

Series of LCO powders with well controlled Li/Co initial stoichiometries were successfully prepared using two different solid state routes. Only one sample shows a slight deviation to the expected Li/Co)th stoichiometry: LCO-6 ($(Li/Co)_{th}$ = 1.00) as traces of surlithiation were detected and therefore mean that it is not stoichiometric. However, no article had reported the preparation of LCO powders with such a narrow range of Li stoichiometries so far (0.98 < Li/Co < 1.04). While the first preparation method is not new as it consists of the heat treatment of mixtures of Co_3O_4 and Li_2CO_3, already known from the literature, we validated a second synthetic path. The formation of an overlithiated LCO in the first step and the use of Co_3O_4 in the second step yields to a proper control of particle sizes in the final LCO powders, which could not be achieved following the classical solid state route due to the flux role from melted Li_2CO_3. The resulting Group 2 samples indeed show two populations of particles whose sizes are respectively ~ 35 µm and ~ 1 µm no matter the final Li/Co ratio targeted for LCO. With a varying Li/Co ratio, these populations are found in different relative amounts within the LCO powders. To this end, Group 2 LCO samples follow the industrial requirements needed to achieve proper packing density.

The validation of both procedures was possible thanks to the combination of characterization techniques such as ICP, XRD, SEM and ^{7}Li MAS NMR. The latter has shown itself to be key when it comes to discussing the proper Li stoichiometries of LCO powders. Indeed, the presence of excess Li within the structure of LCO to form overlithiated phases can only be certified through their NMR spectra, as no difference is observed in the XRD patterns of the series of LCO.

Electrochemical tests confirmed previous findings that the initial Li/Co ratio in LCO does influence the electrochemical variables such as capacity values. Overlithiated LCO always show

lower discharge capacity than their stoichiometric analogues during the 1st cycle. This effect is amplified for larger initial Li/Co. However, no matter the initial Li stoichiometry of the tested LCO powders, poor cycle life is achieved as curves with large hysteresis are quickly obtained after a few cycles. This could be related to structural instabilities experienced in the high voltage electrochemical window. The mechanisms for phase transitions seems to be influenced by the initial Li/Co ratio of LCO. While two voltage jumps can be clearly seen at the end of the 1st cycle up to 4.7 V for stoichiometric LCO, only one is visible for overlithiated LCO. A proper investigation of the phase transition mechanisms depending on the initial Li/Co of LCO may therefore be carried out based on these results. As they showed the most pronounced differences, samples LCO-5 $(Li/Co)_{th} = 0.98$) and LCO-8 $(Li/Co)_{th} = 1.04$) will now be used as reference samples for Part B.

A.5 Bibliography Part A

(1) Nakai, I.; Takahashi, K.; Shiraishi, Y.; Nakagome, T.; Izumi, F.; Ishii, Y.; Nishikawa, F.; Konishi, T. X-Ray Absorption Fine Structure and Neutron Diffraction Analyses of de-Intercalation Behavior in the $LiCoO_2$ and $LiNiO_2$ Systems. *J. Power Sources* **1997**, *68* (2), 536–539. https://doi.org/10.1016/S0378-7753(97)02598-6.

(2) Ménétrier, M.; Saadoune, I.; Levasseur, S.; Delmas, C. The Insulator-Metal Transition upon Lithium Deintercalation from $LiCoO_2$: Electronic Properties and ^{7}Li NMR Study. *J. Mater. Chem.* **1999**, *9* (5), 1135–1140. https://doi.org/10.1039/A900016J.

(3) Kellerman, D. G.; Galakhov, V. R.; Semenova, A. S.; Blinovskov, Y. N.; Leonidova, O. N. Semiconductor-Metal Transition in Defect Lithium Cobaltite. *Phys. Solid State* **2006**, *48* (3), 548–556. https://doi.org/10.1134/S106378340603022X.

(4) Dahéron, L.; Dedryvère, R.; Martinez, H.; Ménétrier, M.; Denage, C.; Delmas, C.; Gonbeau, D. Electron Transfer Mechanisms upon Lithium Deintercalation from $LiCoO_2$ to CoO_2 Investigated by XPS. *Chem. Mater.* **2008**, *20* (2), 583–590. https://doi.org/10.1021/cm702546s.

(5) Chen, C.-H.; Hwang, B.-J.; Chen, C.-Y.; Hu, S.-K.; Chen, J.-M.; Sheu, H.-S.; Lee, J.-F. Soft X-Ray Absorption Spectroscopy Studies on the Chemically Delithiated Commercial $LiCoO_2$ Cathode Material. *J. Power Sources* **2007**, *174* (2), 938–943. https://doi.org/10.1016/j.jpowsour.2007.06.083.

(6) Yoon, W.-S.; Kim, K.-B.; Kim, M.-G.; Lee, M.-K.; Shin, H.-J.; Lee, J.-M.; Lee, J.-S.; Yo, C.-H. Oxygen Contribution on Li-Ion Intercalation−Deintercalation in $LiCoO_2$ Investigated

by O K-Edge and Co L-Edge X-Ray Absorption Spectroscopy. *J. Phys. Chem. B* **2002**, *106* (10), 2526–2532. https://doi.org/10.1021/jp013735e.

(7) Graetz, J.; Hightower, A.; Ahn, C. C.; Yazami, R.; Rez, P.; Fultz, B. Electronic Structure of Chemically-Delithiated $LiCoO_2$ Studied by Electron Energy-Loss Spectrometry. *J. Phys. Chem. B* **2002**, *106* (6), 1286–1289. https://doi.org/10.1021/jp0133283.

(8) Montoro, L. A.; Abbate, M.; Rosolen, J. M. Changes in the Electronic Structure of Chemically Deintercalated $LiCoO_2$. *Electrochem. Solid-State Lett.* **2000**, *3* (9), 410–412. https://doi.org/10.1149/1.1391162.

(9) Niemöller, A.; Jakes, P.; Eichel, R.-A.; Granwehr, J. In Operando EPR Investigation of Redox Mechanisms in $LiCoO_2$. *Chem. Phys. Lett.* **2019**, *716*, 231–236. https://doi.org/10.1016/j.cplett.2018.12.022.

(10) Delmas, C.; Fouassier, C.; Hagenmuller, P. Structural Classification and Properties of the Layered Oxides. *Phys. BC* **1980**, *99* (1), 81–85. https://doi.org/10.1016/0378-4363(80)90214-4.

(11) Mendiboure, A.; Delmas, C.; Hagenmuller, P. New Layered Structure Obtained by Electrochemical Deintercalation of the Metastable $LiCoO_2$ (O2) Variety. *Mater. Res. Bull.* **1984**, *19* (10), 1383–1392. https://doi.org/10.1016/0025-5408(84)90204-6.

(12) Komaba, S.; Yabuuchi, N.; Kawamoto, Y. A New Polymorph of Layered $LiCoO_2$. *Chem. Lett.* **2009**, *38* (10), 954–955. https://doi.org/10.1246/cl.2009.954.

(13) Berthelot, R.; Carlier, D.; Pollet, M.; Doumerc, J.-P.; Delmas, C. Synthesis and Investigations on an O4-$LiCoO_2$ Polytype. *Electrochem. Solid-State Lett.* **2009**, *12* (11), A207–A210. https://doi.org/10.1149/1.3204643.

(14) Gummow, R.; Thackeray, M.; David, W.; Hull, S. Structure and Electrochemistry of Lithium Cobalt Oxide Synthesised at 400°C. *Mater. Res. Bull.* **1992**, *27* (3), 327–337. https://doi.org/10.1016/0025-5408(92)90062-5.

(15) Lundblad, A.; Bergman, B. Synthesis of $LiCoO_2$ Starting from Carbonate Precursors II. Influence of Calcination Conditions and Leaching. *Solid State Ion.* **1997**, *96* (3–4), 183–193. https://doi.org/10.1016/S0167-2738(97)00017-9.

(16) Wicker, S. A.; Walker, E. H. Revisited: Decomposition or Melting? Formation Mechanism Investigation of $LiCoO_2$ via In-Situ Time-Resolved X-Ray Diffraction. *Inorg. Chem.* **2013**, *52* (4), 1772–1779. https://doi.org/10.1021/ic301516a.

(17) Timoshevskii, A. N.; Ktalkherman, M. G.; Emel'kin, V. A.; Pozdnyakov, B. A.; Zamyatin, A. P. High-Temperature Decomposition of Lithium Carbonate at Atmospheric Pressure. *High Temp.* **2008**, *46* (3), 414–421. https://doi.org/10.1134/S0018151X0803019X.

(18) Ktalkherman, M. G.; Emelkin, V. A.; Pozdnyakov, B. A. Production of Lithium Oxide by Decompostion Lithium Carbonate in the Flow of a Heat Carrier. *Theor. Found. Chem. Eng.* **2009**, *43* (1), 88–93. https://doi.org/10.1134/S0040579509010114.

(19) Lundblad, A.; Bergman, B. Synthesis of $LiCoO_2$ Starting from Carbonate Precursors I. The Reaction Mechanisms. *Solid State Ion.* **1997**, *96* (3–4), 173–181. https://doi.org/10.1016/S0167-2738(97)00016-7.

(20) Antolini, E.; Ferretti, M. Synthesis and Thermal Stability of $LiCoO_2$. *J. Solid State Chem.* **1995**, *117* (1), 1–7. https://doi.org/10.1006/jssc.1995.1238.

(21) Sun, Y.-K.; Oh, I.-H.; Hong, S.-A. Synthesis of Ultrafine $LiCoO_2$ Powders by the Sol-Gel Method. *J. Mater. Sci.* **1996**, *31* (14), 3617–3621. https://doi.org/10.1007/BF00352769.

(22) Oh, I.-H.; Hong, S.-A.; Sun, Y.-K. Low-Temperature Preparation of Ultrafine $LiCoO_2$ Powders by the Sol–Gel Method. *J. Mater. Sci.* **1997**, *32* (12), 3177–3182. https://doi.org/10.1023/A:1018650717723.

(23) Yoon, W.-S.; Kim, K.-B. Synthesis of $LiCoO_2$ Using Acrylic Acid and Its Electrochemical Properties for Li Secondary Batteries. *J. Power Sources* **1999**, *81–82*, 517–523. https://doi.org/10.1016/S0378-7753(98)00226-2.

(24) Peng, Z. S.; Wan, C. R.; Jiang, C. Y. Synthesis by Sol–Gel Process and Characterization of $LiCoO_2$ Cathode Materials. *J. Power Sources* **1998**, *72* (2), 215–220. https://doi.org/10.1016/S0378-7753(97)02689-X.

(25) Kang, S. G.; Kang, S. Y.; Ryu, K. S.; Chang, S. H. Electrochemical and Structural Properties of HT-$LiCoO_2$ and LT-$LiCoO_2$ Prepared by the Citrate Sol-Gel Method. *Solid State Ion.* **1999**, *120* (1), 155–161. https://doi.org/10.1016/S0167-2738(98)00559-1.

(26) Amatucci, G. G.; Tarascon, J. M.; Larcher, D.; Klein, L. C. Synthesis of Electrochemically Active $LiCoO_2$ and $LiNiO_2$ at 100 °C. *Solid State Ion.* **1996**, *84* (3–4), 169–180. https://doi.org/10.1016/0167-2738(96)00031-8.

(27) Han, C.-H.; Hong, Y.-S.; Park, C. M.; Kim, K. Synthesis and Electrochemical Properties of Lithium Cobalt Oxides Prepared by Molten-Salt Synthesis Using the Eutectic Mixture of LiCl–Li_2CO_3. *J. Power Sources* **2001**, *92* (1), 95–101. https://doi.org/10.1016/S0378-7753(00)00505-X.

(28) Tang, W.; Kanoh, H.; Ooi, K. Preparation of Lithium Cobalt Oxide by LiCl - Flux Method for Lithium Rechargeable Batteries. *Electrochem. Solid-State Lett.* **1998**, *1* (3), 145–146. https://doi.org/10.1149/1.1390665.

(29) Giorgi, L.; Carewska, M.; Patriarca, M.; Scaccia, S.; Simonetti, E.; Di Bartolomeo, A. Development and Characterization of Novel Cathode Materials for Molten Carbonate Fuel Cell. *J. Power Sources* **1994**, *49* (1–3), 227–243.

(30) Antolini, E.; Giorgi, L.; Carewska, M. Formation of Li-and Mg-Doped $LiCoO_2$ Powders: A BET Analysis. *J. Mater. Sci. Lett.* **1999**, *18* (4), 325–327.

(31) Levasseur, S. Contribution à l'étude Des Phases $Li_x(Co, M)O_2$ En Tant Que Matériaux d'électrode Positive Des Batteries Li-Ion. Effets Combinés de La Surstoechiométrie En Lithium et de La Substitution (M= Ni, Mg), Université Sciences et Technologies-Bordeaux I, 2001.

(32) Carewska, M.; Scaccia, S.; Croce, F.; Arumugam, S.; Wang, Y.; Greenbaum, S. Electrical Conductivity and ^{6,7}Li NMR Studies of $Li_{1+Y}CoO_2$. *Solid State Ion.* **1997**, *93* (3), 227–237. https://doi.org/10.1016/S0167-2738(96)00545-0.

(33) Ganguly, P.; Venkatraman, T. N.; Rajamohanan, P. R.; Ganapathy, S. Evidence for Multiple M Sites in AMO_2 Compounds: ^{59}Co Solid State NMR Studies on $LiCoO_2$. *J. Phys. Chem. B* **1997**, *101* (51), 11099–11105. https://doi.org/10.1021/jp9729775.

(34) Peeters, M. P. J.; van Bommel, M. J.; Neilen-ten Wolde, P. M. C.; van Hal, H. A. M.; Keur, W. C.; Kentgens, A. P. M. A ^{6}Li, ^{7}Li and ^{59}Co MAS NMR Study of Rock Salt Type Li_xCoO_2 ($0.48 \leq x \leq 1.05$). *Solid State Ion.* **1998**, *112* (1–2), 41–52. https://doi.org/10.1016/S0167-2738(98)00213-6.

(35) Levasseur, S.; Menetrier, M.; Suard, E.; Delmas, C. Evidence for Structural Defects in Non-Stoichiometric HT-$LiCoO_2$: Electrochemical, Electronic Properties and ^{7}Li NMR Studies. *Solid State Ion.* **2000**, *128* (1–4), 11–24.

(36) Gorshkov, V. S.; Kellerman, D. G.; Karelina, V. V. Magnetic susceptibility study of defect formation in the $LiCoO_2$ complex oxide. *Zhurnal Fiz. Khimii* **1999**, *73* (6), 1041–1045.

(37) Karelina, V. V.; Kellerman, D. G.; Gorshkov, V. S.; Leonidov, I. A.; Patrakeev, M. V. Nonstoichiometry and electric properties of $LiCoO_2$. *Zhurnal Fiz. Khimii* **2001**, *75* (3), 568–572.

(38) Galakhov, V. R.; Karelina, V. V.; Kellerman, D. G.; Gorshkov, V. S.; Ovechkina, N. A.; Neumann, M. Electronic Structure, x-Ray Spectra, and Magnetic Properties of the $LiCoO_{2-\delta}$ and Na_xCoO_2 Nonstoichiometric Oxides. *Phys. Solid State* **2002**, *44* (2), 266–273. https://doi.org/10.1134/1.1451011.

(39) Imanishi, N.; Fujii, M.; Hirano, A.; Takeda, Y. Synthesis and Characterization of Nonstoichiometric $LiCoO_2$. *J. Power Sources* **2001**, *97–98*, 287–289. https://doi.org/10.1016/S0378-7753(01)00740-6.

(40) Imanishi, N.; Yamade, M.; Ichikawa, T.; Hirano, A.; Takeda, Y. Characterization and Electrode Behavior of Li_xCoO_2 (x>1). *Ionics* **2002**, *8* (1–2), 100–107. https://doi.org/10.1007/BF02377759.

(41) Levasseur, S.; Ménétrier, M.; Shao-Horn, Y.; Gautier, L.; Audemer, A.; Demazeau, G.; Largeteau, A.; Delmas, C. Oxygen Vacancies and Intermediate Spin Trivalent Cobalt Ions in Lithium-Overstoichiometric $LiCoO_2$. *Chem. Mater.* **2003**, *15* (1), 348–354. https://doi.org/10.1021/cm021279g.

(42) Levasseur, S.; Ménétrier, M.; Delmas, C. On the Dual Effect of Mg Doping in $LiCoO_2$ and $Li_{1+\delta}CoO_2$: Structural, Electronic Properties, and ^{7}Li MAS NMR Studies. *Chem. Mater.* **2002**, *14* (8), 3584–3590. https://doi.org/10.1021/cm021107j.

(43) Carlier, D.; Cheng, J.-H.; Pan, C.-J.; Ménétrier, M.; Delmas, C.; Hwang, B.-J. DFT+U Calculations and XAS Study: Further Confirmation of the Presence of CoO_5 Square-Based Pyramids with IS-Co^{3+} in Li-Overstoichiometric $LiCoO_2$ http://pubs.acs.org/doi/suppl/10.1021/jp409850q.

(44) Ménétrier, M.; Carlier, D.; Blangero, M.; Delmas, C. On "Really" Stoichiometric $LiCoO_2$. *Electrochem. Solid-State Lett.* **2008**, *11* (11), A179–A182. https://doi.org/10.1149/1.2968953.

(45) Van der Ven, A.; Aydinol, M. K.; Ceder, G.; Kresse, G.; Hafner, J. First-Principles Investigation of Phase Stability in Li_xCoO_2. *Phys. Rev. B* **1998**, *58* (6), 2975–2987. https://doi.org/10.1103/PhysRevB.58.2975.

(46) Reimers, J. N.; Dahn, J. R. Electrochemical and In Situ X-Ray Diffraction Studies of Lithium Intercalation in Li_xCoO_2. *J. Electrochem. Soc.* **1992**, *139* (8), 2091–2097. https://doi.org/10.1149/1.2221184.

(47) Amatucci, G. G.; Tarascon, J. M.; Klein, L. C. CoO_2, The End Member of the Li_xCoO_2 Solid Solution. *J. Electrochem. Soc.* **1996**, *143* (3), 1114–1123. https://doi.org/10.1149/1.1836594.

(48) Ohzuku, T.; Ueda, A. Solid-State Redox Reactions of $LiCoO_2$ ($R\bar{3}m$) for 4 Volt Secondary Lithium Cells. *J. Electrochem. Soc.* **1994**, *141* (11), 2972–2977. https://doi.org/10.1149/1.2059267.

(49) Shao-Horn, Y.; Levasseur, S.; Weill, F.; Delmas, C. Probing Lithium and Vacancy Ordering in O3 Layered Li_xCoO_2 ($x \approx 0.5$) An Electron Diffraction Study. *J. Electrochem. Soc.* **2003**, *150* (3), A366–A373. https://doi.org/10.1149/1.1553787.

(50) Chen, Z.; Lu, Z.; Dahn, J. R. Staging Phase Transitions in Li_xCoO_2. *J. Electrochem. Soc.* **2002**, *149* (12), A1604–A1609. https://doi.org/10.1149/1.1519850.

(51) Xia, H.; Lu, L.; Meng, Y. S.; Ceder, G. Phase Transitions and High-Voltage Electrochemical Behavior of $LiCoO_2$ Thin Films Grown by Pulsed Laser Deposition. *J. Electrochem. Soc.* **2007**, *154* (4), A337–A342. https://doi.org/10.1149/1.2509021.

(52) Seong, W. M.; Yoon, K.; Lee, M. H.; Jung, S.-K.; Kang, K. Unveiling the Intrinsic Cycle Reversibility of a $LiCoO_2$ Electrode at 4.8-V Cutoff Voltage through Subtractive Surface Modification for Lithium-Ion Batteries. *Nano Lett.* **2018**. https://doi.org/10.1021/acs.nanolett.8b02902.

Part B. Investigation of high voltage phase transitions occurring during the Li-de-intercalation of LCO-based electrodes

Part B. Investigation of high voltage phase transitions occurring during the Li-de-intercalation of LCO-based electrodes

B.1 Introduction. Bibliographic context

We showed in Part A that even if more charge and discharge capacities (CQ and DQ) are indeed achieved after one cycle of LCO//Li cells with increasing cutoff voltages, the gain of capacity is far from being kept in the next cycles. Poor cycle life is systematically achieved, and increasing polarization is easily observed in good agreement with previous findings[1,2].

Polarization issues appearing over cycling may come from various sources, though they usually reflect the deterioration of either the electronic and ionic conductivities, or its mechanical properties on the whole electrode scale. However, polarization is quite often directly linked to the degradation of the active material itself as it is found in larger proportions than any other components of the electrode (i.e, binder and conductive filler). Historically, it may include i) the formation of a resistive layer on its particles from the parasitic reaction with the electrolyte (SEI), ii) blocked Li-diffusion pathways either due to the formation of the film previously mentioned, or because of major structural re-arrangements overcome by the host structure accompanying the Li-intercalation processes, iii) insufficient percolation between the particles of all components of the electrode due to either volume changes or cracking of the active material particles, as shown in **Figure B1**.

Following these guidelines, only a few groups have indeed investigated both the surface and the bulk properties of cycled LCO in an attempt to explain the rapid decrease of performance of LCO-based cells at high voltage. The major part of the recent literature dedicated to the use of

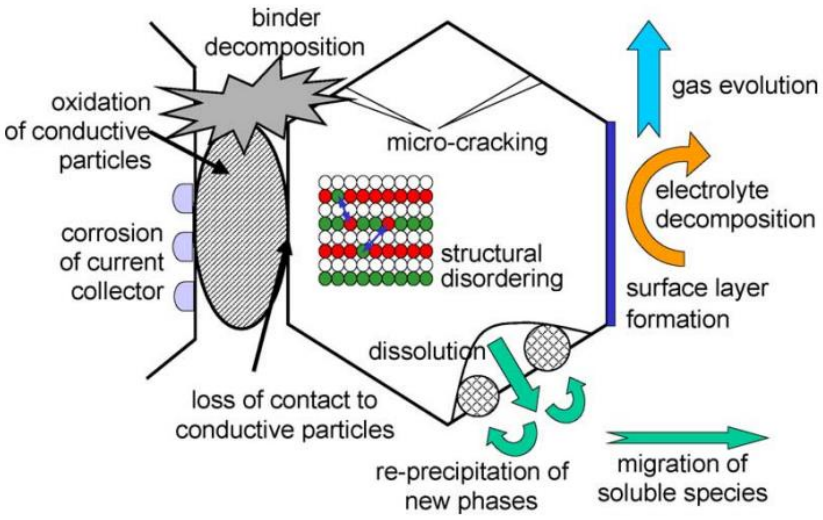

***Figure B1**. Overview of phenomena occurring at the particle scale of cathode materials cycled at high voltage, from Vetter et al.[3].*

LCO at high voltage still remains focused on its optimization through dopings or coatings (which will be more detailed in Part C of this manuscript) rather than properly identifying the root causes for its poor performance. More details for each one of them are exposed in the following, even though more work will certainly be required to understand all the mechanisms involved in each one of the phenomena.

B.1.1 Description of surface-related issues identified during the cycling of LCO at high voltage

The coexistence of organic and inorganic decomposition products from the electrolyte at the surface of cycled LCO particles have been reported[3–6], sharing similar features with the well-known solid electrolyte interphase (SEI) formed at the negative electrode during the 1st discharge of LiBs[7]. Although parameters such as the organic to inorganic species proportions or the thickness may be influenced by either the use of additives[6] in the electrolyte or by a different choice of solvents and salts[4], the chemical nature of the film remains substantially the same from cell to cell. The organic part, mainly composed of alkyl carbonates ROCOOLi and lithium carbonate Li_2CO_3

resulting from the degradation of solvents, confers a porous character to the film. The decomposition products from the $LiPF_6$ salt leads to highly resistive[8] lithium fluoride LiF and oxyfluorophosphate $LiPO_xF_y$. As decomposition products such as alkyl carbonates are known to further react, a more complex overall scheme was proposed by Aurbach et al.[3,9]. They stated that LCO acts as a catalyst in the decomposition of alkyl carbonates. As a consequence, i) carbon dioxide is emitted, ii) Co^{3+} are reduced in Co^{2+}, thereof forming the Co_3O_4 spinel discussed later and iii) Li_2O is formed, which simultaneously reacts with HF (usually resulting from the reaction of $LiPF_6$ with remaining traces of water in the electrolyte) to turn into some more LiF and water. Takahashi et al.[10] later claimed that the oxidation of ethylene carbonate (EC), commonly found as solvent in electrolytes, was responsible for Co-dissolution already observed by several other groups[11–13]. As these reactions are all autocatalytic, no stable capacity can be achieved. Besides, the combination of both the porosity and the poor electronic conductivity of the cathodic SEI has proven to favor the creation of "dead zones" within the electrode and considerably promote particle isolation[3].

The additional presence of Co_3O_4 and $LiCo_2O_4$ spinels at the surface of cycled LCO has also been uncovered by various group. Wang et al.[14] and Gabrisch et al.[15,16] conducted transmission electron microscopy (TEM) investigations on LCO-based electrodes respectively cycled 50 times at 4.35 V and 334 times at 4.2 V. They both observed spinel $LiCo_2O_4$ (*Fd3m* space group) on top of the cycled LCO particles. Not only did Gabrisch et al. see this cubic phase at the surface of LCO, some crystals were found spreading out throughout LCO crystals. Similar observations were reported for LCO particles cycled at higher voltages in much shorter terms. Yazami et al.[17] evidenced the existence of spinel for LCO submitted to a short cycling (several hours) in which only one charge was performed up to 4.7 V. Yano et al.[18] recently observed the spinel on top of

LCO particles cycled up to 4.7 V and submitted to a prolonged floating. They however suggested that the cubic phase was a mixture of both $LiCo_2O_4$ and Co_3O_4. They proposed that at high voltage, the creation of tetravalent CoO_2 units was promoted, which could be easily oxidized into Co_3O_4. In any case, as both spinels exhibit a rather low Li conductivity, they are believed to strongly participate to both the large overall polarization observed over cycling and the capacity fade of LCO.

Observations through TEM investigations also revealed that large amounts of defects such as dislocations (resulting in internal strains) are systematically found in particles of LCO cycled at moderate voltage (E < 4.35 V) and high voltage (E = 4.7 V). However, as the former experiment usually implies hundreds of cycles while much shorter cycling is applied to the latter, accelerated particle aging seems to be promoted again at high voltage. Besides, Yano et al.[18] observed severe cracking of LCO particles, going along with a high density of stacking faults. Pits were also clearly distinguished. Since stacking faults are the result of irreversible CoO_2 plane gliding, which is the main mechanism considered for the formation of the H1-3 and O1 phases (see Part B.1.2.3), it is believed that the repeated structural changes at high voltage are responsible for the severe damages undergone by LCO particles. Gabrisch et al. additionally proposed that dislocations already present in the starting LCO could be initiation sites for CoO_2 gliding[19].

One should note that a cyclic pattern may be identified between all elements previously discussed due to the creation of “fresh” surface through cracks and pits most likely arising from high voltage phase transitions repeating themselves over cycling. Indeed, continuous electrolyte degradation is probably achieved, which promotes continuous formation of both direct SEI products and spinels, gassing, and water.

B.1.2 Identification of the phase transitions occurring at high voltage for the Li_xCoO_2 system

Because of the relation between the phase transitions and all reasons given above leading to the poor electrochemical performance of LCO//Li cells at high voltage, most research groups focus on how to prevent their formation through LCO optimization using coatings and dopings, rather than gaining fundamental knowledge on both H1-3 and O1 phases. Few groups have proposed a description of their respective structures and their real chemical compositions. The following is meant to not only give more insights on the available information, but also to identify the missing components.

B.1.2.1 Background on the end member CoO_2: structure, stability

A summary of all contemplated structures for CoO_2 and their cell parameters reported by the authors mentioned in the following is given in ***Table B.T1****.*

Amatucci et al.[20] first claimed that they achieved complete Li-removal from Li_xCoO_2 when charging a LCO//Li cell up to E = 5.2 V. They identified the structure of CoO_2 to be analogous to the one of CdI_2, and refined its XRD pattern in the *P3m1* space group with cell parameters a = 2.82 Å and c = 4.293 Å. A schematic representation of the CoO_2 structure is given in **Figure B2**, in which the CoO_2 layers are highlighted in blue. An AB-AB sequence is found for the closed packed oxygen planes in CoO_2, differing from the ABC-ABC sequence of O3-LCO. In the nomenclature developed by Delmas et al.[21], CoO_2 is an O1-type phase. Amatucci et al. also reported that i) the poor stability of CoO_2 versus air, decomposing into CoOOH and ii) the Li reinsertion inside O1-CoO_2 was possible and directly led back to an O3-Li_xCoO_2 compound behaving as a solid solution in the whole $0 < x < 0.95$ range.

Further work from other groups have been dedicated to establish whether or not the *P3m1* space group was crystallographically appropriated to describe the O1-structure. Seguin et al.[22] recorded an *in situ* XRD pattern of the CoO_2 end member obtained after full electrochemical Li de-intercalation from $LiCoO_2$, and eventually indexed it in the *Cm* space group. They highlighted how challenging the refinement of CoO_2 XRD patterns could be due to broad and complex diffraction lines, raising the question of structural disorder for the first time. Three different crystallographic sites were extrapolated for Co while no precise oxygen positions could be determined. A follow up work[23] from the same group eventually led to the indexation of CoO_2 XRD pattern in the *P-3m1* space group, which has later been confirmed by work from Yang et al.[24], Motohashi et al.[25] and De Vaulx et al.[26] and is now widely adopted. The Wyckoff positions and occupancies of Co and O are given in **Table B.T2**.

Although the question of the symmetry for the O1-structure seems to be settled, the fluctuations of cell parameters *a* and *c* existing from one article to another are never discussed. For instance, Yang et al.[24] have obtained a CoO_2 phase with a = 2.828 Å and c = 4.237 Å (no uncertainties given), while De Vaulx[26] reported a = 2.8068(1) Å and c = 4.313(4) Å for their phase. It is true that these variations of cell parameters are weak, somehow justifying that they are not debated as they could be uncertainties from refinement, rarely given. However, experimental considerations such as the possibility of remaining Li inside the O1-structure (directly linked to the CoO_2 end member) could also explain the variations of cell parameters. As a matter of fact, the "CoO_2" stoichiometry itself is rather assumed than experimentally demonstrated in the literature. One cannot forget that the favored preparation of supposedly CoO_2 from Li de-intercalation of Li_xCoO_2 in a battery implies severe electrolyte degradation, which considerably complicates the determination of the real Li stoichiometry *x* of their phases.

Symmetry	Cell parameters	Reference	Year of publication
Trigonal (Space group P3m1)	a = b = 2.82 Å c = 4.293 Å	Amatucci et. al[20]	1996
Monoclinic (Space group Cm)	a_m = 4.841 Å b_m = 2.803 Å c_m = 12.747 Å β = 90.1 °	Seguin et. al[22]	1999
Trigonal (Space group P-3m1)	$a_1 = b_1$ = 2.805 Å c_1 = 4.251 Å and $a_2 = b_2$ = 2.821 Å c_2 = 4.240 Å	Tarascon et al.[23]	1999
Trigonal	a = b = 2.828 Å c = 4.237 Å	Yang et. al[24]	2000
Trigonal (Space group P-3m1)	a = b = 2.82 Å c = 4.238 Å	Motohashi et al.[25]	2007
Trigonal (Space group P-3m1)	a = b = 2.806 Å c = 4.313 Å	De Vaulx et al.[26]	2007

Table B.T1. *Summary of crystallographic data available for O1-CoO_2 in the literature.*

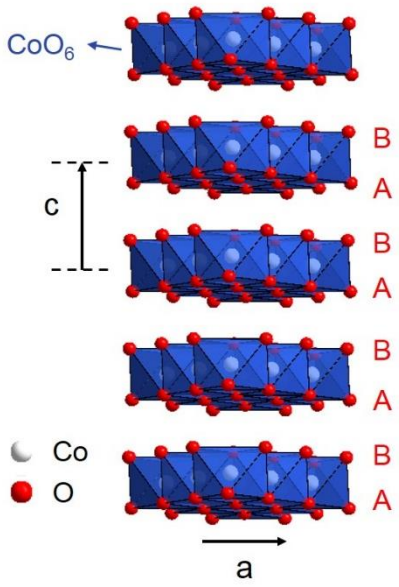

O1 – CoO_2 structure. P-3m1 space group (164)					
Atom	**Site**	**x**	**y**	**z**	**Occupancy**
Co	1a	0	0	0	1.00
O	2d	1/3	2/3	z ~ 0.234	1.00

Table B.T2. *Wyckoff positions and occupancies reported for Co and O in the O1 structure.*

Figure B2: *Schematic representation of the O1 structure. The CoO_2 layers are highlighted in blue. Wyckoff positions, coordinates and occupancies of each atom are given in the jointed Table B.T2.*

This may have contributed to the general confusion consisting of further establishing the formation of the CoO_2 end member through biases. For instance, many groups state that CoO_2 is formed as soon as lines indexed in the *P-3m1* space group appear in the corresponding XRD patterns, without considering that $Li_\varepsilon CoO_2$ ($\varepsilon \rightarrow 0$) phases could share the same symmetry. Another bias resides in determining the formation of "CoO_2" through the final cutoff voltage of their batteries itself. Indeed, as an O1-type structure seems to be formed for E > 4.62 V, a common shortcut is to claim the formation of CoO_2 for any cutoff voltage E > 4.62 V. Besides, applying a common voltage setpoint to LCO materials with various initial Li/Co ratios most likely leads to the formation of de-intercalated Li_xCoO_2 phases with various x values as well. These points will be discussed based on our *in situ* XRD studies in the following.

B.1.2.2 Background on the H1-3 phase: structure, stability, composition

A summary of all contemplated structures for H1-3 and their cell parameters reported by the authors mentioned in the following is given in ***Table B.T3****.*

The first experimental evidence of the H1-3 phase existence was given by Ohzuku and Ueda[27] in 1994. They observed new diffraction lines in three *ex situ* XRD patterns of Li_xCoO_2 electrodes with x = 0.22; 0.21 and 0.19 (corresponding to the XRD patterns shown for Q = 216; 219 and 225 mAh/g, respectively). The new phase (later referred to as H1-3), indexed in the monoclinic symmetry, was though never obtained as a single phase for these three compositions. Remaining hexagonal phase was detected. No proper Li stoichiometry was proposed for the H1-3 phase. Amatucci et al.[20] later confirmed that both a monoclinic with an approximate ~$Li_{0.21}CoO_2$ composition and a hexagonal phase analogous to O3-LCO co-existed in the same x range from *in situ* XRD experiments. The cell parameters reported by these authors for the monoclinic phase were also very comparable to those of Ohzuku and Ueda (see **Table B.T4**). However, they reported the existence of a single monoclinic phase at the peculiar $Li_{0.148}CoO_2$ composition, whose cell parameters differed from those of monoclinic $Li_{0.21}CoO_2$.

Following these two experimental works, Van der Ven et al.[28–30] carried out theoretical calculations and proposed that the new phase observed in the previously mentioned *x* range was an intergrowth compound whose structure was an **H**ybrid of the O**1-** and O**3-** structures (leading to the "H1-3" notation). Following previous findings on the existence of graphite intercalation stage compounds[31], they also identified it as a "stage II" compound. A schematic representation of the H1-3 structure following Van der Ven's predictions is given in **Figure B3**. Unlike the experimental findings mentioned above, a rhomboedral symmetry is considered here (*R-3m* space group).

Chemical formula	Symmetry	Cell parameters	Reference	Year of publication
No precise mention (x < 0.25)	Monoclinic	a_m = 4.91 Å b_m = 2.82 Å c_m = 5.02 Å β = 111.4 °	Ohzuku et Ueda[27]	1994
~ $Li_{0.21}CoO_2$	Monoclinic	a_m = 4.883 Å b_m = 2.816 Å c_m = 4.962 Å β = 113.43 °	Amatucci et. al[20]	1996
~ $Li_{0.148}CoO_2$	Monoclinic	a_m = 4.890 Å b_m = 2.816 Å c_m = 4.93 Å β = 114.42 °	Amatucci et. al[20]	1996
~ $Li_{0.167}CoO_2$	Rhomboedral	$a_{hex} = b_{hex}$ = 2.78 Å c_{hex} = 25.95 Å	Van der Ven et. al[28–30] (theoretical calculations)	1998
~ $Li_{0.12}CoO_2$	Rhomboedral (space group R-3m)	$a_{hex} = b_{hex}$ = 2.823 Å c_{hex} = 27.07 Å and $a_{hex} = b_{hex}$ = 2.819 Å c_{hex} = 27.035 Å	Chen et. al[32]	2002

Table B.T3*. Summary of chemical compositions and crystallographic data reported for the H1-3-Li_xCoO_2*

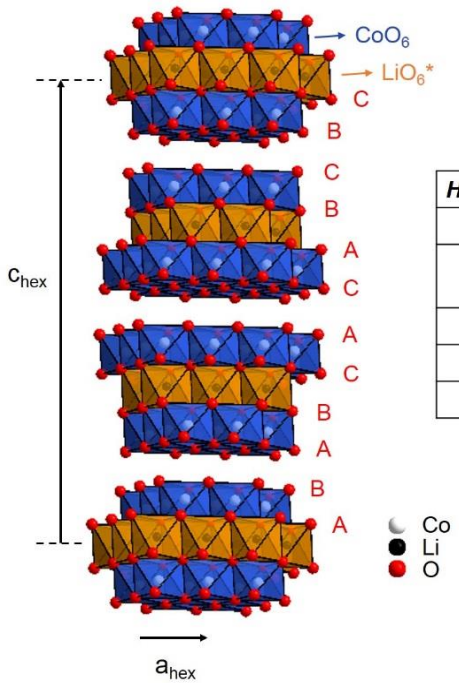

H1-3 – $Li_{\sim 0.167}CoO_2$ structure. R-3m space group (166)					
Atom	**Site**	**x**	**y**	**z**	**Occupancy**
Li	3a	0	0	0	Under debate. 0.24 < occ < 0.38
Co	6c	0	0	z ~ 0.425	1.00
O(1)	6c	0	0	z ~ 0.277	1.00
O(2)	6c	0	0	z ~ 0.115	1.00

Table B.T4*. Wyckoff positions and occupancies reported for Li, Co, and O in the H1-3 structure.*

Figure B3*. Schematic representation of the H1-3 structure as speculated by Van der Ven et. al[28-30]. The CoO_2 layers are highlighted in blue; possible LiO_6 octahedra are in orange. Though all Li sites seem to be occupied every 1/2 plane, only 1/3 of the sites are indeed occupied. The Wyckoff positions, coordinates and occupancies of each atom are given in the jointed table.*

Similarly to O3-$LiCoO_2$, the structure is however represented in the hexagonal system. All corresponding Wyckoff positions and occupancies are given in **Table B.T4**. The CoO_2 layers made of all edge-sharing CoO_6 are highlighted in blue in **Figure B3**. Li-vacant and Li-occupied planes are found continuously alternating. Only 1/3 of octahedral sites are indeed occupied by Li within the same plane. Therefore, the theoretical composition of H1-3-LCO was stated to be $Li_{0.167}CoO_2$, though it is expected to be the most stable phase in a larger composition domain ($0.12 < x < 0.19$). The possibility of two distinct structures in this composition range, as reported by Amatucci et al.[20], was therefore automatically dismissed. Though it does not appear on the schematic representation proposed in **Figure B3**, interlayer distances *d* would be expected to be different depending on the actual Li occupation between the CoO_2 layers. Unfortunately, this cannot be verified through XRD, as an average value is obtained (with $4.52 < d < 5.02$ Å so far). While the oxygen packing was of AB-CA-BC-type on O3-LCO, a more complex AB-CA-CA-BC-BC-AB-AB sequence is reported for H1-3-LCO. Note that since the unit cell is made of 6 layers of CoO_2, H1-3-LCO could also be called O6-LCO following the nomenclature developed by Delmas et al.[21].

Experimental work confirming Van der Ven et al.'s predictions later came from Chen et al.[32]. They successfully prepared the H1-3-Li_xCoO_2 from electrochemical de-intercalation of Li up to $x = 0.12$ using Al_2O_3-coated LCO as positive electrode in a Li cell. They indexed the corresponding *ex situ* XRD pattern in the *R-3m* space group, although two various sets of cell parameters were reported. Values of $a_{hex} = 2.823$ Å and $c_{hex} = 27.07$ Å were first proposed over the refinement on the three first cumulated XRD acquisitions; refinement of the patterns recorded after one hour gave values of $a_{hex} = 2.819$ Å and $c_{hex} = 27.035$ Å. Even if they evoked a possible reactivity of their powder with air due to a lack of tightness of their argon-filled XRD cell, the reason behind

the unstable behavior of H1-3 remains unclear. If it is true that sensitivity to air seems reasonable enough, a de-mixing reaction could also occur.

Note that both works from Chen et al.[32] and Ueda et Ohzuku[27] suggest that the preparation of a H1-3-LCO powder from electrochemical de-intercalation of Li is challenging. The use of an Al_2O_3 coating on top of LCO particles may reveal that the strong degradation of electrolyte previously discussed is incapacitating in the preparation of H1-3 from bare LCO. The preparation of pure H1-3 also looks rather unpredictable, as shown by the systematic biphasic mixtures obtained by Ueda and Ohzuku. The question of the stability of the H1-3 arisen by Chen et al. may add up. This could explain why no further information regarding i) the possibility of not one but two H1-3 phases, ii) the real structure of the H1-3 phase(s), iii) its chemical composition or even iiii) its properties (conductivity, magnetism..) has since been reported, let alone a possible influence of the initial Li/Co in LCO on the final H1-3 structure.

B.1.2.3 The O3 – H1-3 and H1-3 – O1 transitions

For any layered oxide AMO_2 (A = alkali ion, M = transition metal), the creation of vacancies in the interlayer space during the alkali removal is a source for strong electrostatic repulsions between the oxygens of the layers. As a consequence, both the distance between the layers and the M-M bonds vary as a function of *x*, though the change is more pronounced for the former. Besides, for some critical concentrations of remaining A, more energetically favorable configurations may be adopted by A_xMO_2, causing phase transitions. These structural changes may be either reversible or irreversible, the latter being undesired in the case of further applications of AMO_2 as electrode active material in a battery.

Reversible transformations are either achieved by i) a re-arrangement of alkali ions, which occupy non-random positions within the interlayer space (alkali/vacancy ordering) or ii) by a translation of the layers in the (a, b) plane (plane gliding). Both are topotactic transitions, as no M-O bonds are broken, meaning that the constitution of MO_2 layers remain unaltered.

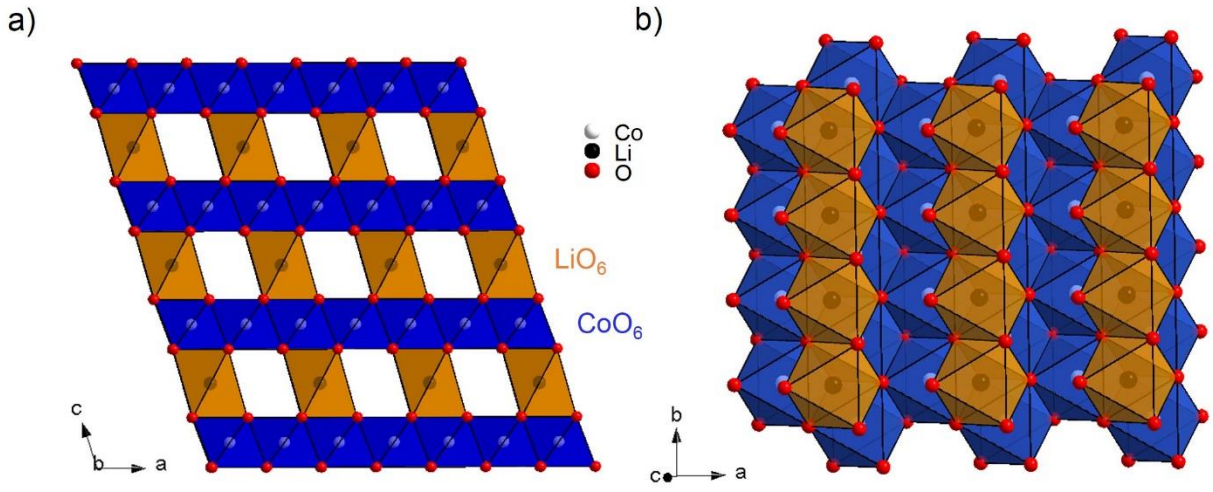

***Figure B4**. Schematic representation of O'3-$Li_{0.5}CoO_2$, **a)** in the (a, c) plane and **b)** in the (a, b) plane.*

Both types of transformation are observed in the Li_xCoO_2 system. The monoclinic transition from an O3 to O'3 phase (the apostrophe denoting the monoclinic distorsion in Delmas' nomenclature[21]) previously described in Part A does correspond to a Li/vacancy ordering when half of the Li is removed from LCO, as illustrated in **Figure B4**. Although Wolverton and Zunger[33] and Van der Ven et al.[30] predicted that Li/vacancy orderings would be energetically favorable for x = 0.33 and x = 0.67 in O3-Li_xCoO_2, their formation have never been experimentally observed (unlike in the analogous P2-Na_xCoO_2 system[34]).

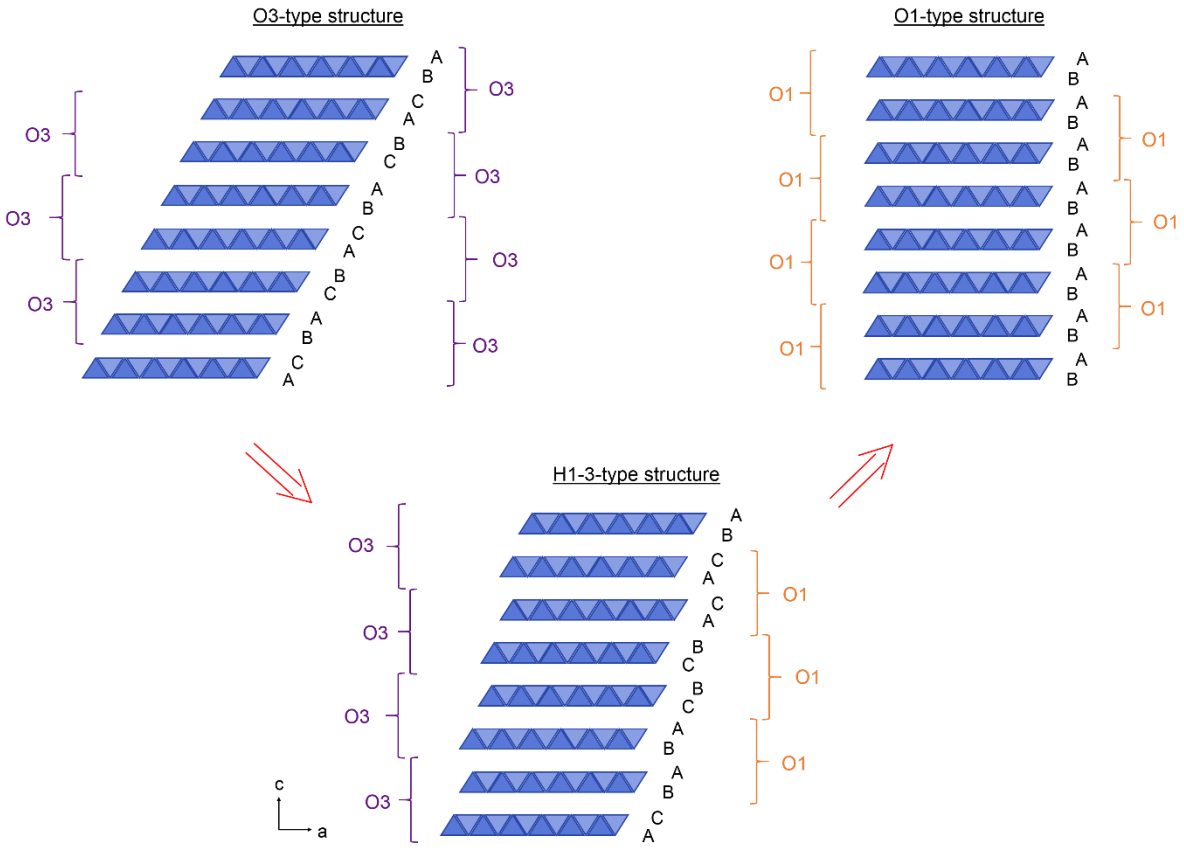

Figure B5. *Schematic representation of the CoO_2 layer stackings in the O3, H1-3 and O1 structures. The letters refer to oxygen positions arbitrarily used to describe these structures (A(0, 0, z_A), B(⅓, ⅔, z_B) and C(⅔, ⅓, z_C)).*

Plane gliding is however involved in the formation of the high voltage phase phases (**Figure B5**), though no experimental evidence has either proved or completely dismissed the possibility of an additional Li-ordering for the H1-3 phase so far. The completion of "ideal" H1-3 and O1 structures through a plane gliding mechanism as depicted in **Figure B5** is however unlikely at high voltage. Indeed, previous studies of the O3 – H1-3 and H1-3 – O1 phase transitions have systematically shown[23,35,32] that broad diffraction lines are observed in the corresponding *in situ* XRD patterns, which could be explained by the existence of substantial amounts of stacking faults within the layered oxide, as they are known to yield to large broadening of specific (hkl) diffraction lines[36]. Besides, as previously mentioned, Yano et al.[18] recently evidenced the existence of stacking faults in $LiCoO_2$-based electrodes formerly cycled 20 times up to 4.7 through TEM. **Figure B6** aims to depict the most plausible types of stacking faults that may be formed during the high voltage cycling of $LiCoO_2$ in i) O3-type structures (**Figure B6.a**), and in the end member O1 structure (**Figure B6.b**), whose formation cause the broadening of XRD peaks in the DIFFAX-modeled XRD patterns shown in **Figure B6.c**. Similarly, **Figure B7** depicts possible faulted structures for the H1-3 phase, although due to both the challenging technical conditions to stabilize the H1-3 phase from electrochemical de-intercalation of Li in $LiCoO_2$ and the insufficient resolution of common characterization techniques such as laboratory XRD, the existence of stacking faults within the H1-3 phase itself has never been directly observed *ex situ*. This may have constituted another complication in further providing answers regarding the structural properties of this phase. The mention of stacking faults throughout the rest of this manuscript will be inherently linked to the description previously provided.

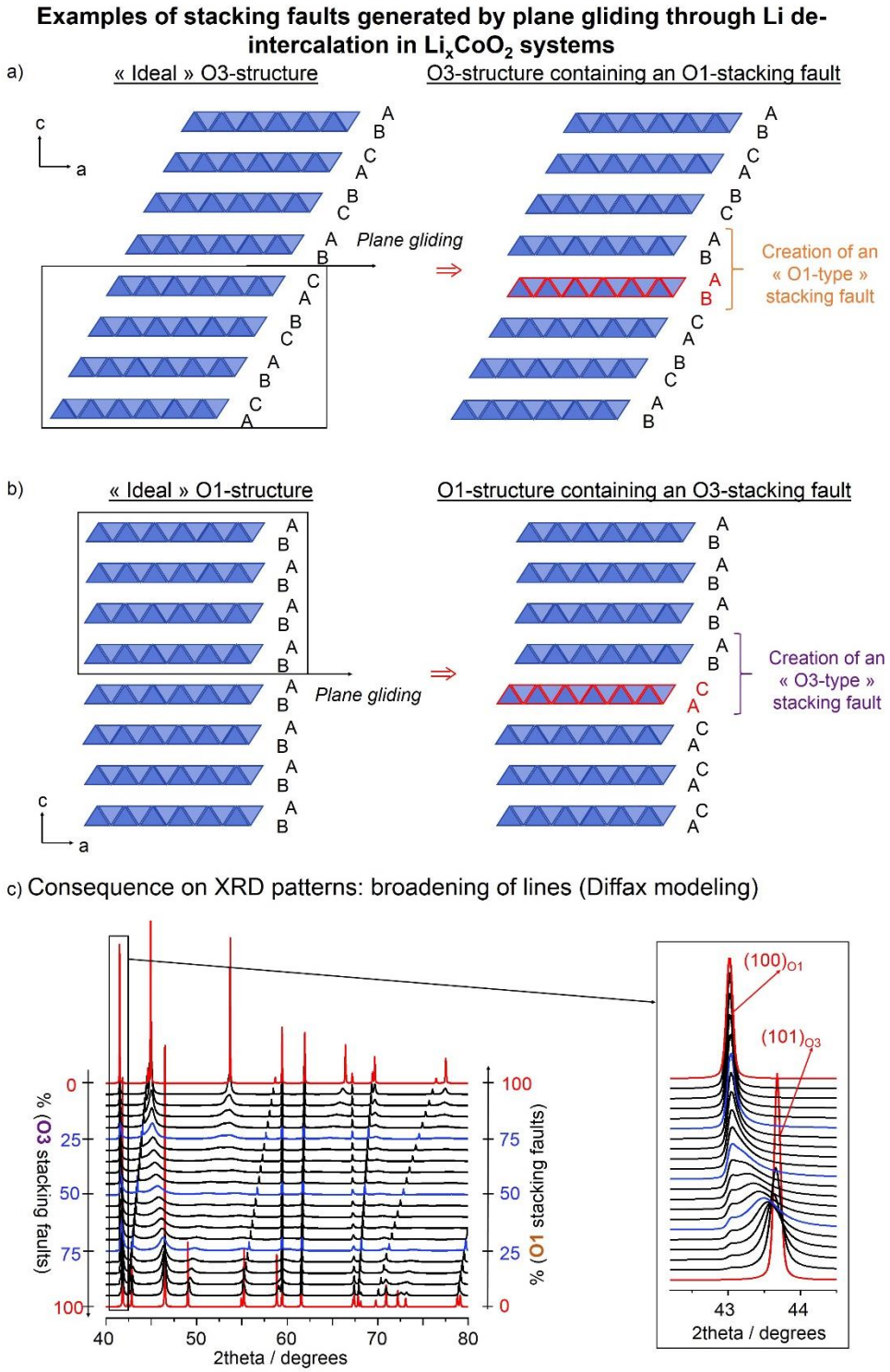

Figure B6. *Schematic representation of the CoO_2 stacking in a) the ideal O3 structure as opposed to an O3 structure containing an O1-type stacking fault, b) the ideal O1 structure as opposed to an O1 structure containing an O3-type stacking fault. The letters refer to oxygen positions arbitrarily used to describe these structures (A(0, 0, z_A), B(⅓, ⅔, z_B) and A(⅔, ⅓, z_C). A simulation of XRD patterns for the O3 and O1 structures with various amounts of stacking faults using DIFFAX is given in c).*

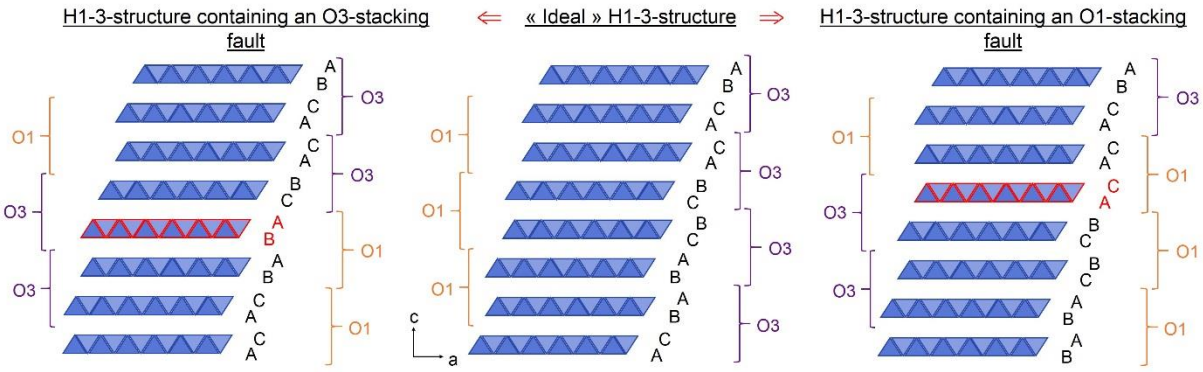

Figure B7. *Schematic representation of the CoO_2 stacking in the ideal H1-3 structure, as opposed to an H1-3 structure containing either an O1-type stacking fault or an O3-type stacking fault. The letters refer to oxygen positions arbitrarily used to describe these structures (A(0, 0, z_A), B(⅓, ⅔, z_B) and A(⅔, ⅓, z_C)).*

In the following, we re-investigated the structural changes experienced by LCO during its 1st full charge in a Li cell, taking into consideration a possible influence of the initial Li/Co ratio (Li/Co = 1.00 or 1.05) through in situ and ex situ X-ray diffraction measurements.

B.2 Preliminary study: in situ XRD investigation of the phase transitions occurring at high voltage for stoichiometric and 4%-overlithiated LCO

In a preliminary study, laboratory in situ XRD was carried out to follow the structural changes occurring at high voltage during the charge of both stoichiometric and overlithiated LCO. This work was published[37] in 2018 and is presented in the following.

B.2.1 Experimental section

Note that three LCO powders were selected for this investigation: i) LCO-5 ($(Li/Co)_{th}$ = 0.98) and LCO-8 ($(Li/Co)_{th}$ = 1.04) were used in order to evaluate the influence of the initial Li/Co ratio on the high voltage phase transitions. A comparison of data collected for both stoichiometric LCO (LCO-5 with $(Li/Co)_{th}$ = 0.98 and d ~ 35 µm; LCO-2 with $(Li/Co)_{th}$ = 1.00 and ~ 1-2 µm) was used to evaluate the influence of the initial particle size on the same transitions. As no such effect was observed, data is presented in Appendix.

As the selection of samples is significantly narrower than in Part A, the stoichiometric LCO (LCO-5) will be now designated by "st-LCO". 4%-overlithiated LCO-8 will be denoted as "overl-LCO".

LCO:C:PVDF electrodes (90:5:5 $\%_{wt}$) with either st-LCO or overl-LCO as active materials were prepared from a slurry using N-methyl-pyrrolidone (NMP) as solvent casted onto 6.5µm-thick-aluminum circles for the *in situ* XRD experiments. Typical active material loading and diameter for an electrode used during *in situ* XRD experiments were respectively 15 mg/cm² and 20 mm. The electrodes were dried overnight under vacuum at T = 120 °C and stored in an argon-filled glovebox, the homemade *in situ* cells were assembled using pure lithium as counter-electrode and 1 M $LiPF_6$ in EC:DEC:DMC as electrolyte. More details can be found in Appendix.

For the *in situ* XRD experiments, electrodes were pre-charged at C/30 up to 4.2 V without collecting any XRD pattern, since the goal of this preliminary experiment was the investigation of the phase transitions occurring at higher voltage. After reaching E = 4.2 V *vs.* Li^+/Li, the charge proceeded at a lower C rate C/100 up to 5.0 V. XRD patterns were collected *in operando* on a PANalytical X'Pert PRO MPD diffractometer, using the Cu $K\alpha_1$ radiation. Special attention was given to the (0 0 ℓ) diffraction peak evolution, that allows to directly follow the changes in the interslab distance which is characteristic of the metal and lithium layer stacking modifications. Therefore, XRD acquisition was recorded every hour between 18 and 21.6°. Due to large exposure time at high voltages leading to substantial electrolyte degradation, we chose to discuss the data versus the cell voltage in the following and not versus state of charge expressed by the lithium amount (*x*).

B.2.2 Results and discussion

In order to better understand those phenomena, we recorded *in situ operando* XRD patterns in the high voltage range for both LCO samples. In **Figure B8**, we plotted the patterns collected for the most intense (0 0 ℓ) diffraction line upon charge in two relevant voltage domains for more clarity: 4.20 - 4.60 V (a, b) and 4.55 - 5.0 V (c,d), respectively corresponding to the successive O3 – H1-3 and H1-3 – O1 phase transitions for supposedly Li-stoichiometric samples only[32,38]. For a better understanding of the mechanisms, we also plotted the evolution of the $d_{(0\,0\,\ell)}$ interslab spacing as a function of the voltage in **Figure B9**. At ~ 4.20 V vs Li^+/Li, the two compounds exhibit a single sharp intense diffraction line, corresponding to the (0 0 3) diffraction peak of a O3-type Li_xCoO_2 structure with a similar interslab distance for the two materials ($d_{(0\,0\,3)}$ = 4.81 Å), higher than the one of the pristine materials ($d_{(0\,0\,3)}$ = 4.68 Å). At 4.20 V vs Li^+/Li, approximately 0.4 Li^+

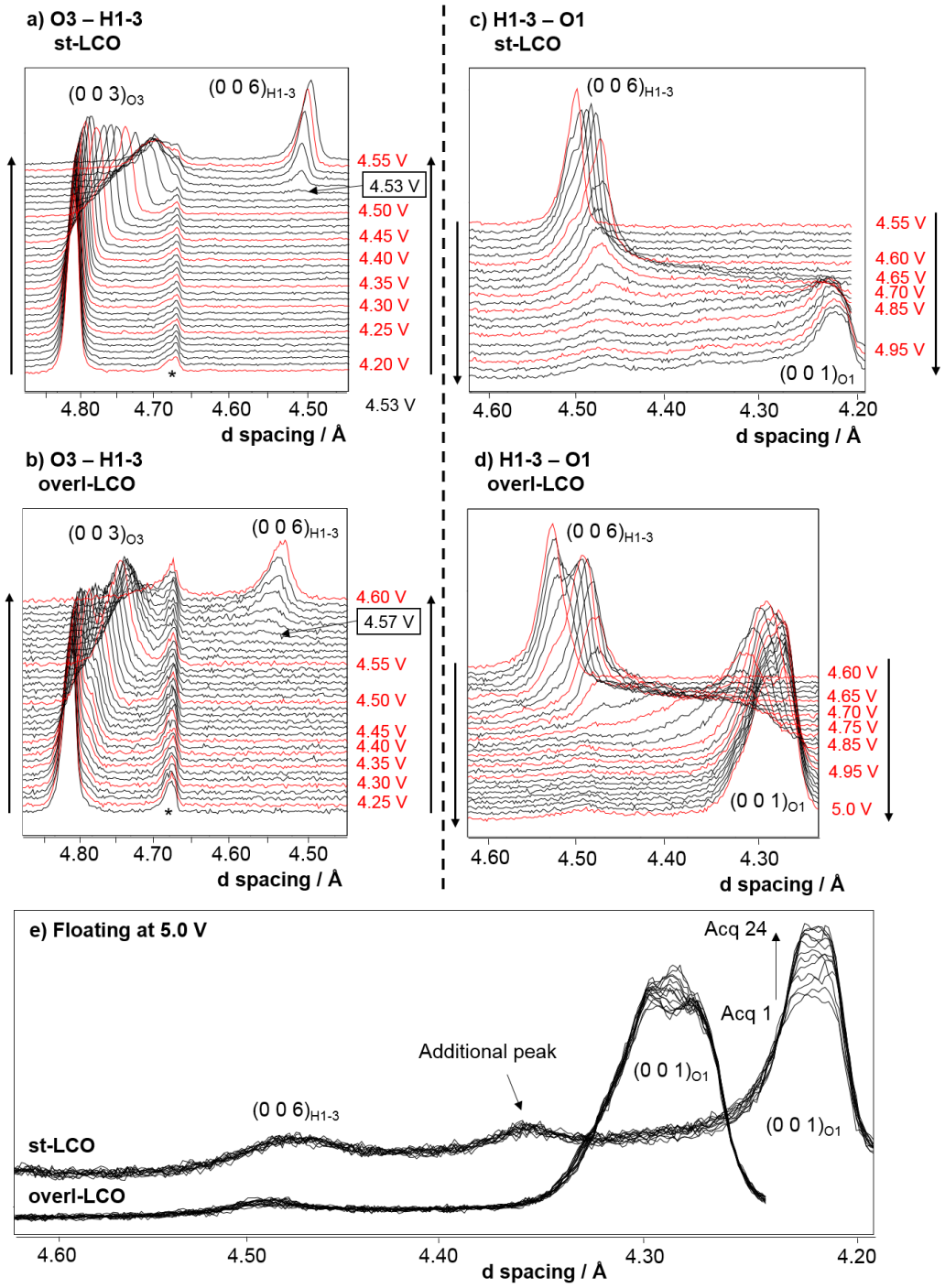

Figure B8. *Cumulated XRD patterns recorded in situ operando during the charge of st-LCO and overl-LCO, plotted as a function of d spacing in the 4.20 – 4.55V (or 4.60 V) vs. Li^+/Li voltage range* ***(a, b)*** *and in the 4.55 (or 4.60 V) - 5.00 V* ***(c, d)*** *range, respectively corresponding to the successive O3 – H1-3 and H1-3 – O1 phase transitions. The black arrows show the evolution of the patterns towards the charge. Figure* ***(e)*** *is dedicated to a comparison of patterns obtained at the very end of the charge, as we maintained a constant potential reaching E = 5.0 V. The peak identified with (*) is a line from the cell.*

ions are remaining in both LCO compounds. A schematic representation of the O3 structure is given in **Figure B9**. As we slowly further de-intercalate Li^+ ions up to 4.55 V, the interlayer distance $d_{(0\,0\,3)}$ decreases as revealed by the shift of peak position on **Figure B8.a** and **Figure B8.b**. This signal also undergoes a clear broadening that we assigned to the competition between nucleation and growth of O1-type stacking faults into the O3-type matrix (as previously described in see **Figure B6**). No other significant change is observed for this $(0\,0\,3)_{O3}$ peak before the appearance of a new peak at 4.53 V and at 4.57 V for st-LCO and overl-LCO, respectively. This peak corresponds to the (0 0 6) diffraction line of the H1-3-type structure (depicted in **Figure B9**). For st-LCO, the associated average interlayer distance $d_{(0\,0\,6)}$ is 4.51 Å, meaning that the corresponding $c_{hex..}$ parameter is approximately 27.06 Å, in good agreement with the value reported by Dahn's group[32] (27.07 Å). Despite the presence of defects in the pristine overl-LCO, the H1-3 phase is formed during Li^+ de-intercalation but appears at slightly higher voltage and does exhibit a higher interlayer distance ($d_{(0\,0\,6)}$ = 4.55 Å). The stability domain of the intermediate H1-3 phase is also different for the two compounds: very narrow for st-LCO (d varies between 4.51 Å and 4.46 Å) and larger for overl-LCO (d varies between 4.55 to 4.45 Å).

Upon further charge up to 5 V, the mechanism observed for the two materials are clearly different (**Figures B8.c** and **B8.d**). For st-LCO, whereas a single transition from H1-3 to O1 structural type is expected from literature[20,32,38], we first observe a gradual broadening and asymmetry of the $(0\,0\,6)_{H1\text{-}3}$ diffraction line towards the lower d values, then the appearance of two new "diffraction lines" corresponding to d = 4.36 Å and 4.23 Å, both still very broad. The line at 4.23 Å can be assigned to the (0 0 1) diffraction line of the O1 structure type already reported in the 1990's by Amatucci *et al.*[20], but the line located at 4.36 Å was not reported so far and might result from intergrowth between H1-3 and O1 structures. The appearance of the new peak at 4.36 Å

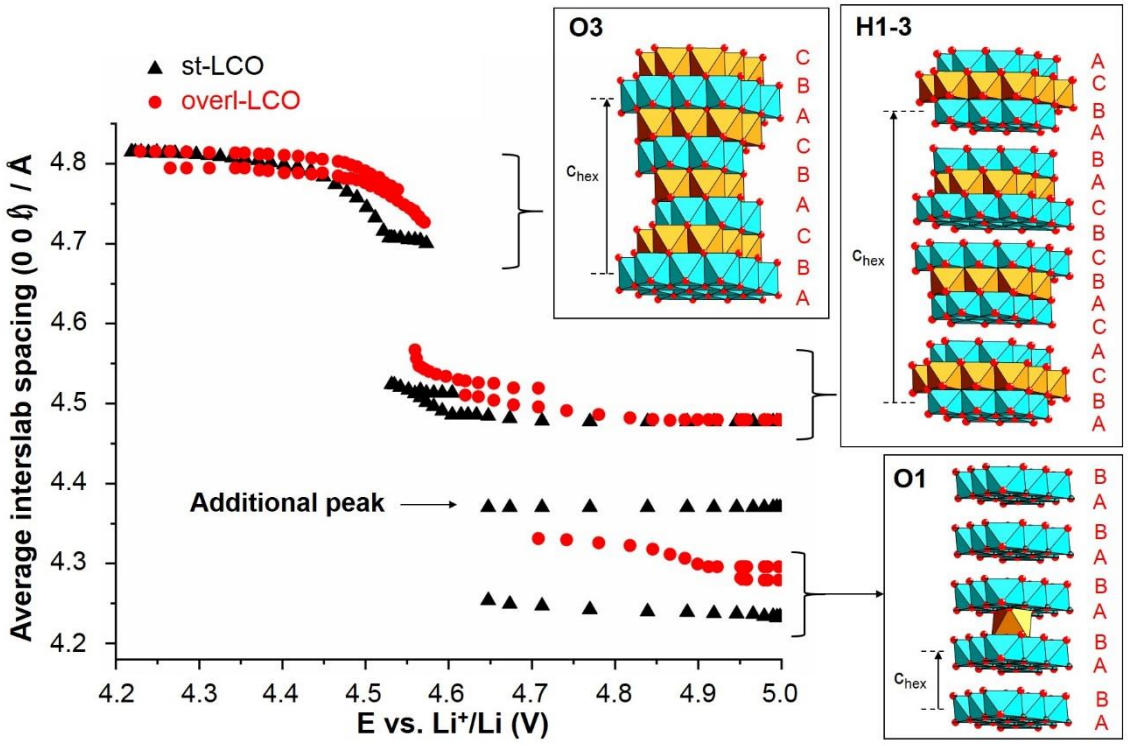

Figure B9. *Plot of the average interlayer distance d(0 0 l) for each phase formed during the charge of st-LCO and overl-LCO as function of E vs. Li^+/Li. The values for d(0 0 l) are reported for each XRD pattern shown in Figure B8. For better understanding, structures for all phases are schematically depicted in small boxes, on the right of the figure. The blue octahedra are CoO_6 units, while the yellow ones are possible LiO_6. Letters in red represent the oxygen stacking, each letter corresponding to an oxygen position as followed: A (0 0 z_A); B (⅓ ⅔ z_B); C (⅔ ⅓ z_C).*

is better seen on the XRD pattern, after we applied a potentiostatic step at E = 5.0 V for several hours following the charge of the compound and recorded a few more patterns (**Figure B8.e**). Since it is located for intermediate d-values between H1-3 and O1 phases, we propose that the intergrowth between these structures is not completely random, thus forming an intermediate stacking. Its formation could be a way to minimize the internal constraints due to the strong d-interslab space diminution from H1-3 to O1 for the system. Note that even after a long floating at 5 V, the diffraction lines for the three phases (H1-3, intermediate and O1) are still observed (**Figure B8.e**).

In any case, from their peak broadening, those structures may contain a high number of stacking faults resulting in overall structural disorder (see previous figures: **Figure B6** and **Figure B7**). For overl-LCO, the mechanism is different, no intermediate peak is observed: the H1-3 structure gradually transform into an O1 structure with the formation of several intermediate stacking faulted structures, with a continuous process.

In addition, it can be noticed that the final O1 structures obtained from both st-LCO and overl-LCO show significant differences regarding their respective interslab spacing. Indeed, a lower value for st-LCO (d_{001} = 4.23 Å) sample is obtained, as compared to overl-LCO (d_{001} = 4.31 Å) sample. This could be related to the presence of vacancies in the $Co_{1-t}O_{2-t}$ slabs, or to some more remaining Li in overl-LCO as compared to its analogue obtained from st-LCO.

B.2.3 Trends and hypotheses from the preliminary study. First conclusions.

Following the conclusions on the effect of the initial Li/Co stoichiometry on Li^+ de-intercalation process at low voltage (below 4.4 V) for LCO materials evidenced by several groups, we showed that the initial Li/Co stoichiometry also affect the mechanisms involved at high voltage. The successive structural transitions from O3 to H1-3 and O1 phase are observed for both samples, but these phases appear at higher voltage and does exhibit different cell parameters for an overlithiated compound. Note that less volume changes are obtained for the overlithiated compound despite a higher irreversible capacity, that may therefore be due to some structural reorganization, stronger electrolyte oxidation and cobalt dissolution. We also showed that for the stoichiometric LCO, the de-intercalation process occurring at high voltage is more complex than already reported, with the formation of an intermediate phase between H1-3 and O1.

B.3 Synchrotron *in situ* and *ex situ* X-ray diffraction for the reinvestigation of the phase transitions occurring in the Li_xCoO_2 system. Influence of the initial Li/Co stoichiometry.

B.3.1 Experimental section

Following the preliminary in situ XRD investigation presented in part B.2, a complementary study was carried out at ALBA synchrotron at the BL04-MSPD beamline (Cerdanyola del Vallès, Spain) in collaboration with François Fauth using the same starting LCO (st-LCO and overl-LCO).

Φ15 mm electrodes of st-LCO and overl-LCO were prepared following the same experimental protocol presented in Part B.2. The typical active material loading per electrode was ~ 17 – 18 mg (12 mg/cm²) for an approximate thickness of ~ 50 µm after calendering (p = 10 tons/electrode).

The battery setup used for this investigation was significantly changed. While in situ XRD in part B.2 was performed using a homemade cell, all *in situ* synchrotron powder X-ray diffraction (*in situ* SXRD) was carried out in regular CR2032 coin cells with Φ3 mm hole drilled beforehand, on top of which kapton windows were glued. To ensure a proper pressure inside the coin cells, an additional spring was systematically added as compared to conventional assembling of CR2032 coin cells. Coin cells were assembled using Li as counter electrode and $LiPF_6$ in EC:DEC:DMC as electrolyte.

High angular resolution *in situ* synchrotron powder X-ray patterns were collected for up to 4 coin cells simultaneously charging / discharging, as the holder was translated according to a

sequential positioning (see Appendix). The patterns were recorded in transmission mode with a wavelength of λ = 0.825957 Å (refined after performing Rietveld refinement on both Si and mixture of CaF_2 + $Na_2Ca_3Al_2F_{14}$ used as standards) and 30-second-accumulation time. The typical 2Θ angular range for an acquisition was 2 - 43 ° with 0.006° angular step using a MYTHEN 6K detector[39]. Note while this detector allows fast acquisitions suitable for operando studies, it does not provide the best angular resolution. After recording the n^{th} XRD pattern, the $(n+1)^{th}$ pattern for the same coin cell was collected 260 seconds later, which takes into account accumulation times for other SXRD patterns recorded for the 3 other coin cells and the time for sample change from positions 1, 2, 3 or 4. A constant rocking of ± 15 ° of the whole setup within the Eulerian cradle was applied to reduce the effect of the preferred orientation of crystallites, though not entirely suppressed. Although various experiments were carried out during our synchrotron session (including various C rates), only the results obtained at the outcome of the charge of st-LCO and overl-LCO at C/20 are shown within Part B.3, corresponding to a total of ~ 275 SXRD patterns each (3 patterns every Δx = 0.01 Li). An overview of cumulated SXRD patterns collected during the charge of st-LCO and the corresponding charge curve is provided in **Figure B10**. However, chosen zooms will be mainly shown throughout this part of the manuscript due to the many additional diffraction lines corresponding to other battery components probed by the beam (Li, kapton, PVDF, aluminum…) which often overlaps with essential peaks ascribed to the LCO active material (see **Figure B11**). As stated in **Figure B10**, three successive electrochemical windows will be commented upon in the following: a low voltage window ($3.9 < V < 4.3$; $0.4 < x \leq 1.00$, part B.3.2) for st-LCO only, and a high voltage window divided into two separate parts for both st-LCO and overl-LCO: High voltage 1 ($4.3 < V < \sim 4.55$; $0.2 < x \leq 0.4$, part B.3.3) and High voltage 2 ($\sim 4.55 < V < 5.2$; $0.0 < x \leq 0.2$, part B.3.4).

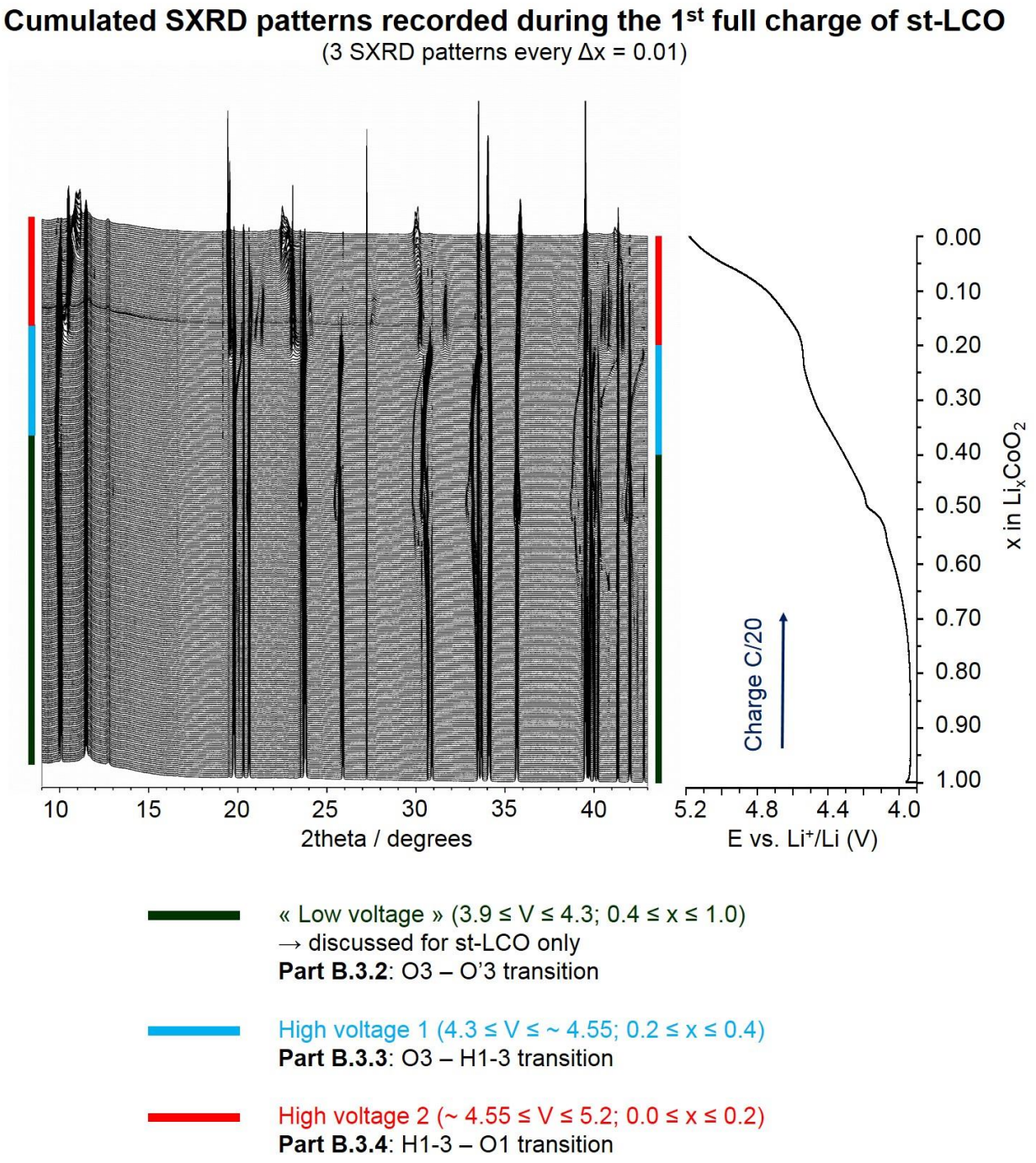

Figure B10. *Cumulated ~ 275 XRD patterns recorded in situ operando during the full charge of st-LCO and collected with λ = 0.825 Å. The associated electrochemical curve is given on the right. The green, blue and red rectangles denote the three successive electrochemical windows that will be commented upon in part B.3.*

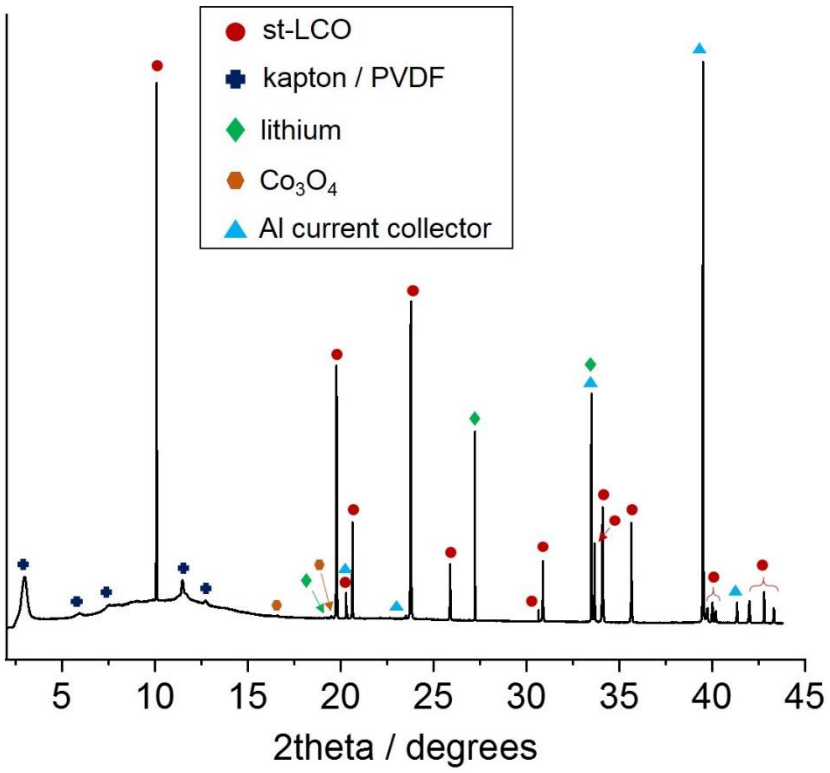

Figure B11. *1st in situ SXRD pattern recorded for a st-LCO based coin cell featuring Li as counter electrode and $LiPF_6$ EC:DEC:DMC as electrolyte. All various contributions from the cell are here identified.*

Additional high angular resolution *ex situ* synchrotron powder X-ray diffraction (*ex situ* SXRD) was also carried out, still on the BL04-MSPD beamline of the ALBA synchrotron on samples prepared from electrochemical Li de-intercalation prepared beforehand and packed in Φ0.3 mm glass capillaries. To do so, Swagelok cells featuring pellets of st-LCO or overl-LCO mixed with acetylene black (90:10 $\%_{wt}$, typical active mass ~ 70 mg) as positive electrode, Li as negative electrode and $LiPF_6$ in EC:DEC:DMC as electrolyte. Cells were galvanostatically charged up to a given potential E_f at C/30, followed by a floating step, as illustrated in **Figure B12**. Cells were disconnected when dI/dt reached ~ 0 $mA.h^{-1}$ and dismantled inside an argon-filled glovebox. The positive electrode powder was recovered and washed three times with DMC before being safely stored for further analysis.

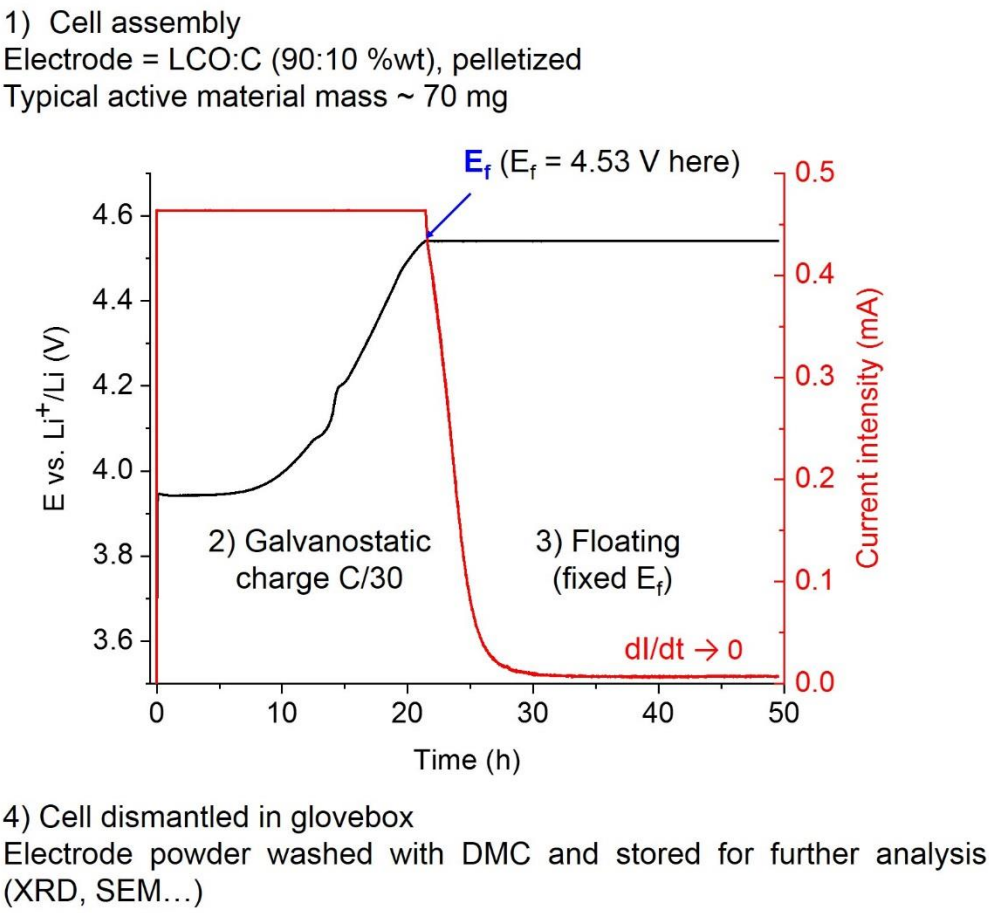

Figure B12. *Schematic guideline used in the preparation of Li de-intercalated Li_xCoO_2 phases (here from st-LCO) throughout this whole manuscript.*

Open-circuit voltage (OCV) measurements were done on st-LCO in order to get the equilibrium voltages associated at precise state of charge (SOC) of the corresponding coin cell. To do so, it was incrementally charged (and discharged) at C/20 every $\Delta x = 0.005$ and further allowed to relax up to reaching a dE/dt = 0.1 mV/h criterion. Due to the use of such a fine criterion and the known degradation of electrolyte for E > 4.4 V vs. Li^+/Li, the charge cutoff voltage was set to ~ 4.3 V. OCV measurements were recorded at the end of each relaxation steps. This method is more currently referred to as galvanostatic intermittent titration technique (GITT).

B.3.2 Re-investigated: the O3 – O'3 transition

As XRD patterns were collected nonetheless at the beginning of the charge of our LCO powders, we took this opportunity to re-investigate the O3 – O'3 transition for stoichiometric LCO.

Figure B13 shows zooms on various 2Θ domains of the cumulated SXRD patterns collected during the charge of st-LCO up to E = 4.30 V. Approximately 0.59 Li are removed from the structure up to this voltage. At the very beginning of the charge, the (003), (104), (110) and (113) diffraction lines arising from the initial $O3_1$-structure of st-LCO (a_{hex} = 2.815 Å; a_{hex} = 14.046 Å) are clearly visible in **Figure B13**. The equivalent peaks for the second $O3_2$-$Li_{0.75}CoO_2$ phase (a_{hex} = 2.811 Å; c_{hex} = 14.22 Å) appear quite instantly, as expected[40] for $1.00 \geq x \geq 0.75$ in Li_xCoO_2 systems ($x_0 \leq 1.00$). In this whole x range, both $O3_1$ and $O3_2$ structures are simultaneously found within the electrode. In the $0.75 \geq x \geq 0.53$ composition range, only the diffraction lines associated to the $O3_2$ structure are found in the associated SXRD patterns, denoting

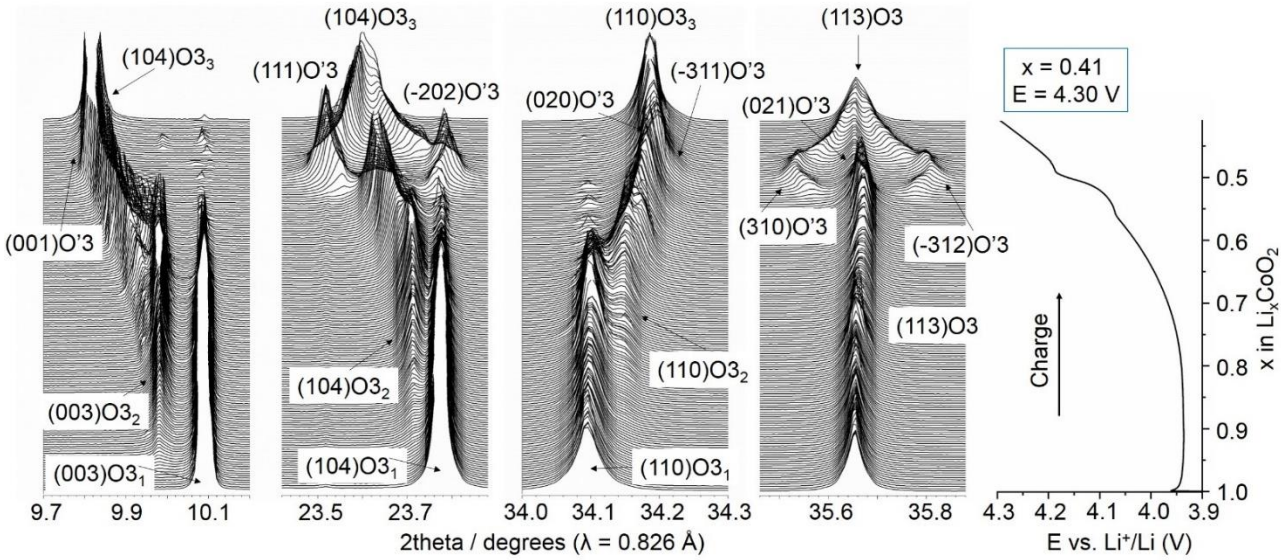

Figure B13. *Zooms on the cumulated SXRD patterns recorded in situ operando during the charge of st-LCO in the $1.0 \geq x \geq 0.41$ range (or 3.90 – 4.30 V vs. Li^+/Li voltage range) at C/20. The corresponding voltage profile of the cell is provided on the right of the figure.*

a monotonous solid solution behavior. 2Θ shifts observed for these lines are mainly due to the increase of c_{hex} parameter with the increasing electrostatic repulsion between the CoO_2 layers due to various Li contents. As a guideline, Le Bail refinement was performed on the SXRD pattern

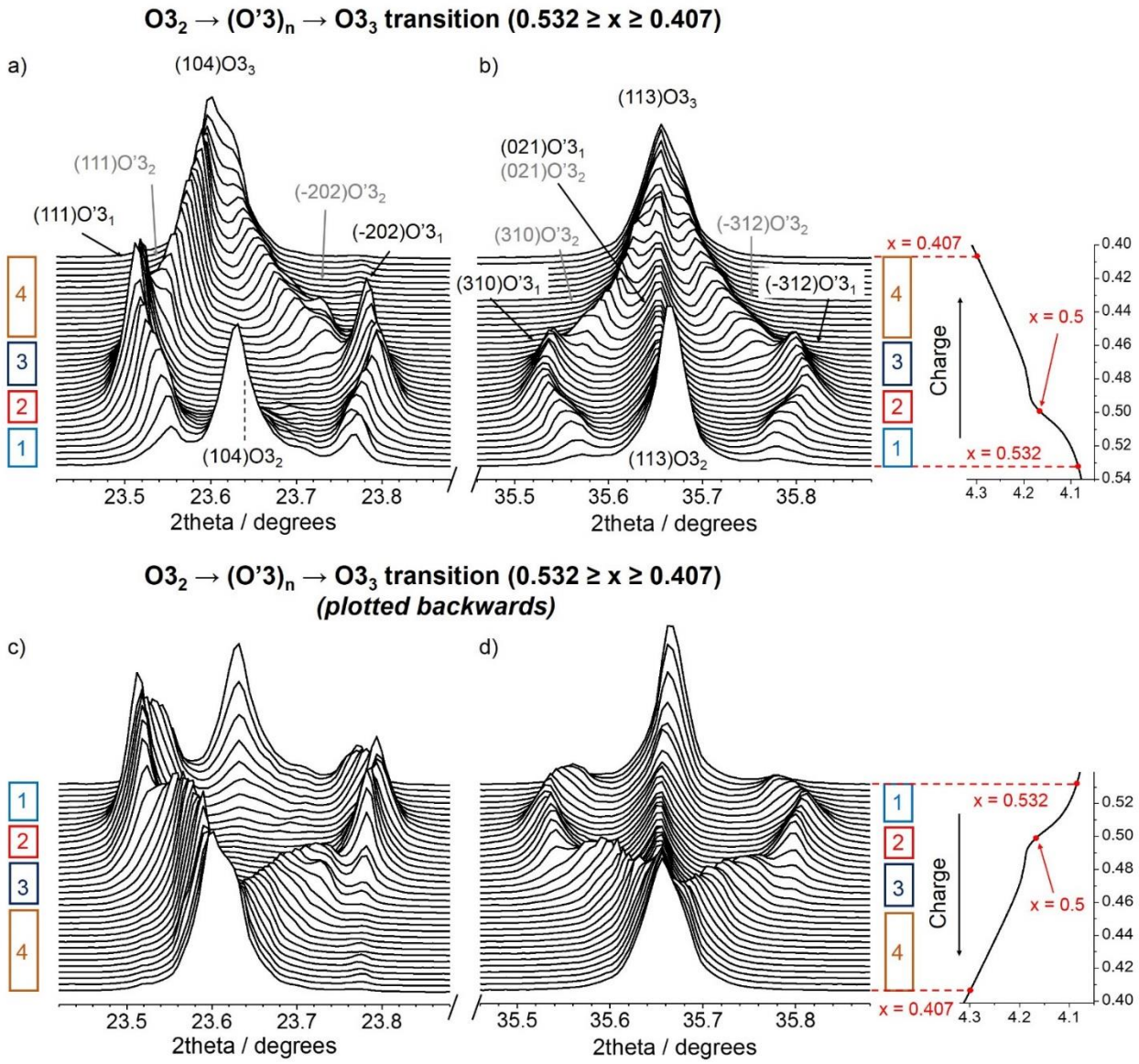

Figure B14*. Changes detected on the* ***a)*** *(104)O3₂ and* ***b)*** *(113)O3₂ diffraction lines during the charge of st-LCO at C/20 in the 0.532 ≥ x ≥ 0.407 range, in which the O3 – O'3 transition is expected. The corresponding voltage profile of the cell is provided on the right of the figure. Rectangles with numbers delimit four domains, each domain being defined by both the nature and the number of phases identified in the SXRD patterns (see Figure B15). Alternative plots of the same data are provided in* ***c)*** *and* ***d).***

corresponding to the overall ~ $Li_{0.54}CoO_2$ composition, which led to final maximum cell parameters of a_{hex} = 2.8074(1) Å and c_{hex} = 14.392(1) Å for the $O3_2$ phase.

When reaching an overall approximative ~ $Li_{0.53}CoO_2$ composition, new diffraction lines appear in the corresponding patterns. This may be more easily seen in the [23.4 – 23.9] and [23.4 – 23.9] 2Θ ranges in **Figure B13**, where the (104)$O3_2$ and (113)$O3_2$ peaks split into either two or three new contributions ((111)O'3; (-202)O'3, and (310)O'3; (021)O'3; (-312)O'3, respectively), better seen in **Figure B14.a** and **B14.b,** or in their alternative backwards plots in **Figure B14.c** and **B14.d**. This denotes the initiation of Li/vacancy ordering in the interlayer space of the $O3_2$ structure, thereof leading to the progressive formation of the O'3-$Li_{0.5}CoO_2$ phase. To our knowledge, the exact mechanism of the O'3 formation has never been reported so far.

As specified by the colored squares on the side of the cumulated SXRD patterns in **Figure B14**, four different domains within the [0.407; 0.532] x range were defined thanks to Le Bail refinements depending on i) the number of phases distinguished in the corresponding patterns and ii) their structures. Le Bail refinements for some of the *operando* patterns at selected voltages are plotted in **Figure B15**.

In **Domain n°1** ($0.532 \leq x < 0.506$, $4.08 \leq V < 4.13$), diffraction lines arising from both the $O3_2$ structure (a_{hex} = 2.8074(1) Å and c_{hex} = 14.392(1) Å) and a monoclinic phase denoted "$O'3_1$" ($a_m \approx 4.862$ Å; $b_m \approx 2.808$ Å; $c_m \approx 5.062$ Å and $\beta_m \approx 107.9$ °, values slightly changing in the domain due to the *in operando* conditions) were simultaneously observed in **Figure B14** and **Figure B15**. The co-existence of two structures seems in good agreement with the small pseudo-plateau always observed (but rarely commented upon) in this composition range in the electrochemical curve of st-LCO. **Domain n°2** ($0.506 \leq x < 0.488$, $4.13 \leq V < 4.19$) is single-phased, with the sole existence of the $O'3_1$ phase detected (a_m = 4.8613(1) Å; b_m = 2.8084(1) Å;

c_m = 5.055(1) Å and β_m = 107.76(1) °). These values are in good agreement with values previously reported by Shao-Horn et. al[41] (a_m = 4.872 Å; b_m = 2.808 Å; c_m = 5.053 Å and β_m = 107.89 °). Note that Le Bail refinement was performed using the *C2/m* space group and not the *P2/m* one – which was supposedly more adapted to describe the structure of O'3-$Li_{0.5}CoO_2$ according to the same authors – as no intensity was observed for the additional peaks expected for a lesser symmetry. The existence of the next domain (**Domain n°3**, $0.488 \leq x < 0.465$ and $4.19 \leq V < 4.21$) came as a surprise since only one monoclinic O'3 phase has always been either reported[27,42] or predicted[29] around the $Li_{0.5}CoO_2$ composition. Indeed, corresponding SXRD patterns reveal the co-existence of two monoclinic structures in such x range: one corresponding to the former O'3_1 structure and a new O'3_2 phase (a_m = 4.862(1) Å; b_m = 2.808(1) Å; $5.062 \leq c_m \leq 5.076$ Å and $108.06 \leq \beta_m \leq 108.62$ °). This also finds a proper agreement with the small pseudo-plateau seen in the electrochemical curve of st-LCO in this x range, although a biphasic mixture of O'3_1 and a hexagonal O3 phase could have been more logically expected. Both O'3_1 and O'3_2 structures exhibit a_m/b_m ratios close to $\sqrt{3}$ at all time of the charge, in agreement with the origin of the monoclinic distorsion (Li/vacancy ordering, differing from the monoclinic distorsion due to a Jahn-Teller distorsion of MO_6 octahedra (M = transition metal) in the O3-$NaNiO_2$ and O3-$NaMnO_2$ systems[43–45]). Eventually, only the latter is exclusively detected in **Domain n°4** ($0.465 \leq x < 0.399$ and $4.21 \leq V < 4.31$). For the final ~ $Li_{0.40}CoO_2$ overall composition, the hexagonal symmetry is recovered by the layered phase (denoted "O3_3") as the SXRD pattern is indexed in the *R-3m* space group with a_{hex} = 2.808 Å and c_{hex} = 14.433 Å.

To better understand the various stages witnessed during the formation of both monoclinic phases, we converted the a_{hex} and c_{hex} cell parameters of both initial O3_2 and final O3_3 structures into their equivalent a_m, b_m, c_m, and β_m ones if they were indexed in the *C2/m* space group (as

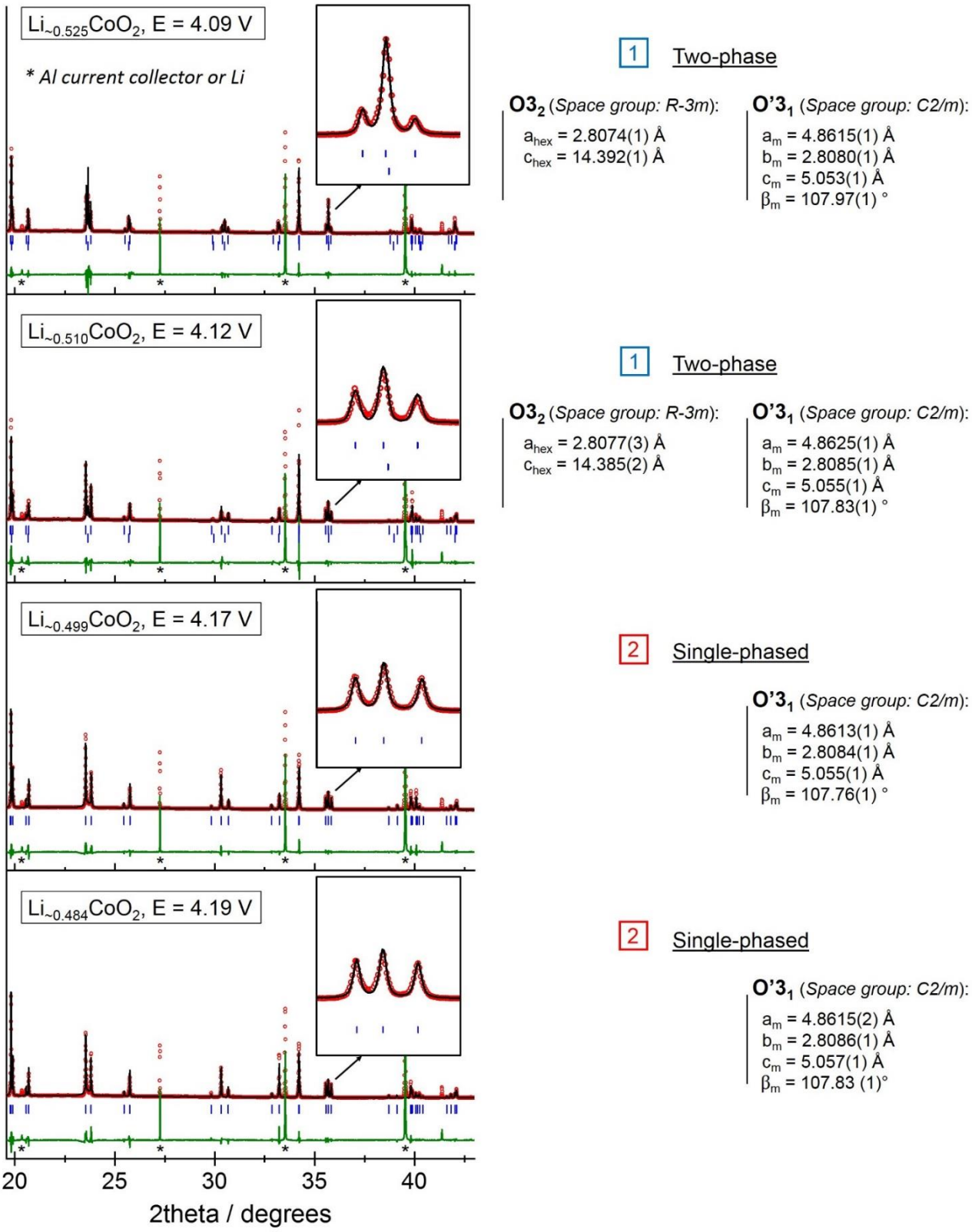

Figure B15*. Le Bail refinement performed on selected SXRD patterns recorded operando during the charge of st-LCO at C/20 in the 0.532 ≥ x ≥ 0.407 range.*

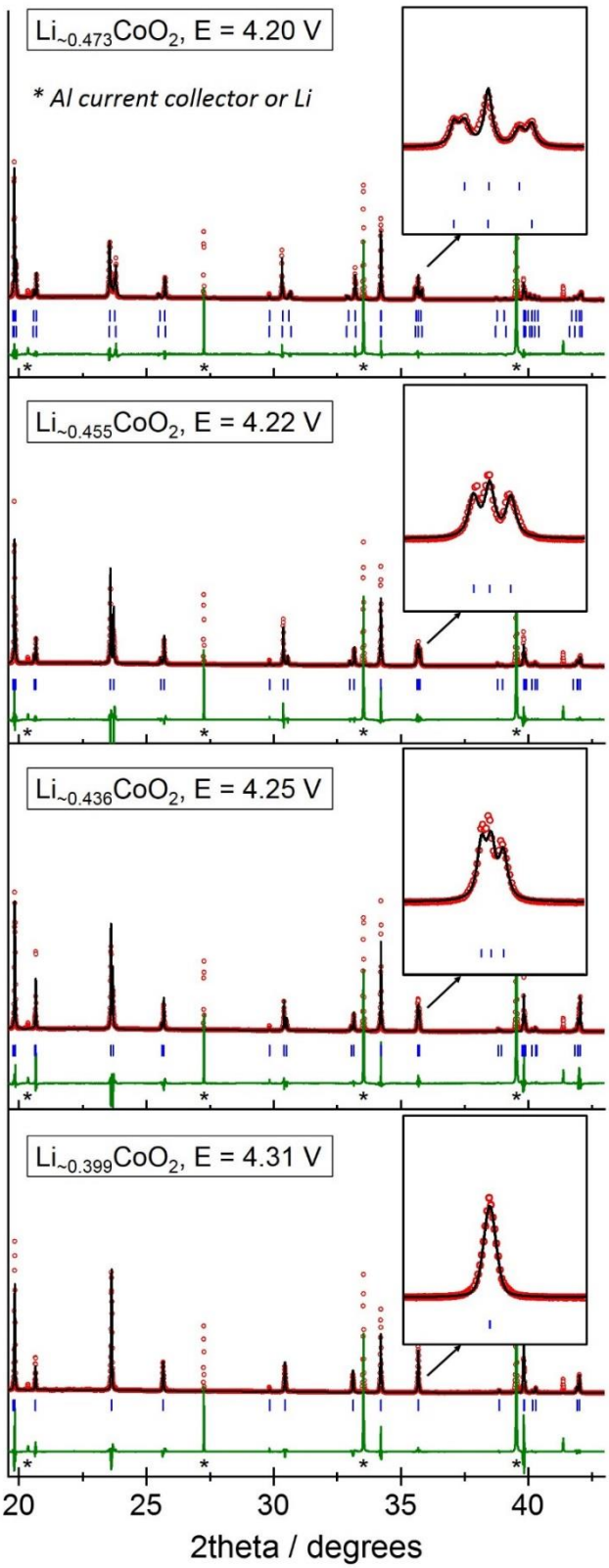

3 Two-phase

O'3$_1$ (*Space group: C2/m*):
a_m = 4.8616(1) Å
b_m = 2.8083(1) Å
c_m = 5.056(1) Å
β_m = 107.83(1) °

O'3$_2$ (*Space group: C2/m*):
a_m = 4.8621(2) Å
b_m = 2.8081(1) Å
c_m = 5.062(1) Å
β_m = 108.06(1) °

4 Single-phased

O'3$_2$ (*Space group: C2/m*):
a_m = 4.8625(2) Å
b_m = 2.8082(1) Å
c_m = 5.067(1) Å
β_m = 108.24(1) °

4 Single-phased

O'3$_2$ (*Space group: C2/m*):
a_m = 4.8622(2) Å
b_m = 2.8077(1) Å
c_m = 5.071(1) Å
β_m = 108.40(1)°

Single-phased

O3$_3$ (*Space group: R-3m*):
a_{hex} = 2.808(1) Å
c_{hex} = 14.432(1) Å

schematically depicted in **Figure B16**). The results are presented in **Table B.T5**. As quite different β_m and c_m values are reported for the $O3_2$ and the first-appearing $O'3_1$ (108.68 ° vs. 107.97 °; 5.062 Å vs. 5.053 Å respectively), it seems clear that the first stage of the "O3 – O'3" transition involves the creation of fully "Li ordered" coherent domains ($O'3_1$) found co-existing with "Li-disordered" ones (from the former $O3_2$). As these patterns were collected *operando*, this means that the Li/vacancy ordering is locally driven instead of being simultaneously and globally initiated everywhere within the particles of active material. It is interesting to note that the $O'3_1$ structure found in equilibrium with the $O3_2$ phase in Domain n°1 showed slightly changing β_m values depending on the x overall content anyway. Indeed, while β_m = 107.97° for the overall $Li_{0.525}CoO_2$ composition (**Figure B15**), a decreased value β_m = 107.83° is reported for ~ $Li_{0.510}CoO_2$, closer to

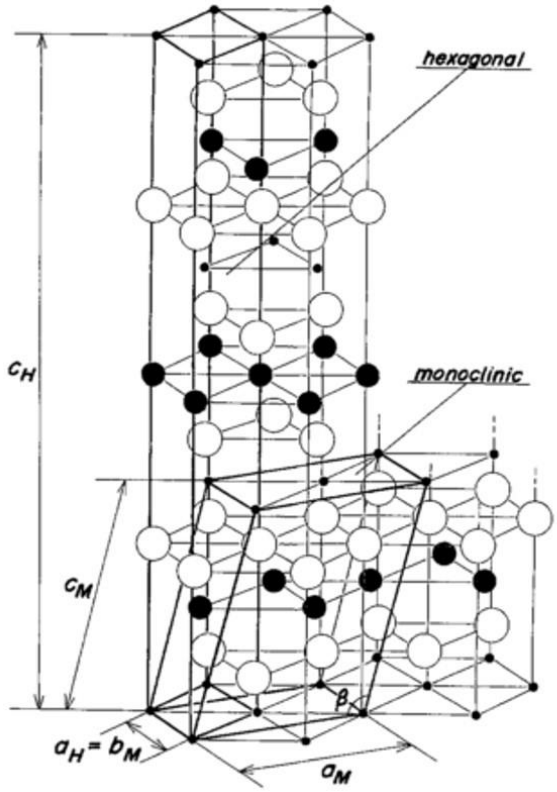

$$a_m = \sqrt{3}\, a_{hex}$$

$$b_m = a_{hex}$$

$$c_m = \frac{c_{hex}}{3\sin(\beta_m)}$$

$$\beta_m = 180 - \arctan\left(\frac{c_{hex}}{\sqrt{3}.\, a_{hex}}\right)$$

***Figure B16**. Schematic representation of the structural relationship between the hexagonal and monoclinic settings in describing $LiMO_2$ (from Ohzuku and Ueda[27]). All formulas used to convert the cell parameters from one setting to another in Table B.T5 are given on the right of the figure.*

the actual β_m reported for O'3-$Li_{0.5}CoO_2$ in both the literature and from our measurements ($\beta_m \approx 107.8°$). Although the first appearing O'3_1 phase most likely is a Li-ordered phase, some small Li-rearrangements could be still occurring to accommodate electrostatic constraints. Such variations are causing the clear shifts of (111)O'3_1 and (-202)O'3_1 positions in **Figure B14.a**, and those of (310)O'3_1, (021)O'3_1 and (-312)O'3_1 in **Figure B14.b**.

Phase	**Cell parameters Hexagonal system (*R-3m* space group)**	**Cell parameters Monoclinic system (*C/2m* space group)**
$O3_2$ (before Li/vacancy ordering)	a_{hex} = 2.808 Å c_{hex} = 14.386 Å	a_m = 4.864 Å b_m = 2.808 Å c_m = 5.062 Å β_m = 108.68 °
$O3_3$ (after Li/vacancy ordering)	a_{hex} = 2.808 Å c_{hex} = 14.433 Å	a_m = 4.864 Å b_m = 2.808 Å c_m = 5.077 Å β_m = 108.62 °

***Table B.T5**. Cell parameters for $O3_2$ and $O3_3$ phases after Le Bail refinement of their SXRD patterns using the R-3m space group, and their equivalent in the monoclinic system.*

A more pronounced evolution of c_m and β_m parameters is observed for the O'3_2 structure in Domain n°4. Indeed, both β_m and c_m conjointly increase with lower x content, for instance with β_m = 108.24° and c_m = 5.067 Å for x = 0.455; β_m = 108.40° and c_m = 5.071 Å for x = 0.436 and final equivalent β_m = 108.62° and c_m = 5.077 Å for x = 0.399 in the $O3_3$ structure when described using a monoclinic unit cell (**Table B.T5**). Such variations are again causing the clear shifts of (111)O'3_2 and (-202)O'3_2 positions in **Figure B14.a**, and those of (310)O'3_2, (021)O'3_2 and (-312)O'3_2 in **Figure B14.b**. The sole existence of the O'3_2 structure progressively converting into the $O3_3$ phase in Domain n°4 suggests that some Li order could still be found within the interlayer space throughout its whole x range of existence. One should however keep in mind that all the SXRD patterns picturing the "O3 – O'3" transition were collected *operando*. At this point, the

existence of a second monoclinic O'32 phase, as well as biphasic domains could also be only observed under dynamical conditions.

Figure B17.a shows the GITT curve recorded for a st-LCO-based coin cell. Results for the open-circuit voltage (OCV) measurements have been gathered in **Figure B17.b**, in which a summary of the potential existing low voltage structures for Li_xCoO_2 are highlighted (according to the *in situ operando* SXRD experiment). The aim of this experiment was to check if voltage plateaus could be clearly seen on both sides of the voltage jump around x = 0.5. As revealed in **Figure B17.a**, two distinct plateaus are indeed observable in equilibrium conditions around ~ 4.06 V ($0.55 \leq x \leq 0.53$) and ~ 4.18 V ($0.47 \leq x \leq 0.49$). According to the previous findings, they could respectively correspond to the two-phase "$O3_2 + O3'_1$" and "$O'3_1 + O'3_2$" domains. However, additional ex situ SXRD patterns would be necessary to properly identify the co-existing structures at equilibrium, which may differ from the ones formed *operando*. In particular, the most thermodynamically stable structures around ~ 4.18 V may be the $O3'_1$ and $O3_3$ forms, with the $O'3_2$ structure only observed *in operando* due to the kinetics associated to the Li removal. *Ex situ* SXRD measurements may still be challenging due to the narrowness of the compositions domains for these plateaus. Similarly, complementary *in situ* and *ex situ* data during the discharge would be mandatory to conclude on the reversibility of these phase transitions.

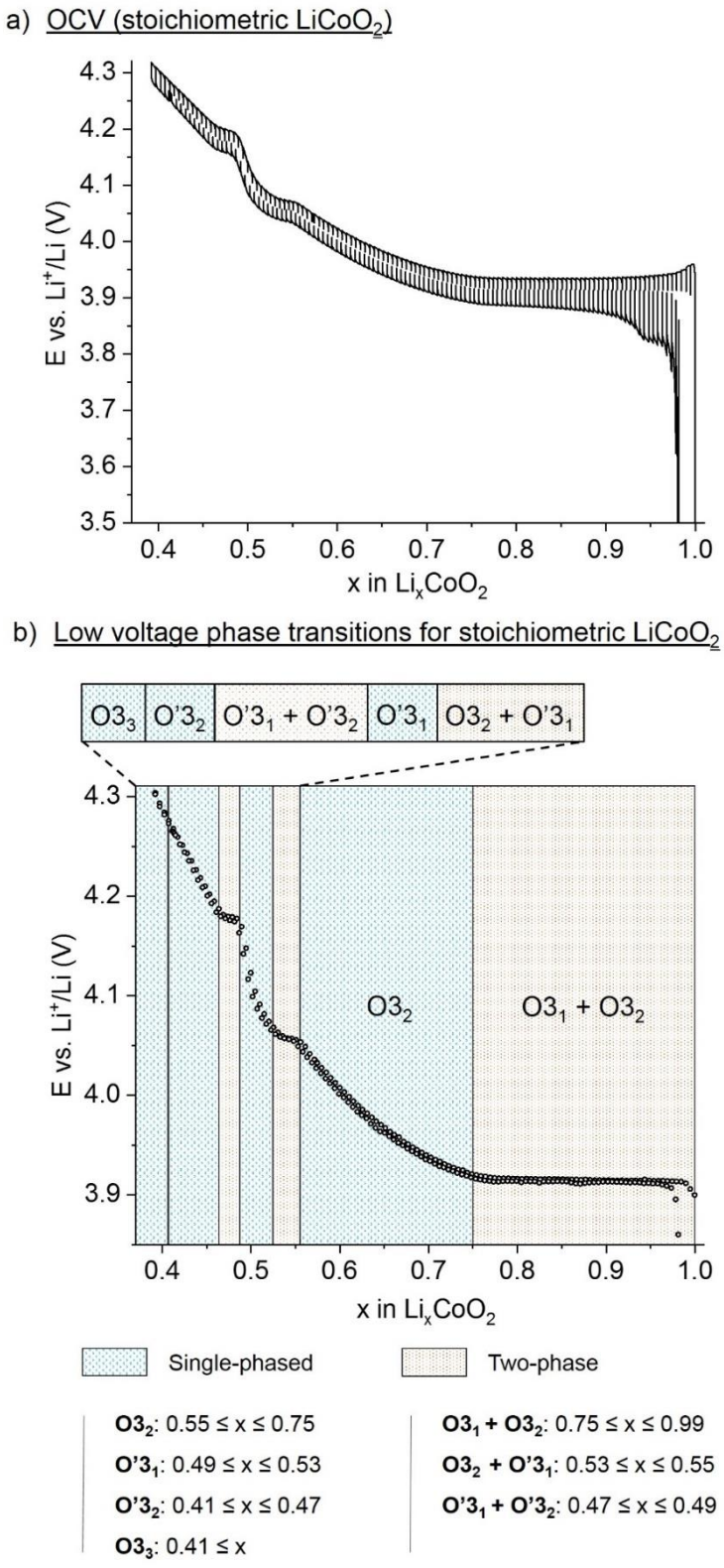

Figure B17. a) *Transient voltage profile of st-LCO vs. Li content obtained from GITT and* ***b)*** *reported equilibrium open-circuit voltage measurements. The various structures adopted by st-LCO during Li de-intercalation, previously identified from in situ SXRD, are also highlighted in* ***b).***

B.3.3 The O3 – H1-3 transition

Figure B18 shows zooms of interest on all cumulated SXRD patterns recorded for both st-LCO (**Figure B18.a**) and overl-LCO (**Figure B18.b**) in the [0.2; 0.4] x composition range (previously denoted as High voltage 1 window). From x = 0.4 to x = 0.237, the $O3_3$ structure is preserved for st-LCO (**Figure B18.a**). A solid solution behavior is still observed, with more pronounced shifts of peak position at lower 2Θ values observed for the $(003)O3_3$ (and $(006)O3_3$) and $(107)O3_3$ lines corresponding to the shrinkage of interlayer space with further Li removal.

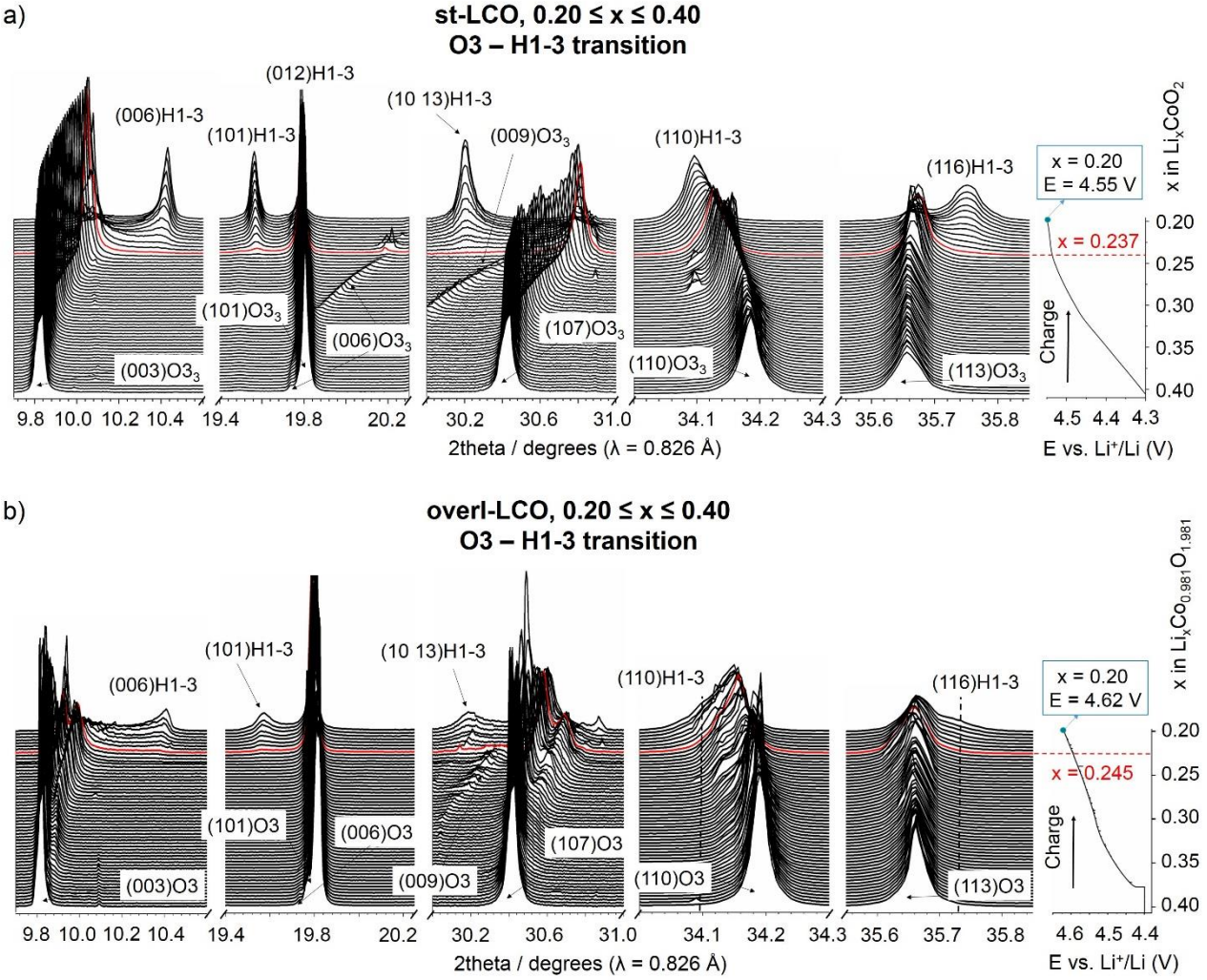

Figure B18*. Zooms on the cumulated SXRD patterns recorded in situ operando during the charge of st-LCO (**a**) and overl-LCO (**b**) in the 0.40 ≥ x ≥ 0.20 range (or 4.30 – 4.55 V vs. Li^+/Li voltage range) at C/20. The corresponding voltage profile of the cell is provided on the right of the figure.*

Similar observations can be done from **Figure B18.b** for overl-LCO, whose O3 structure is well preserved up to x = 0.245, although more than one line may be seen, which is attributed to inhomogeneity throughout the electrode.

Diffraction lines corresponding to the H1-3 structure start to respectively appear at x = 0.237 and x = 0.245 Li remaining contents in st-LCO and overl-LCO. Note that the former $O3_3$ and O3 structures are still simultaneously found within the electrodes of st-LCO and overl-LCO up to x limit of the plot here (x = 0.20). As a matter of fact, this is again evidence that 4% overlithiation does not help hindering the formation of the H1-3 structure during the cycling of LCO at high voltage, in good agreement with the preliminary study in Part B.2. However, as the formation of the H1-3 phase occur at E = 4.60 V for overl-LCO as compared to E = 4.52 V for st-LCO, the excess Li plays a favorable role in delaying it. As polarization issues inside the coin cells may lead to improper conclusions by being the cause of the voltage gap previously evidenced, additional *ex situ* samples were prepared from Li electrochemical de-intercalation of both powders of st-LCO and overl-LCO. The SXRD patterns recorded for Li_xCoO_2 samples prepared from st-LCO and charged up to either E = 4.45 V, E = 4.50 V or E = 4.53 V are shown in **Figure B19**. **Figure B20** shows the SXRD patterns of all $Li_xCo_{0.981}O_{1.981}$ samples prepared from overl-LCO at E = 4.53 V, E = 4.55 V, E = 4.57 V and 4.60 V. Note that no precise Li compositions are given for the Li_xCoO_2 and $Li_xCo_{0.981}O_{1.981}$ powders as electrolyte degradation occurring in this electrochemical window prevented to give reasonable estimations.

Figure B19 confirms that the O3 stacking is preserved up to 4.45 V for st-LCO, whose cell parameters are a_{hex} = 2.809(1) Å and c_{hex} = 14.393(1) Å. The typical diffraction lines for the H1-3 structure are clearly identified in the SXRD pattern of the sample prepared at E = 4.53 V. No diffraction peaks corresponding to remaining $O3_3$ phase are observed in this pattern, confirming

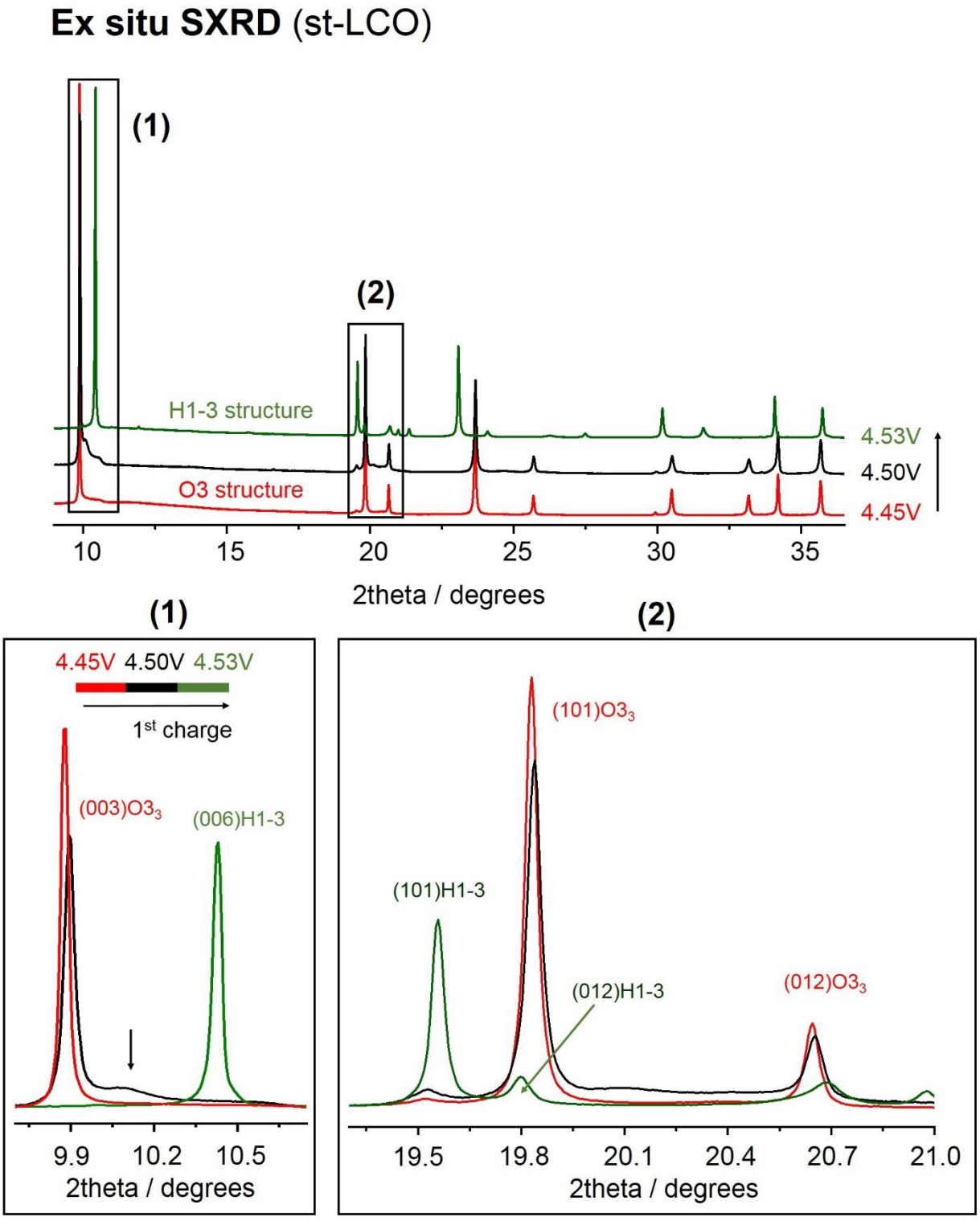

Figure B19. *Ex situ SXRD pattern recorded for various Li_xCoO_2 powders prepared from electrochemical Li de-intercalation of st-LCO charged up to either E = 4.45 V, E = 4.50 V or E = 4.53 V. Zooms focusing on the (00l), (101) and (012) diffraction lines are also given.*

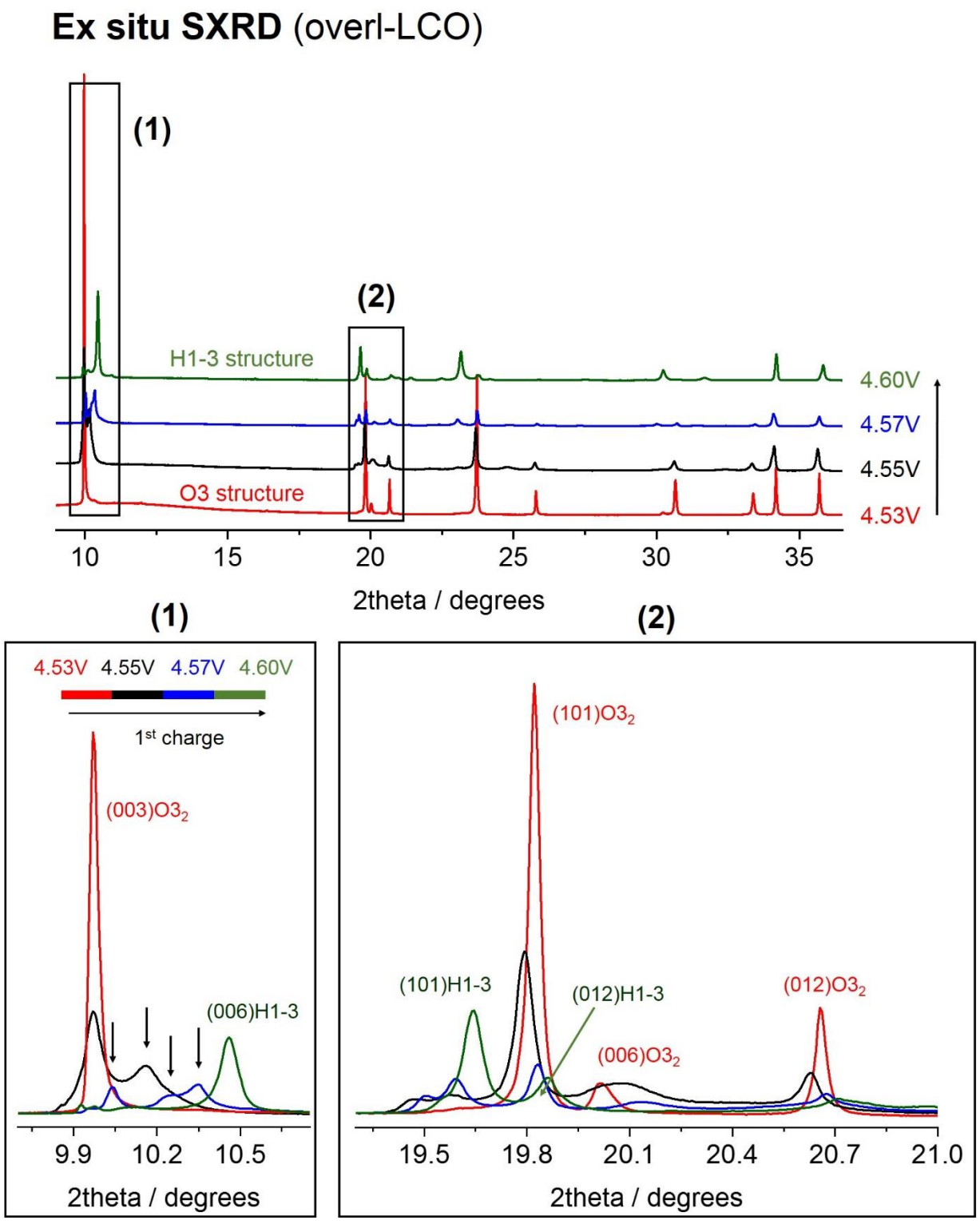

Figure B20*. Ex situ SXRD pattern recorded for various* $Li_xCo_{0.981}O_{1.981}$ *powders prepared from electrochemical Li de-intercalation of overl-LCO charged up to either E = 4.53 V, E = 4.55 V, E = 4.57V or E = 4.60 V. Zooms focusing on the (00l), (101) and (012) diffraction lines are also given.*

we successfully prepared a pure powder of the H1-3 phase. This will however be widely discussed In Part B.4 dedicated to the H1-3 phase itself. While all diffraction lines corresponding to the limit $O3_3$ structure are found in the SXRD pattern of Li_xCoO_2 (E = 4.50 V), additional features may be observed, as for instance evidenced by the arrow in the **(1)** zoom on the (00l) diffraction lines in **Figure B19**. As this feature is found between the (003)$O3_3$ and (006)H1-3 lines, possible intergrowth phases are formed over the preparation of this powder. Besides, continuous signal may be distinguished between the (101)$O3_3$ and (012)$O3_3$ diffraction lines in the SXRD pattern for the same sample in **Figure B19**, zoom **(2)**. This shows that there is a continuous formation of H1-3 domains inside O3 due to local slab gliding (O3 → O1) before the formation of the single phase H1-3.

Figure B20 reveals that the O3 stacking is preserved up to 4.53 V for overl-LCO (a_{hex} = 2.811(1) Å and c_{hex} = 14.258(1) Å), while typical diffraction lines revealing the formation of the H1-3 phase are found in the SXRD pattern of the powder charged up to E = 4.60 V. These ex situ SXRD patterns confirm that the overlithiation of initial LCO helps delaying the formation of the H1-3 structure, thereof occurring at higher voltage, but also seems to stabilize an O3-stacking for shorter interslab spacing. New diffraction lines are found between the (003)O3 and (006)H1-3 diffraction peaks in the SXRD patterns of overl-LCO charged up to E = 4.55 V and E = 4.57 V, as highlighted by the various arrows in **Figure B20** (insert (**1**)). Similarly to st-LCO, intergrowth structures may be formed within the $Li_xCo_{0.981}O_{1.981}$ powders. As more additional lines are found in this 2Θ domain for overl-LCO as compared to st-LCO, the formation of a wider variety of intermediate structures could be favored for the former. Therefore, the formation of the H1-3 structure could thereof be more "continuous" for overl-LCO as opposed to st-LCO. Insert (**2**) in **Figure B20** also reveals the existence of broad lines and non negligible signal between the (101)O3

and (012)O3 lines exhibited by overl-LCO charged up to E = 4.55 V and E = 4.57 V, again suggesting that their corresponding O3 structures may contain a high density of O1 stacking faults.

B.3.4 The H1-3 – O1 transition

Figure B21 shows zooms of interest on all cumulated SXRD patterns recorded for both st-LCO (**Figure B21.a**) and overl-LCO (**Figure B21.b**) in the [0.0; 0.2] x composition range (previously denoted as High voltage 2 window).

From x = 0.20 to x = 0.183, diffraction lines for both the $O3_3$ and the H1-3 structures are found in the SXRD patterns recorded for st-LCO in **Figure B21.a**, as expected with the existence of a small plateau in the corresponding electrochemical profile. From x = 0.183 to x = 0.123, only the diffraction peaks assigned to the H1-3 structure arise, thereof confirming that it exists for various Li compositions. This is in good agreement with previous assumptions from Van der Ven et al.[29] who predicted that the H1-3 phase should be predominantly found in the [0.12; 0.19] x range. More details on the H1-3 phase formed from st-LCO will be given in Part B.4. From x = 0.123 to x = 0.0, all visible diffraction lines undergo severe broadening, making it hard to discuss the exact nature of the phases in this composition range. We believe this could be due to the competition between the nucleation and growth of O1-type stacking faults within the H1-3 phase, eventually leading to an overall structural disorder. Broad features corresponding to an O1 stacking are eventually seen in the final SXRD patterns ($x \leq 0.04$) of the charged st-LCO based electrode (*P-3m1* space group, a = 2.822 Å, c = 4.241 Å), which could match well with the formation of the final end member CoO_2 reported by Amatucci et al.[20]. Note that the complete evolution of the d(00ℓ) and d(110) spacing for st-LCO is plotted in **Figure B22.a**. Besides, additional features (highlighted with the dotted purples lines in **Figure B21.a** found in the same patterns confirm previous findings from the preliminary study in Part B.2, i.e. that an additional (X) phase with d(00ℓ) ~ 4.325 Å is also formed at the end of the charge of st-LCO. The possibility of an intergrowth structure was raised. However, a more plausible hypothesis would be that the (X)

phase is an O1 structure whose interslab is partially occupied by Li in weak amounts, as few and comparable diffraction lines to O1-CoO_2 arise from (X).

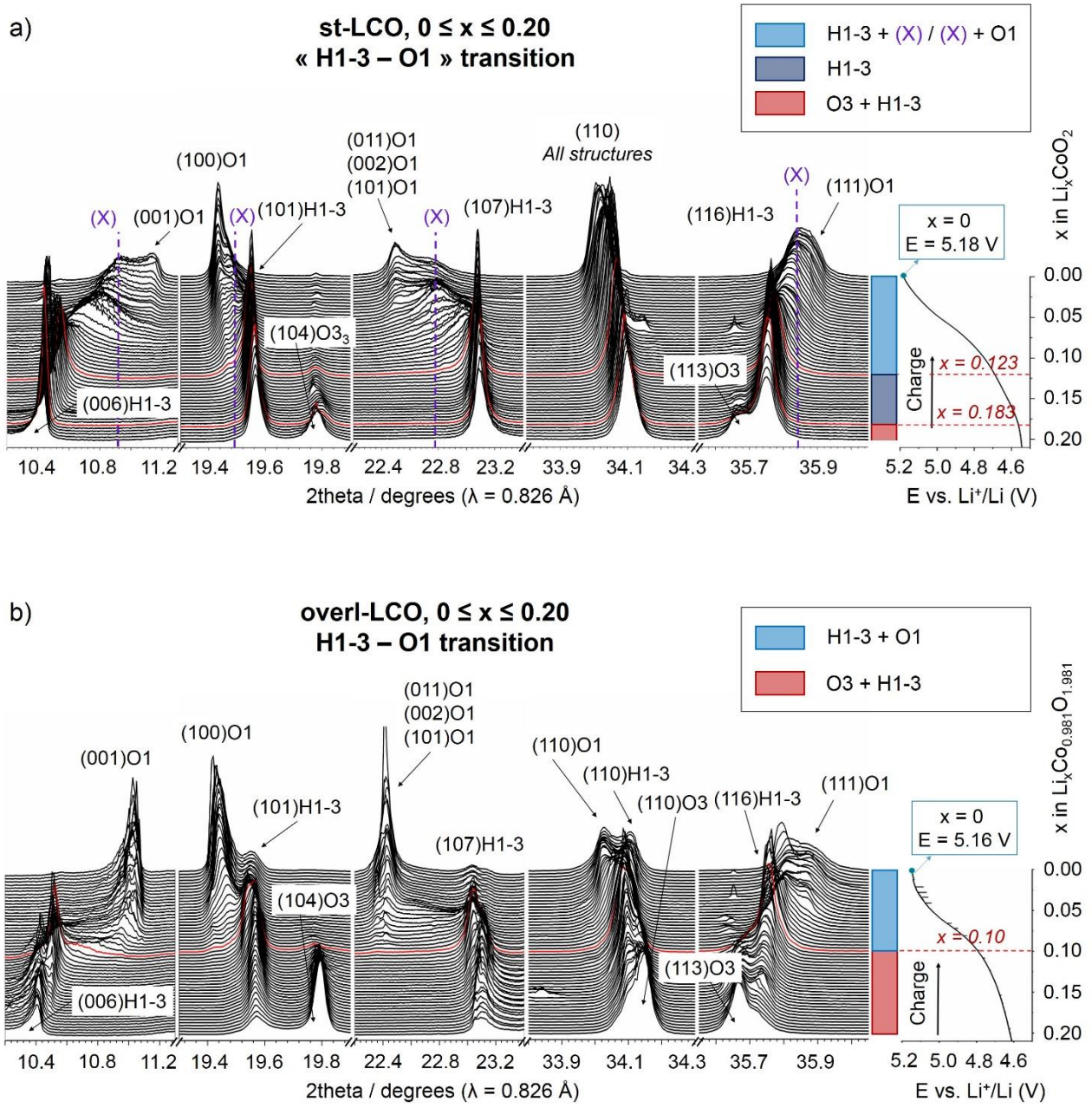

Figure B21*. Zooms on the cumulated SXRD patterns recorded in situ operando during the charge of st-LCO* ***(a)*** *and overl-LCO* ***(b)*** *in the 0.40 ≥ x ≥ 0.20 range (or 4.30 – 4.55 V vs. Li^+/Li voltage range) at C/20. The corresponding voltage profile of the cell is provided on the right of the figure.*

Less complex structural changes are observed in the SXRD patterns recorded for overl-LCO (**Figure B21.b**). Both the O3 and H1-3 structures co-exist from x = 0.20 to x = 0.10, while an O1 structure is gradually formed from x = 0.10 to x = 0.0 in addition to the H1-3 phase. The complete evolution evolution of the d(00ℓ) and d(110) spacing for overl-LCO is plotted in **Figure B22.b**. Significant signal intensity can be observed between the (006)H1-3 and (001)O1 lines, or even between the (107)H1-3 and (101)O1, denoting the nucleation/growth of O1-stacking faults within the H1-3 structure to eventually convert into the O1 structure. Cell parameters for the final O1-structure (*P-3m1* space group) are here a = 2.814 Å and c = 4.279 Å. Again, this is in good agreement with the preliminary study commented in Part B.2. The O1 structure formed from overl-LCO exhibits a higher interslab distance as opposed to the O1 phase obtained from st-LCO. However, at this point, the synchrotron investigation do not give further leads as to explain if such difference is due to some more remaining Li in the interslabs of O1 phase formed from overl-LCO or to the presence of vacancies in the $Co_{1-t}O_{2-t}$ slabs.

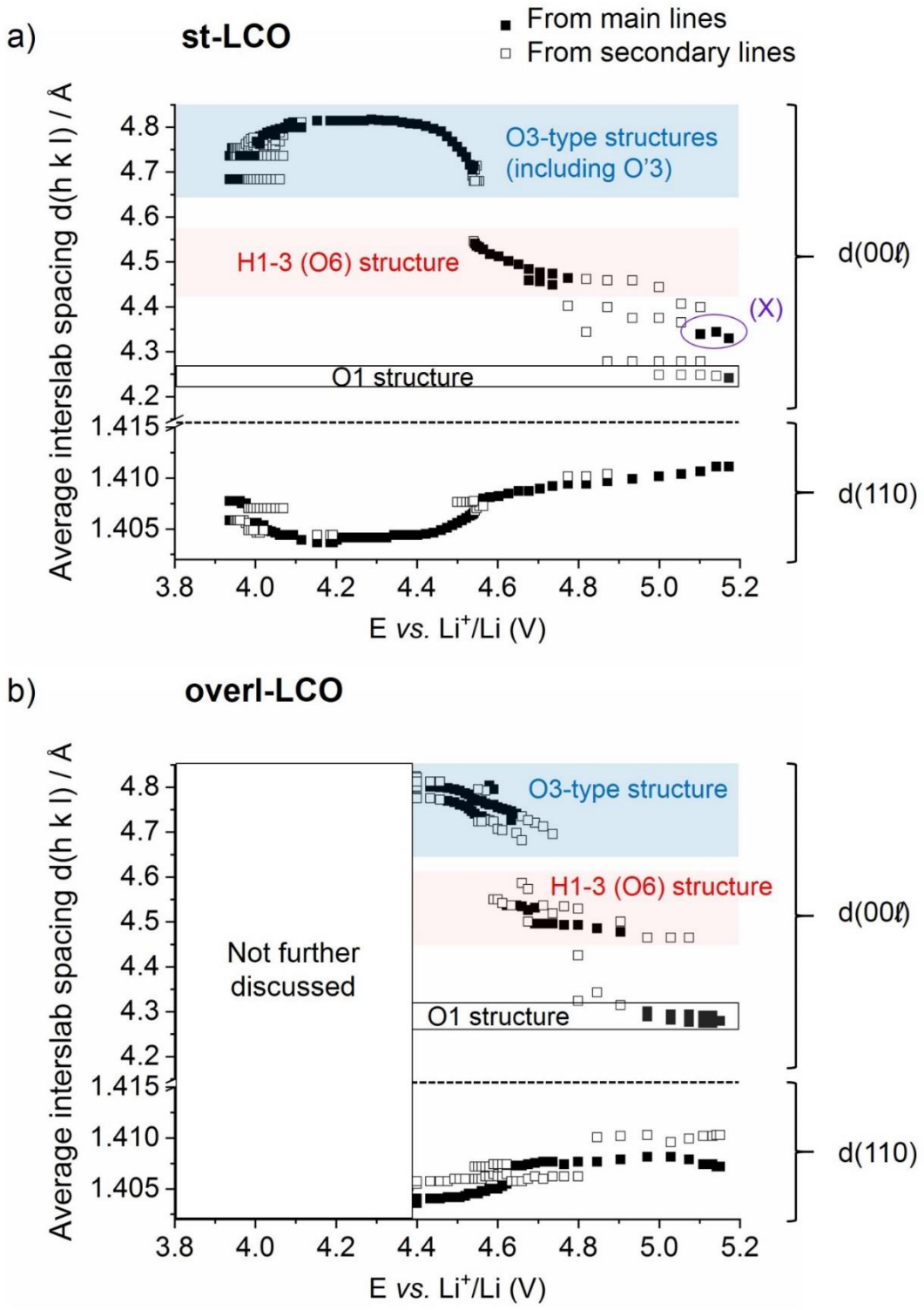

***Figure B22**. Plot of the average interlayer distance d(0 0 l) for each phase formed during the charge of st-LCO and overl-LCO as function of E vs. Li^+/Li. The values for d(0 0 l) are reported for every3 SXRD pattern shown in Figure B18 and Figure B21 (and Figure B13 for the evolution of cell parameters for st-LCO at low voltage).*

B.4. On the chemical and structural properties of H1-3-$Li_{\sim 0.167}CoO_2$

B.4.1 Structural properties

As stated before, a H1-3-Li_xCoO_2 sample was successfully prepared from electrochemical Li de-intercalation of st-LCO, charged up to E = 4.53 V (part B.3.2). As a matter of fact, several other H1-3 samples were secured from this route at slightly changing voltages (E = 4.54, 4.55, and 4.60 V). Their ex situ SXRD patterns are shown in **Figure B23.a**, with zooms provided in

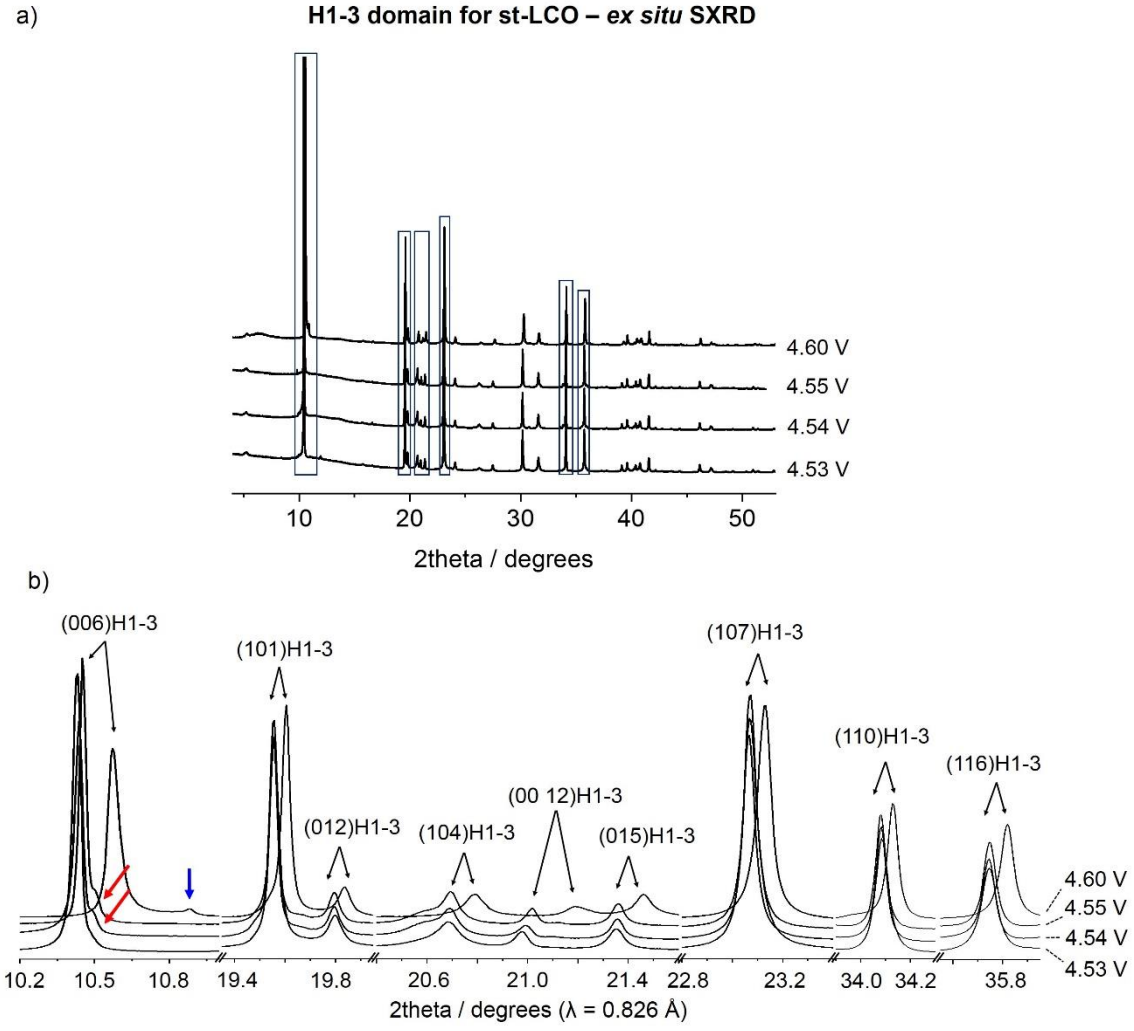

Figure B23. a) *Ex situ SXRD patterns recorded for various H1-3-Li_xCoO_2 powders prepared from electrochemical Li de-intercalation of st-LCO charged up to either E = 4.53 V, E = 4.54 V, E = 4.55 V or E = 4.60 V. Zooms on the most intense diffraction lines are given in* ***b)****.*

Figure B23.b. For comparison purposes, the in situ SXRD patterns recorded in the H1-3 domain during the charge of st-LCO are provided in **Figure B24**.

All peaks expected for this intergrowth of O3- and O1- structures are visible in **Figure B23.a**, with an additional small feature (pointed at with the blue arrow in **Figure B23.b**) around $2\Theta = 10.85$ ° in the pattern of the H1-3-Li_xCoO_2 prepared at E = 4.60 V. With an interslab distance of d = 4.352 Å , this could be a (00ℓ) line arising from the intermediate (X) phase evidenced during the in situ SXRD study. Therefore, it may be possible to partly freeze this structure from the electrochemical Li de-intercalation of st-LCO performed in our conditions. However, as no other additional diffraction lines are seen in this pattern, this statement remains under certain doubt. As this result came late in this project, no additional Li_xCoO_2 samples were prepared at a slightly higher voltage in an attempt to prepare a pure sample of (X) phase.

As expected from the shift of peak positions observed in the H1-3 domain during the *in situ* SXRD experiment, the H1-3-Li_xCoO_2 powders show different cell parameters due to the various voltages involved in their preparation – and thus to various Li contents (x). With an increasing

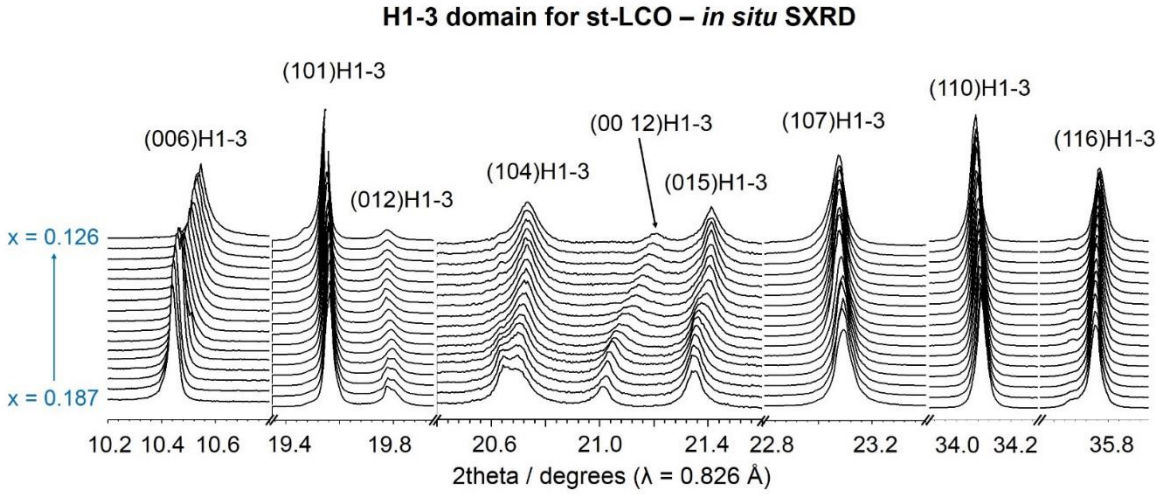

***Figure B24**. Zooms on the cumulated SXRD patterns recorded in situ operando during the charge of st-LCO in the 0.187 ≥ x ≥ 0.126 range (or 4.52 – 4.70 V vs. Li^+/Li voltage range) at C/20.*

voltage, the a_{hex} parameter varies between ~ 2.812 Å and ~ 2.820 Å while the c_{hex} parameter varies between ~ 27.12 Å and ~ 27.04 Å (assuming a *R-3m* space group indexation). Shoulders (evidenced by the red arrows in **Figure B23.b**) at the right of the (006) and (104) diffraction peaks can be seen in the SXRD patterns recorded for the two H1-3-Li_xCoO_2 samples prepared at E = 4.54 V and E = 4.55 V, in good agreement with the preliminary in situ study. Shoulders can also be distinguished on the (012) and (104) lines of the SXRD patterns recorded *operando* (**Figure B24**). While the possibility of not one but two H1-3 phases was first raised, the similarities between the patterns supposedly assigned to the two H1-3 phases suggest they share almost identical structures. At this point, a more reasonable hypothesis would be to assume that only one

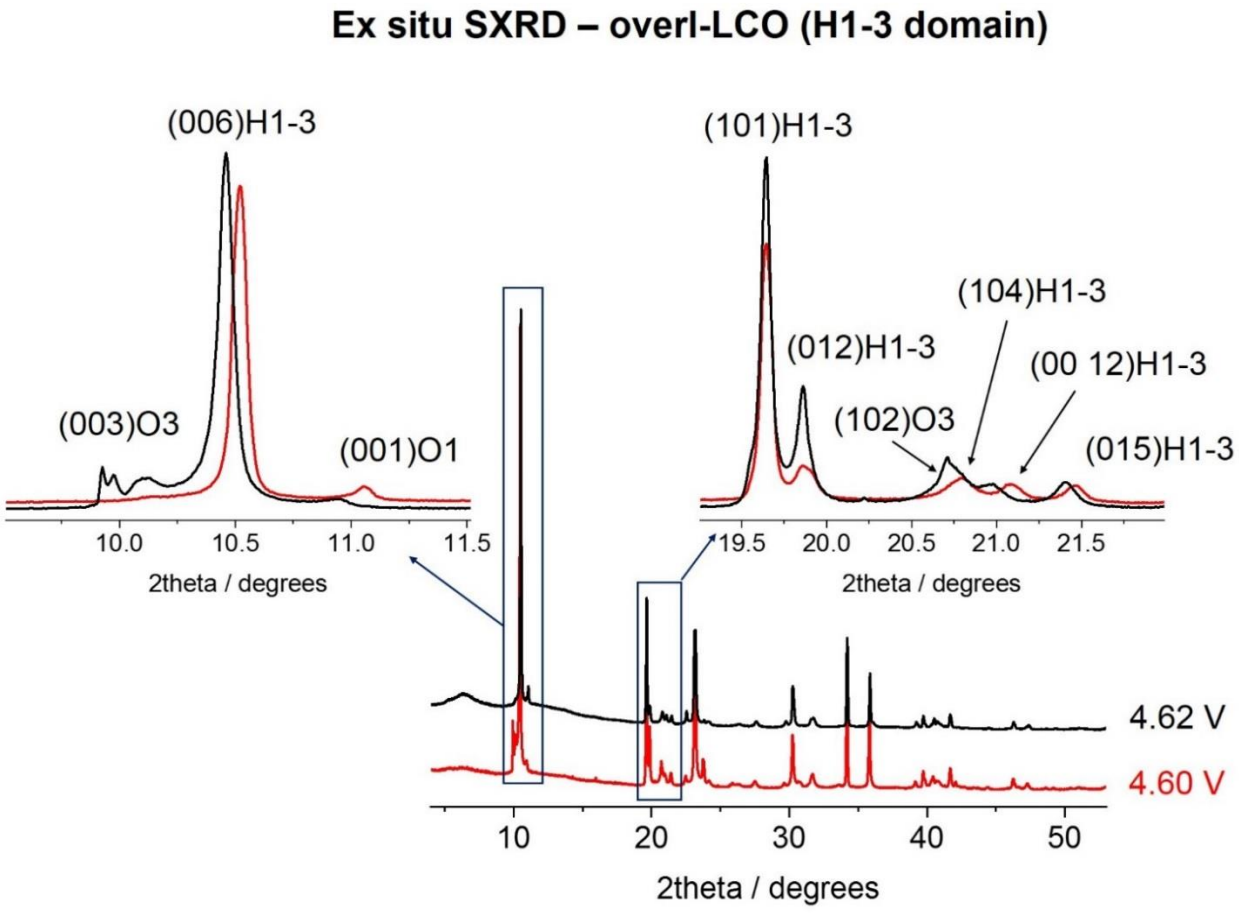

Figure B25*. Ex situ SXRD patterns recorded for $Li_xCo_{1.981}O_{1.981}$ powders prepared from electrochemical Li de-intercalation of overl-LCO charged up to either E = 4.60 V or E = 4.62 V.*

H1-3 phase exists whose structure may contain various amounts of O3 and/or O1-stacking faults. XRD patterns of H1-3 phases containing either type of stacking faults were already simulated using DIFFAX in a still ongoing work (not shown here). First results suggest that the shoulder observed at the left of the (104)H1-3 diffraction line is characteristic of existing O3-type stacking faults in the H1-3 structure. Note that the sample prepared at E = 4.60 V shows broader diffraction lines, which could reflect a higher density of stacking faults contained in this H1-3 phase as compared to all other samples investigated here.

The two attempts to prepare pure powders of H1-3 phase from overl-LCO charged up to E = 4.60 V and 4.62 V (**Figure B25**) were unsuccessful as diffraction lines corresponding to either the O3- or O1-structures were always visible in their SXRD patterns. This finds a good agreement with the in situ SXRD investigation.

In **Figure B26**, Le Bail refinement was performed on the H1-3-Li_xCoO_2 sample prepared at E = 4.53 V using two space groups: *C2/m* (monoclinic, **Figure B26.a**, **B26.b** and **B26.c**) and *R-3m* (hexagonal, **Figure B26.d**, **B26.e** and **B26.f**). The *C2/m* space group is used here just to show why in the early work in literature people used this space group, even though it does not allow to properly describe the original H1-3 stacking as predicted by Van der Ven et al.[28-30] and later confirmed by Chen et al.[32]. Roughly satisfying fits were obtained with both *C2/m* or *R-3m* space groups, as shown in **Figure B26.a** and **Figure B26.d**. However, the presence of extra lines at low angles ($2\theta \sim 5°$ and $2\theta \sim 12°$) and some peaks in the 39 – 42 ° 2θ region are not properly fitted using the *C2/m* space group (**Figure B26.c**). One should note that all diffraction lines at $2\Theta > 40$ ° (with $\lambda = 0.825$ Å) would appear at $2\Theta > 95.7$ ° using a Co anode ($\lambda_{K\alpha1} = 1.789$ Å, $\lambda_{K\alpha2} = 1.791$ Å) or at $2\Theta > 79.3$ ° using a Cu anode ($\lambda_{K\alpha1} = 1.5406$ Å, $\lambda_{K\alpha2} = 1.544$ Å). As data is rarely recorded

at

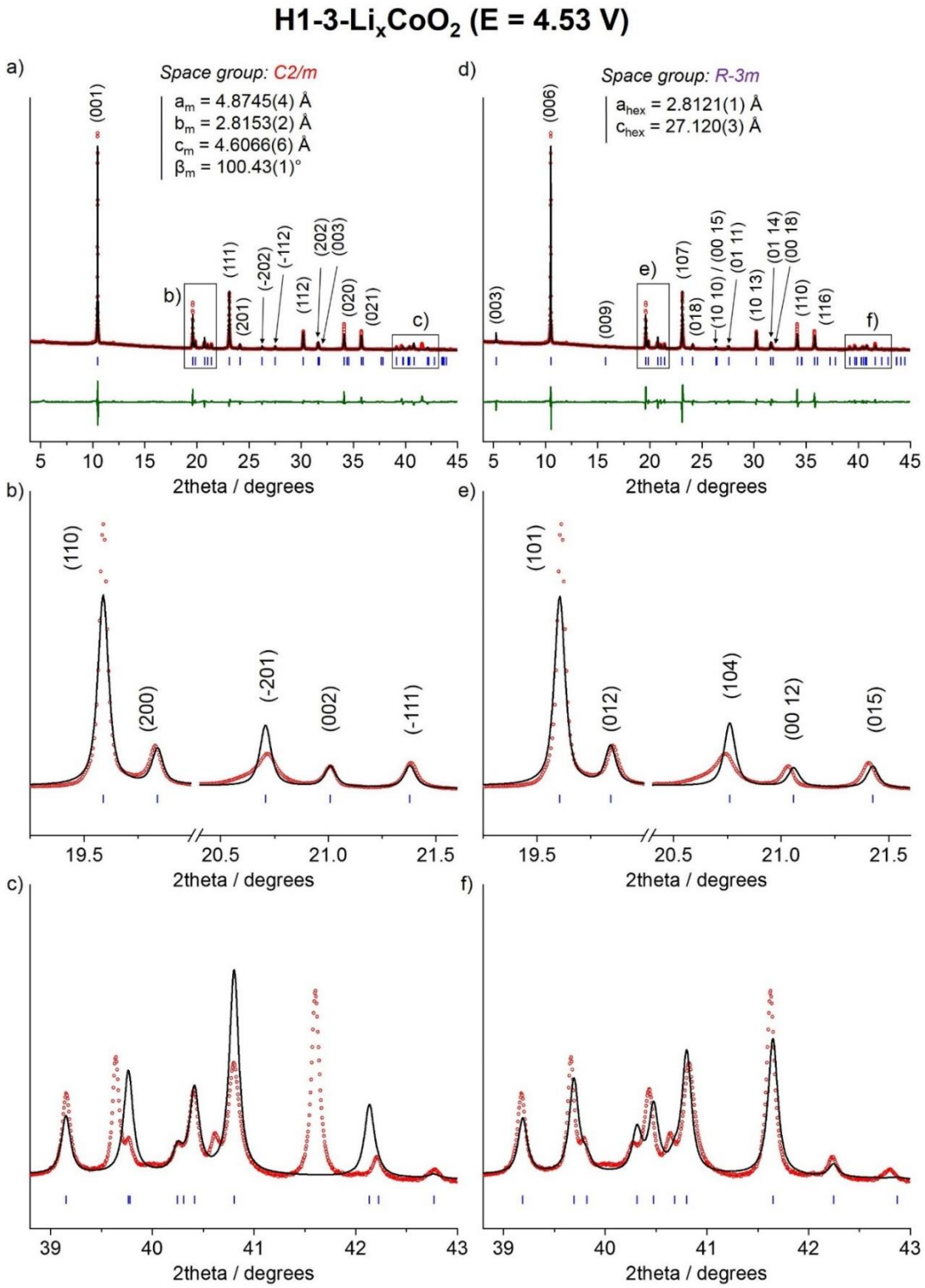

***Figure B26**. Le Bail refinements of SXRD patterns collected for a H1-3-Li$_x$CoO$_2$ sample prepared by Li electrochemical de-intercalation of st-LCO charged up to E = 4.53 V. In **a)**, the C2/m space group was used (with zooms provided in **b)** and **c)**), while refinement was done with the R-3m space group in **d)** (zooms in **e)** and **f)**).*

higher angle and with peaks strongly overlapping, this could explain why the *C2/m* space group was used in the early study in literature.

As shown in both **Figure B26.d** and **B26.e**, all peaks are fitted using the *R-3m* space group to fit the SXRD pattern of the H1-3 phase. Cell parameters are a_{hex} = 2.8121(1) Å and a_{hex} = 27.1210(3) Å. However, deviations of peak positions may be identified in the zoom provided in **Figure B26.e**. The impossibility to accurately fit the peak positions only appeared during the Le Bail refinement of all H1-3-Li_xCoO_2 powders as opposed to other materials (including st-LCO and overl-LCO, whose patterns were recorded at the same time), which raises the question of a possible effect of stacking faults creating local constraints. The hypothesis of an angular dependence of the zero setpoint due to the non negligible X-ray absorption of the Co contained in the samples at λ = 0.825 Å was also excluded for the same reasons. At this point, it still seems reasonable to affirm that refinement of XRD pattern of the H1-3 structure should be performed using the *R-3m* space group. Unfortunately, attempts to record complementary electron diffraction patterns to both confirm the indexation according to a hexagonal unit cell (R-3m space group) and the existence were fruitless. The additional use of softwares such as DIFFAX or FAULTS will still be required.

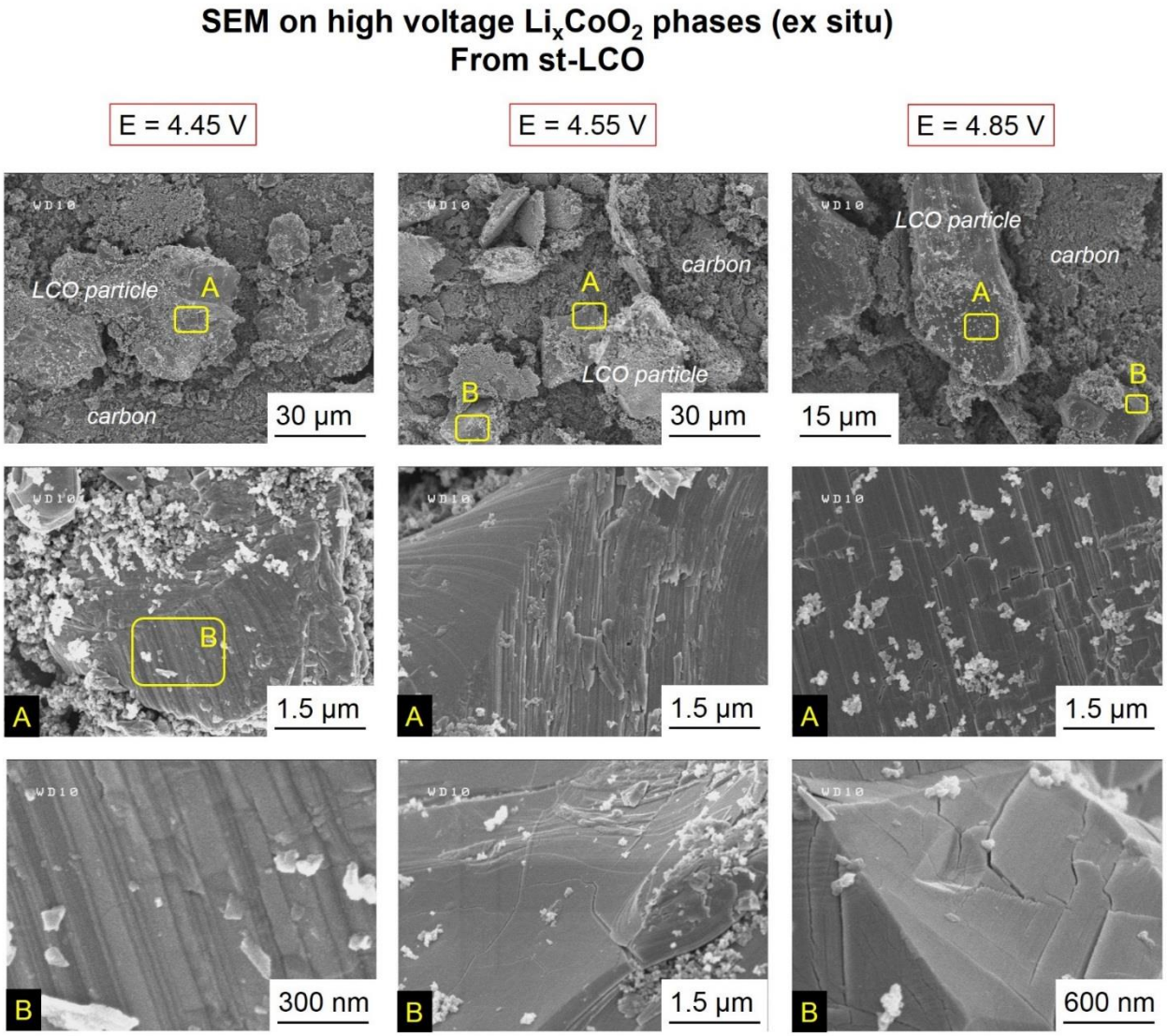

Figure B27*. Ex situ SXRD pattern recorded for various Li_xCoO_2 powders prepared from electrochemical Li de-intercalation of st-LCO charged up to either E = 4.45 V (O3-stacking), E = 4.55 V (H1-3 stacking) or E = 4.85 V (unknown stacking).*

Figure B27 shows the scanning electron micrographs of 3 Li_xCoO_2 powders prepared from Li electrochemical de-intercalation of st-LCO, respectively charged up to E = 4.45 V, E = 4.55 V and E = 4.85 V and recovered after an ~ 30-hour-long floating. Cracks are visible all over the particles of st-LCO for E = 4.55 V and E = 4.85 V but absent for E = 4.45 V. Besides, more severe cracking seems achieved at E = 4.85 V as compared to E = 4.55 V. The formation of the H1-3

structure and possibly of stacking faults most likely leads to particle damaging here, similarly to findings from Yano et al.[18]. However, such effect seems impressive considering the total timeline (1st charge, ~ 30 hour-floating) of our experiment as compared to theirs (20 full cycles, no mention of a floating).

B.4.4 Stability of the H1-3 phase

Chen et al.[32] previously reported a change of cell parameters for their H1-3 sample that they ascribed to its possible reactivity with air due to the lack of tightness of their argon-filled XRD cell (from c_{hex} = 27.07 Å for the first acquisitions to c_{hex} = 27.035 Å after one hour). As we experienced similar issues a cell during an XRD acquisition of one our H1-3 powders (E = 4.54 V), XRD patterns were recorded for this sample (constantly kept on the sample holder) at various aging times (from day 0 to day 43) and are plotted in **Figure B28**. All patterns were recorded using a Co source. A zoom in the [20.5 – 23.5 °] and [77 – 85 °] 2Θ ranges as they allow to directly follow any shifts of the (006), (110) and (116) initial diffraction lines arising from the H1-3 structure. After 43 days under air, the layered structure of the phase is preserved, as all lines are still visible. The (110) peak position remain unchanged, also it appears slightly broader. After 2 days under air, two sets of d(00ℓ) interslab distances are simultaneously found within the layered phase, as two succinct diffraction peaks are seen in the [20.5 – 23.5 °] 2Θ range. Eventually, the average interslab spacing of the layered phase is d(00ℓ) = 4.673 Å past 9 days, which is surprisingly analogous to the initial d(003) in st-LCO (d(003) = 4.682 Å). We observe an increase of d(00ℓ) spacing over time and not a decrease such as in the article published by Chen et al.[32], although our timeline is significantly larger than theirs. No further structural evolution is detected passed this aging time.

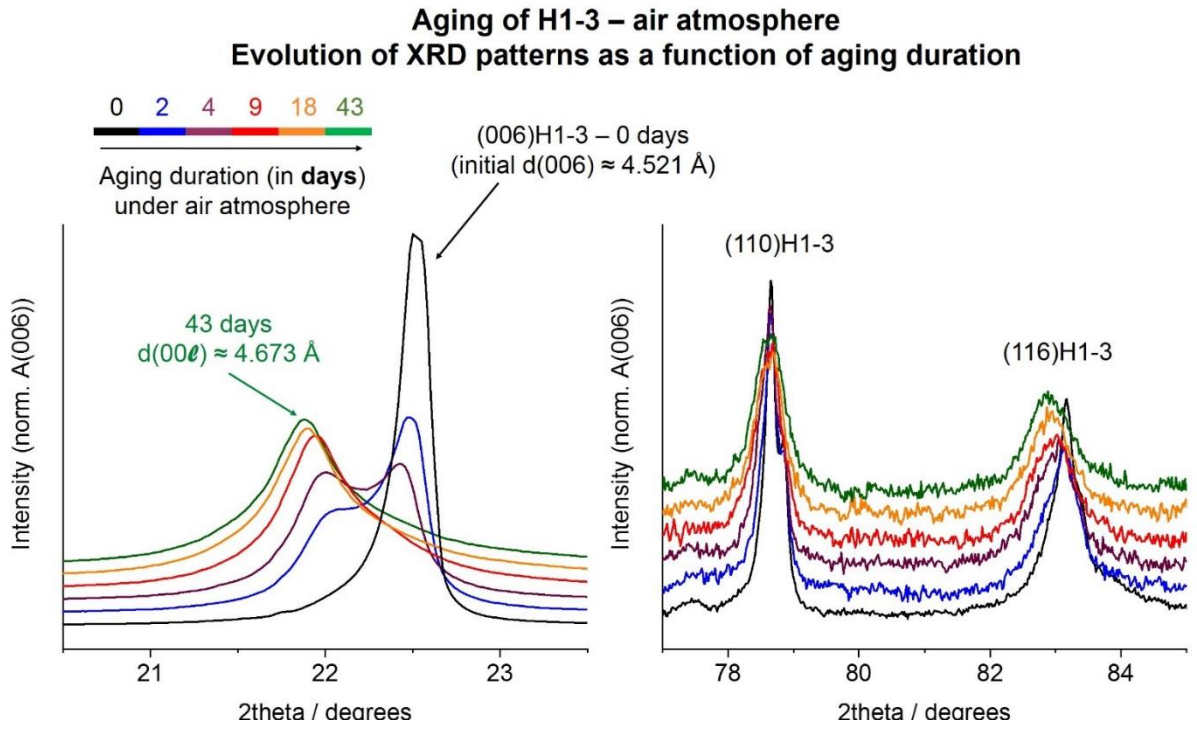

Figure B28. *Ex situ XRD patterns recorded at various aging time for the same H1-3-Li_xCoO_2 powder left under air for 43 days ($\lambda_{CoK\alpha1}$ = 1.789 Å, $\lambda_{CoK\alpha2}$ = 1.793 Å). The powder was initially prepared from electrochemical Li de-intercalation of st-LCO charged up to E = 4.53 V.*

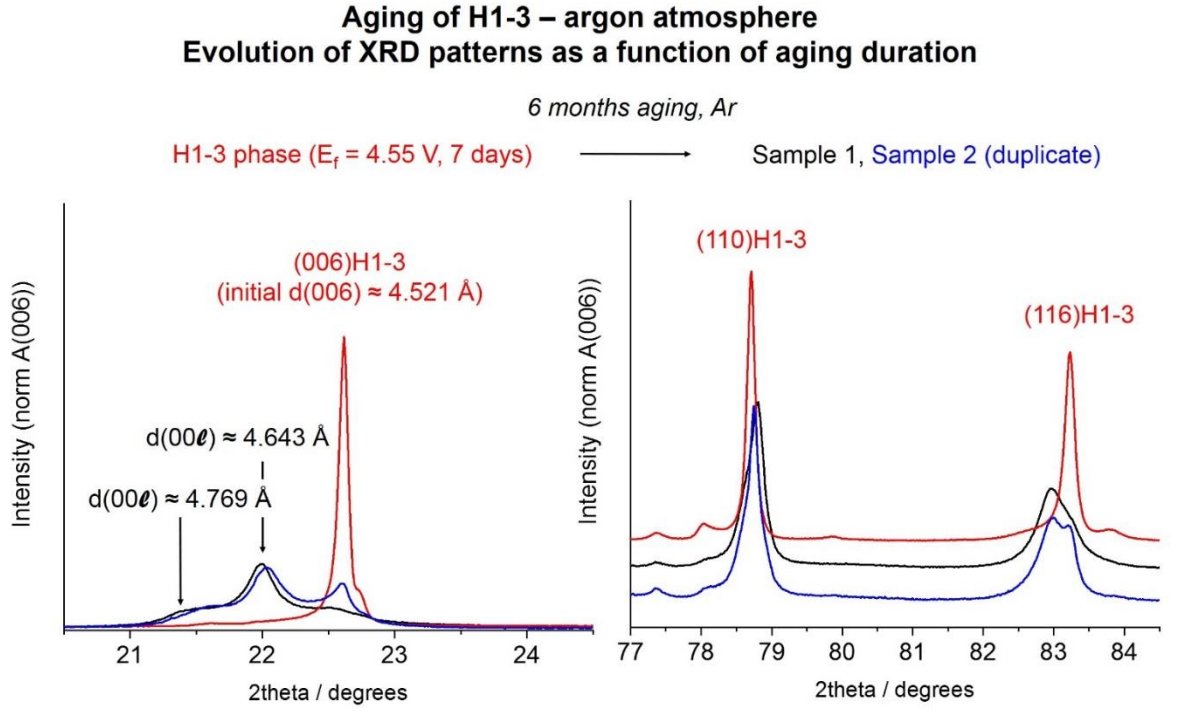

Figure B29. *Comparison of ex situ SXRD patterns collected at t = 7 days and t = 6 months for the same H1-3-Li_xCoO_2 powder safely stored under argon (λ = 0.825 Å). The powder was initially prepared from electrochemical Li de-intercalation of st-LCO charged up to E = 4.54 V.*

We observed a similar evolution in the SXRD patterns of a H1-3 sample prepared from st-LCO at 4.55 V and stored in an argon-filled glovebox for 6 months, as shown in **Figure B29**. The powders were protected from any possible contamination from air or water traces inside the glovebox by first being stored in glass containers and themselves put inside a glass tube containing a sodium piece, closed with a tape-secured rubber cap). Again, the detection of the (110) line suggested that the layered structure of the phase was preserved, although a set of interslab spacings simultaneously coexist in this sample ($d(00\ell)_1$ = 4.521 Å, $d(00\ell)_2$ = 4.643 Å and $d(00\ell)_3$ = 4.769 Å). In the absence of additional XRD patterns (and other characterization techniques), no further effect of the atmosphere on either the kinetics or the nature of the structural evolution previously described can be debated. At this point, we can only assume that the H1-3 phase is unstable on a weekly basis no matter the chemical nature of the atmosphere. A de-mixing of the phase seems unlikely as no diffraction lines with interslab comparable to an O1-stacking was seen in the diffraction patterns. However, an overall homogenization of the Li gradients within the layered phase could still be a cause of varying interslab distances. Another angle could be to consider a partial re-lithiation of the original H1-3 phase through Li transfer from the solid electrolyte interphase (SEI) at the surface of the particles to the bulk.

In any case, the present study seems to corroborate the hypothesis of an intrinsic metastability of the H1-3 phase suspected from the literature, as the Li gradients observed in the initial H1-3 structure may spontaneously evolve to reach a constant repartition. While the nature of the atmosphere does not influence the structural properties of the final product, it could still play a role in the kinetics of this phenomenon. This remains uncertain as the timelines of each experiment (under air, under argon) were drastically changing. This study still reveals the technical

difficulties inherent to the handling of H1-3 powders, which was still suspected due to the lack of knowledge available in the literature.

B.5. General conclusions on Part B

In situ X-ray diffraction measurements have revealed that st-LCO (initial Li/Co = 1.00) experiences more phase transitions than previously reported, both at low and high voltage during its 1st full charge in a half cell setup. In the $0.55 < x < 0.40$ range, the coexistence of two monoclinic phases was detected operando for the Li_xCoO_2 system, although their existence at equilibrium remains unknown. The complementary preparation of Li_xCoO_2 powders from electrochemical Li de-intercalation of st-LCO in this x range is now currently performed within the frame of a Sean Hinkle Master's project. While the formation of the high voltage H1-3 (*R-3m* space group) and O1 (*P-3m1* space group) structures was confirmed, diffraction lines arising from a possible intergrowth (X) structure were additionally detected. The existence of defects generated by the initial presence of excess Li inside the CoO_2 layers of overl-LCO (initial Li/Co = 1.05) does not hinder but delays the formation of the H1-3 and O1 phases, though their cell parameters slightly differ. Besides, the intermediate (X) structure is not formed.

This new intergrowth structure has been additionally detected in the in situ SXRD patterns recorded during the charge of st-LCO at C/10 and C/2 (not shown in this manuscript). Data treatment of the SXRD patterns first suggests that the average interslab spacing in the (X) phase varies with the C rate. Further work will be required to confirm it.

The successful preparation of pure powders of H1-3-Li_xCoO_2 from electrochemical de-intercalation of Li from st-LCO has helped confirming the indexation of its structure using an hexagonal unit cell. However, no information regarding the sites occupied by Li and their occupancy could be gathered. Deeper analysis of the diffraction data still remains challenging to this day due to the existence of stacking faults in all the high voltage phases. DIFFAX modelling

was and is still currently considered in order to more accurately fit the in situ and ex situ experimental patterns (**see Figure B30**), starting with the H1-3 phase.

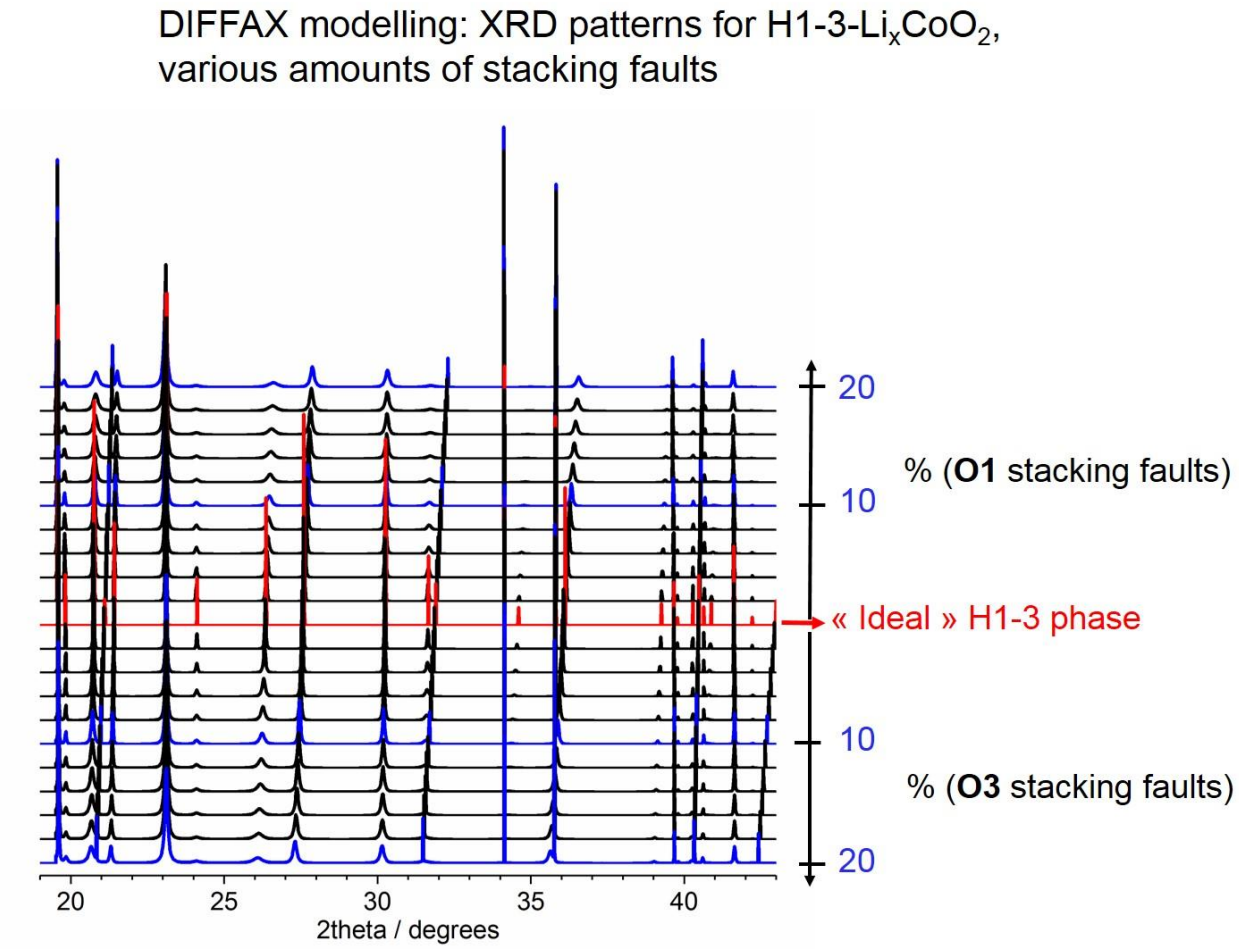

Figure B30. *DIFFAX Simulation of XRD patterns for the H1-3 structure with various amounts of O3 and O1 stacking faults.*

B.6 Bibliography Part B

(1) Seong, W. M.; Yoon, K.; Lee, M. H.; Jung, S.-K.; Kang, K. Unveiling the Intrinsic Cycle Reversibility of a $LiCoO_2$ Electrode at 4.8-V Cutoff Voltage through Subtractive Surface Modification for Lithium-Ion Batteries. *Nano Lett.* **2018**. https://doi.org/10.1021/acs.nanolett.8b02902.

(2) Liu, L.; Chen, L.; Huang, X.; Yang, X.-Q.; Yoon, W.-S.; Lee, H. S.; McBreen, J. Electrochemical and In Situ Synchrotron XRD Studies on Al_2O_3-Coated $LiCoO_2$ Cathode Material. *J. Electrochem. Soc.* **2004**, *151* (9), A1344–A1351. https://doi.org/10.1149/1.1772781.

(3) Aurbach, D.; Markovsky, B.; Rodkin, A.; Cojocaru, M.; Levi, E.; Kim, H.-J. An Analysis of Rechargeable Lithium-Ion Batteries after Prolonged Cycling. *Electrochimica Acta* **2002**, *47* (12), 1899–1911. https://doi.org/10.1016/S0013-4686(02)00013-0.

(4) Würsig, A.; Buqa, H.; Holzapfel, M.; Krumeich, F.; Novák, P. Film Formation at Positive Electrodes in Lithium-Ion Batteries. *Electrochem. Solid-State Lett.* **2005**, *8* (1), A34–A37. https://doi.org/10.1149/1.1836114.

(5) Dahéron, L.; Dedryvère, R.; Martinez, H.; Ménétrier, M.; Denage, C.; Delmas, C.; Gonbeau, D. Electron Transfer Mechanisms upon Lithium Deintercalation from $LiCoO_2$ to CoO_2 Investigated by XPS. *Chem. Mater.* **2008**, *20* (2), 583–590. https://doi.org/10.1021/cm702546s.

(6) Park, Y.; Shin, S. H.; Hwang, H.; Lee, S. M.; Kim, S. P.; Choi, H. C.; Jung, Y. M. Investigation of Solid Electrolyte Interface (SEI) Film on $LiCoO_2$ Cathode in Fluoroethylene Carbonate (FEC)-Containing Electrolyte by 2D Correlation X-Ray Photoelectron

Spectroscopy (XPS). *J. Mol. Struct.* **2014**, *1069*, 157–163. https://doi.org/10.1016/j.molstruc.2014.01.041.

(7) Verma, P.; Maire, P.; Novák, P. A Review of the Features and Analyses of the Solid Electrolyte Interphase in Li-Ion Batteries. *Electrochimica Acta* **2010**, *55* (22), 6332–6341. https://doi.org/10.1016/j.electacta.2010.05.072.

(8) Zaban, A.; Zinigrad, E.; Aurbach, D. Impedance Spectroscopy of Li Electrodes. 4. A General Simple Model of the Li−Solution Interphase in Polar Aprotic Systems. *J. Phys. Chem.* **1996**, *100* (8), 3089–3101. https://doi.org/10.1021/jp9514279.

(9) Markevich, E.; Salitra, G.; Aurbach, D. Influence of the PVdF Binder on the Stability of $LiCoO_2$ Electrodes. *Electrochem. Commun.* **2005**, *7* (12), 1298–1304. https://doi.org/10.1016/j.elecom.2005.09.010.

(10) Takahashi, Y.; Tode, S.; Kinoshita, A.; Fujimoto, H.; Nakane, I.; Fujitani, S. Development of Lithium-Ion Batteries with a $LiCoO_2$ Cathode Toward High Capacity by Elevating Charging Potential. *J. Electrochem. Soc.* **2008**, *155* (7), A537–A541. https://doi.org/10.1149/1.2916685.

(11) Amatucci, G. G.; Tarascon, J. M.; Klein, L. C. Cobalt Dissolution in $LiCoO_2$-Based Non-Aqueous Rechargeable Batteries. *Solid State Ion.* **1996**, *83* (1–2), 167–173. https://doi.org/10.1016/0167-2738(95)00231-6.

(12) Jeon, S.-W.; Lim, J.-K.; Lim, S.-H.; Lee, S.-M. As-Deposited $LiCoO_2$ Thin Film Cathodes Prepared by Rf Magnetron Sputtering. *Electrochimica Acta* **2005**, *51* (2), 268–273. https://doi.org/10.1016/j.electacta.2005.04.035.

(13) Kim, Y. J.; Cho, J.; Kim, T.-J.; Park, B. Suppression of Cobalt Dissolution from the $LiCoO_2$ Cathodes with Various Metal-Oxide Coatings. *J. Electrochem. Soc.* **2003**, *150* (12), A1723–A1725. https://doi.org/10.1149/1.1627347.

(14) Wang, H.; Jang, Y.-I.; Huang, B.; Sadoway, D. R.; Chiang, Y.-M. TEM Study of Electrochemical Cycling-Induced Damage and Disorder in $LiCoO_2$ Cathodes for Rechargeable Lithium Batteries. *J. Electrochem. Soc.* **1999**, *146* (2), 473–480. https://doi.org/10.1149/1.1391631.

(15) Gabrisch, H.; Yazami, R.; Fultz, B. Hexagonal to Cubic Spinel Transformation in Lithiated Cobalt Oxide TEM Investigation. *J. Electrochem. Soc.* **2004**, *151* (6), A891–A897. https://doi.org/10.1149/1.1738677.

(16) Gabrisch, H.; Yazami, R.; Fultz, B. A Transmission Electron Microscopy Study of Cycled $LiCoO_2$. *J. Power Sources* **2003**, *119–121*, 674–679. https://doi.org/10.1016/S0378-7753(03)00234-9.

(17) Yazami, R.; Ozawa, Y.; Gabrisch, H.; Fultz, B. Mechanism of Electrochemical Performance Decay in $LiCoO_2$ Aged at High Voltage. *Electrochimica Acta* **2004**, *50* (2–3), 385–390. https://doi.org/10.1016/j.electacta.2004.03.048.

(18) Yano, A.; Shikano, M.; Ueda, A.; Sakaebe, H.; Ogumi, Z. $LiCoO_2$ Degradation Behavior in the High-Voltage Phase Transition Region and Improved Reversibility with Surface Coating. *J. Electrochem. Soc.* **2017**, *164* (1), A6116–A6122. https://doi.org/10.1149/2.0181701jes.

(19) Gabrisch, H.; Yazami, R.; Fultz, B. The Character of Dislocations in $LiCoO_2$. *Electrochem. Solid-State Lett.* **2002**, *5* (6), A111–A114. https://doi.org/10.1149/1.1472257.

(20) Amatucci, G. G.; Tarascon, J. M.; Klein, L. C. CoO_2, The End Member of the Li_xCoO_2 Solid Solution. *J. Electrochem. Soc.* **1996**, *143* (3), 1114–1123. https://doi.org/10.1149/1.1836594.

(21) Delmas, C.; Fouassier, C.; Hagenmuller, P. Structural Classification and Properties of the Layered Oxides. *Phys. BC* **1980**, *99* (1), 81–85. https://doi.org/10.1016/0378-4363(80)90214-4.

(22) Seguin, L.; Amatucci, G.; Anne, M.; Chabre, Y.; Strobel, P.; Tarascon, J. M.; Vaughan, G. Structural Study of NiO_2 and CoO_2 as End Members of the Lithiated Compounds by in Situ High Resolution X-Ray Powder Diffraction. *J. Power Sources* **1999**, *81–82*, 604–606. https://doi.org/10.1016/S0378-7753(99)00110-X.

(23) Tarascon, J. M.; Vaughan, G.; Chabre, Y.; Seguin, L.; Anne, M.; Strobel, P.; Amatucci, G. In Situ Structural and Electrochemical Study of $Ni_{1-x}Co_xO_2$ Metastable Oxides Prepared by Soft Chemistry. *J. Solid State Chem.* **1999**, *147* (1), 410–420. https://doi.org/10.1006/jssc.1999.8465.

(24) Yang, X. Q.; Sun, X.; McBreen, J. New Phases and Phase Transitions Observed in $Li_{1-x}CoO_2$ during Charge: In Situ Synchrotron X-Ray Diffraction Studies. *Electrochem. Commun.* **2000**, *2* (2), 100–103. https://doi.org/10.1016/S1388-2481(99)00155-1.

(25) Motohashi, T.; Katsumata, Y.; Ono, T.; Kanno, R.; Karppinen, M.; Yamauchi, H. Synthesis and Properties of CoO_2 , the $x = 0$ End Member of the Li_xCoO_2 and Na_xCoO_2 Systems. *Chem. Mater.* **2007**, *19* (21), 5063–5066. https://doi.org/10.1021/cm0702464.

(26) De Vaulx, C.; Julien, M.-H.; Berthier, C.; Hebert, S.; Pralong, V.; Maignan, A. Electronic Correlations in CoO_2, the Parent Compound of Triangular Cobaltates. *Phys. Rev. Lett.* **2007**, *98* (24). https://doi.org/10.1103/PhysRevLett.98.246402.

(27) Ohzuku, T.; Ueda, A. Solid-State Redox Reactions of $LiCoO_2$ ($R\bar{3}m$) for 4 Volt Secondary Lithium Cells. *J. Electrochem. Soc.* **1994**, *141* (11), 2972–2977. https://doi.org/10.1149/1.2059267.

(28) Van der Ven, A.; Aydinol, M. K.; Ceder, G.; Kresse, G.; Hafner, J. First-Principles Investigation of Phase Stability in Li_xCoO_2. *Phys. Rev. B* **1998**, *58* (6), 2975–2987. https://doi.org/10.1103/PhysRevB.58.2975.

(29) Van der Ven, A.; Aydinol, M. K.; Ceder, G. First-Principles Evidence for Stage Ordering in Li_xCoO_2. *J. Electrochem. Soc.* **1998**, *145* (6), 2149–2155.

(30) Van der Ven, A. First Principles Investigation of the Thermodynamic and Kinetic Properties of Lithium Transition Metal Oxides. Thesis, Massachusetts Institute of Technology, 2000.

(31) Guerard, D.; Herold, A. Intercalation of Lithium into Graphite and Other Carbons. *Carbon* **1975**, *13* (4), 337–345. https://doi.org/10.1016/0008-6223(75)90040-8.

(32) Chen, Z.; Lu, Z.; Dahn, J. R. Staging Phase Transitions in Li_xCoO_2. *J. Electrochem. Soc.* **2002**, *149* (12), A1604–A1609. https://doi.org/10.1149/1.1519850.

(33) Wolverton, C.; Zunger, A. First-Principles Prediction of Vacancy Order-Disorder and Intercalation Battery Voltages in Li_xCoO_2. *Phys. Rev. Lett.* **1998**, *81* (3), 606.

(34) Berthelot, R. Contribution à l'étude électrochimique du système P2-Na_xCoO_2 : synthèse et caractérisation de nouveaux oxydes lamellaires ordonnés (A/A')CoO_2 (A, A' = Li, Na, Ag). phdthesis, Université Sciences et Technologies - Bordeaux I, 2010.

(35) Sun, X.; Yang, X. Q.; McBreen, J.; Gao, Y.; Yakovleva, M. V.; Xing, X. K.; Daroux, M. L. New Phases and Phase Transitions Observed in Over-Charged States of $LiCoO_2$-Based Cathode Materials. *J. Power Sources* **2001**, *97–98*, 274–276. https://doi.org/10.1016/S0378-7753(01)00512-2.

(36) Casas-Cabanas, M.; Rodríguez-Carvajal, J.; Canales-Vázquez, J.; Laligant, Y.; Lacorre, P.; Palacín, M. R. Microstructural Characterisation of Battery Materials Using Powder Diffraction Data: DIFFaX, FAULTS and SH-FullProf Approaches. *J. Power Sources* **2007**, *174* (2), 414–420. https://doi.org/10.1016/j.jpowsour.2007.06.216.

(37) Duffiet, M.; Blangero, M.; Cabelguen, P.-E.; Delmas, C.; Carlier, D. Influence of the Initial Li/Co Ratio in $LiCoO_2$ on the High-Voltage Phase-Transitions Mechanisms. *J. Phys. Chem. Lett.* **2018**, 5334–5338. https://doi.org/10.1021/acs.jpclett.8b02252.

(38) Xia, H.; Lu, L.; Meng, Y. S.; Ceder, G. Phase Transitions and High-Voltage Electrochemical Behavior of $LiCoO_2$ Thin Films Grown by Pulsed Laser Deposition. *J. Electrochem. Soc.* **2007**, *154* (4), A337–A342. https://doi.org/10.1149/1.2509021.

(39) Fauth, F.; Peral, I.; Popescu, C.; Knapp, M. The New Material Science Powder Diffraction Beamline at ALBA Synchrotron. *Powder Diffr.* **2013**, *28* (S2), S360–S370. https://doi.org/10.1017/S0885715613000900.

(40) Ménétrier, M.; Carlier, D.; Blangero, M.; Delmas, C. On "Really" Stoichiometric $LiCoO_2$. *Electrochem. Solid-State Lett.* **2008**, *11* (11), A179–A182. https://doi.org/10.1149/1.2968953.

(41) Shao-Horn, Y.; Levasseur, S.; Weill, F.; Delmas, C. Probing Lithium and Vacancy Ordering in O3 Layered Li_xCoO_2 ($x \approx 0.5$) An Electron Diffraction Study. *J. Electrochem. Soc.* **2003**, *150* (3), A366–A373. https://doi.org/10.1149/1.1553787.

(42) Reimers, J. N.; Dahn, J. R. Electrochemical and In Situ X-Ray Diffraction Studies of Lithium Intercalation in Li_xCoO_2. *J. Electrochem. Soc.* **1992**, *139* (8), 2091–2097. https://doi.org/10.1149/1.2221184.

(43) Dyer, L. D.; Borie, B. S.; Smith, G. P. Alkali Metal-Nickel Oxides of the Type $MNiO_2$. *J. Am. Chem. Soc.* **1954**, *76* (6), 1499–1503. https://doi.org/10.1021/ja01635a012.

(44) Chappel, E.; Núñez-Regueiro, M. D.; Chouteau, G.; Isnard, O.; Darie, C. Study of the Ferrodistorsive Orbital Ordering in $NaNiO_2$ by Neutron Diffraction and Submillimeter Wave ESR. *Eur. Phys. J. B - Condens. Matter Complex Syst.* **2000**, *17* (4), 615–622. https://doi.org/10.1007/s100510070099.

(45) Ma, X.; Chen, H.; Ceder, G. Electrochemical Properties of Monoclinic $NaMnO_2$. *J. Electrochem. Soc.* **2011**, *158* (12), A1307–A1312. https://doi.org/10.1149/2.035112jes.

Part C. Optimization of LCO – towards the preparation of high energy density Al-doped $LiCoO_2$ powders by solid state route

Part C. Optimization of LCO – towards the preparation of high energy density Al-doped $LiCoO_2$ powders by solid state route

C.1 Introduction

As revealed in Parts A and B, attempts to reversibly de-intercalate more Li from LCO result in poor cycling performances due to strong degradation of the conventional carbonate-based electrolytes[1,2], structural instabilities[3–7] and cobalt dissolution[8] observed at high voltage ($V > 4.3$ *vs.* Li^+/Li). While Part B of this manuscript was fully consecrated to gaining more fundamental knowledge about the phase transitions occurring at high voltage for the Li_xCoO_2 systems ($x_0 \geq 1.00$), Part C is meant to align with the current LCO-related literature which is almost exclusively dedicated to material optimization through coatings and dopings to address the above-mentioned issues – which (supposedly) includes preventing the O3 – H1-3 – O1 transitions for the latter. Indeed, the substitution of some Co^{3+} ions with various dopants[9–12] M (M = Mg, Ti, Zr, Cr…) or more recently co-dopants[13–15] (M, M') like (Mn, Mg), (Mg, Ti) or (La, Al), has been reported to be an effective strategy to improve the cycle life of LCO at high voltage.

Aluminum ions as dopants were among the first considered, by the means of theoretical calculations from Ceder's group[16], followed by experimental work from Jang *et al.*[17] and other groups[18–20]. The choice for aluminum was motivated by i) the low cost and non-toxicity of aluminum, ii) a similar radius for Al^{3+} compared to Co^{3+} (0.535 Å vs. 0.545 Å) facilitating the substitution of the latter and preserving the initial structure leading to the full solid solution $LiCo_{1-y}Al_yO_2$. Al-doped LCO has been reported to experience: i) less volume changes[17,18], ii) a decreased cobalt dissolution[18], and iii) the suppression of spinel disorder onto the surface of the

particles as compared to LCO[21], even though accelerate capacity fading was also demonstrated[16,22]. The effect of Al doping on the phase transitions observed for LCO at high voltage is though still unclear.

The first step towards a gain of more fundamental knowledge on the real effect(s) of Al doping in LCO would however require a proper control of the initial Li/M stoichiometry (M = Co + Al) – which is (similarly to previous observations on undoped LCO) either missing or such as Li is introduced in excess (Li/M > 1.00). A parasitic effect of Li excess in Al-doped LCO with non-controlled Li stoichiometry may have – so far – led to incorrect conclusions.

Another major issue regards the homogeneity of the Al doping in LCO powders. One could guess that the effects reported for Al doping, especially regarding its electrochemical properties, are strongly dependent on the distribution of Al within LCO, intrinsically linked to its synthesis. Evidencing the Al distribution for a very low Al content in LCO is intuitively more challenging than in the case of larger amounts of Al, as the detection of the dopant may be impossible due to the low resolution of conventional characterization techniques. In most (if not all) articles[17,21,22,18,23] currently considered as pioneering works on Al-doped LCO, the amount of Al *y* in $LiCo_{1-y}Al_yO_2$ is quite significant ($y \geq 0.10$), which could explain why the question of finding appropriate techniques to evidence the distribution of Al in Al-doped LCO ($y < 0.10$) has never really been brought up (though it has temporarily been dealt with[24] for Al-coated LCO). Besides, as precious as these contributions were in gaining knowledge about the potential effect of the substitution of Co^{3+} with Al^{3+} on the electrochemical performance of model $LiCo_{1-y}Al_yO_2$ systems ($y \geq 0.10$), these phases are not viable for further applications in commercial Li-ion cells due to the electrochemical inactivity of Al itself, which severely cuts off the capacity of the battery.

In addition, even with high Al content, a proper Co^{3+}/Al^{3+} mixing is expected and assumed as they are often synthesized in liquid media, featuring co-precipitation routes[17,18,22,23,25,26]. In any case, doped LCO prepared through solvent-friendly routes – no matter how effective they may be in achieving homogeneous doping – show higher time and financial costs, and usually lower particle sizes as compared to solid state routes, which may be interesting to further develop even though achieving a proper Al distribution may be more challenging. Thus, developing proper tools to judge on the distribution of Al within LCO is of great importance to: i) establish the relation between homogeneity of the doping and the electrochemical properties of the material in a Li cell, ii) gain more fundamental knowledge about the role of Al on the structural stability of LCO upon cycling, iii) lay the foundations to help designing a standardized synthesis for Al-doped LCO closer to the current processes used by battery materials manufacturers, i.e. solid routes.

The following aims to discuss the possibility of formation of homogeneous Al-doped LCO samples (or "LCA") from solid state reactions between the oxide precursors (Co_3O_4, Al_2O_3) and lithium carbonate with well-controlled Li and Al stoichiometries. Although the incorporation of Al through interdiffusion of Co^{3+} and Al^{3+} in the layered structure of LCO was recently discussed to try to optimize the synthesis of Al_2O_3-coated LCO[24,27], no article has reported similar attempts to prepare Al-doped LCO to our knowledge. In the meantime, this study also aims to more generally propose a protocol to discuss the homogeneity of Al-distribution in Li-stoichiometric $LiCo_{1-y}Al_yO_2$ with a low Al content.

C.2. Experimental section: general considerations and adopted approaches

C.2.1 Syntheses of Al-doped LCO powders

Although solid state reactions are rather easy to implement thanks to a limited number of steps, a significant number of parameters could still be tuned while trying to design a standard synthesis of Al-doped LCO (or "LCA"). An exhaustive list includes the chemical nature of the precursors, their relative proportions, the temperature and atmosphere for their heat treatment, etc…

Three compositions were initially targeted when we first started the preparation of LCA powders from solid state reaction of Li_2CO_3, Co_3O_4 and Al_2O_3: $LiCo_{0.99}Al_{0.01}O_2$, $LiCo_{0.98}Al_{0.02}O_2$ and $LiCo_{0.96}Al_{0.04}O_2$. However, most of the optimization work has eventually been pursued for the latter. The influence of the heat treatment temperature and the relative proportions of precursors on the final distribution of Al within the LCA powders was also considered, though the effect of the former proved to be quite negligible. Therefore, in the following, we present all results related to the preparation of $LiCo_{0.96}Al_{0.04}O_2$ from the solid state reaction between Li_2CO_3, Co_3O_4 and Al_2O_3, in which Li_2CO_3 was either introduced in stoichiometric proportions (**Approach n°1, section C.3**) or in excess (**Approach n°2, section C.4**) with the metal oxide precursors. All syntheses were carried out in the Umicore R&D center in Cheonan, South Korea. Precise descriptions of each approach are given at the beginning of their respective sections.

C.2.2 General characterization of powders: experimental details and technical background

All characterization was performed under the same experimental conditions in section C.3 (Approach n°1) or section C.4 (Approach n°2).

Scanning electron micrographs were taken using a Hitachi Model S-4500 microscope after metallizing the powders with gold.

Inductively Coupled Plasma (ICP) measurements were carried out on Agilent ICP-720ES equipment after sample dissolution using hotplate heating in concentrated HCl solution.

Powder X-ray diffraction (XRD) patterns were collected on a PANalitycal X'pert PRO MPD diffractometer in Bragg-Brentano θ-θ geometry equipped with a Fe filter, a spinner and X'Celerator multi-strip detector. Each measurement was made within an angular range of 2θ = 10 - 120° and lasted for 15 hours, at 0.016° intervals. The Co-Kα radiation was generated at 35 kV and 30 mA ($\lambda(K_{\alpha 1})$ = 1.789 Å; $\lambda(K_{\alpha 2})$ = 1.793 Å).

Additional high angular resolution synchrotron powder X-ray diffraction (SXRD) was carried out on the BL04-MSPD beamline of the ALBA synchrotron (Cerdanyola del Vallès, Spain). All powders were packed in 0.5 mm diameter capillaries. The typical 2Θ angular range was 0 - 70 ° with 0.006° angular step and 3-minute-long accumulation time. The patterns were recorded in Debye-Scherrer geometry with a wavelength of $\lambda \approx 0.825$ Å.

Data treatment for SXRD: As all data was collected over 4 different synchrotron sessions with slightly different wavelengths, all SXRD patterns have been converted and mainly plotted for the same $\lambda = 0.826$ Å all over Part C, which corresponds to the refined value of λ obtained from Le Bail refinement with FullProf[28] of the two standard samples (Si and $Na_2Ca_3Al_2F_{14}$ + CaF_2,

respectively) during session n°1. A few figures have been converted and plotted for λ_{Co} = 1.790 Å when a comparison with XRD data was necessary. Besides, zero offsets obtained from Le Bail refinement of all SXRD patterns have been input in the corresponding plots, meaning that any change of peak position in the SXRD patterns may directly be assigned to different cell parameters from one sample to another. All provided zooms on specific diffraction peak are normalized to the total peak area, unless it says otherwise in the caption.

^{7}Li MAS NMR spectra were recorded on a Bruker 300 Advance spectrometer at 116.66 MHz (7.05 T magnet), with a standard 2.5 mm Bruker MAS probe. A Hahn echo sequence [$t_{\pi/2}$-τ1-t_{π}-τ2] synchronized with one period of rotor rotation was used for a 30 kHz spinning frequency. The 90° pulse duration was equal to $t_{\pi/2}$ = 2.0 µs and determined using a LiCl 1 M solution. A recycle time of D_0 = 40s was used for st-LCO and LCA samples, whereas a shorter D_0 = 2s was enough for the overl-LCO sample, to avoid T_1 saturation effects.

Single pulse ^{27}Al MAS NMR spectra were recorded on a Bruker 500 MHz spectrometer at 130.33 MHz (11.7 T magnet) using a standard Bruker 2.5 mm MAS probe with a 30 kHz typical spinning frequency. The spectral width was set to 0.5 MHz and the recycle time to D_0 = 5 s, long enough to avoid T_1 saturation effects. As ^{27}Al is a strong quadrupolar nucleus with I = 5/2, a short pulse length of 1.1 µs corresponding to a π/12 pulse determined using an aqueous 1 M $Al(NO_3)_3$ solution was employed. In these conditions, all of the -½ → +½ central transitions are equally excited regardless of the magnitude of the nuclear quadrupole coupling constants and one can extract quantitative data. The external reference was a 1 M $Al(NO_3)_3$ aqueous solution. For the samples containing only 4% of Al, overnight experiments (10240 scans) were carried out to ensure a good signal/noise ratio. No baseline subtraction was done in the figures presented here.

^{59}Co MAS NMR spectra were recorded on a Bruker 500 MHz spectrometer at 120.35 MHz (11.7 T magnet) using a standard Bruker 2.5 mm MAS probe with a 30 kHz typical spinning frequency. The spectral width was set to 0.5 MHz and the recycle time to D_0 = 1 s. A combination of single pulse and rotor-synchronized Hahn echo sequences was used. The single pulse sequence using a short pulse length of 1.1 µs corresponding to a $\pi/16$ pulse was used to extract quantitative data. However, it requires a first-order phasing process with a sin x/x baseline correction due to the dead time of the spectrometer here, not easily determined due to large overlapping signals. The Hahn echo sequence [$t_{\pi/2}$-τ1-t_{π}-τ2] with $t_{\pi/2}$ = 2.5 µs was therefore used to facilitate the phasing of all the signals and to ensure the observation of possible very wide signals which are lost during the receiver dead time. The external reference was a 1M $K_3Co(CN)_6$ aqueous solution.

Electrochemical tests were performed in coin cells, using pure lithium as counter-electrode and 1 M $LiPF_6$ in EC:DEC:DMC as electrolyte. LCA:C:PVDF electrodes (90:5:5 $\%_{wt}$) were prepared from a slurry using N-methyl-pyrrolidone (NMP) as solvent casted onto a 30 µm-thick-aluminum foil. After evaporating the NMP for 2 hours at T = 80 °C, Φ15 mm electrodes were cut in the obtained film with typical active material loading of 10 mg/cm². The electrodes were then dried overnight under vacuum at T = 120 °C and stored in an argon-filled glovebox, whose cell assembling was carried out.

C.3 Approach n°1: preparation of $LiCo_{0.96}Al_{0.04}O_2$ powders from solid state reaction of Li_2CO_3 and $[(Co_3O_4)_{0.32}(Al_2O_3)_{0.02}]$ in stoichiometric proportions

C.3.1 Description of synthesis

A schematic figure summarizing all steps of the synthesis can also be found in ***Figure C1***.

*Precursors***:** A 2 kg-blend containing Co_3O_4 (Umicore) and Al_2O_3 (Umicore) in a Co/Al ratio of 0.96/0.04 was initially prepared as starter. After homogenizing the mixture, it was split into two batches. The first batch (now called Precursor 1) was directly used to prepare P1-LCA. Note that a heat treatment of Precursor 1 at moderate temperature (600 °C) did not lead to any reaction between Co_3O_4 and Al_2O_3 (in good agreement with previous studies[29–31]). In the meantime, a heat treatment at 1000 °C for 10 hours under air flow was applied to the second batch. The fired mixture, now referred to as Precursor 2, was accordingly used to prepare P2-LCA.

LCA samples: Two $LiCo_{0.96}Al_{0.04}O_2$ (LCA) powders samples called "P1-LCA" and "P2-LCA" were both prepared by solid state synthesis of homogenized mixtures of Li_2CO_3 (Umicore) and a Co- and Al- based oxide precursors (P1 or P2, respectively). The mixtures to form the final LCA samples (first intimately blended) were prepared in rather large amounts (220 g) in the ratio Li/(Co+Al) = 0.99. Both were simultaneously heat treated in the same furnace for 12 h under air flow at T = 980 °C, followed by a second annealing at T = 980 °C for 10 h under air. A final post-treatment step using a grinder was mandatory to pulverize the synthesized powder blocks. Additionally, the as-prepared powders were sieved.

For comparison purposes, both non Al-doped stoichiometric (st-LCO, Li/Co = 0.99) and overlithiated $LiCoO_2$ (overl-LCO, Li/Co = 1.05) from Part B are used as reference samples in the following. Additionally, a 4%-Al doped LCO called "Rf-LCA" was prepared by a citrate co-precipitation route, following the experimental protocol detailed in a previous article from

Dahéron *et. al.*[26] A solution of Li_2CO_3, $Al(NO_3)_3.9H_2O$ and $CoCO_3$ in citric acid 0.1 mol/L was heated for 3 hours at T = 80 °C. After ammonia was added to the solution to reach a pH value of 7, the solvent was evaporated using a rotary evaporator. The solid residue was subsequently heat treated 3 times at: i) T = 200 °C for 10 h under air, ii) T = 450 °C for 12 h under O_2 and iii) T = 900 °C for 12 h under O_2. The residue was systematically grinded and pelletized between each heat treatment, and sieved after the last one.

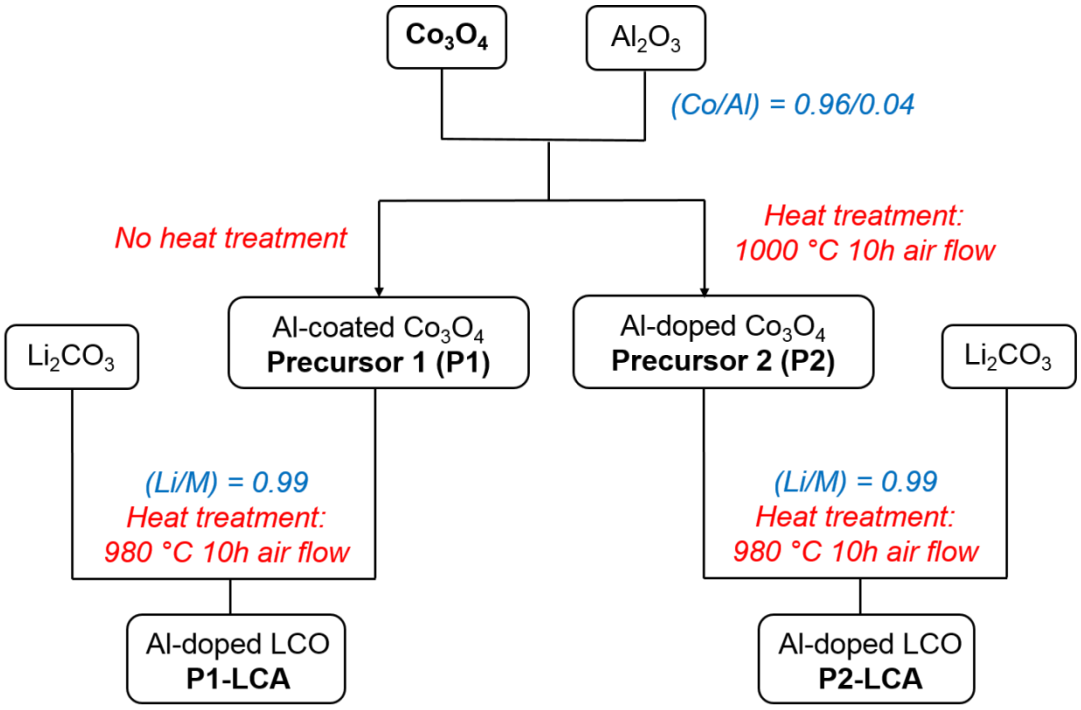

***Figure C1**: Summarizing scheme of syntheses for P1- and P2-LCA from Approach n°1.*

C.3.2 General characterization

C.3.2.1 On the heat treatment of Co_3O_4 and Al_2O_3: what is the chemical nature of both Co/Al precursors?

The major difference between both LCA samples prepared by solid state chemistry regards the used Co/Al-based precursor: homogenized mixture of Co_3O_4 and Al_2O_3 without (Precursor 1) or with a 1000°C heat treatment (Precursor 2). Therefore, a special attention to the Co/Al-based precursor is then given in the following to establish the relevance of the heat treatment of Co_3O_4 and Al_2O_3 with Co/Al = 0.96/0.04 prior to the addition of lithium carbonate, using SEM, SXRD, and ^{27}Al MAS NMR.

SEM micrographs of Precursors are given in **Figure C2**. A population of < 10 nm-sized particles corresponding to Al_2O_3 can be clearly distinguished on top of Co_3O_4 particles whose average size is several hundreds of nanometers for Precursor 1 (**Figure C2.a**). On the other hand, only one type of bigger particles (µm-size) is observed for Precursor 2 (**Figure C2.b**). This suggests that the reaction between Al_2O_3 and Co_3O_4 has occurred at 1000°C, jointly with crystalline growth usually observed at high temperatures.

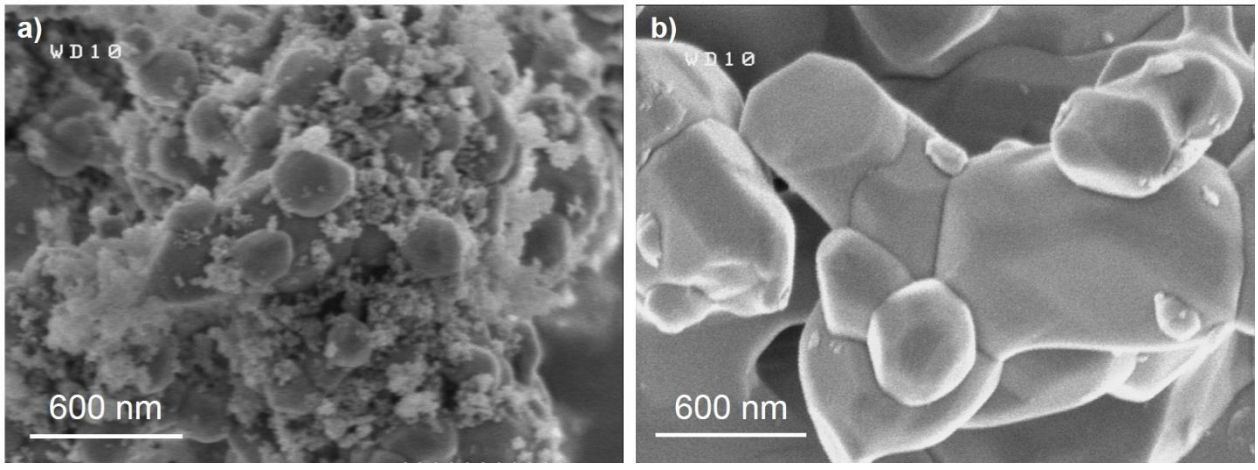

Figure C2. *SEM micrographs of the powders of* ***a)*** *Precursor 1 (Co_3O_4 + Al_2O_3) and* ***b)*** *Precursor 2 (Co_3O_4 + Al_2O_3, heat treated at 1000°C for 10h under air).*

SXRD patterns for Precursors 1 and 2 are plotted in **Figure C3**. A reference pattern, i. e. from Co_3O_4, is also provided for better comparison. Recording of XRD patterns using synchrotron radiation was motivated by the expected noticeable gain in detection limit that may reveal information regarding impurities or alumina itself. No matter the Al content *z*, the evolution of the $a_{cub.}$ cell parameter for $Co_{3-z}Al_zO_4$ is expected to be negligible due to comparable ionic radiuses of Co^{3+} (0.545 Å) and Al^{3+} (0.535 Å). Values of 8.084 Å for Co_3O_4, 8.086 Å for Co_2AlO_4 and 8.104 Å

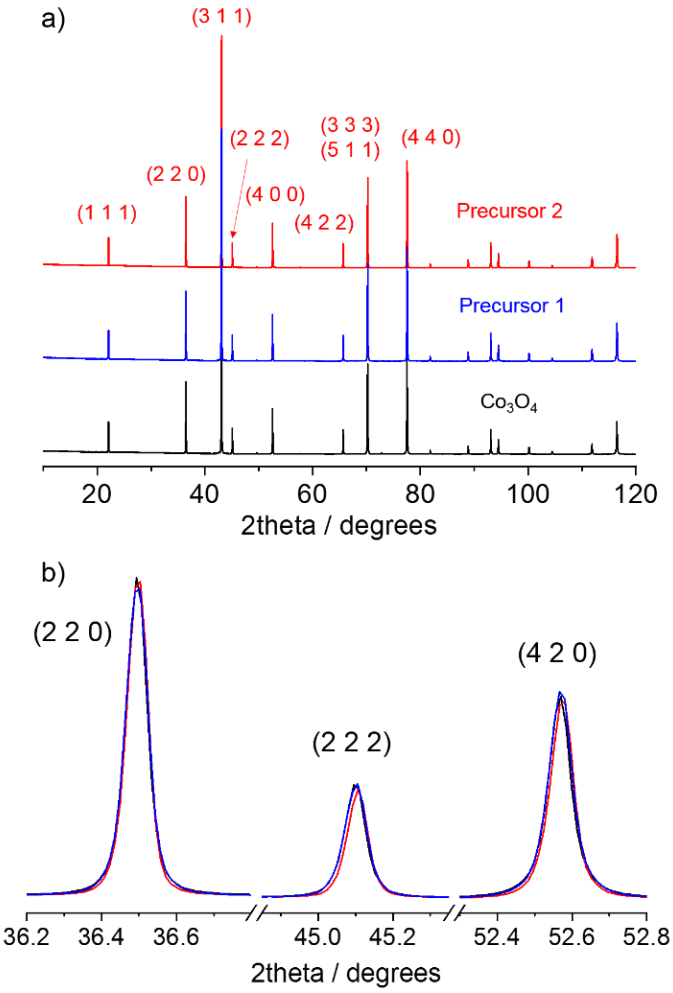

Figure C3. a) *Synchrotron X-ray diffraction (SXRD) patterns obtained for a non-doped Co_3O_4 (black), as compared to the mixtures of Co_3O_4 + Al_2O_3 (Precursor 1, in blue) or heat treated at T = 1000 °C (Precursor 2, in red). All patterns were collected for λ = 0.826 Å, but are converted here to $\lambda(Co_{K\alpha 1})$ = 1.790 Å. Miller indexes are specified for the most intense peaks. Zooms focusing on (2 2 0), (2 2 2) and (4 2 0) peaks are provided in* ***b)****.*

for $CoAl_2O_4$ are typically reported for $a_{cub.}$[30]. Thus, not surprisingly the diffraction peaks for Co_3O_4, Precursor 1 and Precursor 2 are found at identical 2Θ positions. All peaks can be indexed in the *Fd3m* space group with a cell parameter a_{cub} equal to 8.084(2) Å. In particular, no signal ascribed to the presence of crystalline alumina could be detected for either Precursor 1 or Precursor 2 in **Figure C3** – even though alumina is clearly seen in **Figure C2** for the former. The Al_2O_3 present in P1 does, must be really disordered with very small particles size (< 10 nm). After such heat treatment, used to form Precursor 2, the formation of mix-$Co_{3-z}Al_zO_4$ phase is expected[29,30,32,33]. The diffraction peaks of Precursor 1 are found to be slightly broader than those of Precursor 2 (T = 1000 °C). No additional information regarding the Al distribution itself within the precursors could be gathered from SXRD.

Figure C4 shows the ^{27}Al MAS NMR spectra recorded for the different precursors used for the LCA materials synthesis. The Al_2O_3 exhibits a spectrum typical of the γ-form of Al_2O_3 with two broad signals localized around 65 and 9 ppm, assigned respectively to Al in tetrahedral and octahedral environments[34–36]. The strong asymmetrical broadening of the signals toward lower shifts originates from distributions of quadrupolar couplings typically observed in disordered compounds. The Co_3O_4 mixed with Al_2O_3 (Precursor 1) still logically exhibits the same ^{27}Al MAS NMR signature as γ-Al_2O_3, therefore un-reacted. On the contrary, as no signal is observed in the same recording conditions after a heat treatment of these precursors at 1000 °C for 10h (Precursor 2), we conclude that Al_2O_3 did react with Co_3O_4 in good agreement with the SEM observations and with the literature (a minimum temperature of 800 °C was reported[29–31] for the reaction of Co_3O_4 and γ-Al_2O_3 to form $Co_{3-z}Al_zO_4$). The absence of signal for Al in doped Co_3O_4 is most likely due to strong hyperfine coupling with paramagnetic cobalt species either leading to very fast relaxation times or to such a broadening that they cannot be resolved in our conditions.

Similar effect was also reported for $CoAl_2O_4$ and for other paramagnetic materials[37,38]. Therefore, no further information about the distribution of Al within Precursor 2 could be gathered here. Nonetheless, at this point, SEM, SXRD and ^{27}Al MAS NMR helped proving the different chemical natures of Precursor 1 or 2, the latter containing an Al-doped spinel phase as opposed to the former.

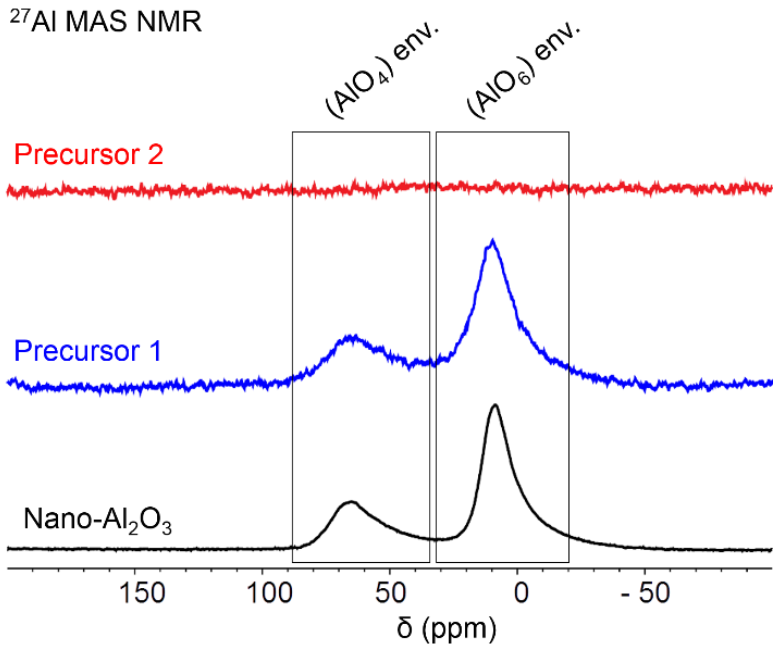

Figure C4. *^{27}Al MAS NMR spectra recorded at 130.33 MHz using a 30kHz spinning frequency for Precursor 1, (Co_3O_4 + Al_2O_3) in blue) and Precursor 2 (Co_3O_4 + Al_2O_3, heat treated at T = 1000 °C) (in red), as compared to the spectra of pure alumina (in black).*

C.3.2.2 Characterization of resulting LCA powders

As aluminum is found in different environments for Precursor 1 or 2, (i. e. included in Co_3O_4 matrix or not), two final associated LCA materials were prepared after addition of Li_2CO_3. The goal of this study was to investigate the homogeneity of the aluminum distribution within the LCA phases and evaluate its influence on the electrochemical behavior, without any interference due to the presence of Li excess. Therefore, we strictly prepared the samples using Li/(Co+Al) = 0.99 in the precursors mixture in order to get real stoichiometric LCA samples with Li/(Co+Al) = 1.00 with possibly remaining spinel and Al_2O_3.

Sample	Li/(Co+Al)	Al/(Co+Al)
P1-LCA	*0.995*	*0.038*
P2-LCA	*0.992*	*0.040*

Table C.T1. *Measured ICP ratios for the two final LCA powders prepared from approach n°1.*

Table C.T1 gives the final Al/(Co+Al) and Li/(Co+Al) ratios measured with ICP for P1- and P2-LCA. Both samples exhibit Al/(Co+Al) values close to the expected 4 % one (Al/(Co+Al) = 0.038 for P1-LCA) and Al/(Co+Al) = 0.040 for P2-LCA). A good control of the final Al content was possible thanks to great quantities of Co_3O_4 and Al_2O_3 precursors, whose initial mixture was prepared in the kilogram-scale. Accurate control of the final Li/(Co+Al) was also possible, as revealed by the measured values always found slightly below 1.00 (Li/(Co+Al) = 0.995 for P1-LCA, and Li/(Co+Al) = 0.992 for P2-LCA). Such good agreement with the ratio Li/(Co+Al) = 0.99 applied to the mixtures Li_2CO_3 + Precursor (1 or 2) was again possible thanks to large quantities involved in their preparation (~ 220 g-mixtures). Laboratory XRD and ^{7}Li MAS NMR were carried out to verify the presence of remaining unreacted Co_3O_4 and the stoichiometry of the LCA samples. In **Figure C5.a**, all XRD patterns show the peaks

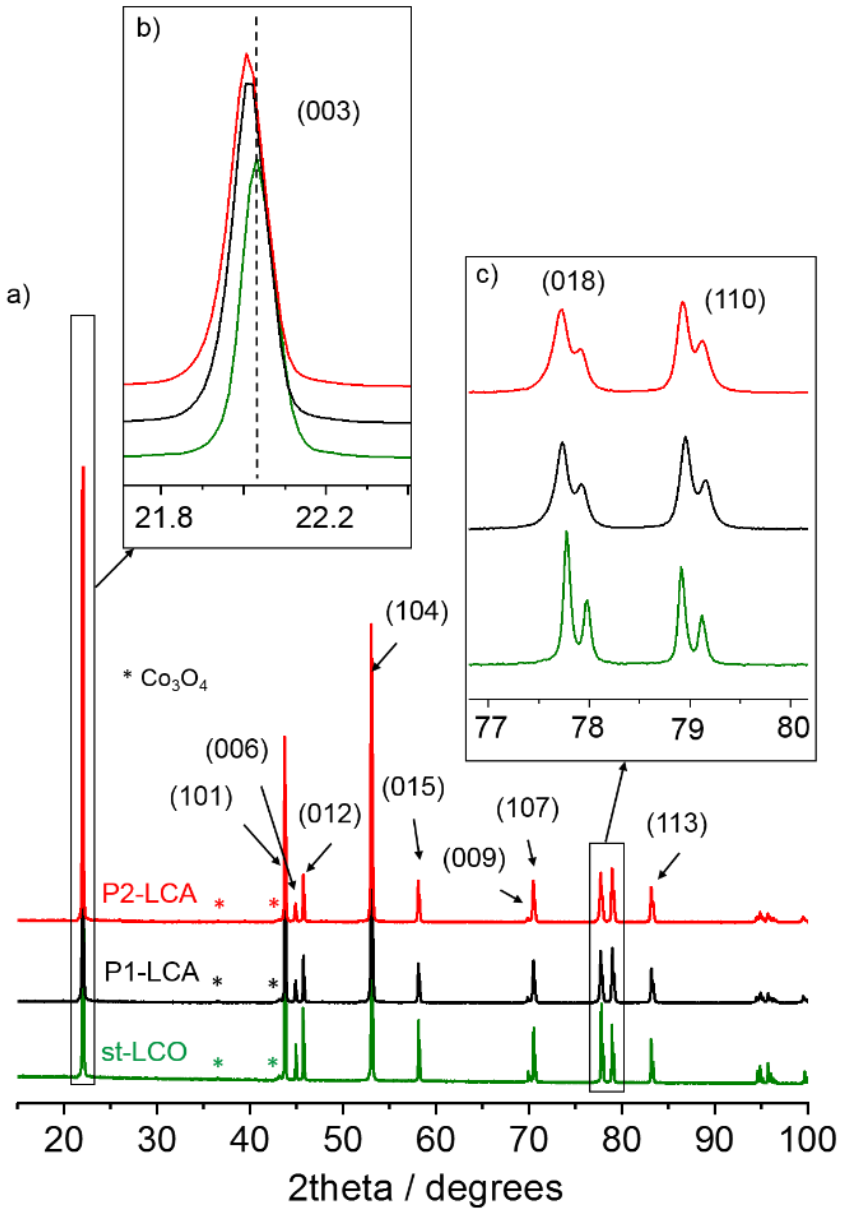

Figure C5. a) *X-ray diffraction (XRD) data recorded for P1- and P2-LCA as compared to undoped LCO (st-LCO). These patterns were collected using a laboratory diffractometer equipped with a cobalt source ($\lambda(Co_{K\alpha 1})$ = 1.789 Å, $\lambda(Co_{K\alpha 2})$ = 1.793 Å). Miller indexes are specified for all the peaks visible for $2\Theta < 90°$. A zoom on the (003) diffraction peak is given in* ***b)****, while (018) and (110) peaks are presented in* ***c)****.*

associated to a layered crystallized (O3) structure indexed in the *R-3m* space group, similarly to the un-doped $LiCoO_2$ we used as reference here (st-LCO). A small overall peak broadening can be observed with the addition of aluminum in the samples. A slightly higher c_{hex} parameter is obtained

from refinement of the XRD patterns for 4 % Al-doped P1-LCA and P2-LCA (respectively 14.063(7) and 14.065(8) Å) compared to their non-doped analogue st-LCO (14.047(1) Å). Such change (0.13%) is clearly highlighted in **Figure C5.b** with the shift observed for the (003) peak. The evolution of the a_{hex} parameter follows the reverse trend, as both LCA samples show a decreased value of 2.814(1) Å as opposed to 2.815(2) Å for st-LCO. The change trend of the cell parameters are here in good agreement with the observations already reported in the literature for LCA with larger aluminum content[17,18,23,39]. Two additional weak peaks are observed at $2\Theta° = 36.5$ ° and $2\Theta = 43.1$ ° in all XRD patterns. These peaks correspond to the (220) and (311) peaks arising from remaining traces of spinel (*Fd3m* space group) cobalt-based oxide precursors, as expected from the use of the Li/(Co+Al) = 0.99 ratio in the precursors mixture.

Figure C6 shows the recorded ^{7}Li MAS NMR spectra for P1- and P2-LCA. Both are plotted and compared to that of undoped $LiCoO_2$ materials prepared with and without an excess of lithium carbonate designed as st-LCO (stoichiometric, Li/Co = 1.00) and overl-LCO (overlithiated, Li/Co = 1.05). As already reported, and widely commented upon in Part A, ^{7}Li MAS NMR is the key technique to probe the Li/Co stoichiometry in those materials[40,41]; in st-LCO, Li is present in a single diamagnetic environment as all cobalt ions are in low spin state (LS-Co^{3+}), leading to a single signal located at -0.4 ppm. On the other hand, several signals are observed for overl-LCO. Indeed, intermediate spin state paramagnetic (IS-Co^{3+}) cobalt ions are formed due to the presence of Li in the Co site associated with an O vacancy[40]. Due to the Fermi contact interaction, adjacent Li can exhibit negative or positive shifted signals (out of the narrow chemical shifts range of ^{7}Li), depending on its environment. Therefore, the spectrum of overl-LCO does exhibit a large number of more shifted signals in addition to the main signal at -0.4 ppm (**Figure C6**). Since the ^{7}Li MAS NMR spectra of the two 4% Al-doped LCA samples do not exhibit those extra signals, this confirms

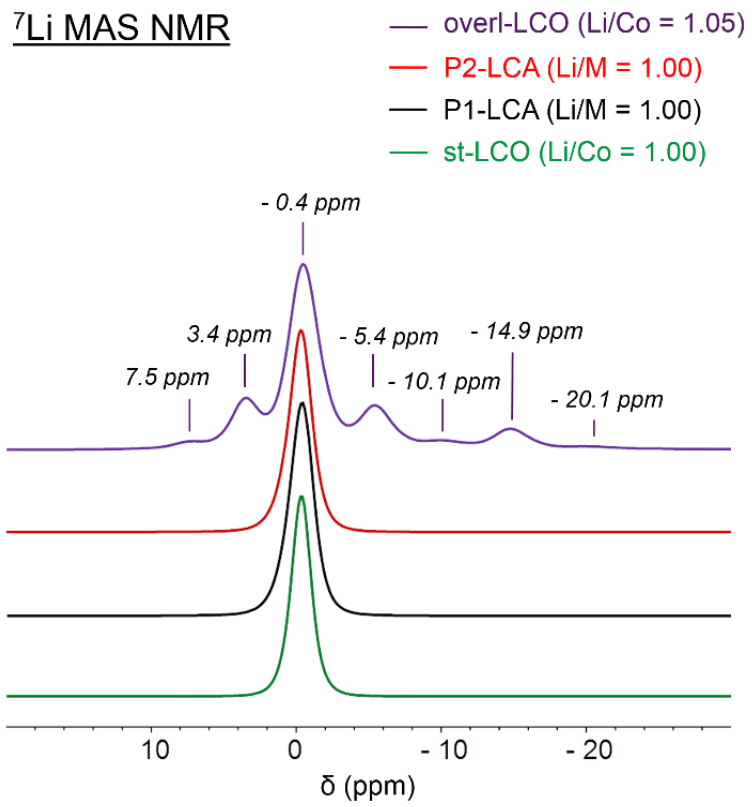

Figure C6. *^{7}Li MAS NMR spectra recorded at 116.66 MHz using a 30kHz spinning frequency of the P1-LCA and P2-LCA samples compared with the ones of undoped LCO samples prepared in the stoichiometric conditions (Li/Co = 1.00, st-LCO) or with an excess of Li-carbonate (Li/Co = 1.05, overl-LCO) used as references.*

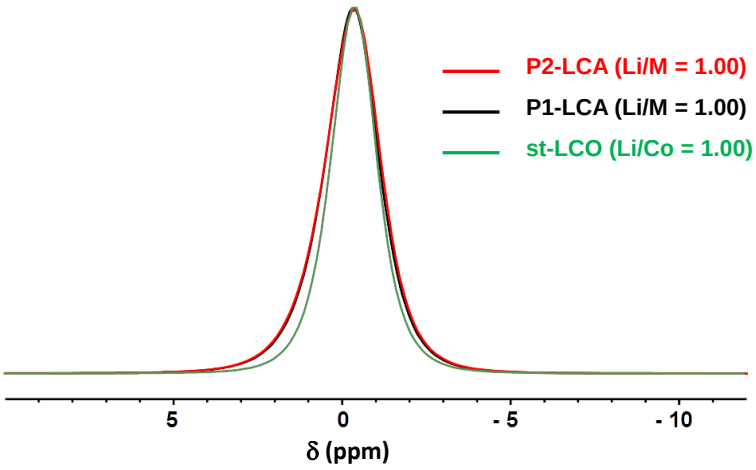

Figure C7. *Zoom on the ^{7}Li MAS NMR spectra recorded at 116.66 MHz using a 30kHz spinning frequency of the P1-LCA and P2-LCA samples compared with the ones of undoped LCO samples prepared in the stoichiometric conditions (Li/Co = 1.00, st-LCO).*

that these materials are really Li-stoichiometric and do not contain any paramagnetic species. These results are therefore in good agreement with the previous Li/(Co+Al) ratios measured by ICP. Moreover, long T_1 relaxation times, typical for diamagnetic materials, were observed (~5 s). Note that the ^{7}Li MAS signal of the two LCA samples is slightly broader than the one of st-LCO due to a distribution of Li environment versus Co/Al in the materials (**Figure C7**).

C.3.3 Homogeneity of Al-doping within P1- and P2-LCA

C.3.3.1 Results

To further investigate the homogeneity of Al distribution within P1- and P2-LCA – which could not be debated from laboratory XRD or ^{7}Li MAS NMR, SXRD patterns and ^{27}Al and ^{59}Co MAS NMR spectra were collected.

Figure C8.a gives a general view of the collected patterns for P1- and P2-LCA and first leads to the similar conclusions as laboratory XRD, i.e. pure layered phases crystallizing in the *R-3m* space group were obtained, with small traces of spinel precursor impurity. Diffraction peaks for Al-doped samples are also found broader and at different 2Θ positions than those of undoped st-LCO, as shown by the shifts of the (018) and (110) diffraction peaks which are mainly characteristics of the $c_{hex.}$ And a_{hex} parameters respectively (**Figure C8.c** and **C8.d**). This confirms the substitution of Co^{3+} with Al^{3+} in LCA samples which leads to a decrease of the $a_{hex.}$ parameter and an increase of the $c_{hex.}$ one. Note that **Figure C8.c** and **C8.d** were normalized to the overall peak area. An alternative plot of the data after normalization to the peak maxima is also provided in **Figure C9**. Moreover, strong additional peak asymmetries can clearly be observed for P1- and P2-LCA, while it does not exist for st-LCO. This asymmetry is found for any of the diffraction peaks collected within our 2Θ range, as shown by **Figure C8.b**; it varies with the (hkl) values of the diffraction lines. As shown by Gaudin et al.[23] for the $Li(Co_{1-y}Al_y)O_2$ solid solution prepared by a precipitation route, the $c_{hex.}$ increases of 1% in the overall composition range ($0 \leq y \leq 1$) whereas the $a_{hex.}$ parameter decreases of 0.5% (see **Figure C10**). As shown in **Figure C8.b**, the asymmetry of the (10l) lines is observed towards smaller 2θ angles for LCA samples, since the variation of c_{hex} is predominating. On the other hand, as the (110) line is only affected by the $a_{hex.}$ parameter, the asymmetry is observed toward higher angles (**Figure C8.d**).

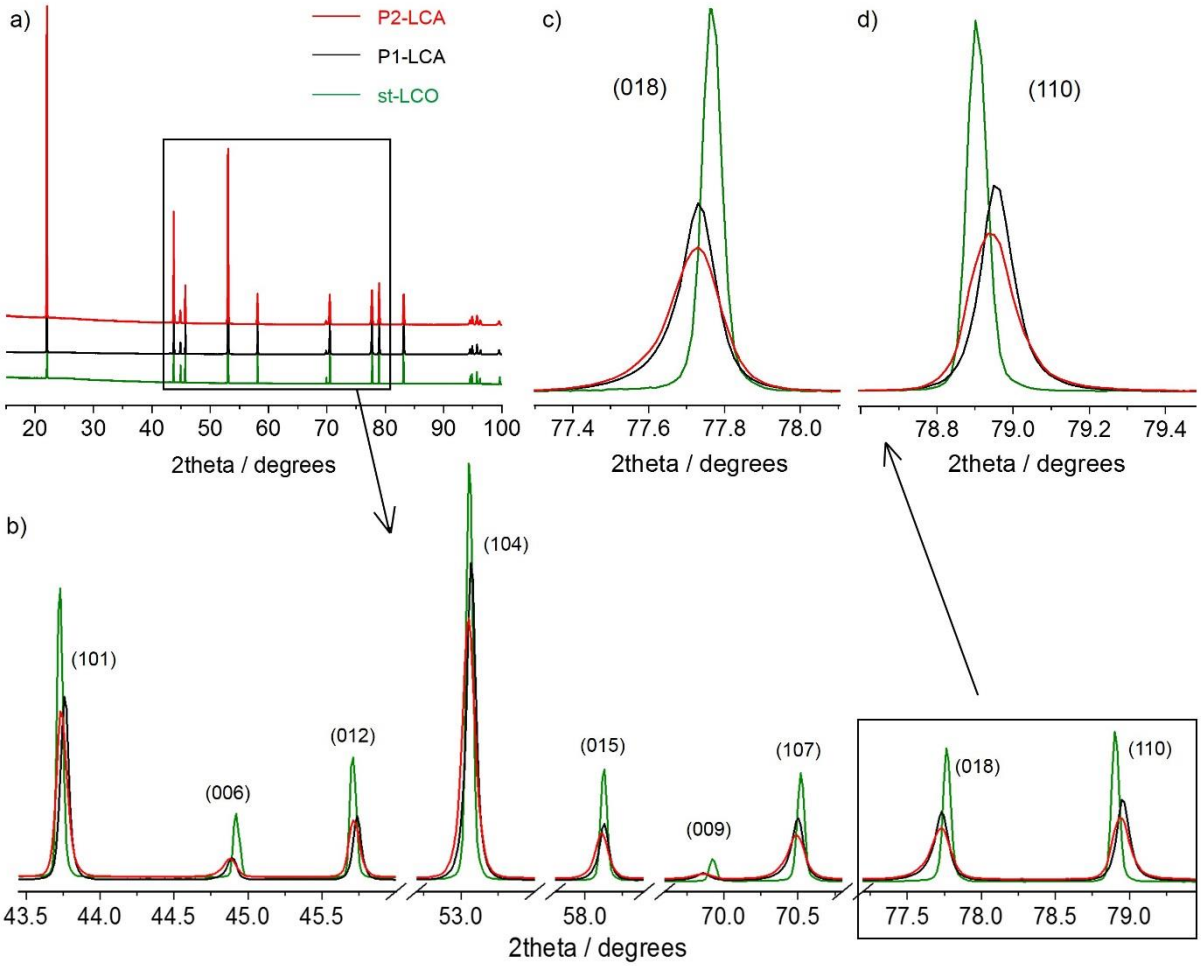

Figure C8. a) *Synchrotron X-ray diffraction (SXRD) patterns obtained for P1- and P2-LCA, as compared to undoped $LiCoO_2$ (st-LCO). All patterns were collected for λ = 0.826 Å, but are converted here to $\lambda(Co_{Ka1})$ = 1.790 Å for better comparison with all XRD patterns showed in Figure C7. Zooms on several lines is shown in b) and a larger zoom in (0 1 8) and (1 1 0) peaks is provided in* ***c)*** *and* ***d)****.*

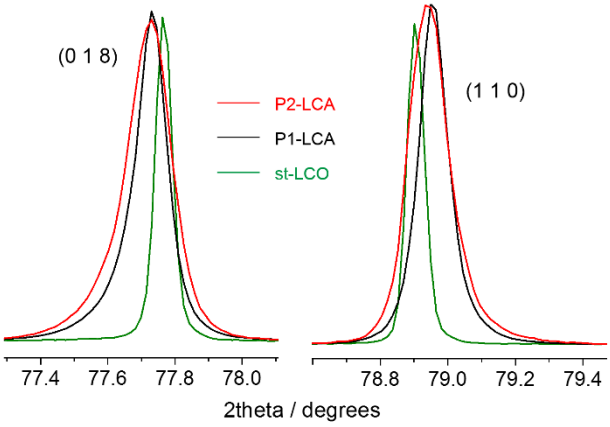

Figure C9. *Zoom on the (0 1 8) and (1 1 0) SXRD peaks normalized to the (1 1 0) peak maximum, as opposed to Figure C10.b and C10.c in which the data was normalized to the peak areas.*

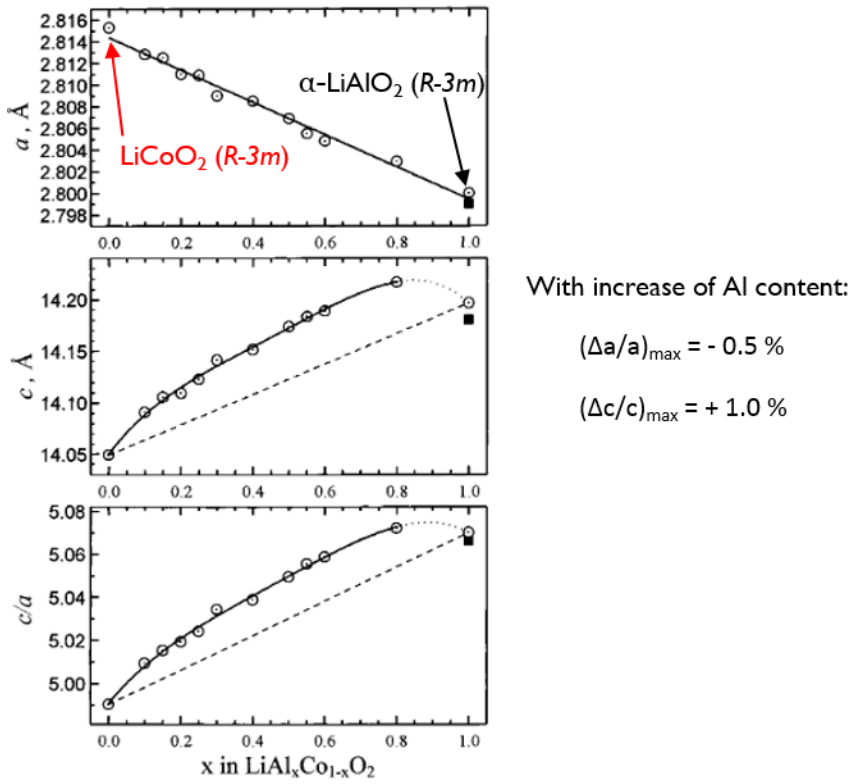

Figure C10. *Evolution of cell parameters reported by Gaudin et al.*[23] *for the* $LiCo_{1-x}Al_xO_2$ *(0 < x < 1) solid solutions.*

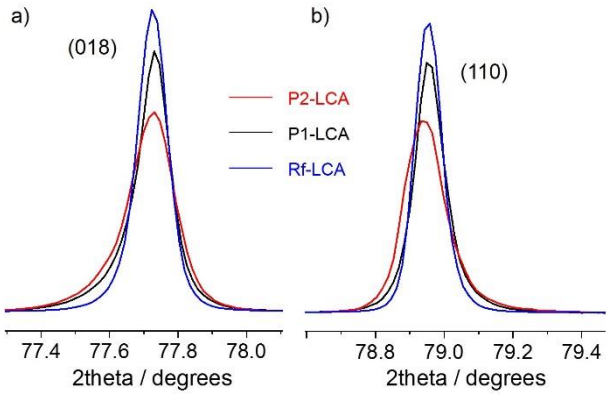

Figure C11. a) *Zoom on the a) (0 1 8) and b) (1 1 0) SXRD peaks for P1- and P2-LCA normalized to the peak areas, as compared to the reference sample prepared from co-precipitation (Rf-LCA).*

This may be more easily distinguished in **Figure C9**. This asymmetry is further evidence of the presence of a distribution of Al concentration in the particles of the two LCA samples. Nevertheless, P2-LCA shows slightly more asymmetry than P1-LCA, suggesting that an even less homogeneous distribution of Al is achieved for P2-LCA. In **Figure C8.d**, the (110) peak for P2-LCA also exhibits a shoulder centered at the (110) peak position of the undoped st-LCO, implying that domains without Al within P2-LCA do exist (their contribution better seen for this diffraction line). In **Figure C11**, the shape of the (110) and (018) diffraction lines of P1-LCA and P2-LCA is compared to the one of Rf-LCA sample prepared by precipitation route, known to yield a more homogenous doping[23,25,42]: as expected, lines for Rf-LCA are symmetrical due to a homogeneous Al/Co cation mixing. Therefore, these SXRD results first suggest that i) in our solid state synthesis conditions, heterogeneous Al distribution was observed and ii) the final Al distribution is dependent on the Co- and Al-based oxide precursor type (with or without a 1000°C heat treatment).

^{27}Al MAS NMR was additionally used to probe the different Al environments distribution in the LCA materials at a local scale. Complete spectrum included spinning sidebands manifold can be found in **Figure C12**. A zoom on the central transitions is shown in **Figure C13.** As shown in **Figure C13.a**, the P2-LCA compound clearly exhibits seven signals. They can be assigned to the different Al environments versus second Co neighbors in the transition metal (TM) layer, as already reported by Gaudin et al[23] for $Li(Co_{1-y}Al_y)O_2$ samples prepared by a precipitation route (see **Figure C14**). The signal located around ~ 62 ppm is assigned to Al surrounded only by LS-Co^{3+} ions as second neighbors denoted as Al-(Al_0Co_6). Note that this signal exhibits a clear second order quadrupolar lineshape that was fitted using DMFit[43] (see **Figure C15**) leading to δ_{iso} = 64.7 ppm, ν_Q = 386 kHz and η = 0.15 as parameters. The set of other signals located equally spaced by 7-8 ppm, located at ~ 55, ~ 48, ~ 40, ~ 33, ~ 26, ~ 18 ppm are assigned to Al surrounded by n Al^{3+} and (6-n) Co^{3+} as second neighbors with n varying respectively from 0 to 6, denoted Al-(Al_nCo_{6-n}).

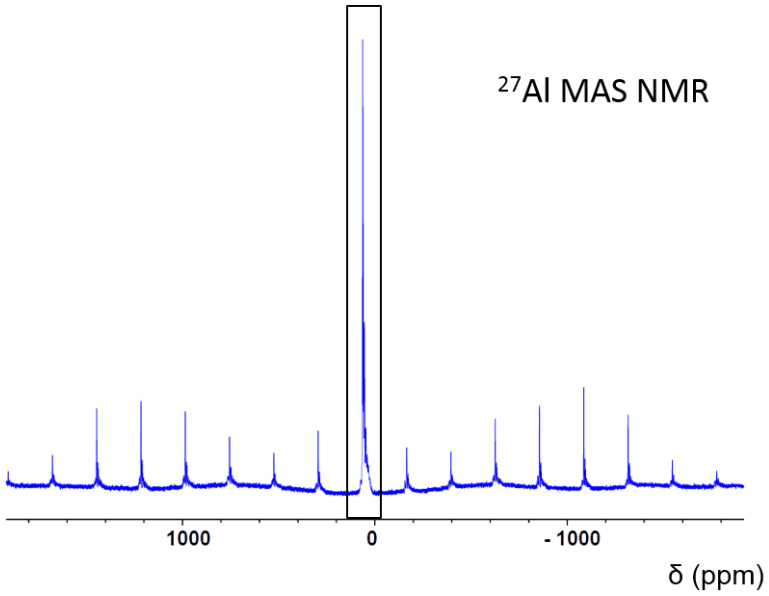

Figure C12. *Typical entire spectra recorded for ^{27}Al MAS NMR for the P2-LCA sample. The zone of the isotropic signals is surrounded by a rectangle and plotted in Figure C13, all other signals are spinning side bands.*

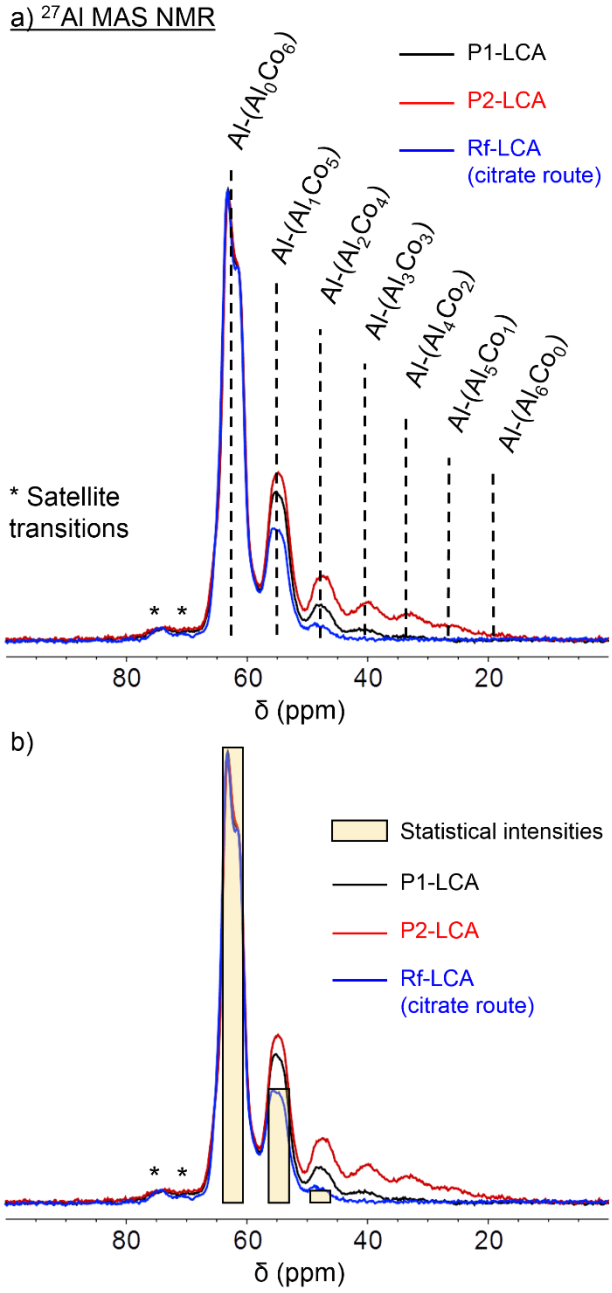

Figure C13. a) *^{27}Al MAS NMR spectra recorded at 130.33 MHz using a 30 kHz spinning frequency of the P1-LCA and P2-LCA samples compared with the one recorded for a 4% Al doped LCA samples prepared by a citrate route used as reference and* ***b)*** *comparison with the theoretical intensity distribution of the different Al environments versus Co, expected for a 4% Al-doped sample.*

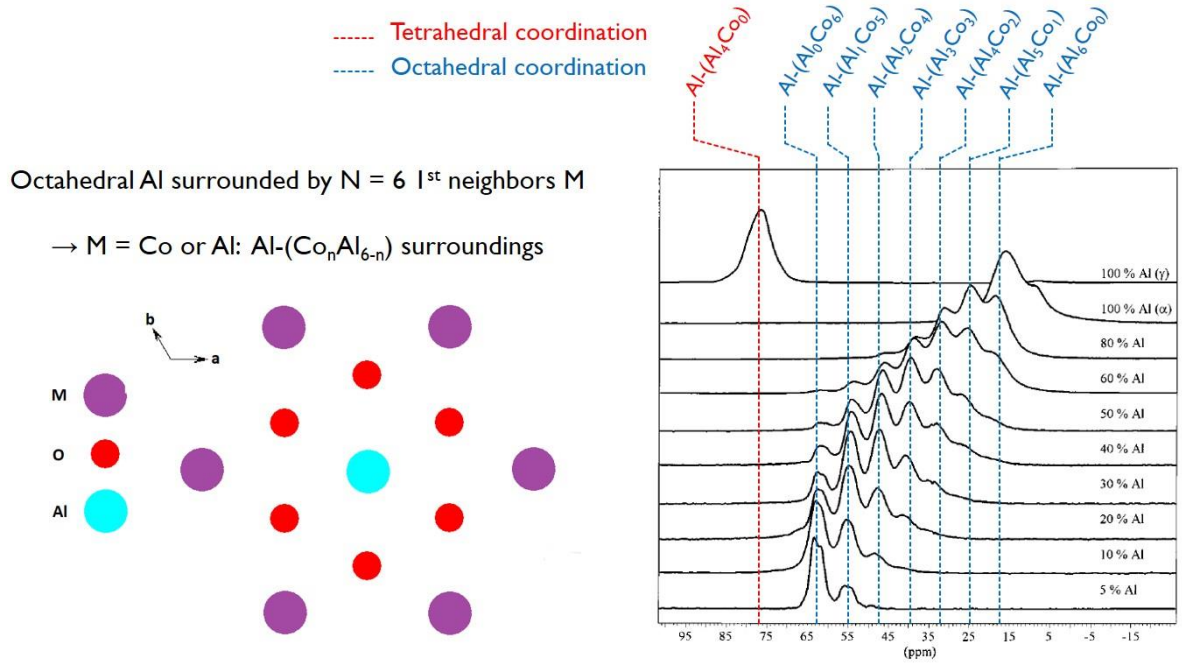

Figure C14. *Schematic representation of Al surroundings in $LiCo_{1-x}Al_xO_2$ in the (a, b) plane and associated ^{27}Al NMR spectra evidenced by Gaudin et al[23].*

Those signals do not exhibit a clear second order lineshape anymore due to a distribution of possible local configurations for each Al-(Al_nCo_{6-n}) ($0 \leq n \leq 6$) environment. Small signals located around 69 and 73 ppm are satellite transitions expected for the main signal arising from Al-(Al_0Co_6) environments. Satellites transitions of the other signals are probably overlapping their neighboring signal on the left, preventing a highly precise quantitative analysis. Nevertheless, we computed the probability P for a composition y = 0.04 and (6-n) cobalt atoms as second neighbors using a binomial law:

$$P(y, 6-n) = C_6^{6-n} y^n (1-y)^{6-n}$$

The resulting theoretical intensity distribution is schematically depicted by the grey rectangles in **Figure C13.b**. For such a low Al-doping amount, negligible signal intensity is expected for Al-(Al_3Co_3) environments and for Al-richer ones (n > 3). Therefore, the two LCA prepared by solid-

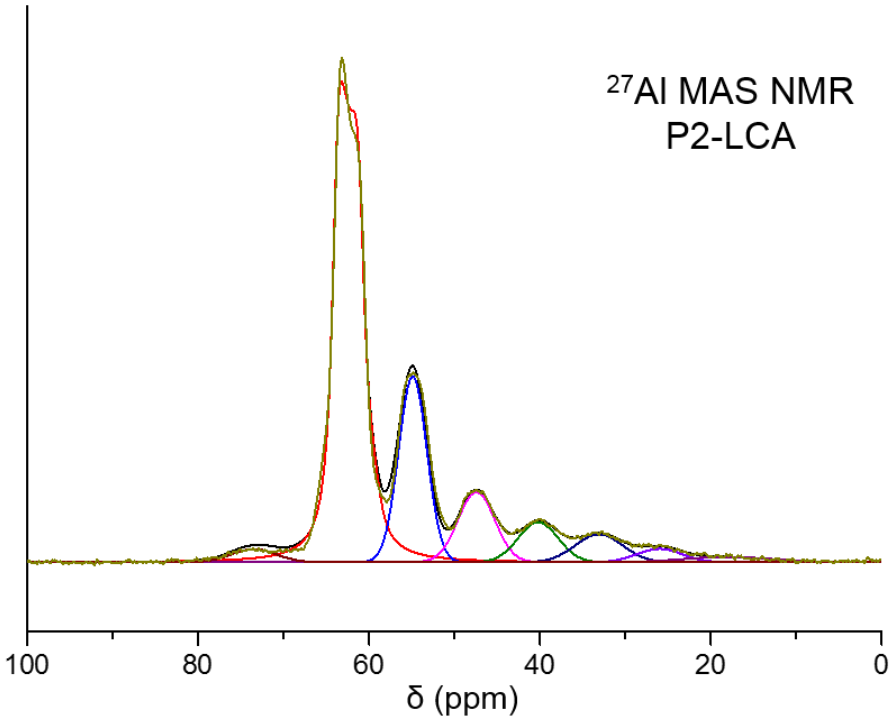

Signals	Position (ppm)	Intensity %	vQ (kHz)	η
Al-(Al_0Co_6)	64.7	83.31	386	0.15
Al-(Al_1Co_5)	54.9	8.72	-	-
Al-(Al_2Co_4)	47.4	3.29	-	-
Al-(Al_3Co_3)	40.2	1.84	-	-
Al-(Al_4Co_2)	33.1	1.31	-	-
Al-(Al_5Co_1)	26.0	0.64	-	-
Al-(Al_6Co_0)	18.2	0.26	-	-
(satellites)	73.5	0.63	-	-

Figure C15. *Typical fit of a ^{27}Al MAS NMR spectrum, here, P2-LCA, performed using DMFit[43].*

state route do not exactly follow this trend, confirming inhomogeneity in the Al-distribution within the samples suspected from SXRD. We also compared these materials to the 4% Al-doped $LiCoO_2$ material obtained from a citrate precursor route (Rf-LCA). Signals assigned to Al-rich

environments are less intense for the latter than those of P1- and P2-LCA, and closely follows the intensity distribution theoretically expected. Therefore, this result confirms the homogeneity of Al distribution for LCA prepared by the citrate route while infirming it for P1- and P2-LCA. Nevertheless, the departure from the ideal Al distribution is larger for P2-LCA than for P1-LCA in good agreement with the SXRD results.

^{59}Co MAS NMR was reciprocally used to characterize the Co local environments in the materials. This is the first report of ^{59}Co MAS NMR study of Al-doped $LiCoO_2$ samples. The complete spectrum of P2-LCA included spinning sidebands manifold can be found in **Figure C16**. **Figure C17** shows the spectra recorded for P1- and P2-LCA compared with those of undoped stoichiometric $LiCoO_2$ (st-LCO) and 4% doped via the citrate route (Rf-LCA). The MAS spectra are observed to break into spinning side bands and the resolution is good enough to evidence different signals. For st-LCO, a single resonance is observed at 14132 ppm in agreement with Siegel *et al*.[44] and is assigned to the single octahedral LS-Co^{3+} site in the material. In the Al-doped

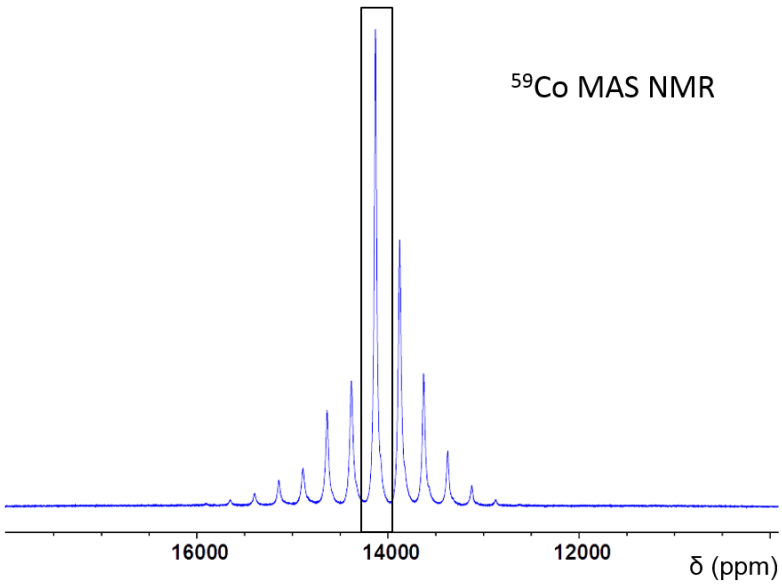

Figure C16. *Typical entire spectra recorded for ^{59}Co MAS NMR for the P2-LCA sample. The zone of the isotropic signals is surrounded by a rectangle, all other signals are spinning side bands.*

samples, a set of other as broad signals are observed located at 14105, 14077, 14047, and 14021 ppm, respectively attributed to Co with various 2nd (Al_nCo_{6-n}) neighbor environments as given in **Figure C17**. Here, no signal is observed for Co environments with more than 4 Al surroundings. Despite broader signals than those observed for ^{27}Al MAS NMR, distinct signals can be resolved and more homogeneous samples exhibit weaker signal broadening. Indeed, the ^{59}Co NMR chemical shift range is very large and the shift position is very sensitive to the local environments (distances, angles). For example, a signal was observed at 14115 ppm in O3-$LiCoO_2$ by Siegel *et al.*[44] and at 14722 ppm in O3-$NaCoO_2$[45]. An inhomogeneous Al-doping in $LiCoO_2$ thus generates a larger distribution of distances and angles, leading to a broadening of the lines.

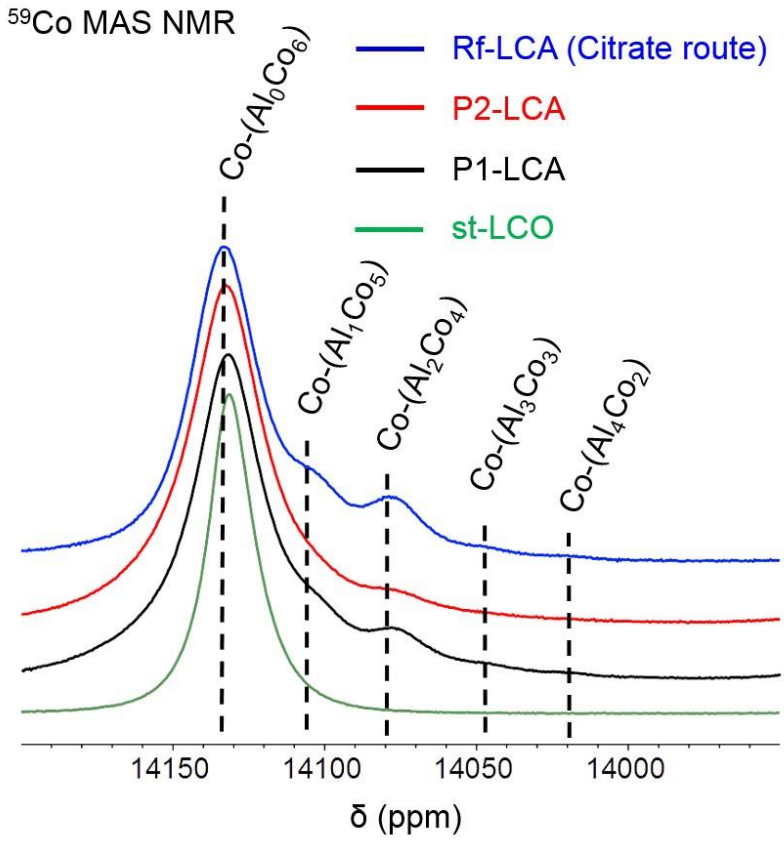

Figure C17. *^{59}Co MAS NMR spectra recorded at 120.35 MHz using a 30 kHz spinning frequency of the P1-LCA and P2-LCA samples compared with the ones recorded for undoped st-LCO and a 4% Al doped LCA samples prepared by a citrate route used as references.*

C.3.3.2 Discussion

SXRD, ^{27}Al and ^{59}Co MAS NMR all lead to the same conclusions. Our solid state synthesis route, even performed at relatively high temperature (980°C) with either a Al_2O_3 precursor mixed with Co_3O_4 (Precursor 1) or with a pre-heat treatment of this precursor at 1000°C (Precursor 2), do not allow to prepare materials as homogeneous as the one prepared by the citrate route. A small gradient in composition is remaining in the P1- and P2-LCA samples. Nevertheless, the Al-doping of LCO was effective, since no signal of remaining Al_2O_3 is observed by ^{27}Al MAS NMR. While we initially thought that a pre-heat treatment of the Al and Co precursor might help to get homogeneous LCA samples, the opposite effect is though observed, P2-LCA sample shows even more inhomogeneity of Al distribution than P1-LCA. These differences may arise from several causes. The formation of segregated cobalt aluminate domains for Precursor 2 most likely leads to further heterogeneous Al distribution in the final P2-LCA phase, though we could not collect data to verify it. A preferential reaction between Li_2CO_3 and γ-Al_2O_3 may also be a little more favorable for the final Al distribution within P1-LCA. The particle size may also have played a role, as homogenization processes may be harder in the bigger particles of Precursor 2 as opposed to Precursor 1 during the formation of the associated LCA. Even though no clear conclusions on the precursors can be drawn, differences of Al distribution were still evidenced in both resulting LCA prepared from solid state synthesis thanks to the remarkable resolutions of SXRD and ^{27}Al MAS NMR.

C.3.4 Consequences on the 1st cycle curves of LCA//Li cells

In the case of LCA powders, it seems reasonable to expect differences in the electrochemical profiles depending on the homogeneity of the Al distribution within the samples. **Figure C18.a** shows the 1st cycle between 3.0 and 5.0 V for coin cells with either st-LCO, P1-LCA, P2-LCA and Rf-LCA as positive electrodes. Typical features characteristic of stoichiometric $LiCoO_2$ (st-LCO) are clearly seen: i) the voltage jump corresponding to the O3 ↔ O'3 monoclinic transition resulting from the formation of a Li-vacancy ordering at x = 0.5, (**Figure C18.b** and **Figure C18.c)**; ii) the formation of the H1-3 phase around x ≈ 0.17, also revealed by a clear change of slope. The homogeneously Al-doped material Rf-LCA shows none of the above, as revealed by the overall sloppy profile of the electrochemical curve. In particular, the O3 ↔ O'3 monoclinic transition does not occur (**Figure C18.c)**. Note that in the case of LCO, even a very little excess of Li found in the Co layers hinders the Li-vacancy ordering at x = 0.5[40,41]. The occurrence of this transition is thus extremely sensible to the local perturbations within LCO-type materials. Since we controlled the initial Li/(Co+Al) ratios in this study, only the presence of homogeneously distributed Al^{3+} in substitution of some Co^{3+} can explain the absence of the O3 ↔ O'3 monoclinic transition. As a matter of fact, this could then be considered a first indirect tool to probe the dopants repartition within the doped LCO, when an accurate control of the Li/(Co+Al) = 1.00 is achieved. For both P1 and P2-LCA, this O3 ↔ O'3 monoclinic transition occurs – as clearly evidenced by the small change of slope in the near x = 0.5 region (**Figure C18.b)** and in the derivative dx/dV curve (**Figure C18.c)**. One can assume the coexistence of un-doped and Al doped domains due to the inhomogeneous distribution of Al ions to explain this behavior. This supports the previous conclusions obtained from SXRD and MAS NMR, i.e. that non homogeneous Al-doping was

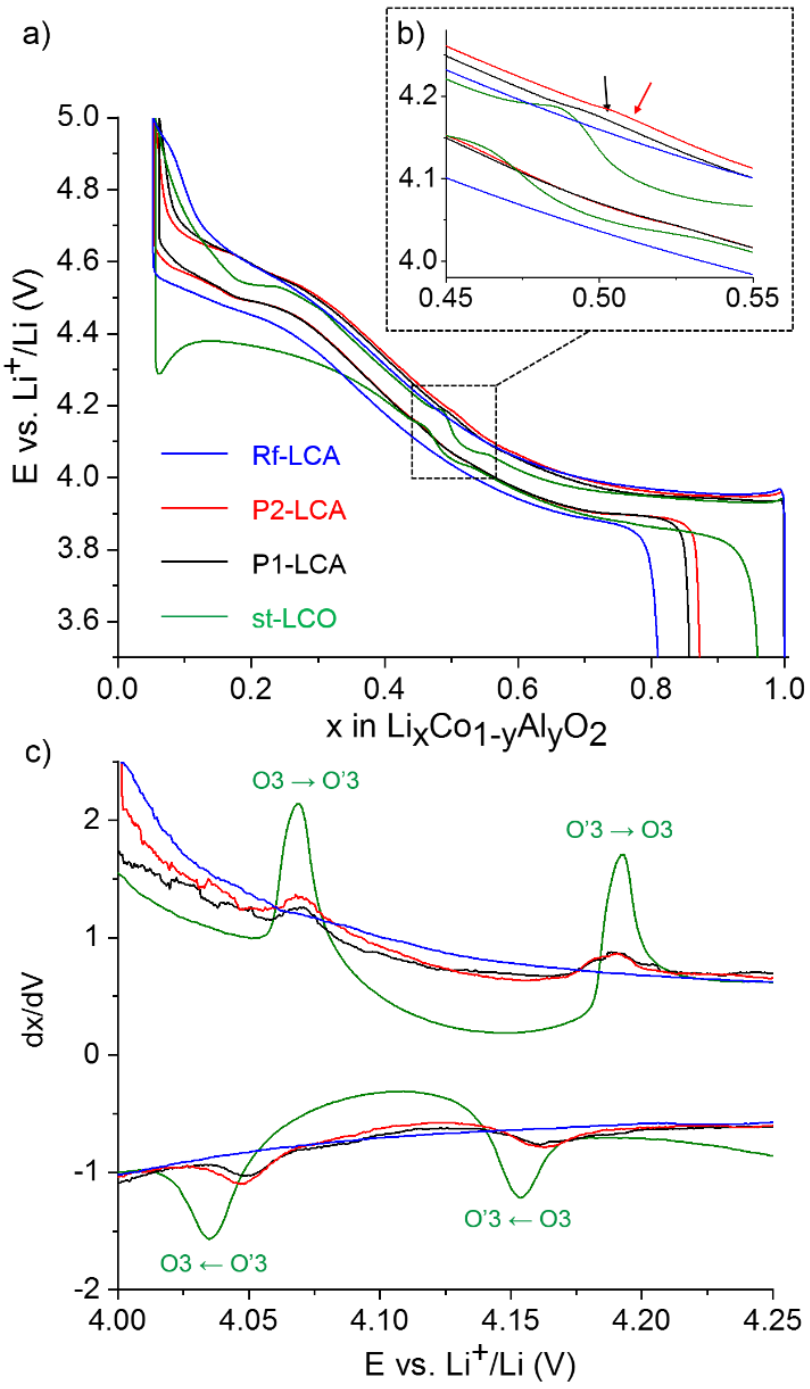

Figure C18. a) *1st cycle for P1-LCA (in black) and P2-LCA (in red) at C/20 as positive electrode in Li//LCA cells, as compared to those of the reference LCA prepared from a co-precipitation route (Rf-LCA) and undoped LCO (st-LCO). A zoom corresponding to the O3 ↔ O'3 transition is given in* ***b)****. Associated dx/dV curves for 4.00 – 4.25 V window are plotted in* ***c)****.*

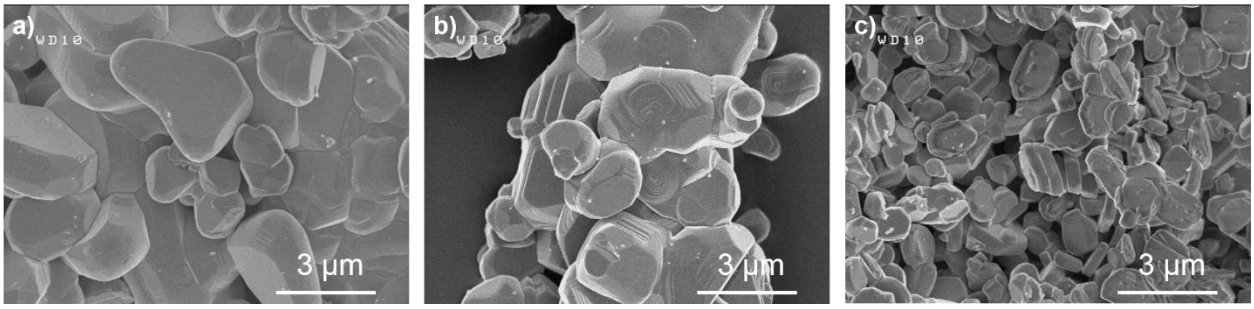

Figure C19. *SEM micrographs of the powders of* ***a)*** *P1-LCA,* ***b)*** *P2-LCA and* ***c)*** *Rf-LCA.*

achieved by our solid state synthesis of LCA. It is though impossible to discriminate between P1- and P2-LCA respective performances after one cycle. Note that the polarization at high voltage, in discharge, is substantial for st-LCO compared to any other LCA. However, aluminum content itself cannot strictly explain this improvement: other parameters such as the difference in particle size observed in **Figure C19** may also play a role. Nonetheless, this polarization makes it hard to discuss the existence, or not, of the H1-3 phase itself for LCA samples, especially for Rf-LCA. Weak changes of slope can still be observed in the high voltage region for all LCA, mainly evidenced during the discharge. Additionally, all Al-doped LCO show higher irreversible capacity vs undoped $LiCoO_2$, following previous conclusions[18].

C.3.5 Conclusions on the preparation of LCA from the solid state reaction of stoichiometric amounts of Li_2CO_3 and Co/Al-based oxide(s)

In this first section of Part C, we succeeded in preparing Al-doped LCO (LCA) powders with low Al content (4%) and well controlled Li/(Co+Al) stoichiometries (≤ 1.00) from solid state reaction of (Co_3O_4, Al_2O_3) and Li_2CO_3 in stoichiometric proportions. We established a reliable protocol to characterize the Al distribution within these LCA powders at different scales through the combined use of synchrotron XRD with ^{27}Al and ^{59}Co MAS NMR. Although both samples investigated in this section showed poor homogeneity of Al doping, this is still a first encouraging step towards the preparation of LCA powders from a solid state route.

Doping the Co_3O_4 spinel precursor by reacting it with Al_2O_3 may be avoided, as it most likely leads to an inhomogeneous mixture of Co_3O_4 and $Co_{3-z}Al_zO_4$ as precursor, eventually reflecting in the final $LiCo_{0.96}Al_{0.04}O_2$ powder. Using Li_2CO_3 with an unreacted mixture of Co_3O_4 and Al_2O_3 in stoichiometric proportions instead does not lead to a homogeneous Al doping for the resulting LCA powder either – though the distribution of Al appears to be slightly more homogeneous in this case.

The comparison of the electrochemical performance of both LCA powders with a reference LCA sample prepared from co-precipitation route confirmed the inhomogeneity of Al doping, as typical features (such as the O3 ↔ O'3 transition) obtained for un-doped LCO were still distinguished for the former. Nonetheless, higher irreversible capacity was achieved at the outcome of the 1st cycle for all LCA as compared to undoped LCO, confirming previous findings from Myung *et al.*[18]. As we carefully controlled the Li/(Co+Al) stoichiometries of all LCA powders through ^{7}Li MAS NMR, the possible contribution of Li excess to the increase of capacity losses at cycle n°1 is discarded.

C.4. Approach n°2: preparation of $LiCo_{0.96}Al_{0.04}O_2$ powders from solid state reaction of Li_2CO_3 and $[(Co_3O_4)_{0.32}(Al_2O_3)_{0.02}]$ in non-stoichiometric proportions

Two series of LCA samples were prepared varying the initial amount for lithium carbonate. The main difference resides here in the control of particle size. In the following, Group A samples gather LCA powders synthesized without any specific control of morphology and particle size. On the other hand, Group B samples refer to LCA powders with 40 µm-sized spherical particles. Results for each one of this group are respectively presented in Section C.4.1 and C.4.2. Electrochemical properties for both groups of samples will be commented in Section C.4.3. A global discussion regarding Approach n°2 will be performed in Section C.4.4.

C.4.1. LCA Samples without control of particle size (Group A)

C.4.1.1. Description of synthesis

A schematic figure summarizing all steps of the synthesis can also be found in ***Figure C20.***

Group A samples were prepared in three different steps. In step 1, a 2kg-mixture of Co_3O_4 (Umicore) and Al_2O_3 (Umicore) in the ratio Co/Al = 0.96/0.04 was intimately blended and heat treated at T = 1000 °C for 10 hours under air flow. This precursor is equivalent to Precursor 2 in the previous section. Note that this synthesis was carried out before concluding that a heat treatment of Co_3O_4 and Al_2O_3 to form a mix-$Co_{3-z}Al_zO_4$ was unfavorable from the results shown in section C.3.

The final Al-doped Co_3O_4 was subsequently used in addition of Li_2CO_3 (total mass ~ 220g) during Step 2 to form the LCA powders. Four different samples were prepared from this mixture heat treated at T = 1000 °C for 10 hours under air flow, depending on the final $(Li/M)_1$ ratio targeted for the LCA powders (M = (Co+Al)): $(Li/M)_1$ = 1.00, 1.02, 1.04 or 1.06. Therefore, at the outcome of Step 2, all samples were named "LCA-X" with X = 1.00, 1.02, 1.04 or 1.06 depending on their

respective $(Li/M)_1$ ratios. As we showed in Part A that remaining Li excess in the powders lead to increased irreversible capacity losses when they are used in Li-cells (in good agreement with previous findings[41,46,47]), a Li-adjustment step (Step 3) was carried out to recover stoichiometric samples. To do so, the Co- and Al-based oxide precursor used in Step 1 (mix-$Co_{3-z}Al_zO_4$) was added. Mixtures of LCA-X (~100g) and required amounts of mix-$Co_{3-z}Al_zO_4$ were heat treated for 10 hours at T = 980 °C under air flow to reach a final $(Li/M)_2 \approx 1.00$. A target $(Li/M)_2$ composition slightly lower than 1.00 was used in order to get stoichiometric LCA samples even if small amounts of Co and Al precursors might persist. The four final Li-adjusted samples were named "Adj-LCA-X" with X = 1.00, 1.02, 1.04 or 1.06. Note that pulverization using a grinder and sieving were systematically performed between each steps.

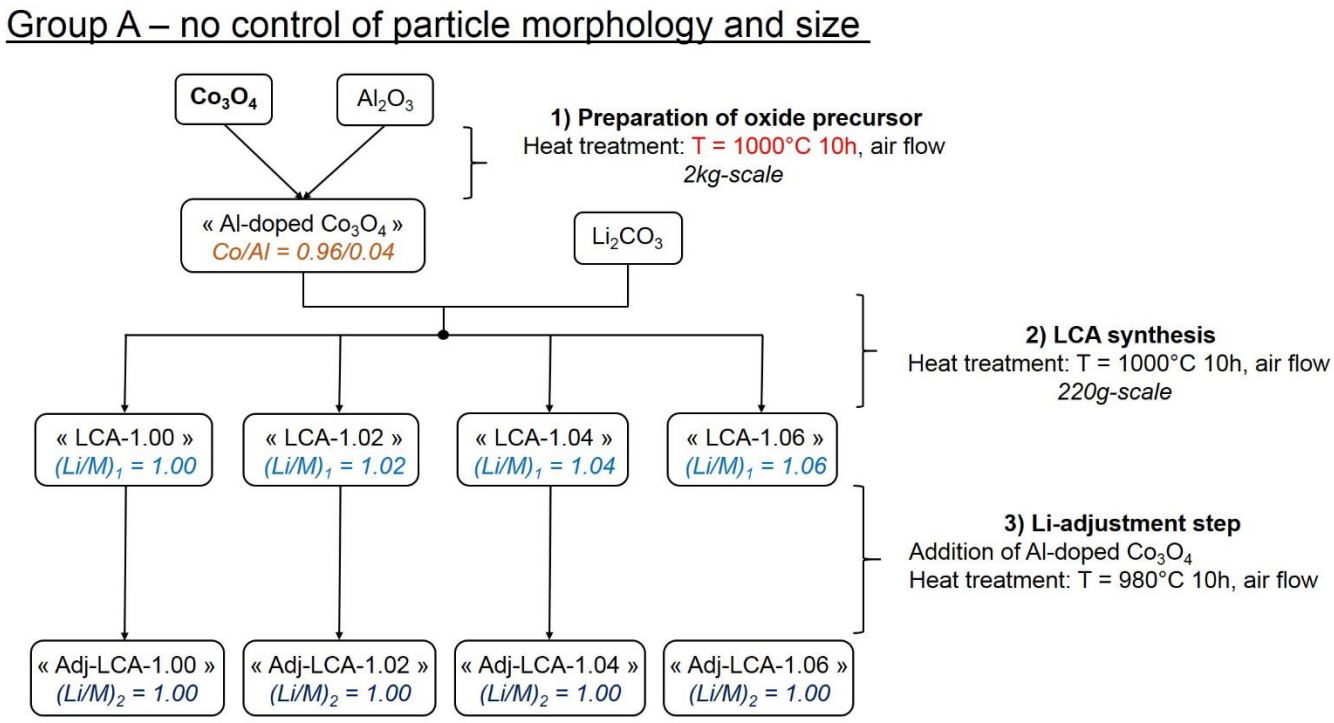

Figure C20. *Summarizing schematic representation of synthetic routes for Group A powders (Approach n°2).*

C.4.1.2. Results

C.4.1.2.1. General characterization

Table C.T2 gives the Li and Al contents for all LCA powders before and after adjustment of the Li-stoichiometry measured by ICP. After addition of Li_2CO_3 and subsequent heat treatment in Step 2, all final ratios measured for "LCA-X" powders (X = 1.00, 1.02, 1.04, or 1.06) show good agreement with the initial targeted $(Li/M)_1$: values of 0.995, 1.017, 1.035 and 1.049 are respectively obtained for samples respectively prepared with (Li/M) = 1.00, 1.02, 1.04 and 1.06. As the outcome of the Step 3, all final (Li/M) drop below 1.00, with $(Li/M)_2$ = 0.992 or 0.998 for all "Adj-LCA-X" samples (X = 1.00, 1.02, 1.04, or 1.06), suggesting that all samples should be Li-stoichiometric with possible traces of spinel precursor impurity.

Sample	$(Li/M)_1$ (Before Li-adjustment)	$(Li/M)_2$ (After Li-adjustment)	Al/M
LCA-1.00	*0.995*	*0.992*	*0.0400*
LCA-1.02	*1.017*	*0.998*	*0.0402*
LCA-1.04	*1.035*	*0.998*	*0.0402*
LCA-1.06	*1.049*	*0.998*	*0.0401*

Table C.T2. *Measured ICP ratios for Group A powders, before $(Li/M)_1$ and after Li-adjustment $(Li/M)_2$ and Al/M.*

Complementary ^{7}Li MAS NMR measurements were performed on the four Li-adjusted Adj-LCA-X and one non adjusted sample (LCA-1.04). A comparison of ^{7}Li MAS NMR spectra for LCA-1.04 and Adj-LCA-1.04 is therefore presented in **Figure C21.a**, while spectra for all adjusted Adj-LCA-X are plotted in **Figure C21.b**. In **Figure C.21.a**, a set of signals at 7.5; 3.4; -5.4; -10.1, -14.9 and -20.1 ppm is found in addition to the main contribution observed

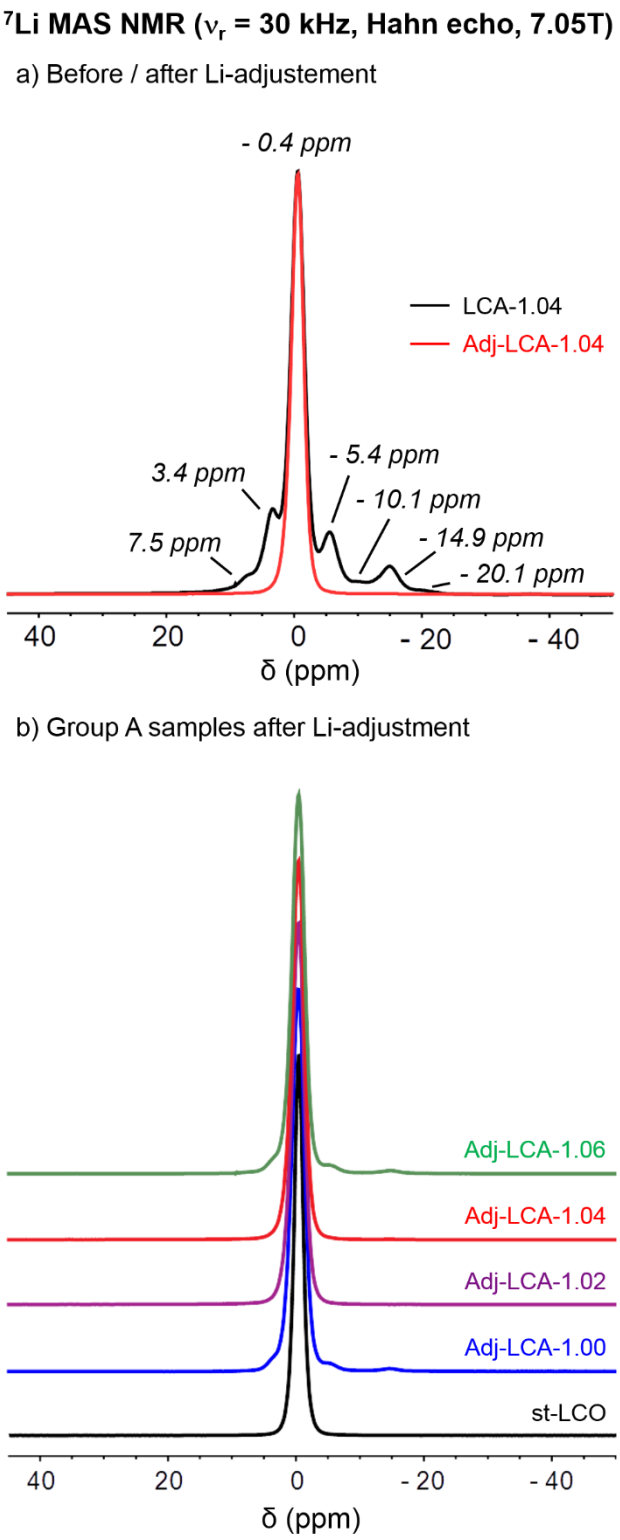

Figure C21. *^{7}Li MAS NMR spectra recorded at 116.66 MHz using a 30 kHz spinning frequency of a) LCA-1.04 and Adj-LCA-1.04; b) all Li-adjusted samples from Group A, compared with the one of undoped LCO sample prepared in the stoichiometric conditions (Li/Co = 1.00, st-LCO).*

at - 0.4 ppm for LCA-1.04, revealing the presence of paramagnetic IS-Co^{3+} due to remaining Li excess in the layers, similarly reported[40,41,46] for overlithiated LCO. Note that the chemical nature of this intermediate overlithiated phase will be discussed in section C.4.3.

Figure C21.b reveals that the Li-adjustment step (Step 3) was successfully performed for all Adj-LCA-X. Indeed, Adj-LCA-1.02 and Adj-LCA-1.04 are clearly Li-stoichiometric, as revealed by the single contribution observed at -0.4 ppm in their spectra, and only a negligible amount of the additional signals at -14.9, -3.4 and -5.4 ppm is found in the spectra of Adj-LCA-1.00 and Adj-LCA-1.06.

Figure C22 shows the scanning electron micrographs for the LCA samples before Li-adjustment, while scanning electron micrographs for LCA after Li-adjustment (Adj-LCA) are given in **Figure C23**. The average particle size exhibited by all samples increases with the initial $(Li/M)_1$ ratio, ranging from ~ 1 µm for Adj-LCA-1.00 ($(Li/M)_1$ = 1.00) to ~ 15 - 20 µm for Adj-LCA-1.06 ($(Li/M)_1$ = 1.06). Particles of Adj-LCA-1.04 and Adj-LCA-1.06 show intermediate average diameters, with respective values of ~ 3 – 6 µm and ~ 10 – 15 µm. This was expected as the beneficial flux role of melted Li_2CO_3 on the crystalline growth of LCO during the synthesis was already reported[48–50]. A population of < 1 µm particles can additionally be observed for the two samples prepared with the highest initial $(Li/M)_1$ (1.04 or 1.06). This second population of particles is not observed on the micrographs for non Li-adjusted samples provided in **Figure C22**. Thus, this smaller-sized population corresponds to LCA formed during the Li-adjustment step from the reaction between Li excess and the spinel precursor. A similar population most likely exists for Adj-LCA-1.02, but is harder to distinguish as the difference of particle size between the two populations is much less pronounced. Note that it is not expected for Adj-LCA-1.00, since no

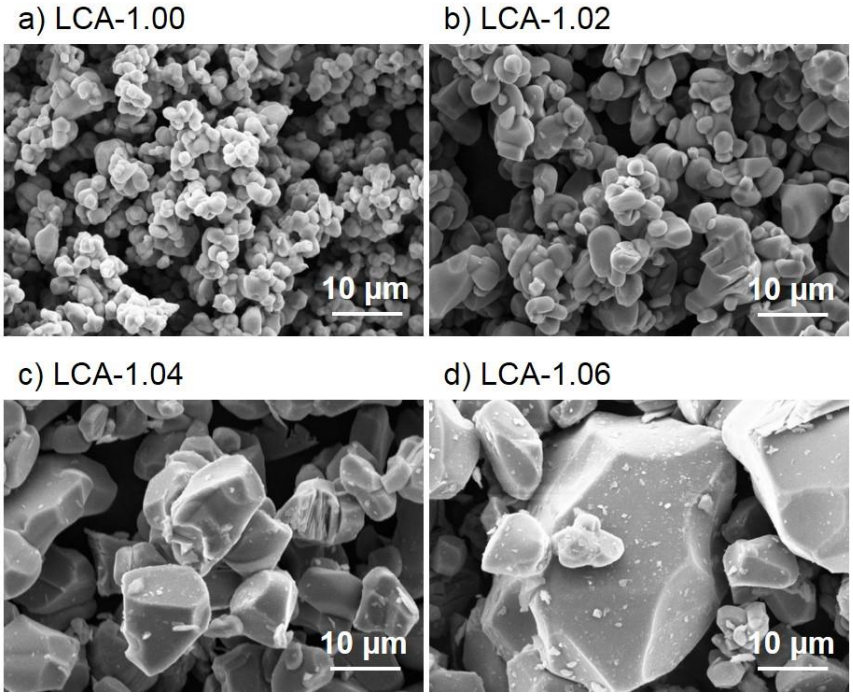

Figure C22. *SEM micrographs of the non Li-adjusted powders from group A:* ***a)*** *LCA-1.00,* ***b)*** *LCA-1.02,* ***c)*** *LCA-1.04, and* ***d)*** *LCA-1.06.*

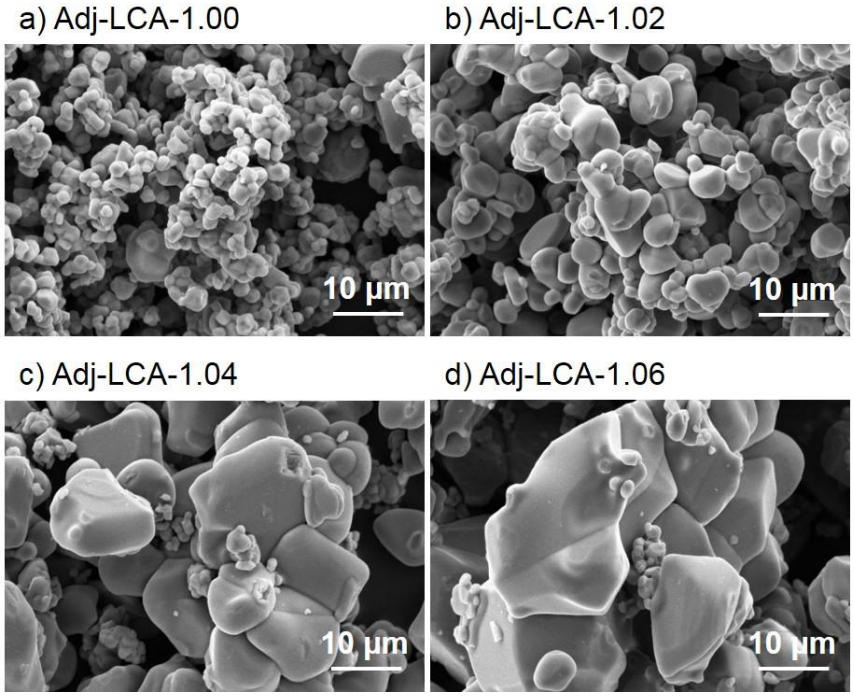

Figure C23. *SEM micrographs of the Li-adjusted powders from group A:* ***a)*** *Adj-LCA-1.00,* ***b)*** *Adj-LCA-1.02,* ***c)*** *Adj-LCA-1.04, and* ***d)*** *Adj-LCA-1.06.*

mix-$Co_{3-z}Al_zO_4$ was added during the final "Li-adjustment" step, as $(Li/M)_1$ was already below 1.00 ($(Li/M)_1$ = 0.995 for LCA-1.00) – even though the sample was nevertheless heat treated in the same conditions as its analogues with higher initial $(Li/M)_1$ for more consistency.

Synchrotron X-ray diffraction (SXRD) patterns of Li-adjusted LCA only are plotted in **Figure C24.** They confirm that all Adj-LCA powders are well crystallized layered phases, showing thin diffraction peaks all indexed in the *R-3m* space group. Le Bail refinement was performed on all patterns and gave similar average cell parameters for all 4 samples: $a_{hex} \approx 2.814$ Å; $c_{hex} \approx 14.064$ Å. Note that these values are just indicative as they were obtained using the 2Θ° position of the diffraction peak maxima. However, as discussed in section C.3, the homogeneity of Al doping strongly affects the shape of diffraction peaks, leading to strong broadening and

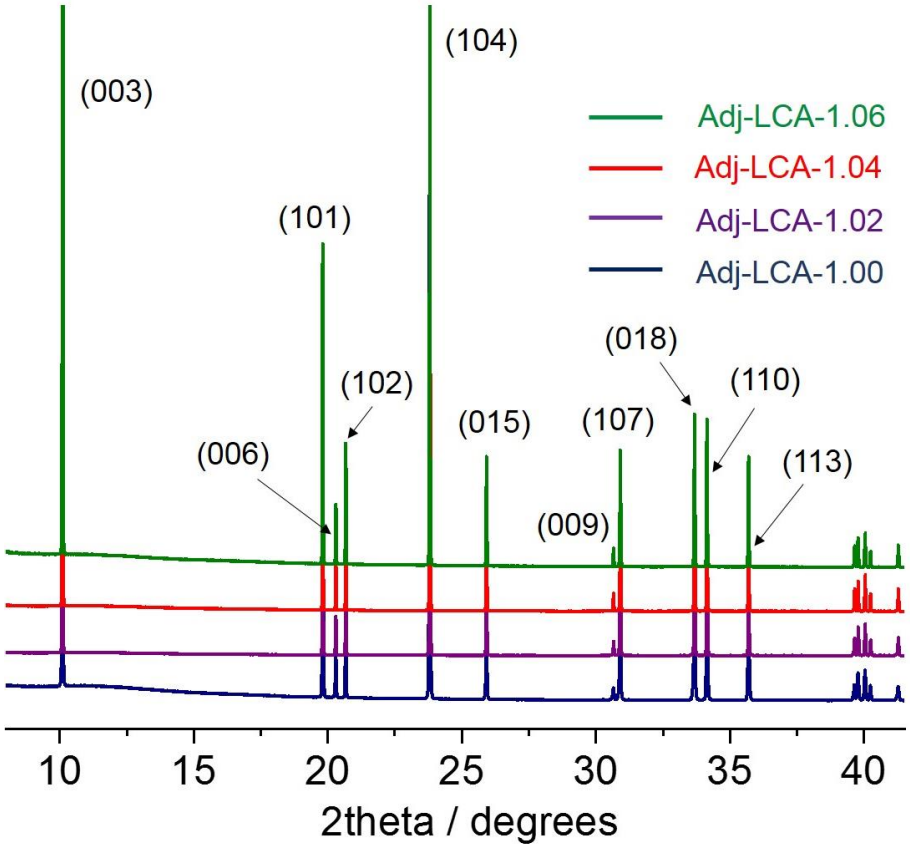

Figure C24. *Synchrotron X-ray diffraction (SXRD) patterns obtained for all Li-adjusted LCA from Group A. All patterns were collected for λ = 0.826 Å. Miller indexes for the main peaks are also given.*

asymmetry in the case of an inhomogeneous Al distribution within Al-doped LCO. Additionally, no diffraction peaks of a spinel impurity are found in these patterns despite the $(Li/M)_2$ in good agreement with ^7Li MAS NMR studies, meaning that the samples are either really stoichiometric or contain a negligible amount of Li excess.

C.4.1.2.2. Homogeneity of Al-doping as a function of initial $(Li/M)_1$

By further analysis of the synchrotron XRD patterns together with the ^{27}Al and ^{59}Co MAS NMR study of the samples, we can more finely characterize the homogeneity of the Al distribution in those LCA samples as similarly done in the previous section C.3. Note that in this paragraph, only the homogeneity of the final Li-adjusted LCA (Adj-LCA-X) is discussed (i.e., at the outcome of Step 3), as they are the most interesting samples for electrochemical application. Some characterizations of the LCA-X samples before Li-adjustement will be given and commented in Part C.4.4.

Zooms on the (018) and (110) peaks from the SXRD patterns shown in **Figure C24** are given in **Figure C25**. A comparison of the (018) and (110) peak shapes for two powders prepared from solid route (Adj-LCA-1.00 and Adj-LCA-1.04, respectively) and the reference citrate sample is also given in **Figure C26**. In section C.3, we demonstrated that pronounced peak asymmetry can be seen in the SXRD patterns of inhomogeneously Al-doped LCO, due to the existence of Al- gradients within the materials whose contribution appears at slightly different $2\Theta°$ positions. This is especially highlighted in **Figure C26** as no pronounced asymmetry is found in the diffraction peaks of the citrate Rf-LCA sample. However, the asymmetry is clearly visible on the left of the (018) diffraction peak in **Figure C25.a** and **Figure C26.a,** and on the right of the (110) peak in **Figure C25.b** and **Figure C26.b** for the LCA sample prepared in Li-stoichiometric conditions (Adj-LCA-1.00) – acting as a first evidence of the poor homogeneity of Al distribution in this sample. As a matter of fact, this sample is strictly equivalent to P2-LCA from section C.3 – meaning that a bad overall Al distribution was thus expected for Adj-LCA-1.00. This peak asymmetry is significantly decreased in the case of an initial $(Li/M)_1 = 1.02$, and suggests that Al is more homogeneously distributed in Adj-LCA-1.02 as compared to Adj-LCA-1.00. For both

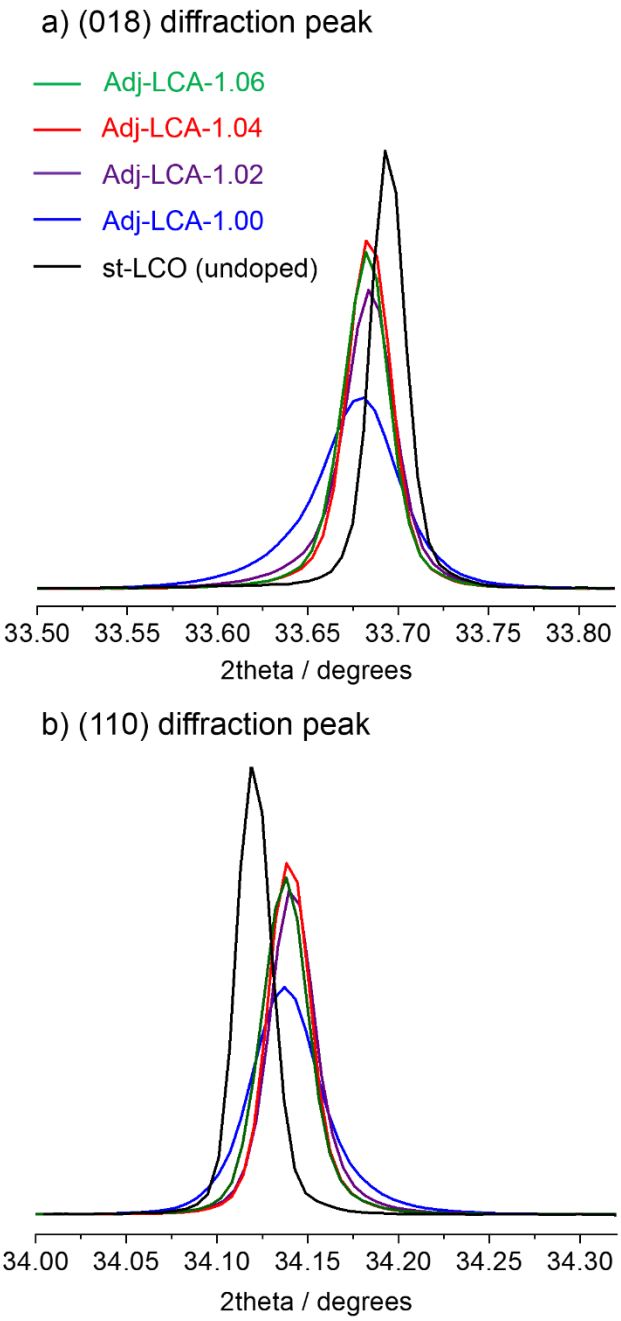

Figure C25. *Zoom on the a) (0 1 8) and b) (1 1 0) diffraction peaks from the Synchrotron X-ray diffraction (SXRD) patterns shown in Figure C23.*

Adj-LCA-1.04 and 1.06, no peak asymmetry is visible at all, and a homogeneous Al-doping is thus expected. Therefore, Li excess during the preparation of LCA seems to be extremely favorable to synthesize homogeneously Al-doped LCO from a solid state synthesis route.

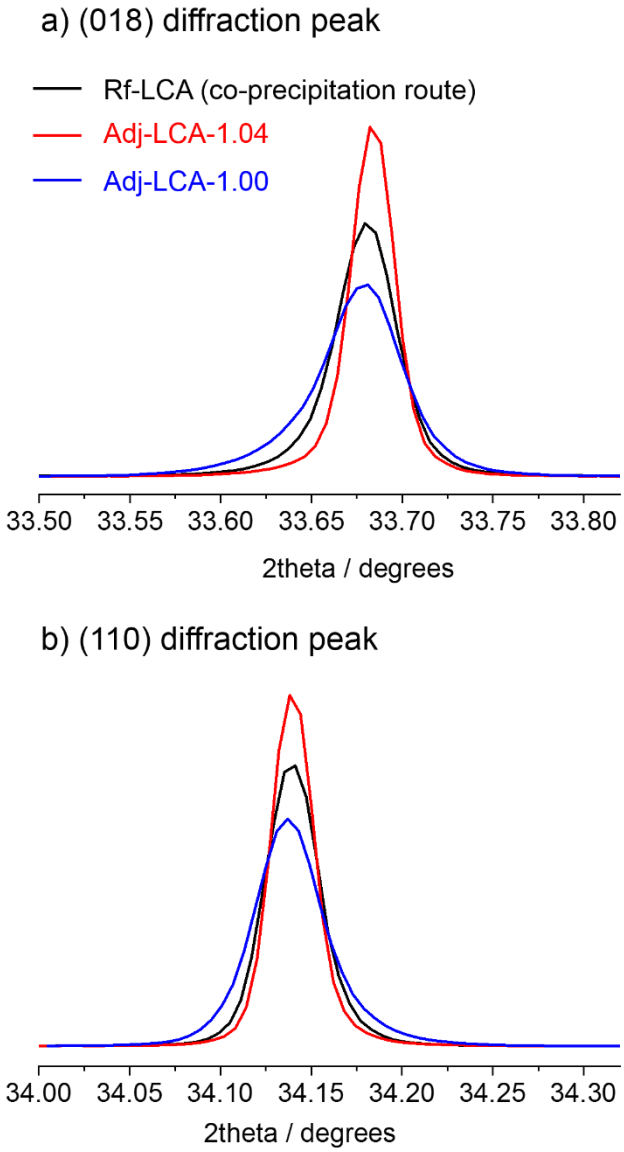

Figure C26. *Comparison of a) (018) and b) (110) diffraction peak shapes for two samples prepared from solid state reaction (Adj-LCA-1.00 and Adj-LCA-1.04) vs. a sample prepared from a co-precipitation route.*

^{27}Al and ^{59}Co MAS NMR were additionally carried out to probe the local Al (or Co) environments. Zooms on the central transitions for ^{27}Al and ^{59}Co MAS NMR are respectively given in **Figure C27** and **Figure C28** for all adjusted samples**.** One should remember that larger chemical shift range and broadening are usually obtained in the ^{59}Co MAS NMR spectra as compared to ^{27}Al MAS NMR spectra, leading to less resolved peaks. Therefore, even though they are complementary to the ^{27}Al MAS NMR results, they are less extensively commented in the following. In **Figure C27.a**, all signals are assigned to a specific Al in octahedral oxygen coordination with various type of second coordination sphere denoted as "Al-(Al_nCo_{6-n})" with $0 \leq n \leq 6$ (or "Co-(Al_nCo_{6-n})" in **Figure C28**, respectively) previously explained in **Figure C14**. For all samples, the most intense contributions mostly arise from Co-rich environments, i.e. Al-(Al_0Co_6) at ~ 62 ppm, Al-(Al_1Co_5) at ~ 55 ppm and Al-(Al_2Co_4) at ~ 48 ppm, in good agreement with a low probability of Al to be surrounded by itself (inherent to the low 4%$_{at}$ content in the Adj-LCA-X). Intense contributions from Co-rich environments are similarly found in the ^{59}Co MAS NMR spectra in **Figure C28** at ~ 14132 pm for Co-(Al_0Co_6), ~ 14105 ppm for Co-(Al_1Co_5), and ~ 14047 ppm for Co-(Al_2Co_4).

For the more thorough comparison shown in **Figure C27.c**, we used the reference 4% Al-doped LCO sample Rf-LCA prepared from a citrate route. Due to the synthesis of the precursor in solution, a homogeneous Co^{3+}/Al^{3+} cation mixing is expected. This sample was used in section C.3, in which the ^{27}Al MAS NMR spectrum matched with the expected signal distribution for a sample showing a purely statistical Al distribution, thus considered homogeneous.

The spectrum for Adj-LCA-1.00 confirms previous conclusions drawn from the SXRD data, i.e. unwanted Al-richer domains are found within this sample. Indeed, signals respectively corresponding to Al-(Al_3Co_3), Al-(Al_4Co_2), Al-(Al_5Co_1) and Al-(Al_6Co_0), i.e. Al-rich

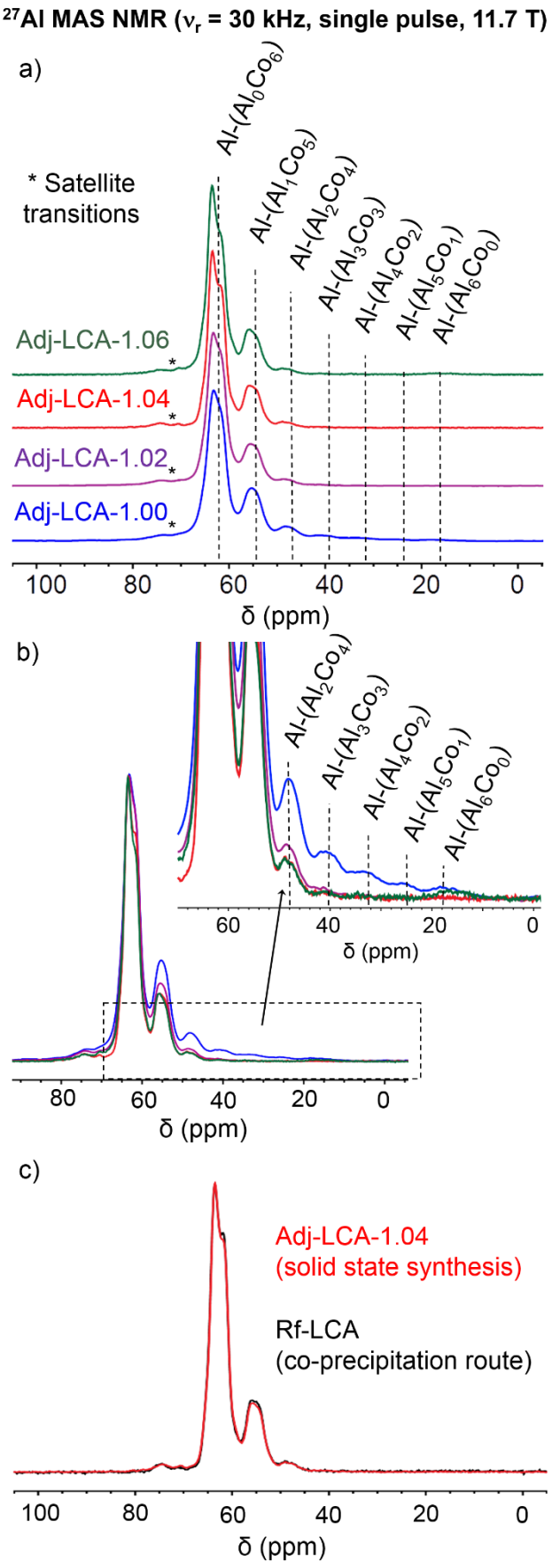

Figure C27*. a)* *^{27}Al MAS NMR spectra recorded at 130.33 MHz using a 30 kHz spinning frequency of all Li-adjusted samples from Group A. A different plot is provided in b), where all spectra are superimposed and normalized to the maximum of the main contribution. A comparison of Adj-LCA-1.04 spectrum with the one recorded for a 4% Al doped LCA sample prepared by a citrate route used as reference is given in c).*

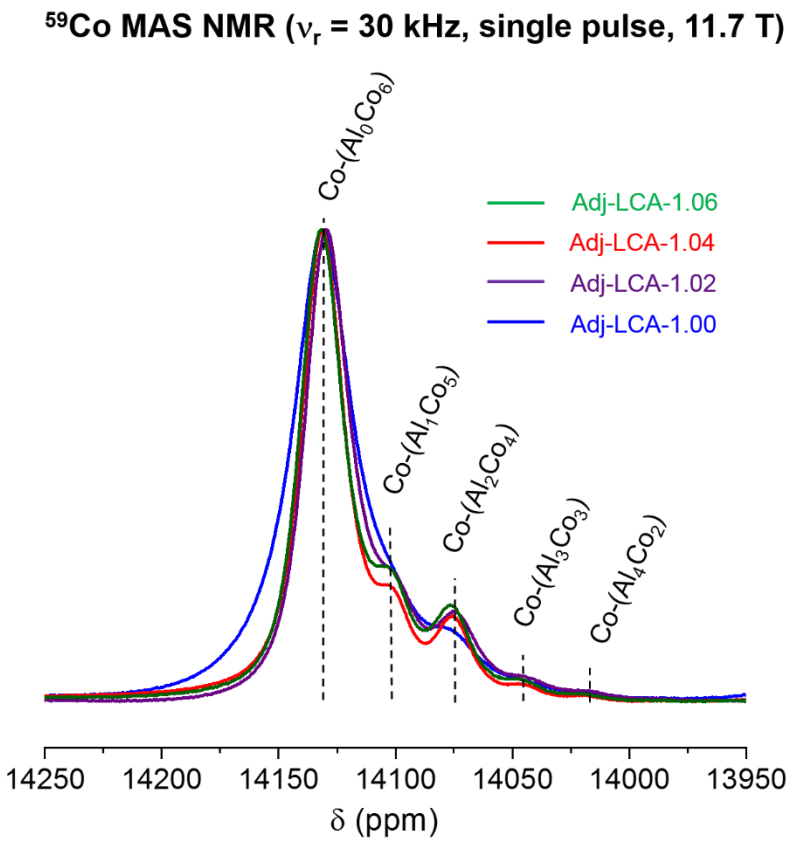

Figure C28. *^{59}Co MAS NMR spectra recorded at 120.35 MHz using a 30 kHz spinning frequency of all Li-adjusted samples from Group A.*

surroundings, appear at ~ 40 ppm, ~ 33 ppm, ~ 26 ppm and ~ 18 ppm in the zoom provided in **Figure C27.b.**

This supports previous conclusions that poor homogeneity of Al doping in LCO is achieved in Li-stoichiometric conditions $(Li/M)_1 \leq 1.00$ prepared from solid state route. Spectra obtained for the three other samples – all prepared with an initial excess of Li_2CO_3 – yield to a significantly improved Al distribution. As a matter of fact, the perfect superimposition of spectra for Adj-LCA-1.04 and Rf-LCA in **Figure C27.c** highlights that an equivalent homogeneous Co/Al cation mixing is found in both samples. We thus confirm, using NMR as a local scale probe, that we can prepare homogeneously Al-doped LCO samples from a solid state route by using a Li

excess in a first step of the synthesis and readjust the stoichiometry to Li/M = 1.00 in a second step. Besides, the exact amount of excess Li_2CO_3 required to achieve homogeneous doping does not seem to take a random value. Indeed, the spectra of Adj-LCA-1.02 and Adj-LCA-1.06 are not identical to the one of Adj-LCA-1.04. No signals corresponding to Al-rich contributions ($n \geq 3$) are found in the spectrum of Adj-LCA-1.02 (**Figure C27.b)**, but the intensity ratio for the existing ones does not exactly follow the predictions for a really homogeneous Al doping either: contributions arising from Al-(Al_1Co_5), Al-(Al_2Co_4) and Al-(Al_3Co_3) environments are slightly enhanced at the expense of the Al-(Al_0Co_6) signal. On the other hand, a small contribution from an Al-(Al_6Co_0) surrounding is visible at ~ 18 ppm in the spectrum of Adj-LCA-1.06 (**Figure C27).**

It seems clear that the use of an excess of Li_2CO_3 in the preparation of LCA by solid route is the key to achieve homogeneous Al-doping. In order to prepare materials with a high energy density, we thus aim to prepare homogeneous LCA with large particle size (d ~ 40 µm) using the same synthesis approach as group A, but starting a new large-particle-Co/Al oxide precursor as described below.

C.4.2 LCA Samples with controlled particle size (Group B)

C.4.2.1. Description of synthesis

Group B samples were also prepared in three steps. In Step 1, a 2kg-mixture of spherical $CoCO_3$ (Umicore, 40µm particles) and Al_2O_3 was intimately homogenized and heat treated for 3 hours at T = 600 °C under air flow. An Al-coated Co_3O_4 was obtained at the outcome of Step 1, as revealed by the typical signals arising from unreacted Al_2O_3 in its ^{27}Al MAS NMR spectrum shown in **Figure C29**. The next two steps were identical as compared to **Group A** samples. Al-coated Co_3O_4 was mixed with Li_2CO_3 to prepare the final LCA powders in various $(Li/M)_1$ ratios (1.00, 1.04 or 1.06), here named "LCA-X-40µm" (X = 1.00, 1.04 or 1.06). The final Li-adjustment step (Step 3) following previous descriptions was carried out to reach final $(Li/M)_2 \approx 1.00$ and the powders were subsequently named "Adj-LCA-X-40µm" (X = 1.00, 1.04 or 1.06).

As we first evidenced the beneficial role of Li excess in our synthesis in section C.4.1, the discussion below will now be entirely focused on samples prepared in Li excess conditions ($(Li/M)_1 > 1.00$), though we also prepared an analogous sample with $(Li/M)_1 = 1.00$. This additional sample will be used as reference for the Al MAS NMR study only.

A schematic figure summarizing all steps of the synthesis can also be found in ***Figure C30.***

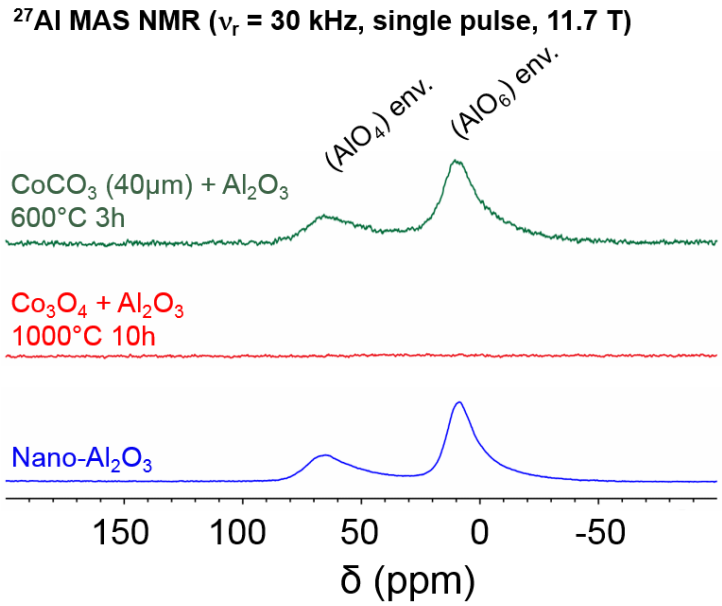

Figure C29. *^{27}Al MAS NMR spectra recorded at 130.33 MHz using a 30kHz spinning frequency for ($CoCO_3$ + Al_2O_3) heat treated at 600 °C for 3 hours (in green) and (Co_3O_4 + Al_2O_3) heat treated at T = 1000 °C for 10 hours (in red), as compared to the spectra of pure alumina (in blue). Note that Group A samples were formed from the red precursors, while Group B samples were obtained from the green precursor.*

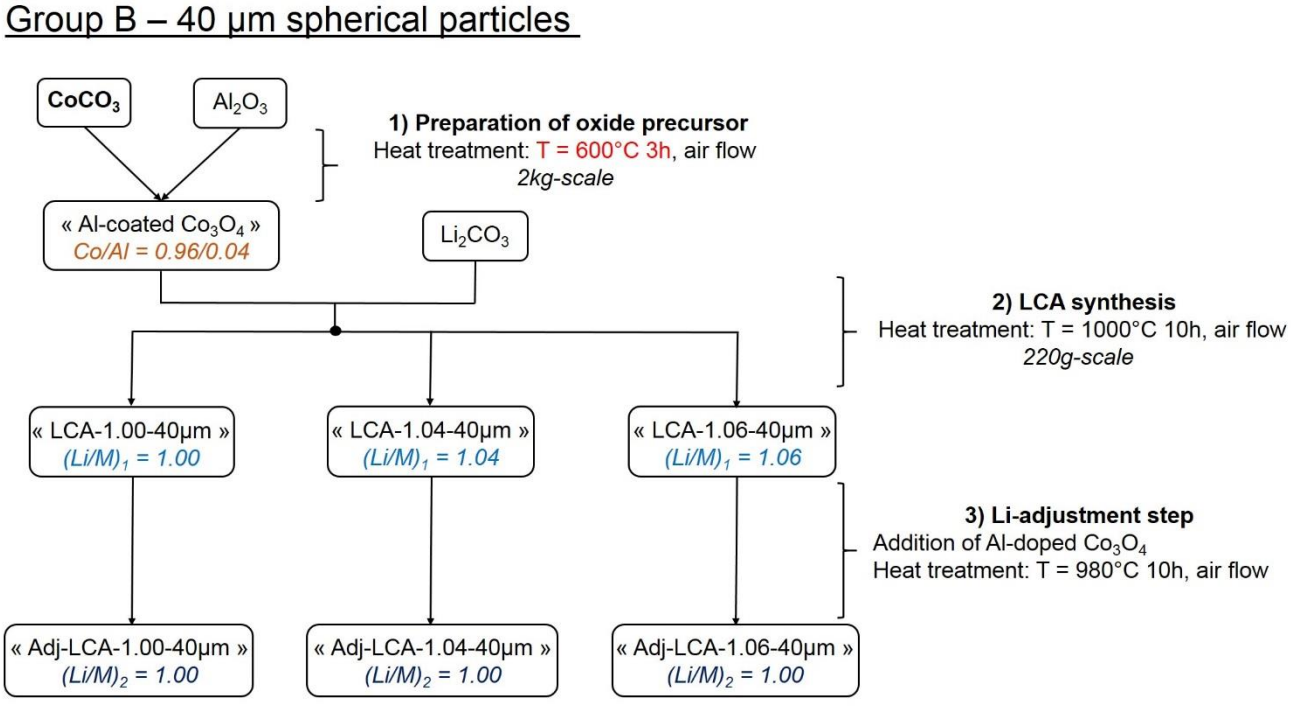

Figure C30. *Schematic representation of the synthetic routes for Group B samples (Approach n°2).*

C.4.2.2. Results

C.4.2.2.1. General characterization

Table C.T3 gives the Li and Al contents for Group B LCA powders before and after adjustment of the Li-stoichiometry measured by ICP. After addition of Li_2CO_3 and subsequent heat treatment (Step 2), the final ratios measured for LCA-1.04-40µm and LCA-1.06-40µm are found slightly below their targeted $(Li/M)_1$, with reported values of 1.028 and 1.044. At the outcome of the Li-adjustment step (Step 3), all final $(Li/M)_2$ drop below 1.00 as expected, with $(Li/M)_2$ = 0.999 or 0.992 respectively measured for Adj-LCA-1.04-40µm and Adj-LCA-1.06-40µm. A proper control of the final Al content was also achieved, as all measured Al/M ratios are close to 0.04.

Sample	$(Li/M)_1$ (Before Li-adjustment)	$(Li/M)_2$ (After Li-adjustment)	Al/M
LCA-1.04-40µm	*1.028*	*0.999*	*0.0380*
LCA-1.06-40µm	*1.044*	*0.992*	*0.0388*

Table C.T3. *Measured ICP ratios for Group B powders, before $(Li/M)_1$ and after Li-adjustment $(Li/M)_2$ and Al/M.*

^{7}Li MAS NMR was also carried out to check the final Li-stoichiometries of Adj-LCA-1.04-40µm and Adj-LCA-1.06-40µm after Li-adjustment. A spectrum was also recorded for non Li-adjusted LCA-1.06-40µm. **Figure C31.a** therefore shows the ^{7}Li MAS NMR spectra of LCA-1.06-40µm (before Li-adjustment) and Adj-LCA-1.06-40µm (after Li-adjustment); all spectra for Adj-LCA-X-40µm are plotted in **Figure C31.b**. Again, the second step of the synthesis was successfully performed, as Adj-LCA-1.06-40µm shows a single contribution at – 0.4 ppm, meaning that it is indeed Li stoichiometric, unlike LCA-1.06-40µm whose spectrum exhibits

additional signals typically distinguished for overlithiated samples (**Figure C31.a**). Some of these contributions are also found in the spectrum of Adj-LCA-1.04-40µm at ~ 4, - 5 and - 15 ppm (**Figure C31.b**). The intensity of these contributions are though negligible, especially as compared to the real overlithiated phase presented in **Figure C31.a** (Adj-LCA-1.06-40µm), making it clear that Li excess is found as traces in the final Adj-LCA-1.04-40µm sample.

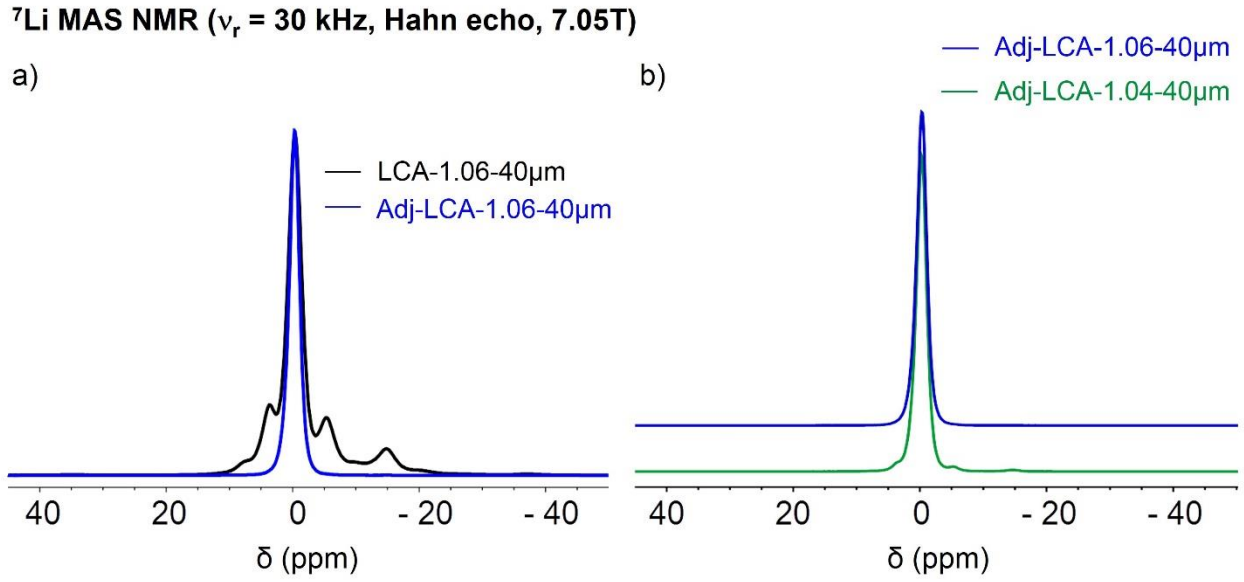

Figure C31. *^{7}Li MAS NMR spectra recorded at 116.66 MHz using a 30 kHz spinning frequency of a) LCA-1.06-40µm and Adj-LCA-1.06-40µm; b) Li-adjusted samples from Group B: Adj-LCA-1.04-40µm and Adj-LCA-1.06-40µm.*

Figure C32 shows the SEM images obtained for the two samples we prepared with $(Li/M)_1$ = 1.04 and 1.06 exhibiting well controlled size and spherical morphology after Li-adjustment (namely "Adj-LCA-1.04-40µm" and "Adj-LCA-1.06-40µm") as compared to the homogeneous Adj-LCA-1.04 from section C.4.1. The typical average particle size for these powders is ~ 40 µm, though a second population of small particles is again observed due to the addition of mix-$Co_{3-z}Al_zO_4$ during the second step of the synthesis. The spherical character and similar sizes of the particles from one sample to another were well preserved despite the flux role of Li_2CO_3.

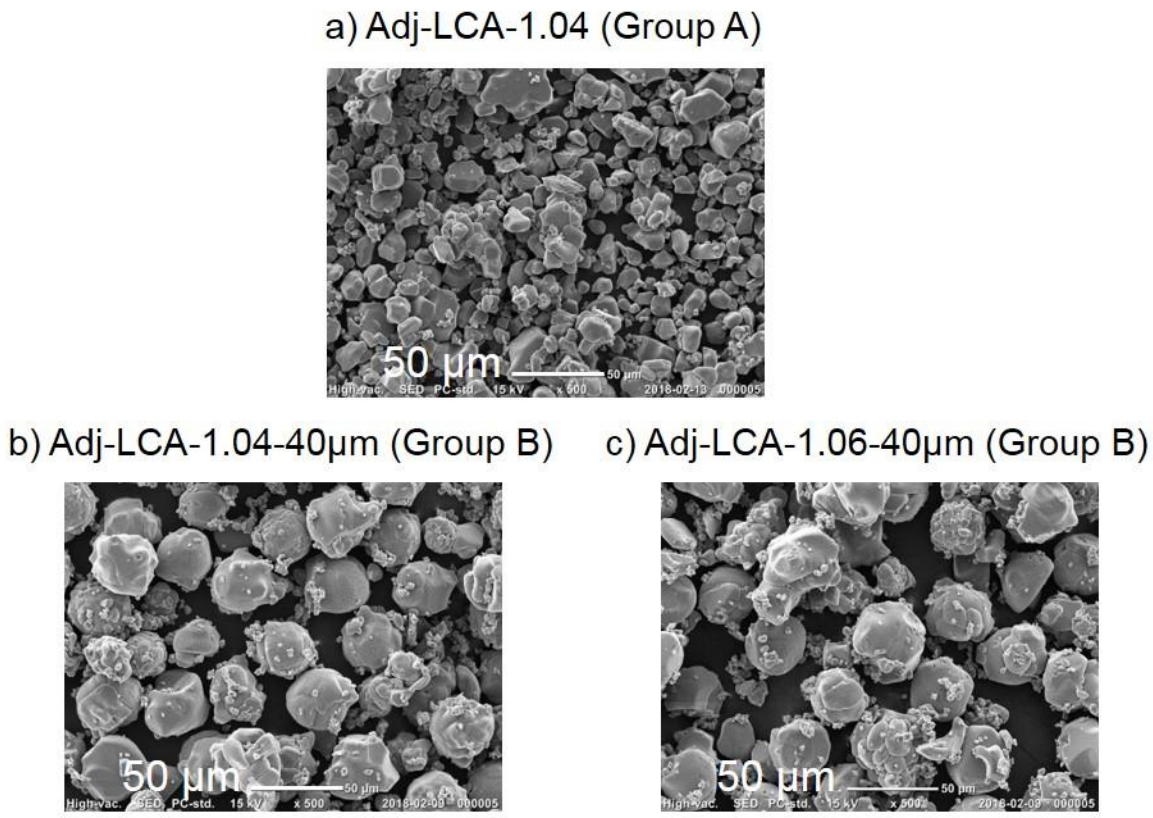

Figure C32. *Comparison of SEM micrographs of Adj-LCA-1.04 from group A (a), with Li-adjusted samples from Group B: b) Adj-LCA-1.04-40µm and c) Adj-LCA-1.06-40µm.*

Both final Adj-LCA-1.04-40µm and Adj-LCA-1.06-40µm powders are well crystallized layered phases, as all diffraction peaks are indexed in the *R-3m* space group. The corresponding SXRD patterns are plotted in **Figure C33**. Le Bail refinement was performed on both patterns and gave similar average cell parameters: $a_{hex} \approx 2.814$ Å; $c_{hex} \approx 14.064$ Å. These values are identical as those reported for Group A samples. No peaks for spinel impurity can be found in these patterns.

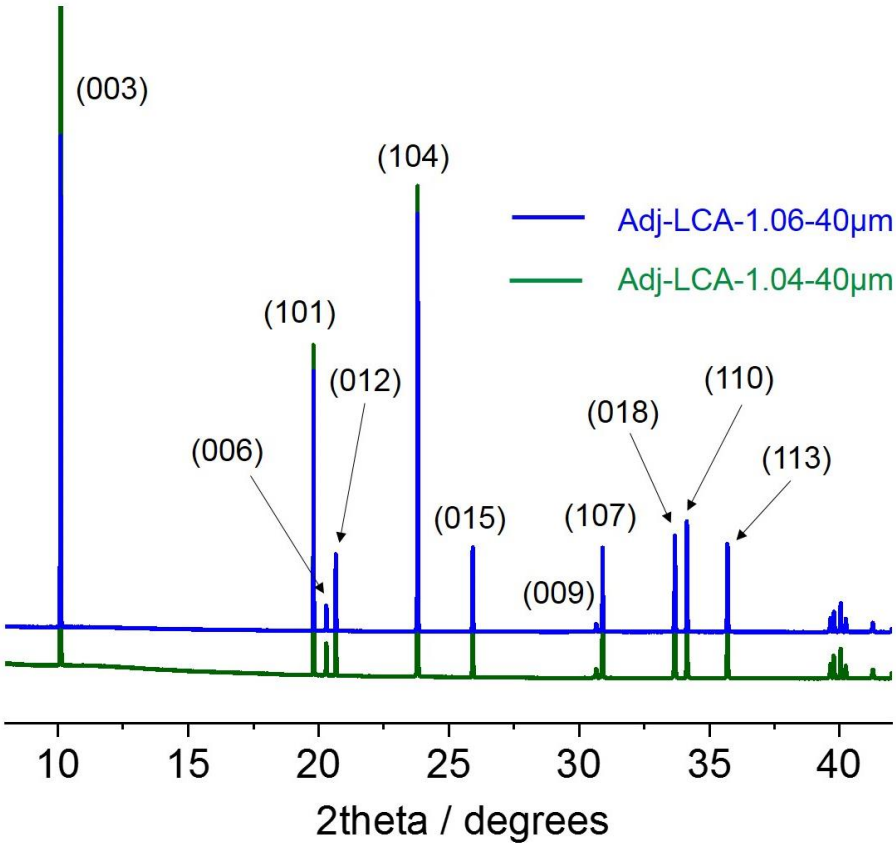

Figure C33. *Synchrotron X-ray diffraction (SXRD) patterns obtained for Li-adjusted LCA from Group B. All patterns were collected for λ = 0.826 Å. Miller indexes for the main peaks are also given.*

C.4.2.2.2. Homogeneity of Al-doping for 40µm-sized LCA

Zooms on the (0 1 8) and (1 1 0) diffraction peaks from the SXRD patterns plotted in **Figure C33** can be respectively found in **Figure C34.a** and **Figure C34.b,** in which they are compared to those of undoped st-LCO and homogeneously Al-doped Adj-LCA-1.04 from Group A, now considered as reference. If it is true that both Adj-LCA-1.04-40µm and Adj-LCA-1.06-40µm samples show weakly pronounced asymmetry (especially as compared to the diffraction peaks of Adj-LCA-1.04), it is still negligible. Therefore, one should not expect variations of Al concentrations within Adj-LCA-1.04-40µm and Adj-LCA-1.06-40µm. This result is a first step towards the validation of our solid route to even prepare homogeneously doped LCA with large particle size.

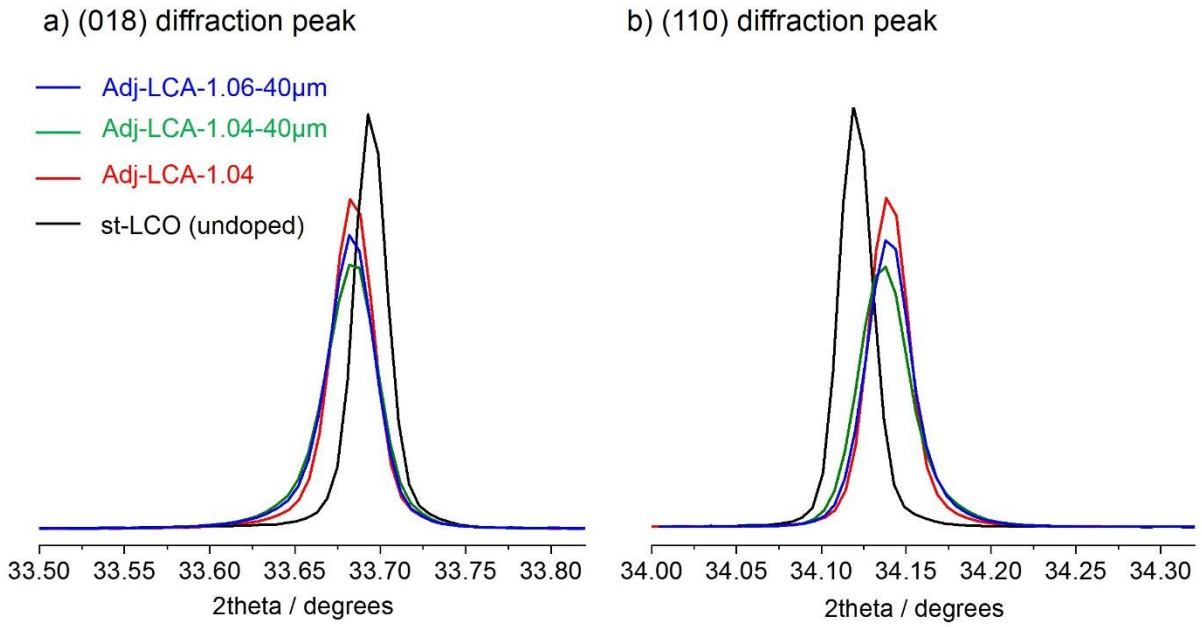

Figure C34. *Zoom on the a) (0 1 8) and b) (1 1 0) diffraction peaks from the Synchrotron X-ray diffraction (SXRD) patterns collected for Li-adjusted samples from Group B, as compared to st-LCO and Adj-LCA-1.04.*

^{27}Al and ^{59}Co MAS NMR spectra were subsequently recorded and zooms on the central transitions are given in **Figure C35.a** for ^{27}Al NMR, and in **Figure C35.b** for ^{59}Co NMR. Spectra for Adj-LCA-1.04-40µm and Adj-LCA-1.06-40µm are there compared to those of the most homogeneously doped powder from Group A samples (i.e. Adj-LCA-1.04). As mentioned earlier, since we also prepared a 40µm-sized LCA powder with stoichiometric amounts of precursors (Adj-LCA-1.00-40µm), a comparison of its ^{27}Al and ^{59}Co NMR spectra with those of Adj-LCA-1.06-40µm is additionally provided in **Figure C36.a** and **C36.b.**

In **Figure C35.a**, the two powders prepared with Li excess, Adj-LCA-1.04-40µm and Adj-LCA-1.06-40 µm respectively, show rather similar spectra with three main contributions at ~ 62, 55 and 48 ppm, arising from Al-(Al_0Co_6), Al-(Al_1Co_5) and Al-(Al_2Co_4) – though obtained in slightly different intensity ratios. Intense contributions from Co-rich environments are similarly found in their ^{59}Co MAS NMR spectra in **Figure C35.b** at ~ 14132 pm for Co-(Al_0Co_6), ~ 14105 ppm for Co-(Al_1Co_5), and ~ 14047 ppm for Co-(Al_2Co_4). No intensity is detected for Al-rich contributions, confirming that the preparation with Li excess was determinant to achieve proper Al distribution within the powders. Even though the spectra of these two samples do not perfectly superimpose to our homogeneously doped sample from Group A, our attempts to synthesize LCA with significantly large particle size from simple solid state reaction was successful. The most homogeneous Al distribution for Group B samples seems to be obtained for Adj-LCA-1.06-40µm, meaning that trying to apply the process using a precursor with higher particle size requires to add some more Li_2CO_3. Indeed, the most homogeneous sample from Group A was obtained for $(Li/M)_1 = 1.04$, while making it to $(Li/M)_1 = 1.06$ here was necessary to approach similar Al distributions for Group B samples.

In Figure C36.a, numerous Al-rich contribution signals are found at ~ 40, 33, 26 and 18 ppm for Adj-LCA-1.00-40µm, corresponding to Al-(Al_3Co_3), Al-(Al_4Co_2), Al-(Al_5Co_1) and Al-(Al_6Co_0) surroundings. Contributions found at ~ 14132 pm for Co-(Al_0Co_6), ~ 14105 ppm for Co-(Al_1Co_5), and ~ 14047 ppm for Co-(Al_2Co_4) however show decreased intensity in the

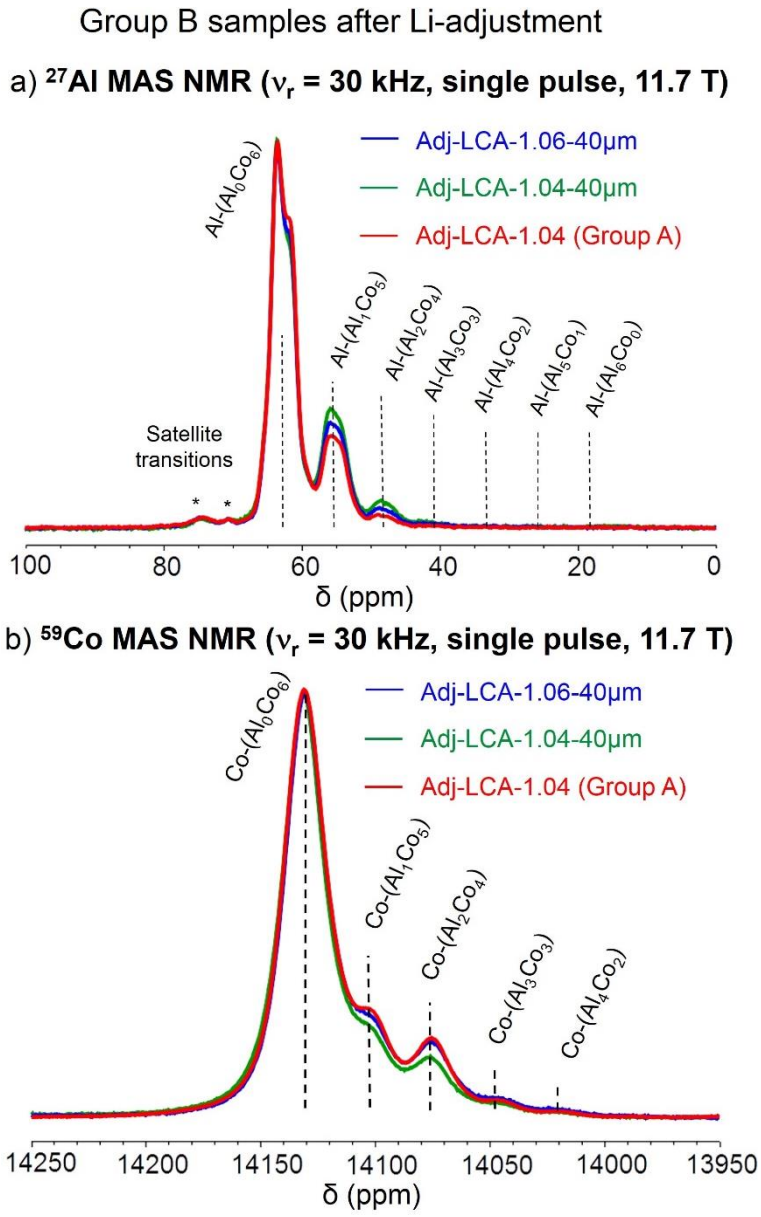

Figure C35*. Central transitions observed in the a) ^{27}Al MAS NMR spectra recorded at 130.33 MHz and b) ^{59}Co MAS NMR spectra recorded at 120.35 of Li-adjusted samples from Group B. Spectra for the most homogeneously doped LCA sample from Group A (Adj-LCA-1.04) has been added for comparison purposes in a) and b). All spectra are normalized to the maximum of the main contribution.*

^{59}Co NMR spectrum of Adj-LCA-1.00-40µm in **Figure C36.b**. This clearly reveals again the necessity to work in Li excess conditions during the first step of our synthesis to get homogenous samples. As a matter of fact, these signals show even more intensity as compared to its analogue from Group A (Adj-LCA-1.00), confirming that a limitation arising from the size of the particles exist and may be linked to interdiffusion issues.

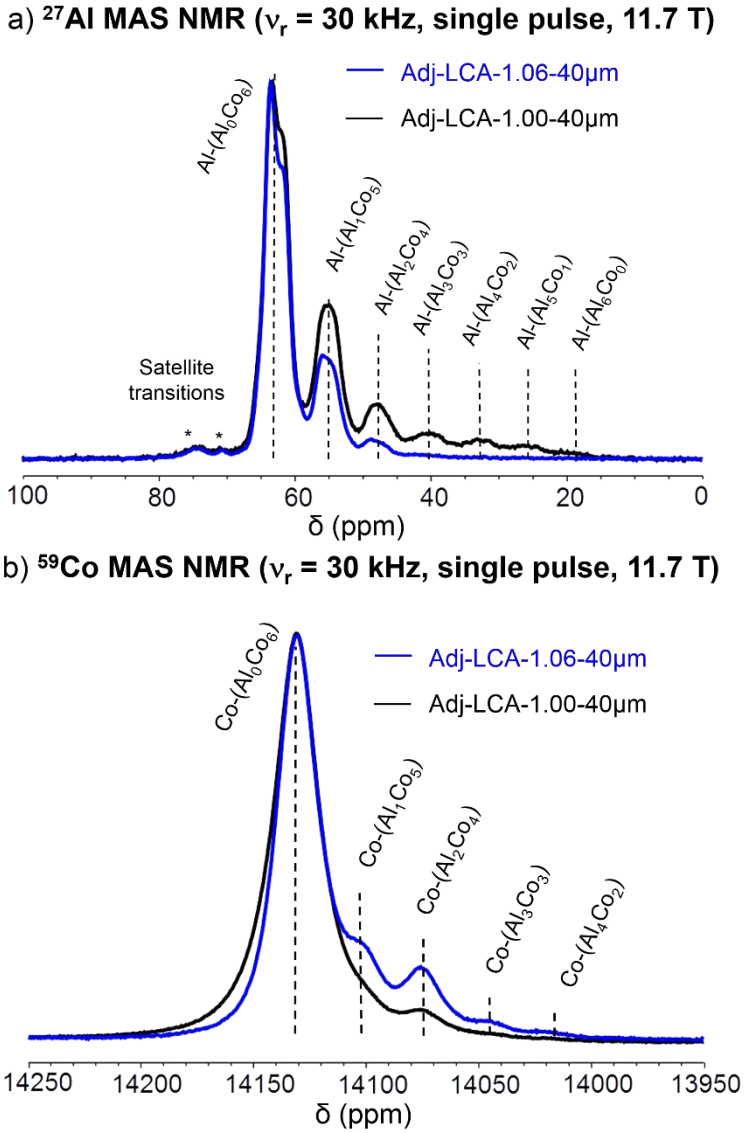

Figure C36*. Central transitions observed in the* ***a)*** *^{27}Al and b) ^{59}Co MAS NMR spectra for Adj-LCA-1.00-40µm and Adj-LCA-1.06-40µm. All spectra are normalized to the maximum of the main contribution.*

C.4.3 Electrochemistry of LCA samples prepared with Approach n°2

Li-adjusted samples from Group A and B were cycled in coin cells at C/20 up to 5.0 V. The 1st cycle curves obtained Group A $Li_xCo_{0.96}Al_{0.04}O_2$ systems as compared to undoped st-LCO are plotted in **Figure C37.a** in which a zoom on the [0.45; 0.55] x range is also provided**.** The corresponding derivative dx/dV curve for the zoom is plotted in **Figure C37.b**. The 1st cycle curves obtained for Group B $Li_xCo_{0.96}Al_{0.04}O_2$ systems are also given in **Figure C38**. All Adj-LCA-X and Adj-LCA-X-40µm show more irreversible capacity losses (Q_{irr}) as compared to undoped st-LCO, in good agreement with previous works[16,18,51]; Q_{irr} seems to be quite comparable no matter the homogeneity of Al doping. As expected, the 1st cycle curves show significant differences from one sample to another. The electrochemical profile of the sample we identified as the least homogeneously doped, namely Adj-LCA-1.00 and Adj-LCA-1.00-40µm (**Figures C37.a** and **C38**, respectively), exhibits characteristics typically reported for undoped LCO, such as i) a plateau at E = 3.95 V at the beginning of the charge and ii) a weak voltage jump around x = 0.5, denoting the O3 ↔ O3' transition, in good agreement with the first study in section C.3. This series of events is just one more evidence to highlight the poor homogeneity of Al doping achieved for Adj-LCA-1.00 and Adj-LCA-1.00-40µm, and ultimately confirms that Li-stoichiometric conditions for the preparation of homogeneously Al-doped LCO by solid state route are not recommended. Although these samples are not homogeneously doped, the presence of Al has again a beneficial effect on the polarization observed at high voltage (V > 4.5) compared to st-LCO (**Figure C37.a**). As a matter of fact, this beneficial effect is observed for all Adj-LCA-X powders, which suggest that it may be independent of the Al distribution within the powders. The change of slope due to the Li/vacancies ordering at x = 0.5 is not detected for all other samples Adj-LCA-X (X = 1.02, 1.04 or 1.06) and Adj-LCA-1.06-40µm. All show pseudo-plateaus during the removal of the first Li at an expected[16] slightly higher voltage than st-LCO (E = 3.98 V). Adj-LCA-1.02 and Adj-LCA-1.04

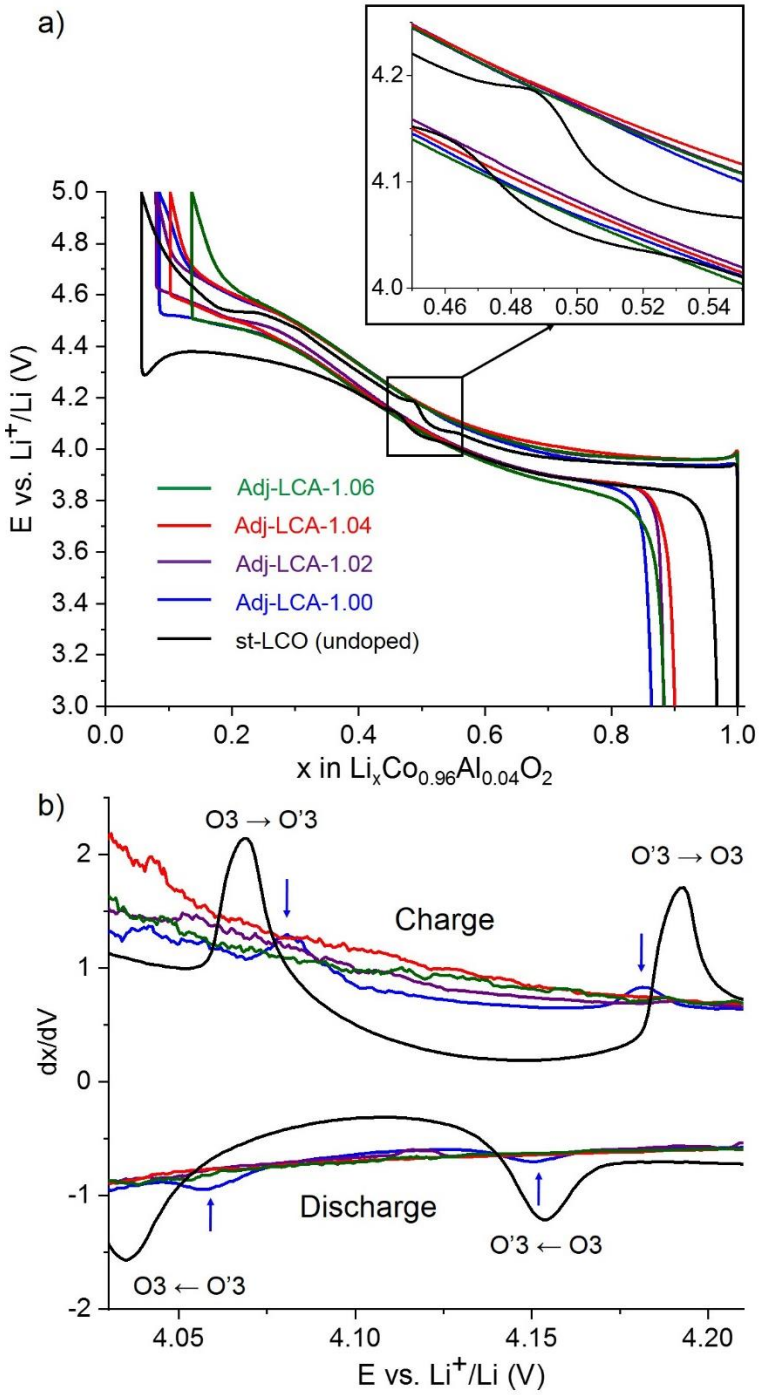

Figure C37. a) *1st cycle for Adj-LCA-X (Group A) at C/20 as positive electrode in Li//LCA cells, as compared to the 1st cycle curve of undoped LCO (st-LCO). A zoom corresponding to the O3 ↔ O'3 transition is given. Associated dx/dV curves for 4.00 – 4.25 V window are plotted in* ***b)****.*

show a comparable 1st cycle, no matter the small differences observed at the local scale for their Al distribution in their ^{27}Al MAS NMR spectra. Even though the curve for Adj-LCA-1.06 is as smooth as the others, higher polarization at high voltage may make it less appealing for a further use in a battery. A similar effect is reported for Adj-LCA-1.06-40µm (**Figure C38**).

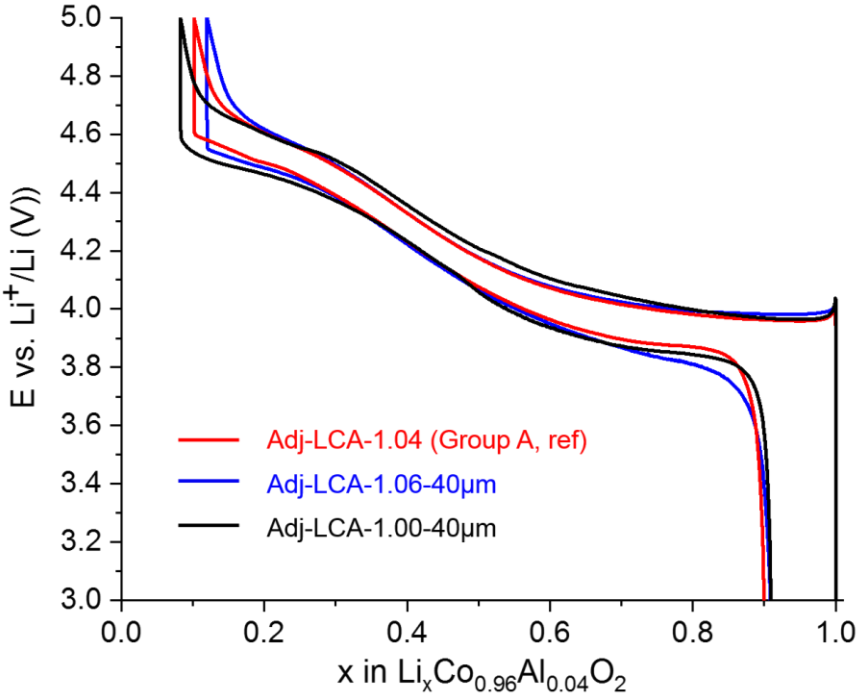

Figure C38. *1st cycle for Adj-LCA-X-40µm (Group B) at C/20 as positive electrode in Li//LCA cells, as compared to the 1st cycle curve of the mot homogeneously doped sample from Group A (Adj-LCA-1.04).*

Figure C39 shows the 1st cycle dx/dV curves (high voltage window only V > 4.4 V) for all Li-adjusted LCA from Group A as compared to st-LCO. The peak observed at ~ 4.53 V for st-LCO denotes the O3 – H1-3 transition. Such feature is considerably harder to distinguish in the dx/dV curves during the charge of all Adj-LCA-X samples. However, a clear peak is seen in the dx/dV curve of Adj-LCA-1.00 during its discharge, which could well correspond to the H1-3 – O3 transition. For this inhomogeneously doped sample, the formation of the H1-3 is clearly not hindered. Note that this peak is most likely absent of the dx/dV curve of st-LCO during the discharge because of the substantial polarization reported at high voltage for this sample. All other

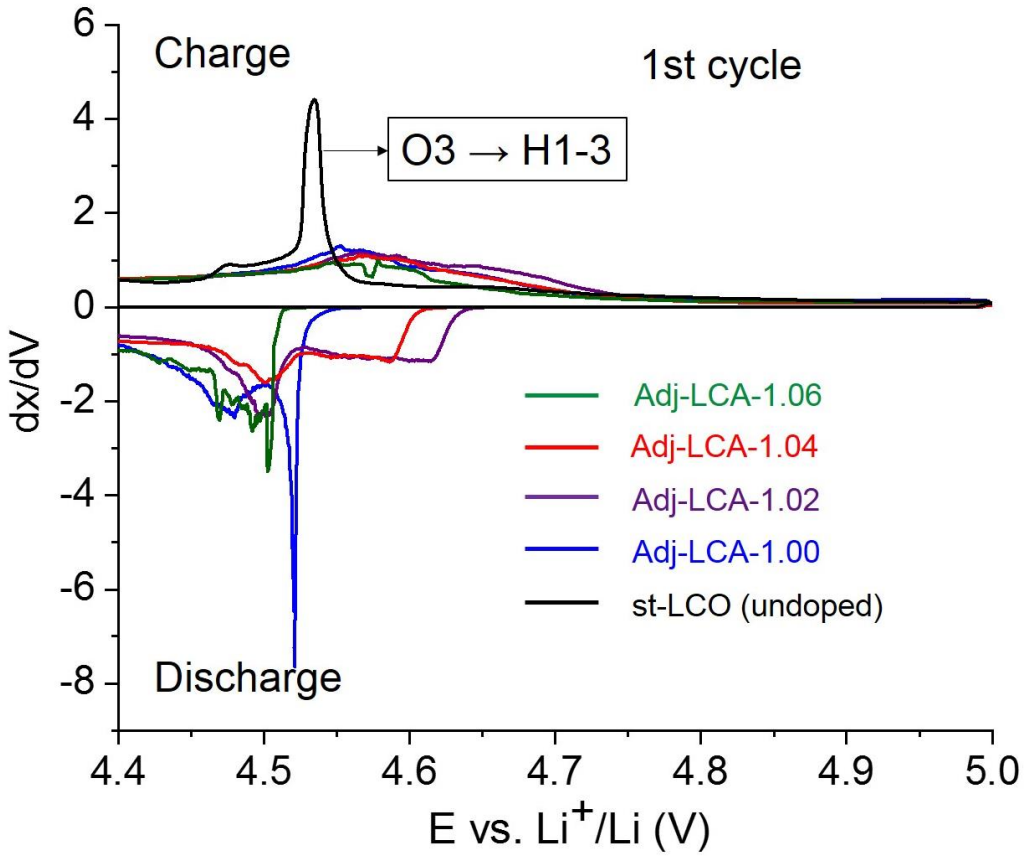

***Figure C39**. 1st cycle [4.4 – 5.0 V] dx/dV curves for Group A Adj-LCA-X samplesas compared to undoped st-LCO.*

adjusted samples seem to also experience transitions at high voltage, but with less defined voltage plateaus. Although in situ XRD would certainly help to draw proper conclusions to understand the deintercalation/intercaltion mechanisms, 4% Al doping, modifies the electrochemical processes at high voltage. Further work will be required to study those processes depending on the Al-homogeneity.

C.4.4 Discussion. On the beneficial effect of excess Li_2CO_3 for the synthesis of homogeneous 4% Al-doped LCO

Results previously commented in sections C.4.1 and C.4.2 helped highlighting the importance of using an excess of Li_2CO_3 to achieve homogeneous Al-doping in LCA prepared by solid state reaction. The formation of intermediate overlithiated layered phases previously evidenced by ^{7}Li MAS NMR (**Figure C21.a** and **Figure C31.a**) in the powders of non Li-adjusted LCA-1.04 (Group A) and LCA-1.06-40µm (Group B) proves that most (if not all) Li_2CO_3 reacts at the outcome of the 2nd step in Approach n°2. Therefore, getting a deeper understanding on why and how excess Li_2CO_3 significantly improves the Al distribution in LCA goes through gaining knowledge of the reaction mechanisms involved during this step – which could be partially obtained through a more thorough characterization of the intermediate LCA-1.04 and LCA-1.06-40µm powders.

Figure C40 shows the laboratory XRD patterns collected for these two samples, in the absence of SXRD data. Le Bail refinement was performed nonetheless and reveals that only one crystallized phase is formed at the outcome of Step 2 in Approach n°2. Indeed, no lines corresponding to either Li_2CO_3 or mix-$Co_{3-z}Al_zO_4$ / [Co_3O_4 + Al_2O_3] are observed in the XRD patterns of LCA-1.04 and LCA-1.06-40µm. Both patterns are indexed in the *R-3m* space group, similarly to the final LCA phases, with a_{hex} = 2.8141(6) Å; c_{hex} = 14.059(5) Å and a_{hex} = 2.8143(2) Å; c_{hex} = 14.062(2) Å respectively obtained for LCA-1.04 and LCA-1.06-40µm. These values show great analogy with the cell parameters obtained for the final associated Li-adjusted LCA ($a_{hex} \approx 2.814$ Å; $c_{hex} \approx 14.064$ Å). Therefore, complete formation of Al-doped LCO was performed after the 2nd step of Approach n°2, no matter the metal oxide precursor used.

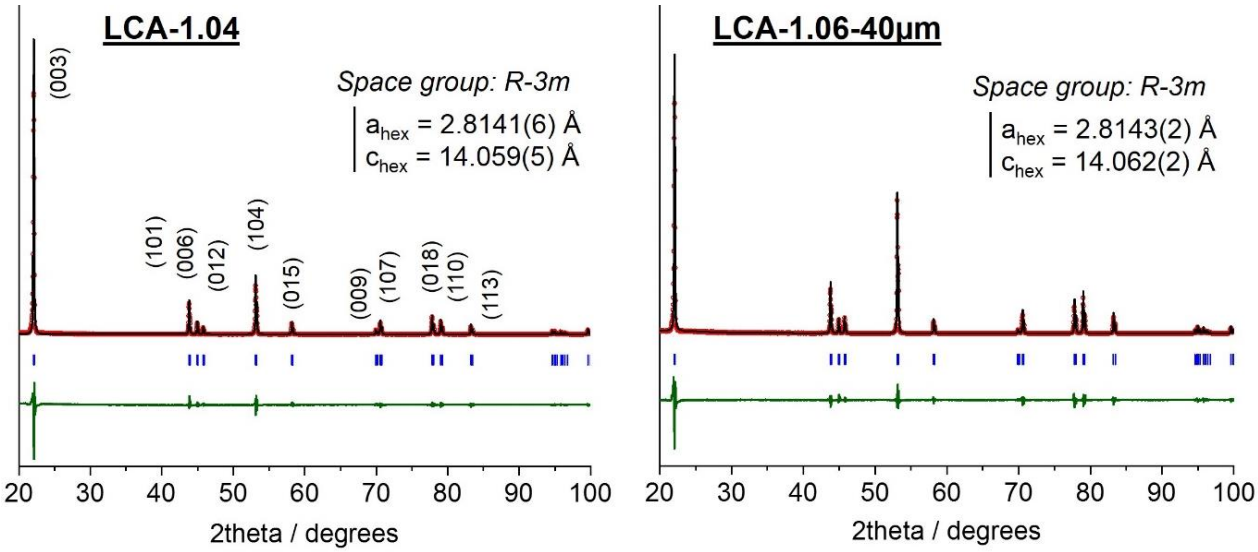

Figure C40*. XRD patterns collected for the intermediate LCA-1.04 (Group A) and LCA-1.06-40µm (Group B). Cell parameters were obtained from Le Bail refinements (also shown here). The Miller indexes for the mains peaks are also provided.*

Complementary ^{27}Al MAS NMR spectra for LCA-1.04 and LCA-1.06-40µm are respectively plotted in **Figures C41.a** and **C41.b**, as compared to the spectra of their final Li-adjusted analogues (Adj-LCA-1.04 and Adj-LCA-1.06-40µm). One could note that the spectra of LCA-1.04 and LCA-1.06-40µm are strictly equivalent, in addition to their XRD patterns, thereof suggesting that the chemical nature of the intermediate layered product formed after the 2nd step of the synthesis is equivalent no matter the initial Co/Al precursor used. This may be surprising as a mix-$Co_{3-z}Al_zO_4$ was used in the preparation of LCA-1.04, while an unreacted mixture of Co_3O_4 and Al_2O_3 was employed for LCA-1.06-40µm. While the use of the latter seemed to positively influence the Al distribution in LCA prepared with $(Li/M)_1 \leq 1.00$ (**section C.3.2.1, Approach n°1**), the choice of one type of oxide precursor over the other seems no longer relevant in the preparation of homogeneous LCA with $(Li/M)_1 \geq 1.00$ (**Approach n°2**). Besides, Al NMR spectra for LCA-1.04 and LCA-1.06-40µm do confirm the formation of an intermediate overlithiated LCA before the Li-adjustment step. Indeed, a new broad highly shifted signal located at ~ 205 ppm is

observed in **Figures C41.a** and **C41.b**. As it is located out of the typical chemical shift range observed for Al in diamagnetic environments (such as LS-Co^{3+} and Al^{3+}), it can be assigned to Al in the vicinity of paramagnetic IS-Co^{3+} undergoing Fermi contact interaction. This is illustrated in **Figure C42**. Moreover, other additional intensity is observed around 70 ppm. Although it was recently assigned to Al found in tetrahedral coordination[52], this additional signal could be most

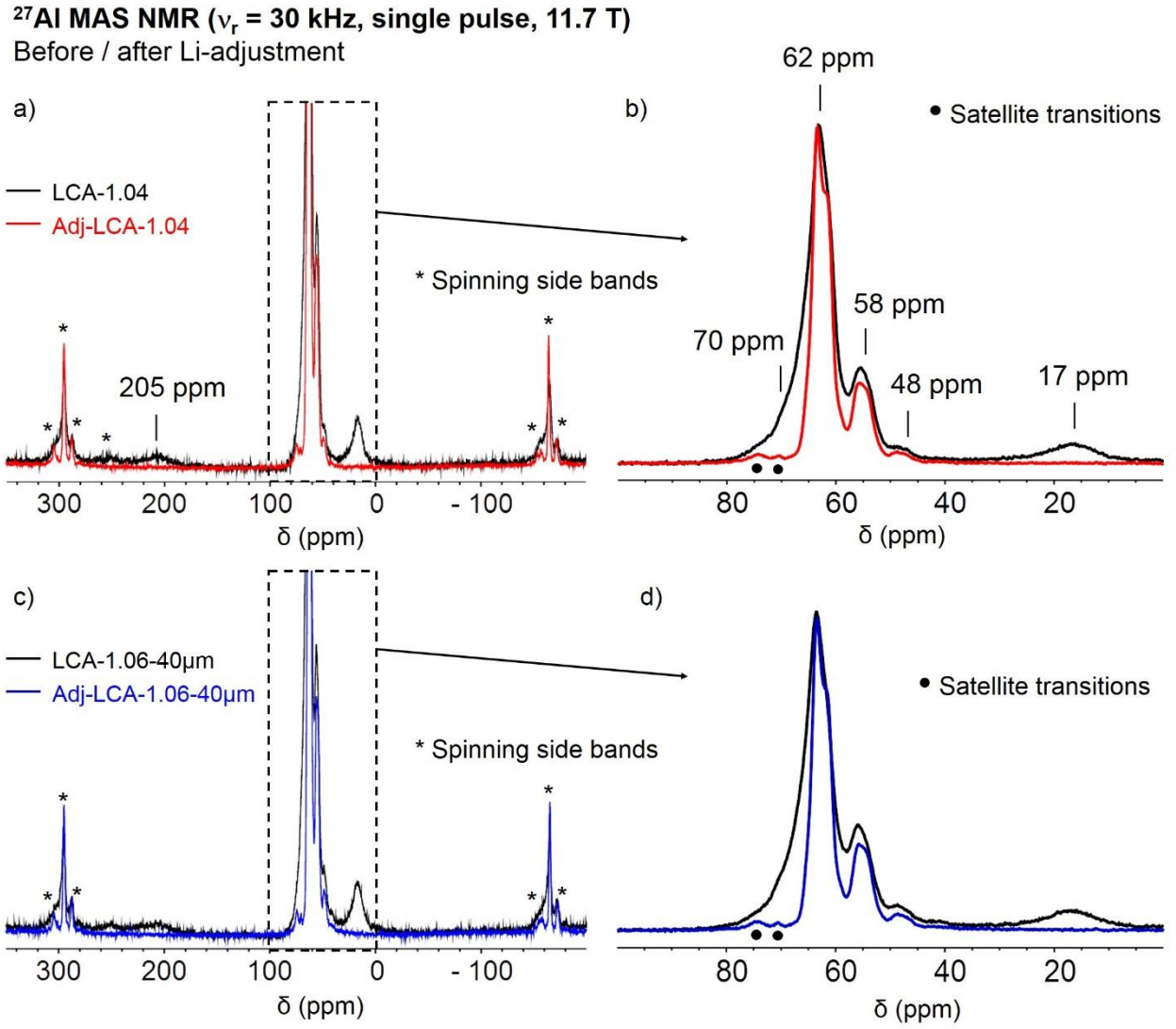

***Figure C41**.a) [27]Al MAS NMR spectra recorded at 130.33 MHz using a 30 kHz spinning frequency for non Li-adjusted LCA-1.04 (Group A), as compared to its Li-adjusted analogue Adj-LCA-1.04. A zoom on the central transitions is given in b). c) [27]Al MAS NMR spectra recorded at 130.33 MHz using a 30 kHz spinning frequency for non Li-adjusted LCA-1.06-40µm (Group B), as compared to its Li-adjusted analogue Adj-LCA-1.06-40µm. A zoom on the central transitions is given in d).*

likely due to Al in AlO_5 environment with no IS-Co^{3+} close by (see **Figure C43**). In addition to these extra signals, signals assigned to Al in "Al-(Al_nCo_{6-n})" environments with $0 \leq n \leq 6$ are still observed in the [0, 100 ppm] range. The most intense signals at ~ 62 ppm, ~ 55 ppm and ~ 48 ppm respectively arise from Al-(Al_0Co_6), Al-(Al_1Co_5) and Al-(Al_2Co_4) surroundings, with intensity ratio approximately following the expectations for a statistical distribution of Al for a 4% doped sample. However, the existence of an intense signal ascribed to Al-(Al_6Co_0) surroundings at ~ 17 ppm suggests that Al-rich domains (α-$LiAlO_2$ type) are still found within LCA-1.04 and LCA-1.06-40µm. These domains are most likely too narrow to diffract, which explains that peaks arising from the layered α-$LiAlO_2$ phase are not found in the corresponding XRD patterns. Indeed, the difference of cell parameters between LCA ($a_{hex} \approx 2.814$ Å; $c_{hex} \approx 14.064$ Å) and α-$LiAlO_2$ ($a_{hex} \approx 2.800$ Å; $14.18 \leq c_{hex} \leq 14.22$ Å)[23,53,54] should be large enough to distinguish additional peaks in the hypothesis of large Al-rich regions. Insufficient resolution coming from the use of routine XRD could also make the observation of additional diffraction peaks impossible.

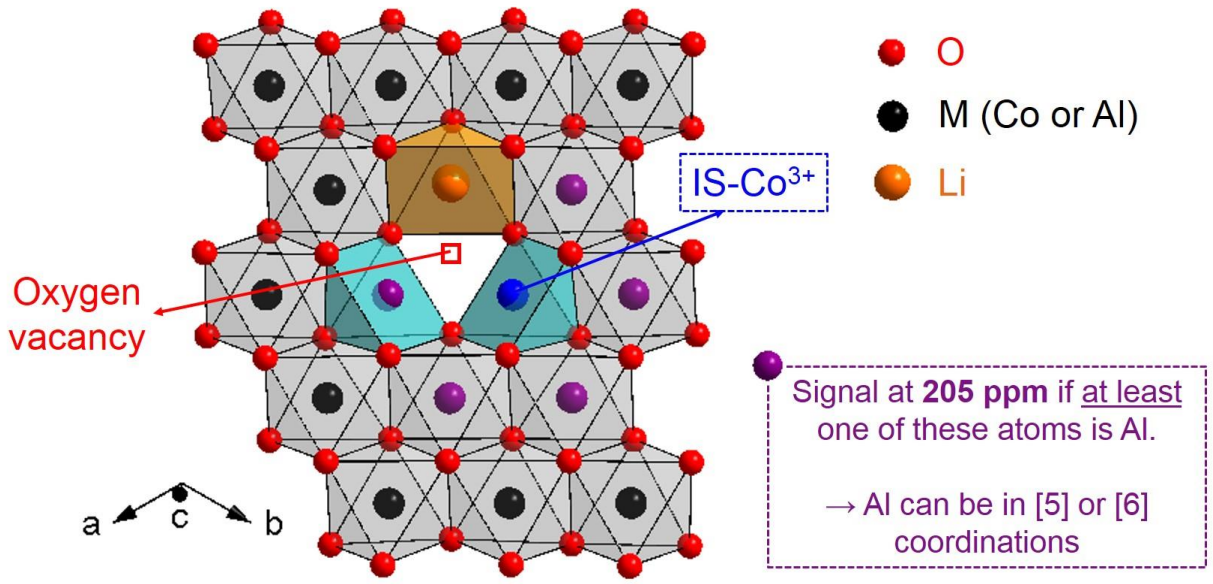

***Figure C42**. Schematic representation of the Al repartition giving rise to the signal observed at ~ 205 ppm in the ^{27}Al NMR spectra of the intermediate LCA-1.04 (Group A) and LCA-1.06-40µm (Group B).*

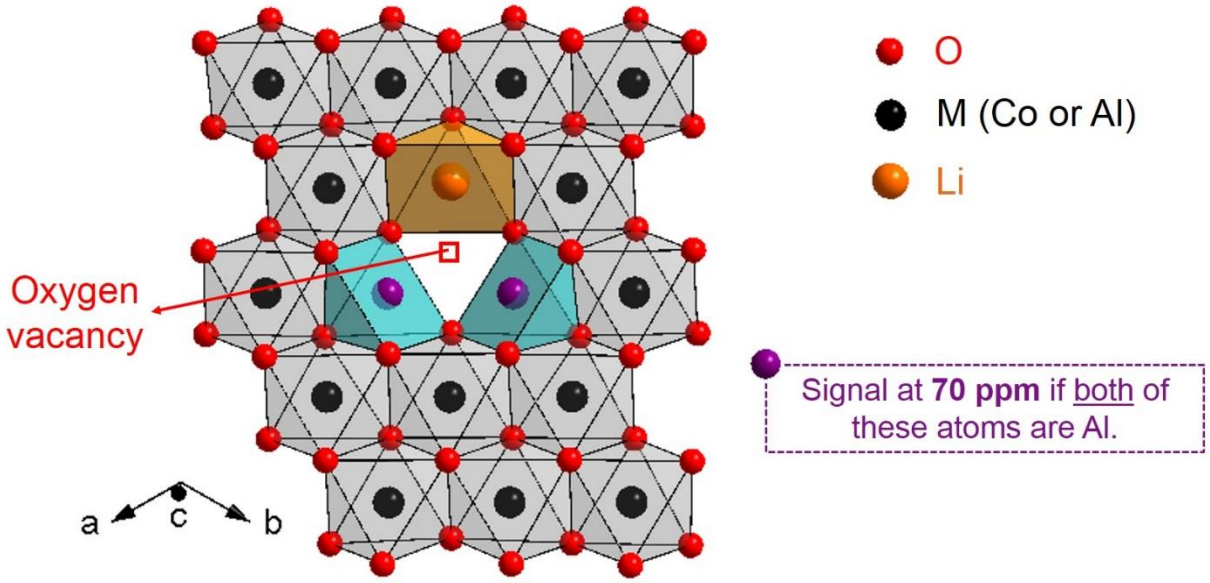

Figure C43*. Schematic representation of the Al repartition giving rise to the signal observed at ~ 70 ppm in the ^{27}Al NMR spectra of the intermediate LCA-1.04 (Group A) and LCA-1.06-40µm (Group B).*

Therefore, we propose that the intermediates LCA-1.04 and LCA-1.06-40µm are overlithiated 4% Al-doped LCO in which homogeneously Al-doped domains ("overl-LCA") coexist with inhomogeneous α-$LiAlO_2$ type environments. This hypothetical Al distribution is schematically represented in **Figure C44**. Additional data would be required to determine if the inhomogeneities are found at the inter- or intra- particle scale, as well as in the bulk or at the surface. This result also highlights that the 3rd step of our synthesis is more than a simple "Li-adjustment" step we assumed it to be so far: as no α-$LiAlO_2$ type environments are found in the final adjusted LCA samples initially prepared with $(Li/M)_1 > 1.00$, a parallel reaction must have occurred which has helped homogenizing the Al gradients within the powders.

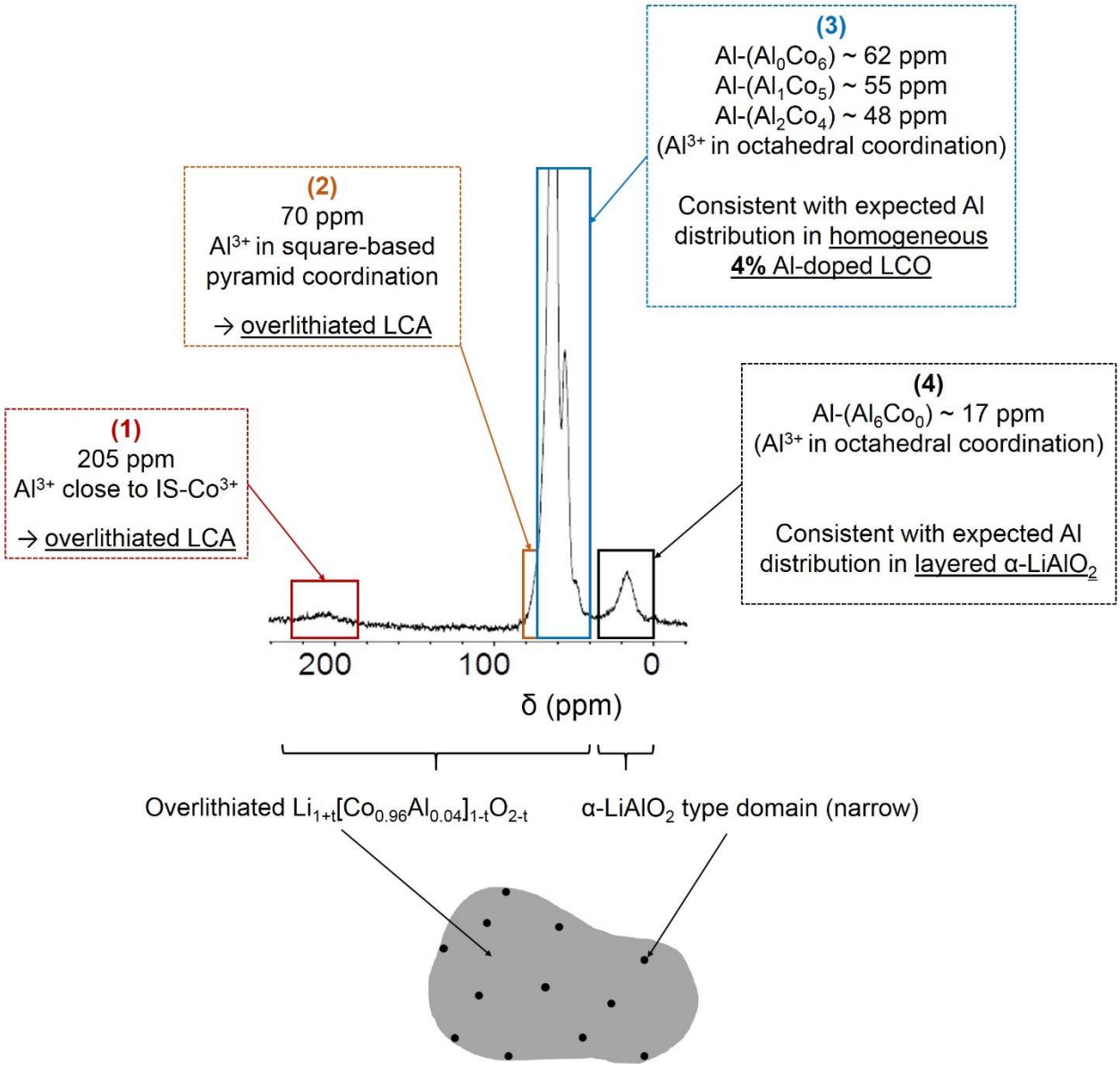

Figure C44*. Summary of conclusions drawn from* ^{27}*Al MAS NMR results and associated schematic representation.*

Figure C45 shows the Al NMR spectrum recorded for the intermediate LCA-1.00-40µm as compared to the one of Adj-LCA-1.00-40µm (**Figure C45.a**), and to the one of LCA-1.06-40µm (**Figure C45.b**). No signals assigned to Al close to paramagnetic IS-Co^{3+} are logically found in the former; this spectrum actually shows great similarities with the spectrum observed for

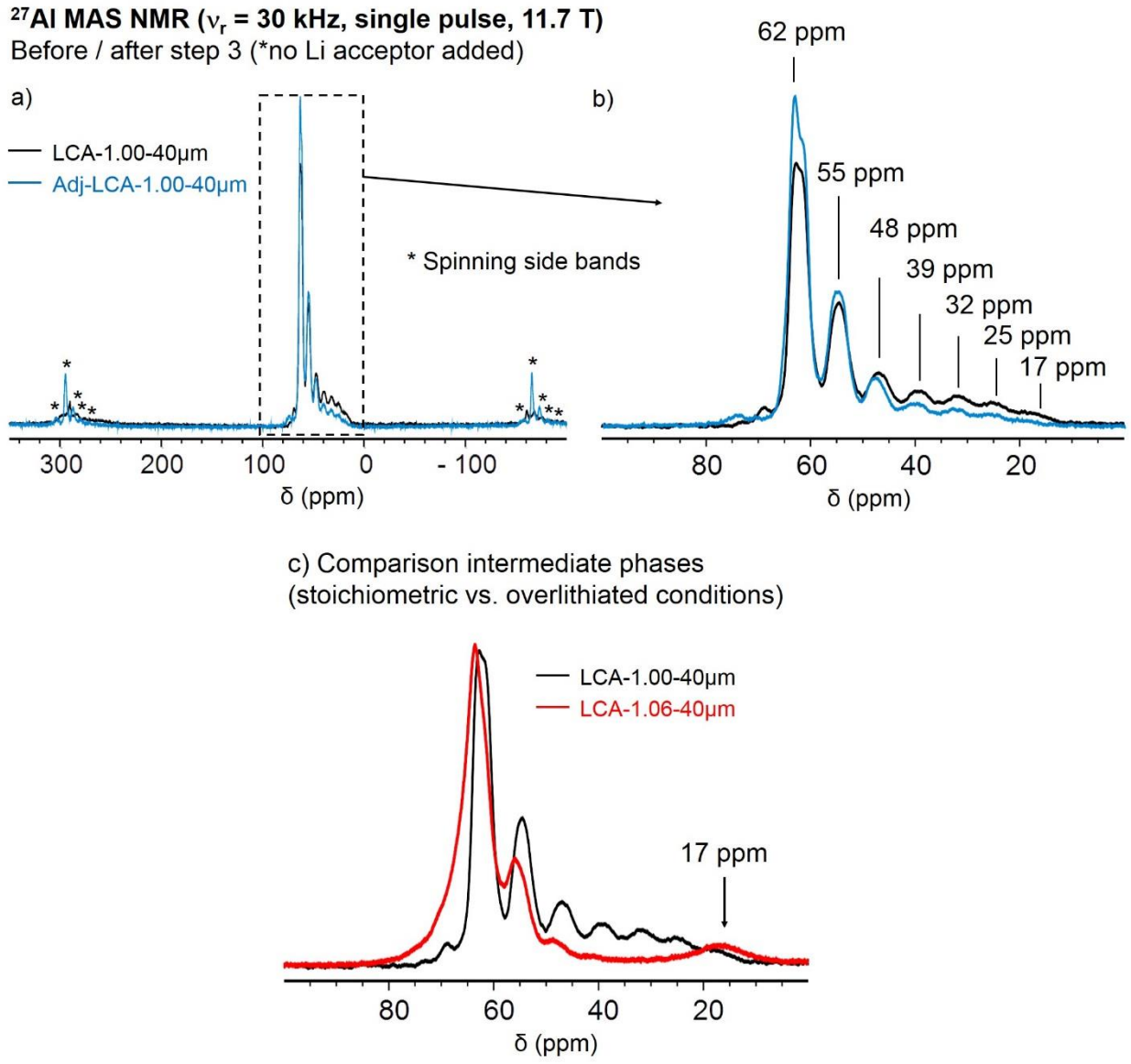

Figure C45*.a) [27]Al MAS NMR spectra recorded at 130.33 MHz using a 30 kHz spinning frequency for non Li-adjusted LCA-1.00-40µm (Group B), as compared to its "Li-adjusted" analogue Adj-LCA-1.00-40µm. A zoom on the central transitions is given in b). As this material was prepared in stoichiometric conditions, no addition of mix-$Co_{3-z}Al_zO_4$ was necessary. c) Comparison of the [27]Al MAS NMR spectra recorded for non Li-adjusted LCA-1.00-40µm and LCA-1.06-40µm.*

Adj-LCA-1.00-40µm. Only the series of signals ascribed to Al-(Al_nCo_{6-n}) at ~ 62, 55, 48, 40, 33, 26 and 18 ppm ($0 \leq n \leq 6$) can be seen, which proves the formation of LCA with inhomogeneous Al distribution after the heat treatment of mix-$Co_{3-z}Al_zO_4$ and Li_2CO_3 introduced in stoichiometric proportions. The intensity for the contribution at ~ 18 ppm is interestingly negligible: significantly less α-$LiAlO_2$ type environments are found in LCA-1.00-40µm as compared to LCA-1.06-40µm. The formation of α-$LiAlO_2$ seems to be somehow favored when excess Li_2CO_3 is involved in the preparation of our 4% Al-doped LCO.

Thus, the formation of overl-LCA and α-$LiAlO_2$ type surroundings in Step 2 of our synthesis seems somehow favorable to achieve homogeneous Al distribution in the final 3rd step in which mix-$Co_{3-z}Al_zO_4$ is added. The absence of formation of both overl-LCA and α-$LiAlO_2$ could explain why no homogeneous Al distribution may be obtained for LCA from Approach n°1. A reasonable hypothesis could be that the interdiffusion of the transition metal ions is made easier in these media, which eventually helps completing a statistical distribution of Al within the powders of Adj-LCA-X(-40µm) samples at the outcome of Step 3. One could also imagine that the defects generated by the presence of excess Li inside the layers of overl-LCA in non Li-adjusted LCA somehow contributes to the homogenization of Al gradients during the 3rd step of the synthesis. Note that a side attempt to form LCA from the reaction of undoped overl-LCO (Li/M = 1.08) with Al_2O_3 and mix-$Co_{3-z}Al_zO_4$ at 980 °C for 10 hours did not lead to a homogeneous distribution of Al in the final powder (see **Figure C46**). Indeed, the SXRD and Al NMR results plotted in **Figure C46** suggest that the formation of a mixture of $LiCoO_2$ + $LiCo_{0.7}Al_{0.3}O_2$ was achieved. Such result suggests that if Al is not yet in the close vicinity of the defects induced by the presence of Li excess inside the layers of the intermediate overlithiated phase, no homogeneous Al distribution is again obtained. At this point, a reasonable hypothesis taking account all previous

results would be that homogeneous Al doping may be achieved through the co-diffusion of Li and Al within a mandatory intermediate overl-LCA.

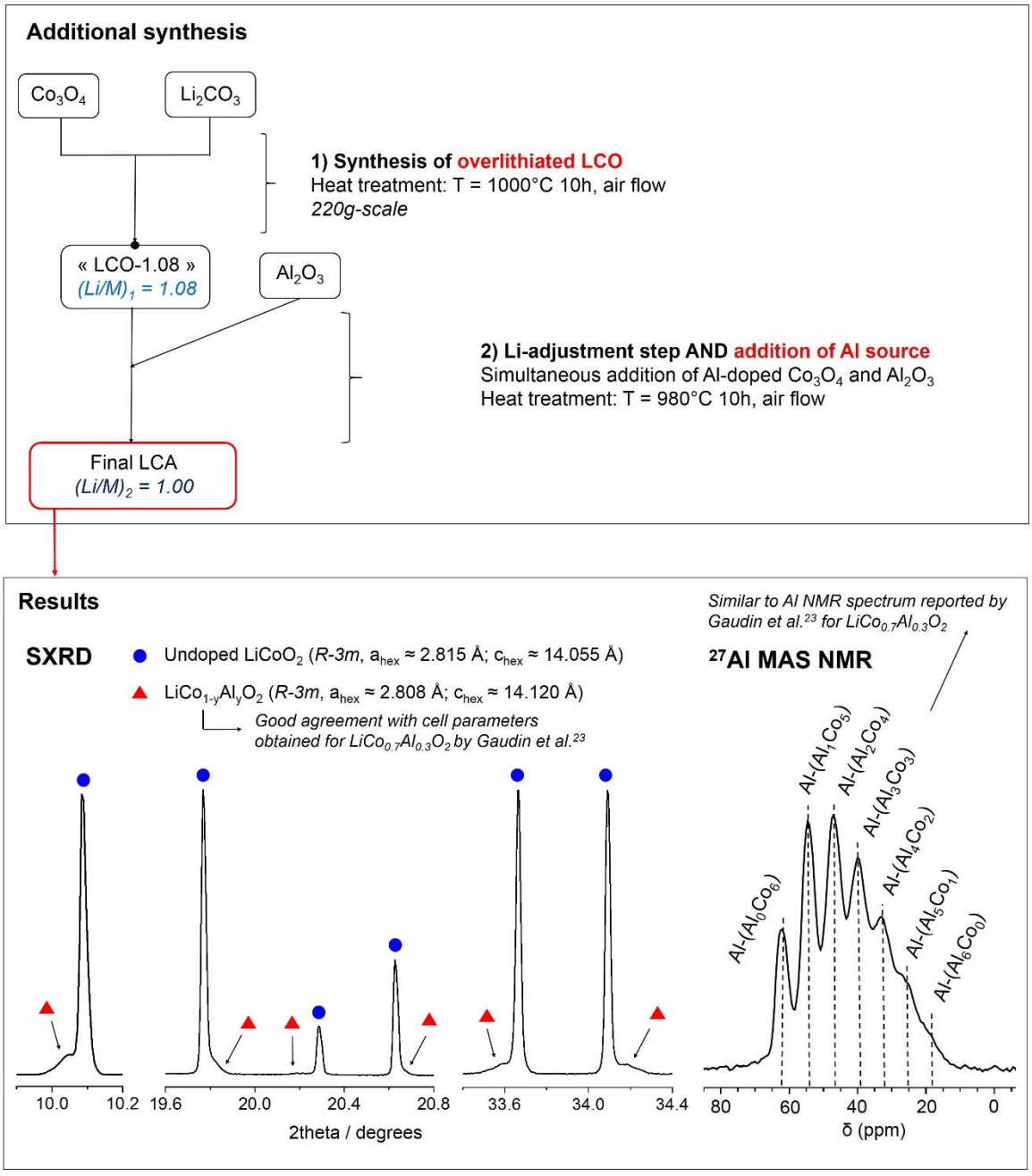

Figure C46*. Additional attempt to form a $LiCo_{0.96}Al_{0.04}O_2$ phase according to the synthesis reported in a). Zooms on peaks of interest in the SXRD pattern and ^{27}Al MAS NMR spectrum of the final synthesized phase are also given.*

C.5 General conclusions for Part C

In Part C, we successfully prepared various 4% Al-doped LCO (LCA) powders with well controlled Li and Al stoichiometries by solid state reaction of Li_2CO_3 and oxide precursors (Co_3O_4 and Al_2O_3) introduced either in stoichiometric proportions (**Approach n°1, $(Li/M)_1 \leq 1.00$**) or non stoichiometric proportions (**Approach n°2, $(Li/M)_1 > 1.00$**).

Although the powders obtained from Approach n°1 were indeed LCA materials, inhomogeneous Al doping was systematically evidenced by the means of synchrotron X-ray diffraction and ^{27}Al / ^{59}Co MAS NMR. The chemical nature of the metal oxide precursor (mix-$Co_{3-z}Al_zO_4$ or an unreacted mixture of Co_3O_4 and Al_2O_3) proved to have an effect on the final Al distribution in the LCA powders prepared in such conditions, though its impact was relatively weak.

Aluminum was more homogeneously distributed in LCA powders prepared with an excess of Li_2CO_3 (Approach n°2). For the first time, a LCA powder prepared by solid state route with $(Li/M)_1 = 1.04$ (in the absence of any specific control of particle morphology or size) showed a comparable Al distribution to a LCA sample obtained from a co-precipitation route. The viability of this approach was also confirmed for the preparation of LCA powders with large particles (~ 40 µm), which is a clear requirement to achieve proper packing density in the LCA-based electrodes. Introducing slightly more Li_2CO_3 was however mandatory to achieve homogeneous doping in this case ($(Li/M)_1 = 1.06$). Although we only showed results for 4% Al-doped LCO powders throughout this part, Approach n°2 was also validated for the preparation of homogeneous 10% Al-doped LCO by Adam Bertrand during his Master's degree internship. A logical follow-up would be to implement Approach n°2 to other dopants and/or co-dopants, such as Mg, Ti, etc.

The inhomogeneity of Al doping in LCA powders prepared according to Approach n°1 was also evidenced through electrochemical testing in Li cells. Indeed, the changes of slope associated to the monoclinic transition typically expected for stoichiometric LCO was still observed in the 1st cycle curves for these LCA samples when it should not. Electrochemical profiles for all samples prepared with the second approach were smoother and somehow all comparable, which prevented us to establish a finer relation between the homogeneity of Al doping for LCA powders prepared with Approach n°2 ($(Li/M)_1 > 1.00$) and possible structural changes when cycled in Li cells. In any case, the dx/dV profiles at high voltage for each one of the LCA tested suggested that the formation of the H1-3 phase could be not completely hindered with 4% Al doping. A more systematic study, comparable to the one performed in Part B, would be required to draw proper conclusions to this end and link the electrochemical properties at high voltage to the Al-distribution in the samples.

At this point of the project, we believe that the addition of excess Li_2CO_3 drives the formation of an intermediate phase mainly composed of overlithiated $Li_{1+t}[Co_{0.96}Al_{0.04}]_{1-t}O_{2-t}$ with very α-$LiAlO_2$ domains at the local scale. The homogenization of Al distribution during the heat treatment of this intermediate could possibly be performed through a favorable co-diffusion of Li and Al in both these media, which could explain why the synthesis of homogeneous LCA from the reaction between overlithiated $Li_{1+t}Co_{0.961-t}O_{2-t}$ and Al_2O_3 is unsuccessful. The defects generated by the presence of excess Li inside the layers of overl-LCA most likely play a key role in the co-diffusion process, as no homogeneously doped LCA powders can be synthesized when Li_2CO_3 is introduced in stoichiometric proportions. It may be related to the good affinity of Al^{3+} in [5] environments found around the Li excess in the transition metal (TM) plane. Efforts will be required to properly understand the exact mechanisms of reaction involved in the successful preparation of LCA by Approach n°2.

C.6 Bibliography Part C

(1) Zhuang, Q.; Xu, J.; Fan, X.; Wei, G.; Dong, Q.; Jiang, Y.; Huang, L.; Sun, S. $LiCoO_2$ Electrode/Electrolyte Interface of Li-Ion Batteries Investigated by Electrochemical Impedance Spectroscopy. *Sci. China Ser. B Chem.* **2007**, *50* (6), 776–783. https://doi.org/10.1007/s11426-007-0088-7.

(2) Würsig, A.; Buqa, H.; Holzapfel, M.; Krumeich, F.; Novák, P. Film Formation at Positive Electrodes in Lithium-Ion Batteries. *Electrochem. Solid-State Lett.* **2005**, *8* (1), A34–A37. https://doi.org/10.1149/1.1836114.

(3) Ohzuku, T.; Ueda, A. Solid-State Redox Reactions of $LiCoO_2$ ($R\bar{3}m$) for 4 Volt Secondary Lithium Cells. *J. Electrochem. Soc.* **1994**, *141* (11), 2972–2977. https://doi.org/10.1149/1.2059267.

(4) Amatucci, G. G.; Tarascon, J. M.; Klein, L. C. CoO_2, The End Member of the Li_xCoO_2 Solid Solution. *J. Electrochem. Soc.* **1996**, *143* (3), 1114–1123. https://doi.org/10.1149/1.1836594.

(5) Chen, Z.; Lu, Z.; Dahn, J. R. Staging Phase Transitions in Li_xCoO_2. *J. Electrochem. Soc.* **2002**, *149* (12), A1604–A1609. https://doi.org/10.1149/1.1519850.

(6) Xia, H.; Lu, L.; Meng, Y. S.; Ceder, G. Phase Transitions and High-Voltage Electrochemical Behavior of $LiCoO_2$ Thin Films Grown by Pulsed Laser Deposition. *J. Electrochem. Soc.* **2007**, *154* (4), A337–A342. https://doi.org/10.1149/1.2509021.

(7) Duffiet, M.; Blangero, M.; Cabelguen, P.-E.; Delmas, C.; Carlier, D. Influence of the Initial Li/Co Ratio in $LiCoO_2$ on the High-Voltage Phase-Transitions Mechanisms. *J. Phys. Chem. Lett.* **2018**, 5334–5338. https://doi.org/10.1021/acs.jpclett.8b02252.

(8) Amatucci, G. G.; Tarascon, J. M.; Klein, L. C. Cobalt Dissolution in $LiCoO_2$-Based Non-Aqueous Rechargeable Batteries. *Solid State Ion.* **1996**, *83* (1–2), 167–173. https://doi.org/10.1016/0167-2738(95)00231-6.

(9) Needham, S. A.; Wang, G. X.; Liu, H. K.; Drozd, V. A.; Liu, R. S. Synthesis and Electrochemical Performance of Doped $LiCoO_2$ Materials. *J. Power Sources* **2007**, *174* (2), 828–831. https://doi.org/10.1016/j.jpowsour.2007.06.228.

(10) Zou, M.; Yoshio, M.; Gopukumar, S.; Yamaki, J. Performance of $LiM_{0.05}Co_{0.95}O_2$ Cathode Materials in Lithium Rechargeable Cells When Cycled up to 4.5 V. *Chem. Mater.* **2005**, *17* (6), 1284–1286. https://doi.org/10.1021/cm048734o.

(11) Yu, J.; Han, Z.; Hu, X.; Zhan, H.; Zhou, Y.; Liu, X. The Investigation of Ti-Modified $LiCoO_2$ Materials for Lithium Ion Battery. *J. Power Sources* **2014**, *262*, 136–139. https://doi.org/10.1016/j.jpowsour.2014.03.073.

(12) Prahasini, P.; Sivakumar, M.; Subadevi, R.; Wang, F. M. Synthesis and Characterization of Cu Doped $LiCoO_2$ Cathode Material for Lithium Batteries Using Microwave Assisted Sol-Gel Synthesis. *Adv. Mater. Res.* **2012**, *584*, 345–349. https://doi.org/10.4028/www.scientific.net/AMR.584.345.

(13) Liu, A.; Li, J.; Shunmugasundaram, R.; Dahn, J. R. Synthesis of Mg and Mn Doped $LiCoO_2$ and Effects on High Voltage Cycling. *J. Electrochem. Soc.* **2017**, *164* (7), A1655–A1664. https://doi.org/10.1149/2.1381707jes.

(14) Liu, Q.; Su, X.; Lei, D.; Qin, Y.; Wen, J.; Guo, F.; Wu, Y. A.; Rong, Y.; Kou, R.; Xiao, X.; et al. Approaching the Capacity Limit of Lithium Cobalt Oxide in Lithium Ion Batteries via Lanthanum and Aluminium Doping. *Nat. Energy* **2018**. https://doi.org/10.1038/s41560-018-0180-6.

(15) Zhang, M.; Tan, M.; Zhao, H.; Liu, S.; Shu, X.; Hu, Y.; Liu, J.; Ran, Q.; Li, H.; Liu, X. Enhanced High-Voltage Cycling Stability and Rate Capability of Magnesium and Titanium Co-Doped Lithium Cobalt Oxides for Lithium-Ion Batteries. *Appl. Surf. Sci.* **2018**, *458*, 111–118. https://doi.org/10.1016/j.apsusc.2018.07.091.

(16) Ceder, G.; Chiang, Y.-M.; Sadoway, D. R.; Aydinol, M. K.; Jang, Y.-I.; Huang, B. Identification of Cathode Materials for Lithium Batteries Guided by First-Principles Calculations. *Nature* **1998**, *392* (6677), 694.

(17) Jang, Y.-I.; Huang, B.; Wang, H.; Sadoway, D. R.; Ceder, G.; Chiang, Y.-M.; Liu, H.; Tamura, H. $LiAl_yCo_{1-y}O_2$ ($R\bar{3}m$) Intercalation Cathode for Rechargeable Lithium Batteries. *J. Electrochem. Soc.* **1999**, *146* (3), 862–868. https://doi.org/10.1149/1.1391693.

(18) Myung, S.-T.; Kumagai, N.; Komaba, S.; Chung, H.-T. Effects of Al Doping on the Microstructure of $LiCoO_2$ Cathode Materials. *Solid State Ion.* **2001**, *139* (1–2), 47–56. https://doi.org/10.1016/S0167-2738(00)00828-6.

(19) Lee, Y.; Woo, A. J.; Han, K.-S.; Ryu, K. S.; Sohn, D.; Kim, D.; Lee, H. Solid-State NMR Studies of Al-Doped and Al_2O_3-Coated $LiCoO_2$. *Electrochimica Acta* **2004**, *50* (2–3), 491–494. https://doi.org/10.1016/j.electacta.2004.02.063.

(20) Xu, H.-T.; Zhang, H.; Liu, L.; Feng, Y.; Wang, Y. Fabricating Hexagonal Al-Doped $LiCoO_2$ Nanomeshes Based on Crystal-Mismatch Strategy for Ultrafast Lithium Storage. *ACS Appl. Mater. Interfaces* **2015**, *7* (37), 20979–20986. https://doi.org/10.1021/acsami.5b06844.

(21) Wang, H.; Jang, Y.-I.; Huang, B.; Sadoway, D. R.; Chiang, Y.-M. Electron Microscopic Characterization of Electrochemically Cycled $LiCoO_2$ and $Li(Al,Co)O_2$ Battery Cathodes. *J. Power Sources* **1999**, *81–82*, 594–598. https://doi.org/10.1016/S0378-7753(99)00108-1.

(22) Yoon, W.-S.; Lee, K.-K.; Kim, K.-B. Structural and Electrochemical Properties of $LiAl_yCo_{1-y}O_2$ Cathode for Li Rechargeable Batteries. *J. Electrochem. Soc.* **2000**, *147* (6), 2023–2028.

(23) Gaudin, E.; Taulelle, F.; Stoyanova, R.; Zhecheva, E.; Alcántara, R.; Lavela, P.; Tirado, J. L. Cobalt(III) Effect on ^{27}Al NMR Chemical Shifts in $LiAl_xCo_{1-x}O_2$. *J. Phys. Chem. B* **2001**, *105* (34), 8081–8087. https://doi.org/10.1021/jp0105948.

(24) Han, B.; Paulauskas, T.; Key, B.; Peebles, C.; Park, J. S.; Klie, R. F.; Vaughey, J. T.; Dogan, F. Understanding the Role of Temperature and Cathode Composition on Interface and Bulk: Optimizing Aluminum Oxide Coatings for Li-Ion Cathodes. *ACS Appl. Mater. Interfaces* **2017**, *9* (17), 14769–14778. https://doi.org/10.1021/acsami.7b00595.

(25) Alcántara, R.; Lavela, P.; Relaño, P. L.; Tirado, J. L.; Zhecheva, E.; Stoyanova, R. X-Ray Diffraction, EPR, and ^6Li and ^{27}Al MAS NMR Study of $LiAlO_2$−$LiCoO_2$ Solid Solutions. *Inorg. Chem.* **1998**, *37* (2), 264–269. https://doi.org/10.1021/ic9707220.

(26) Dahéron, L.; Dedryvère, R.; Martinez, H.; Flahaut, D.; Ménétrier, M.; Delmas, C.; Gonbeau, D. Possible Explanation for the Efficiency of Al-Based Coatings on $LiCoO_2$: Surface Properties of $LiCo_{1-x}Al_xO_2$ Solid Solution. *Chem. Mater.* **2009**, *21* (23), 5607–5616. https://doi.org/10.1021/cm901972e.

(27) Zhao, Y.; Li, J.; Dahn, J. R. Interdiffusion of Cations from Metal Oxide Surface Coatings into $LiCoO_2$ During Sintering. *Chem. Mater.* **2017**, *29* (12), 5239–5248. https://doi.org/10.1021/acs.chemmater.7b01219.

(28) Rodriguez-Carvajal, J. FULLPROF: A Program for Rietveld Refinement and Pattern Matching Analysis. *Physica B.(1993), 192, 55*.

(29) Garcia Casado, P.; Rasines, I. The Series of Spinels $Co_{3-s}Al_sO_4$ ($0 < s < 2$): Study of Co_2AlO_4. *J. Solid State Chem.* **1984**, *52* (2), 187–190. https://doi.org/10.1016/0022-4596(84)90190-7.

(30) Zayat, M.; Levy, D. Blue $CoAl_2O_4$ Particles Prepared by the Sol−Gel and Citrate−Gel Methods. *Chem. Mater.* **2000**, *12* (9), 2763–2769. https://doi.org/10.1021/cm001061z.

(31) Lee, G.-Y.; Ryu, K.-H.; Kim, H.-G.; Kim, Y.-Y. The Preparation of Blue $CoAl_2O_4$ Powders by the Malonate Method: The Effect of the Amount of Malonic Acid Used, the Formation Pathway of $CoAl_2O_4$ Crystallites and the Characteristics of the Prepared Powders. *Bull. Korean Chem. Soc.* **2009**, *30* (2), 373–377.

(32) Bolt, P. H.; Habraken, F. H.; Geus, J. W. Formation of Nickel, Cobalt, Copper, and Iron Aluminates From α- and γ-Alumina-Supported Oxides: A Comparative Study. *J. Solid State Chem.* **1998**, *135* (1), 59–69.

(33) Azurdia, J.; Marchal, J.; Laine, R. M. Synthesis and Characterization of Mixed-Metal Oxide Nanopowders Along the CoO_x-Al_2O_3 Tie Line Using Liquid-Feed Flame Spray Pyrolysis. *J. Am. Ceram. Soc.* **2006**, *0* (0), https://doi.org/10.1111/j.1551-2916.2006.01155.x.

(34) Smith, M. E. Application Of ^{27}Al NMR Techniques to Structure Determination in Solids. *Appl. Magn. Reson.* **1993**, *4* (1–2), 1–64. https://doi.org/10.1007/BF03162555.

(35) O'Dell, L. A.; Savin, S. L. P.; Chadwick, A. V.; Smith, M. E. A ^{27}Al MAS NMR Study of a Sol–Gel Produced Alumina: Identification of the NMR Parameters of the θ-Al_2O_3 Transition Alumina Phase. *Solid State Nucl. Magn. Reson.* **2007**, *31* (4), 169–173. https://doi.org/10.1016/j.ssnmr.2007.05.002.

(36) Samain, L.; Jaworski, A.; Edén, M.; Ladd, D. M.; Seo, D.-K.; Javier Garcia-Garcia, F.; Häussermann, U. Structural Analysis of Highly Porous γ-Al_2O_3. *J. Solid State Chem.* **2014**, *217*, 1–8. https://doi.org/10.1016/j.jssc.2014.05.004.

(37) Gaudon, M.; Apheceixborde, A.; Ménétrier, M.; Le Nestour, A.; Demourgues, A. Synthesis Temperature Effect on the Structural Features and Optical Absorption of $Zn_{1-x}Co_xAl_2O_4$ Oxides. *Inorg. Chem.* **2009**, *48* (19), 9085–9091. https://doi.org/10.1021/ic900482v.

(38) Kim, J.; Ilott, A. J.; Middlemiss, D. S.; Chernova, N. A.; Pinney, N.; Morgan, D.; Grey, C. P. ^{2}H and ^{27}Al Solid-State NMR Study of the Local Environments in Al-Doped 2-Line Ferrihydrite, Goethite, and Lepidocrocite. *Chem. Mater.* **2015**, *27* (11), 3966–3978. https://doi.org/10.1021/acs.chemmater.5b00856.

(39) Takahashi, Y.; Kijima, N.; Akimoto, J. Single-Crystal Synthesis and Structure Refinement of the $LiCoO_2$–$LiAlO_2$ Solid-Solution Compounds: $LiAl_{0.32}Co_{0.68}O_2$ and $LiAl_{0.71}Co_{0.29}O_2$. *J. Solid State Chem.* **2005**, *178* (12), 3667–3671. https://doi.org/10.1016/j.jssc.2005.09.016.

(40) Levasseur, S.; Ménétrier, M.; Shao-Horn, Y.; Gautier, L.; Audemer, A.; Demazeau, G.; Largeteau, A.; Delmas, C. Oxygen Vacancies and Intermediate Spin Trivalent Cobalt Ions in Lithium-Overstoichiometric $LiCoO_2$. *Chem. Mater.* **2003**, *15* (1), 348–354. https://doi.org/10.1021/cm021279g.

(41) Levasseur, S.; Menetrier, M.; Suard, E.; Delmas, C. Evidence for Structural Defects in Non-Stoichiometric HT-$LiCoO_2$: Electrochemical, Electronic Properties and ^{7}Li NMR Studies. *Solid State Ion.* **2000**, *128* (1–4), 11–24.

(42) Zhecheva, E.; Stoyanova, R.; Gorova, M.; Alcántara, R.; Morales, J.; Tirado, J. L. Lithium−Cobalt Citrate Precursors in the Preparation of Intercalation Electrode Materials. *Chem. Mater.* **1996**, *8* (7), 1429–1440. https://doi.org/10.1021/cm960009t.

(43) Modelling one- and two-dimensional solid-state NMR spectra - Massiot - 2002 - Magnetic Resonance in Chemistry - Wiley Online Library https://onlinelibrary.wiley.com/doi/abs/10.1002/mrc.984.

(44) Siegel, R.; Hirschinger, J.; Carlier, D.; Matar, S.; Ménétrier, M.; Delmas, C. ^{59}Co and ^{6,7}Li MAS NMR in Polytypes O2 and O3 of $LiCoO_2$. *J. Phys. Chem. B* **2001**, *105* (19), 4166–4174. https://doi.org/10.1021/jp003832s.

(45) Siegel, R.; Hirschinger, J.; Carlier, D.; Ménétrier, M.; Delmas, C. ^{59}Co, ^{23}Na NMR and Electric Field Gradient Calculations in the Layered Cobalt Oxides $NaCoO_2$ and $HCoO_2$. *Solid State Nucl. Magn. Reson.* **2003**, *23* (4), 243–262. https://doi.org/10.1016/S0926-2040(03)00017-1.

(46) Levasseur, S. Contribution à l'étude Des Phases $Li_x(Co,M)O_2$ En Tant Que Matériaux d'électrode Positive Des Batteries Li-Ion. Effets Combinés de La Surstoechiométrie En Lithium et de La Substitution (M= Ni, Mg), Université Sciences et Technologies-Bordeaux I, 2001.

(47) Imanishi, N.; Yamade, M.; Ichikawa, T.; Hirano, A.; Takeda, Y. Characterization and Electrode Behavior of Li_xCoO_2 (x>1). *Ionics* **2002**, *8* (1–2), 100–107. https://doi.org/10.1007/BF02377759.

(48) Antolini, E.; Giorgi, L.; Carewska, M. Formation of Li-and Mg-Doped $LiCoO_2$ Powders: A BET Analysis. *J. Mater. Sci. Lett.* **1999**, *18* (4), 325–327.

(49) Giorgi, L.; Carewska, M.; Patriarca, M.; Scaccia, S.; Simonetti, E.; Di Bartolomeo, A. Development and Characterization of Novel Cathode Materials for Molten Carbonate Fuel Cell. *J. Power Sources* **1994**, *49* (1–3), 227–243.

(50) Wicker, S. A.; Walker, E. H. Revisited: Decomposition or Melting? Formation Mechanism Investigation of $LiCoO_2$ via In-Situ Time-Resolved X-Ray Diffraction. *Inorg. Chem.* **2013**, *52* (4), 1772–1779. https://doi.org/10.1021/ic301516a.

(51) Perkinsa, J. D.; Bahna, C. S.; Parillaa, P. A.; McGrawb, J. M.; Fuc, M. L.; Duncana, M.; Yua, H.; Ginleya, D. S. $LiCoO_2$ and $LiCo_{1-x}Al_xO_2$ Thin Film Cathodes Grown by Pulsed

Laser Ablation. *J. Power Sources* **1999**, *81–82*, 675–679. https://doi.org/10.1016/S0378-7753(99)00266-9.

(52) Faenza, N. V.; Pereira, N.; Halat, D. M.; Vinckeviciute, J.; Bruce, L.; Radin, M. D.; Mukherjee, P.; Badway, F.; Halajko, A.; Cosandey, F.; et al. Phase Evolution and Degradation Modes of R$\bar{3}$m $LixNi_{1-y-z}Co_yAl_zO_2$ Electrodes Cycled Near Complete Delithiation. *Chem. Mater.* **2018**, *30* (21), 7545–7574. https://doi.org/10.1021/acs.chemmater.8b02720.

(53) Poeppelmeier, K. R.; Chiang, C. K.; Kipp, D. O. Synthesis of High Surface Area Lithium Aluminate (α-$LiAlO_2$). *Inorg. Chem.* **1988**, *27* (25), 4523–4524. https://doi.org/10.1021/ic00298a002.

(54) Marezio, M.; Remeika, J. P. High-Pressure Synthesis and Crystal Structure of α-$LiAlO_2$. *J. Chem. Phys.* **1966**, *44* (8), 3143–3144. https://doi.org/10.1063/1.1727203.

General conclusion

While $LiCoO_2$ remains one of the most used positive electrode materials in Li-ion batteries, fundamental knowledge regarding the phase transitions it experiences during the Li removal at high voltage was and is still missing. This project was dedicated to further understand the mechanisms of formation of such high voltage phases, and evaluate a possible influence of either the initial Li/Co stoichiometry in the pristine LCO powders or Al doping to hinder their completion.

In the first part of this manuscript, series of $LiCoO_2$ samples with well controlled initial Li/Co stoichiometries ($1.00 \leq Li/Co \leq 1.04$) and particle sizes were successfully synthesized from a solid state route, following the current industrial requirements. While their structures were evidenced by X-ray diffraction (XRD), ^{7}Li MAS NMR was key to detect the local defects in overlithiated LCO, generated by the use of an excess of Li_2CO_3 during their synthesis. Electrochemical testing confirmed the poor cycle stability of all LCO powders at high voltage, no matter their initial Li content. However, smoother 1st cycle profiles were systematically obtained for overlithiated LCO as compared to its stoichiometric analogue, first suggesting the existence of defects could impact the formation of the high voltage phases.

The *in situ* XRD data collected during the 1st charge of a stoichiometric LCO (st-LCO, initial Li/Co = 1.00) and an overlithiated LCO (overl-LCO, Li/Co = 1.05), and presented in a second part, revealed that the expected H1-3 and O1 structures were formed nonetheless at high voltage for both compounds, though with stacking faults, and delayed in the case of overl-LCO. Besides, the formation of an additional intergrowth structure at high voltage and a more complex O3 – O'3 – O3 phase transition at low voltage were evidenced in the case of st-LCO. *Ex situ* XRD performed on H1-3-Li_xCoO_2 powders prepared from Li electrochemical de-intercalation from both st-LCO and overl-LCO revealed that the initial Li/Co has no influence of its structure itself.

Although the use of Al doping was first motivated by a possible beneficial effect on the structural stability of LCO over cycling, the question of homogeneity of doping quickly arose. The investigation of phase transitions overcome by 4% Al-doped LCO (LCA) during the removal of Li at high voltage was subsequently delayed in order to first ensure that a homogeneous distribution of Al was found within the various pristine powders synthesized by solid state reaction of Co_3O_4, Li_2CO_3 and Al_2O_3. Thanks to SXRD and ^{27}Al MAS NMR, we showed that the use of an excess of Li_2CO_3 to first form an overlithiated LCA seems key to obtain final Li-adjusted LCA powders with satisfactory homogeneity of doping. As a matter of a fact, this is the first time the synthesis of homogeneously Al-doped LCO from a solid state route is reported. Al gradients were always achieved in samples prepared with precursors introduced in stoichiometric conditions. The viability of the process to prepare LCA powders with higher Al content was recently confirmed by Adam Bertrand during his master's thesis. Further work would now require to establish i) a possible influence of the dopant on the formation of the high voltage phases and ii) the effect of the homogeneity of doping, doping amount and Li stoichiometry in LCA on their electrochemical properties, which may be done in a new PhD student (Fatima El-Rami) in a new launched project.

Appendix

(1) In situ XRD performed at ICMCB (Part B)

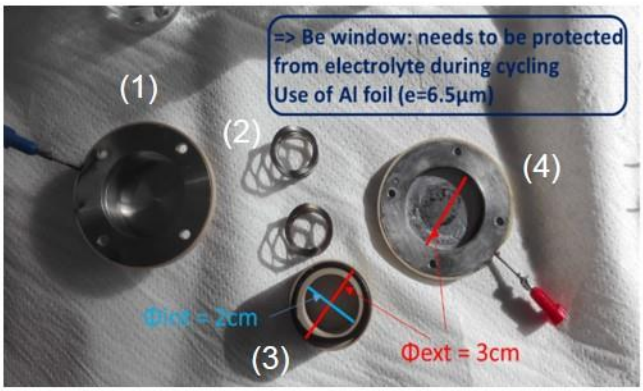

a) Homemade cell used for the in situ XRD measurements (Part B).

b) Electrodes of LCO:C:PVDF, casted onto 6.5-µm-thick aluminum foils. The latter is used as current collector and to protect the beryllium window.

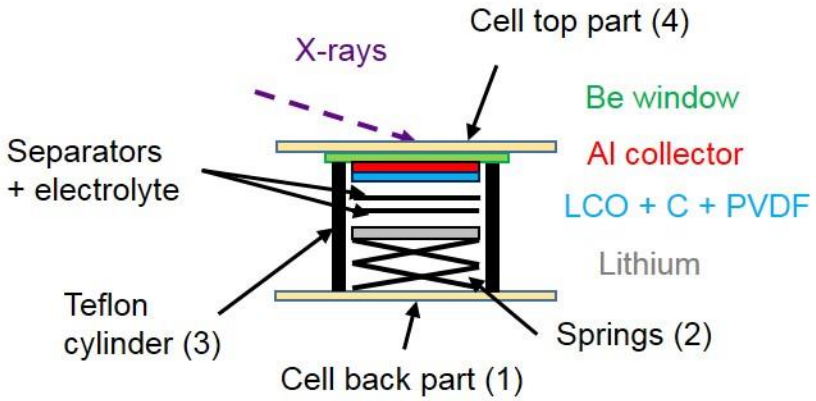

c) Schematic depiction of the cell assembly.

(2) In situ XRD data recorded at high voltage for two stoichiometric $LiCoO_2$ with varying particle size (Part B)

a)

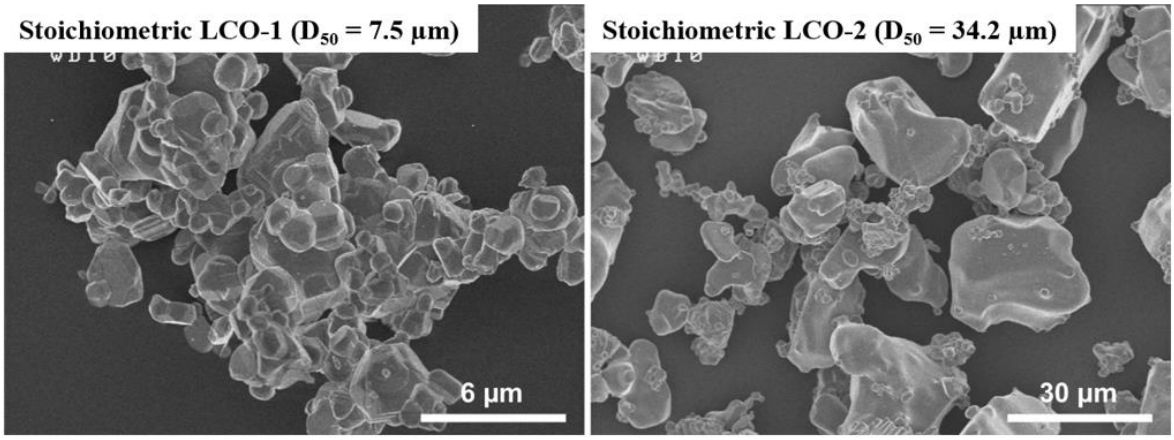

b)

Sample reference	Li:Co – ICP	BET specific surface area (m^2/g)	D_{50} (µm)
Stoichiometric LCO-1	1.00	0.50	7.5
Stoichiometric LCO-2	0.99	0.14	34.2

c)

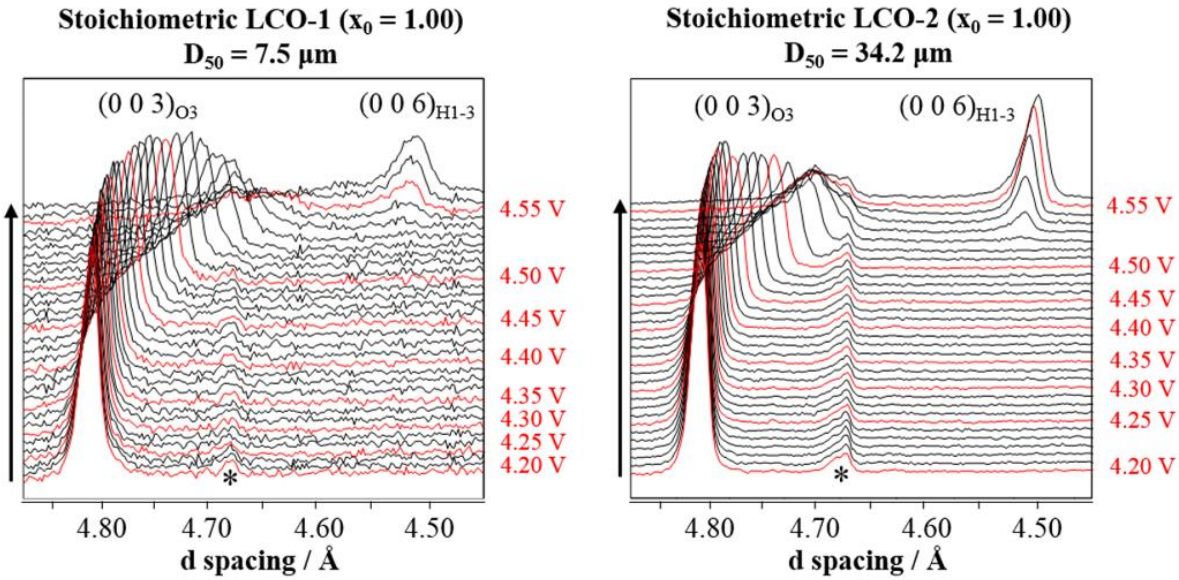

a) Scanning electron micrographs obtained for the two different st-LCO materials. ICP measured Li/Co ratios, BET specific surface areas and D_{50} for both samples are given in table b). c) Cumulated XRD patterns recorded in situ operando during the charge of the two stoichiometric LCO samples between ~ 4.20 V – 4.60 V plotted as a function of d spacing. It represents here the average distance between two layers of CoO_6 units. XRD patterns are plotted from the bottom to the top as we charge the compounds. The peak identified with (*) is a line from the cell.

(3) Additional information for in situ synchrotron X-ray diffraction (Part B)

ALBA Synchrotron, Cerdanyola del Vallès

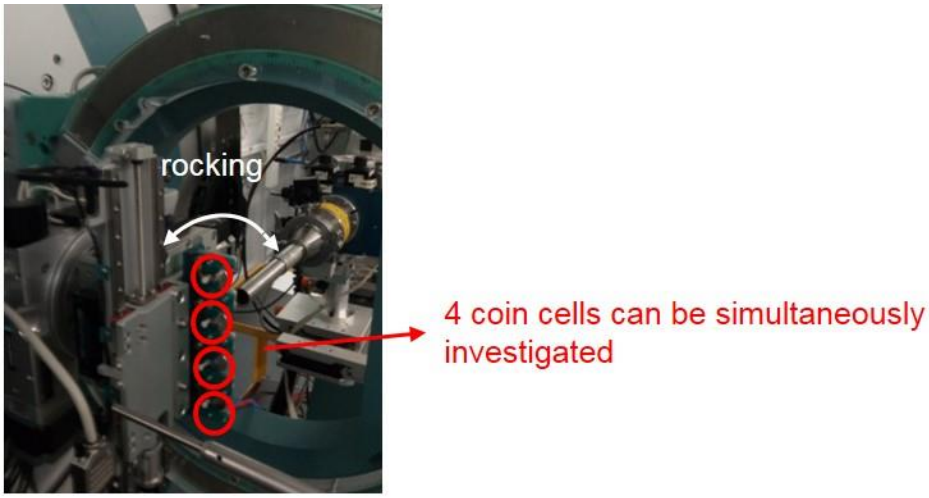

Measurement setup at the MSPD-BL04, ALBA synchrotron